The Dissertation Committee for Paul Alexander Wadsworth certifies that this is the approved version of the following dissertation:

Regulation of signaling and function of the voltage-gated sodium channel complex by protein:protein interactions

Committee:

Fernanda Laezza, MD, PhD, Mentor

B. Montgomery Pettitt, PhD, Chair

Michael Laposata, MD, PhD

Kristen Peek, PhD

Krishna Rajarathnam, PhD

Consuelo Walss-Bass, PhD

Regulation of signaling and function of the voltage-gated sodium channel complex by protein:protein interactions

by

Paul Alexander Wadsworth, B.S.

Dissertation

Presented to the Faculty of the Graduate School of

The University of Texas Medical Branch

in Partial Fulfillment

of the Requirements

for the Degree of

Doctor of Philosophy

The University of Texas Medical Branch

March, 2020

Dedication

This Dissertation is dedicated to my parents, Marion and Roy Wadsworth, for their unwavering encouragement and support.

Acknowledgements

First, I would of course like to acknowledge and give a special thanks to my mentor, Dr. Fernanda Laezza, for her constant support and guidance over the past four years. In addition to providing much insight into drug discovery, pharmacology, electrophysiology, and many other disciplines about which nothing of when I began, she has undoubtedly tolerated far more of my opinions and comments than deserved. I will always appreciate the time and effort you gave me, as well as your enthusiasm and excitement for rational drug design.

I would like to extend gratitude to my committee members for their time and support of my education. To Dr. Pettitt for your insight and critical analyses that provided a deeper understanding into molecular interactions. To Dr. Laposata for so freely offering advice and mentorship on my path to becoming as physician scientist. To Dr. Rajarathnam for providing insight into biochemistry, as well as challenging me to become a better scientist. To Dr. Peek for providing exposure to the population health sciences, as well as your enthusiasm toward helping make my project more translational. To Dr. Walss-Bass for your support and suggestions.

A big thanks to my sister, Annie Wadsworth, for your help with protein purification, PTS (including analysis), and all the other nonsense I asked of you.

Additionally, I give a huge thanks to Dr. Jake Lowry for his constant support of my work, be it in the form of scathing criticisms (founded or not), theoretical conversations, or simple day-to-day acts, all helping to elevate me to the status of celebrated scientist.

I must also thank Dr. Clifford Stephan and Ivy Nguyen (at A&M Houston) for their integral support with the HTS project, including the many, many plates that Ivy made and shipped to me as part of the hit validation studies.

I would also like to thank all of my laboratory members for their day-to-day help, and in particular to Dr. Aditya Singh for your fundamental contributions to many aspects of this project, especially related to molecular biology and electrophysiology. And I could not forget Dr. Neli Panova, who provided many small and unseen acts of support during my first two years, as well as for teaching me how to culture cells.

Finally, I would like to acknowledge and thank the PhRMA Foundation for awarding the PhRMA Fellowship in Pharmacology to me, and the financial support provided.

Regulation of signaling and function of the voltage-gated sodium channel complex by protein:protein interactions

Publication No._____

Paul Alexander Wadsworth

The University of Texas Medical Branch, 2020

Supervisor: Fernanda Laezza

As fundamental determinants of neuronal function, voltage-gated Na^+ (Nav) channels are important targets for therapeutic development against a wide range of health conditions. Dysfunction of Nav channels in the CNS is associated with disorders ranging from neurological (i.e., epilepsy, neurodegeneration) to psychiatric (i.e., major depression disorder, schizophrenia). Unfortunately, commercially available drugs targeting Nav channels are directed against highly conserved domains across Nav isoforms, giving rise to severe side effects such as cardiotoxicity and movement disorders. Thus, there is an unmet need for discovering new probes and pathways that regulate Nav channels that could potentially help designing new medications.

Recent evidence suggests that protein:protein interactions (**PPI**) between Nav channels and their accessory proteins play a key role in regulating neuronal firing, and that minimal disturbances to these tightly controlled PPI can lead to persistent maladaptive plasticity. These PPI interfaces are highly specific and provide ideal targets for drug

development, especially in the CNS where selectivity and specificity are vital for limiting side effects. However, for the most part how these protein:channel interactions are regulated in the cell is still poorly understood, and methods for assessing these interactions are lacking. Therefore, the goal of the present study was to develop robust assays to reconstitute the Nav channel complex in cells and identify cellular pathways and small molecules regulating PPI interfaces with the Nav channel complex.

Specifically, we focused on the PPI between Nav1.6 and its regulatory protein, fibroblast growth factor 14 (**FGF14**). Using a newly developed assay we screen cellular pathways followed by biophysical validation, we discovered a mechanism by which the JAK2 tyrosine kinase might directly influence neuronal firing through phosphorylation of FGF14. Furthermore, we conducted a high-throughput screening of ~45,000 small molecules and identified potent modulators of the FGF14:Nav1.6 complex that are functionally active and predicted to be permeable to the blood-brain barrier. While providing a robust in-cell screening platform that can be adapted to search for any channelopathy-associated regulatory protein, these results lay the potential groundwork for a new class of drugs targeting Nav channels with a broad range of applicability for CNS disorders.

TABLE OF CONTENTS

List of Tables

List of Figures

List of Abbreviations

AD	Alzheimer's Disease
AIS	Axon Initial Segment
ALK	Anaplastic Lymphoma Kinase
BDNF	Brain-Derived Neurotrophic Factor
CAMK2	Ca2+/Calmodulin Dependent Protein Kinases
CC_NCI	Custom Clinical and National Cancer Institute
CK2	Casein-Kinase II
CNS	Central Nervous System
CTB	CellTiter Blue
DMEM	Dulbecco Modified Essential Medium
DMSO	Dimethyl Sulfoxide
EM	Electron Microscopy
EPR	Electron Paramagnetic Resonance
GFP	Green Fluorescence Protein
GSK3β	Glycogen Synthase Kinase 3β
GCC	Gulf Coast Consortium
HEK293	Human Epithelial Kidney-293 cells
HPRD	Human Protein Reference Database
HTS	High-Throughput Screening
IPTG	Thio-β-D-Galacto-Pyranoside
iFGF	intracellular Fibroblast Growth Factor
FLT3	FMS-like tyrosine kinase 3
JAK2	Janus Kinase 2
LCA	Split-Luciferase Complementation Assay
LDH	Lactate Dehydrogenase
LTI	Long-Term Inactivation
MALDI	Matrix-Assisted Laser Desorption/Ionization
MEK1	Mitogen-Activated Protein Kinase Kinase (Aka MAPK2K1)
MD	Molecular Dynamics
MSN	Medium Spiny Neuron
NAc	nucleus accumbens
Nav	Voltage-Gated Na^+ Channel
PDGFR	platelet-derived growth factor receptor
PDK1	pyruvate dehydrogenase kinase 1
PI3K	phosphoinositide 3-kinases
PKA/C/G	Protein Kinase A/C/G
PLK1	polo-like kinase 1
PNS	Peripheral Nervous System
PPI	Protein:Protein Interactions
PTS	protein thermal shift
RAF	rapidly accelerated fibrosarcoma
ROCK1	rho-associated coiled-coil-containing protein kinase 1

RTK	Receptor Tyrosine Kinase
SCA27	spinocerebellar ataxia 27
SH2	Src Homology 2
SPR	Surface Plasmon Resonance
STAT3	Signal Transducer And The Activator Of Transcription 3
TNF-α	Tumor Necrosis Factor-α
TrkA/B/C	Tropomyosin receptor kinase A/B/C
VEGFR	vascular endothelial growth factor receptor
UTKinase	UT Austin Combined Kinase Collection
Z’	Z’-factor

Chapter 1. Introduction

Portions of this chapter have been published in Frontiers in Cellular Neuroscience as:

Intracellular Fibroblast Growth Factor 14: Emerging Risk Factor for Brain Disorders.

Di Re J, **Wadsworth PA**, Laezza F.

Available from: http://www.ncbi.nlm.nih.gov/pubmed/28469558

1.1. STRUCTURE AND FUNCTION OF VOLTAGE-GATED Na^+ CHANNELS

Voltage-gated Na^+ (Nav) channels, with the support of a diverse ensemble of auxiliary proteins tightly regulating their function, serve as the primary molecular determinants of neuronal excitability[1–4]. The fundamental component of a Nav channel consists of the pore-forming α subunit (~260 kDa), of which there are nine isoforms (Nav1.1-1.9) formed by four transmembrane domains (D1~D4) each containing six segments (S1~S6) and extracellular domains[5–7]. Transmembrane segments S1 to S4 in domain I-IV form voltage sensors which are responsible for channel opening, whereas transmembrane segments S5 to S6 from each of four domains form the central pore which allows Na^+ ions to permeate the cell (from the extracellular side to the intracellular side). Although highly homologous, the intracellular loops, as well as the N- and C-terminal tails, confer structural and functional specificity to each isoform through interactions with accessory subunits.

Despite a long period of challenges in determining the structure of large membrane proteins including Nav channels, advances within the past decade have been rapid. First, prokaryotic Nav channels were resolved using X-ray crystallography[1,5], followed by electron paramagnetic resonance (EPR) spectroscopy demonstrating the role of the C-terminal tail in these channels[8]. More recently, advances in cryo-electron microscopy (cryo-EM) have led to the identification of eukaryotic Nav channels[7], including the human Nav channel (cardiac Nav1.5) structure at atomic resolution (**Figure 1.1**)[9]. Although these remarkable achievements have led to a far more refined understanding of the structure-function relationship, in the native environment Nav channels form large macromolecular

complexes with accessory proteins that control the channel's biophysical properties. However, the structural organization and physiologic role of these accessory proteins is still not fully understood.

Additionally, Nav channel isoforms exhibit marked molecular differences, as well as diverge with respect to their localization within specific tissue types. Specifically, Nav1.1-1.3 and 1.6 channel isoforms are localized in the central nervous system (CNS); Nav1.7-1.9 channel isoforms are localized in the peripheral nervous system (PNS); the Nav1.4 channel isoform is localized in skeletal muscle; and the Nav1.5 channel isoform is localized in cardiac muscle[10,11]. Given their ubiquity throughout these organs, it is unsurprising that Nav channel dysfunction has been associated with a multitude of channelopathies including epilepsy[12–14], pain[15–17], schizophrenia[18,19], and cardiac arrhythmias[20,21].

1.2. NAV CHANNELS AS A PHARMACOLOGIC TARGET

Nav channel blockers are currently being used in conjunction with conventional neuropsychopharmacological agents for the treatment of bipolar disorder, depression, Alzheimer's disease and schizophrenia, elucidating the role of Nav channels in both neurologic and neuropsychiatric disorders[1,22]. Moreover, a number of recent reports indicate that Nav channels play important roles in cancer cell migration and proliferation[23,24],19-23 the development of diabetes[25] and other human diseases progression[1]. Given their primacy in the pathophysiology of CNS disorders, PNS disorders,

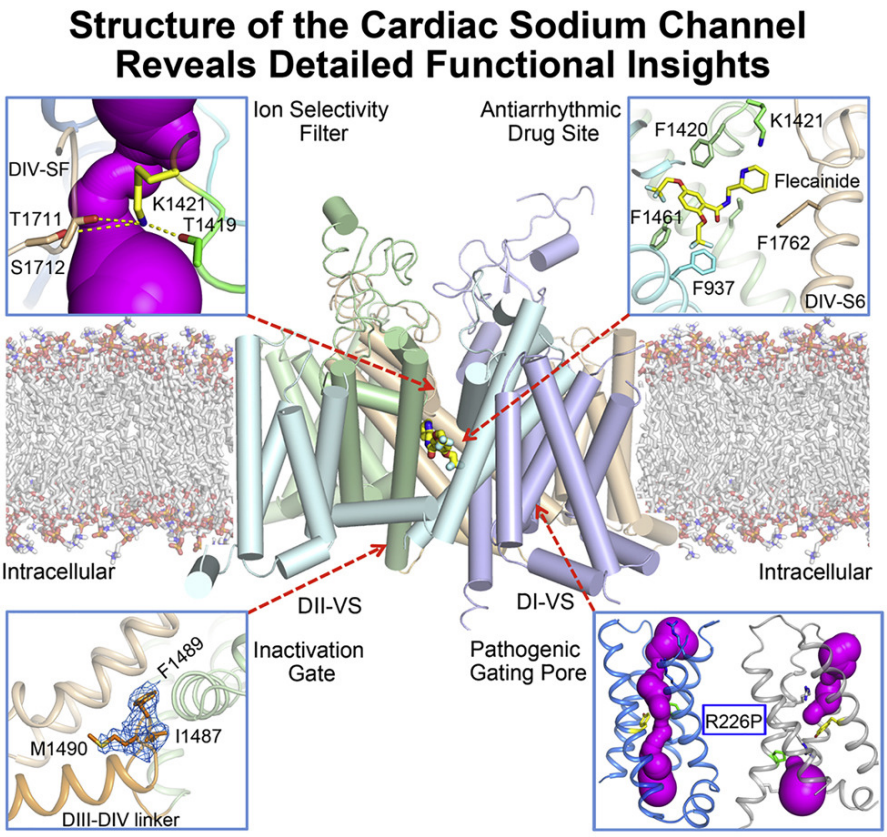

Figure 1.1. The high-resolution structure of the cardiac Nav1.5 channel, resolved by cryo-EM. Graphical abstract taken with permission from Jiang et al, Cell (2020). The Nav1.5 channel is highly homologous to the Nav1.6 channel, which is studied in the project presented here.

cancer and other human diseases, Nav channels have been the target of many drug discovery campaigns.

Nav1.6, coded by SCN8A gene, is one of the most abundantly distributed Nav channels in the human CNS[26,27]. Accumulated studies revealed that Nav1.6 pays crucial roles in the pathogenesis of epilepsy[28]. During electrical induction of status epilepticus, the expression of Nav1.6 increases in medial entorhinal cortex (mEC) layer II neurons[29]. These neurons became hyperexcitable, and the neuronal hyperexcitability was suppressed by a Nav1.6 inhibitor[29]. Similarly, direct evidences have been observed that loss of Nav1.6 function suppress the neuronal excitability in SCN8A null mice model[28]. Interestingly,

membranes containing Nav1.6 are more excitable than those containing only Nav1.1 and Nav1.2, and dysfunction of Nav1.6 lead to a higher threshold for initiation of action potentials[30]. Overall, Nav1.6 displays an important role in electrical and chemical signaling in the CNS. Therefore, selective inhibition of Nav1.6 may offer a new avenue for the treatment of human CNS disorders without the undesirable side effects that arise from off-target effects. However, the practical aspects of achieving this goal are far more complicated. One of the major obstacles in designing selective Nav1.6 modulators arises from the high sequence homology shared by Nav isoforms.

1.3. Developing Isoform-Specific Drugs Targeting Nav Channels

Abundant translational relevance has made the Nav channel an appealing target for drug development. Despite strong interest in developing drugs targeting Nav channels, approved medications including local anesthetics (i.e. lidocaine) and anti-epileptic drugs (i.e., carbamazepine, lamotrigine) target highly conserved sites (not isoform specific). A series of aryl sulfonamide Nav1.6 inhibitors were recently reported that demonstrated potent anticonvulsant activity in mouse models of epilepsy[31]. Unfortunately, these compounds failed due to both cross-reactivity with Nav1.2 channels and poor pharmacokinetics. Recent advances in development of analgesic medications have led to several classes of drugs targeting Nav1.7. Unfortunately, these medications have many side effects, including the more recent Nav1.7 modulators which have poor "Target Engagement" (low clinical efficacy despite promising pre-clinical evidence) (**Table 1.1**). Hence, there is a need for new drug design strategies that would enable isoform-specific modulation of Nav channels, and thereby treatments for specific diseases.

Drug candidate	Target, Mechanism	Pain Management Efficacy	Indications	Limitations	Side effects/Abuse Liability
Sulfonamides	State-dependent Nav1.7 inhibition/bind to depolarized conformation of voltage sensor of α subunit	Limited *in vivo* efficacy	Post-surgical acute pain, chronic pain, inherited erythromelalgia	Poor clinical endpoints/ low target engagement/poor selectivity	Potentially high due to high exposure multiples
Cystine Knot Peptides	State-independent Nav1.7 inhibition/bind to extracellular voltage-sensor of α subunit	Limited *in vivo* efficacy	Post-surgical pain, chronic pain, severe pain	Low target engagement	Unknown
Guanidinium compounds	State-independent Nav1.7 inhibition/bind to extracellular vestibule of α subunit	Demonstrated preclinical efficacy	Acute post-operative pain	Preclinical	Potential side effects

Table 1.1. Known pain medications targeting Nav1.7.
Compelling evidence from human genetic studies demonstrating pain insensitivity in patients carrying single point mutations of Nav1.7 have spurred a great interest in pursuing this channel isoform as a target for novel anti-pain medications. There are three broad groups of Nav1.7 drug candidates: *i*) sulfonamides; *ii*) cystine knot peptides; *iii*) guanidinium compounds.

Protein:protein interactions (**PPI**) between Nav channels and their accessory proteins fine-tune neuronal excitability, and mutations in either the channel itself[32,33] or these regulatory proteins[18,34–38] give rise to neuropsychiatric disorders that have few viable treatment options. PPI interfaces are specific and flexible, making them ideal scaffolds for probe and drug design[39,40] especially within the CNS where selectivity and specificity are vital for limiting side effects[41]. Thus, one potential approach for developing isoform selective inhibitors of Nav1.6 is through identifying small molecules targeted against PPI interfaces of Nav1.6 and its accessory proteins, such as the intracellular fibroblast growth factor 14 (**FGF14**).

1.4. Druggability of the FGF14:Nav1.6 Complex

Studies have shown that the PPI complex between the Nav1.6 channel and FGF14 is a functionally relevant regulator of neuronal excitability in the cortico-mesolimbic circuit and cerebellum[42,43,52–54,44–51]. Single-nucleotide polymorphisms in exonic regions of FGF14 cause spinocerebellar ataxia 27 (**SCA27**), an autosomal dominant disease associated with complex neuropsychiatric symptoms[36–38,42,51,55,56], while intronic SNPs or changes in the expression level of FGF14 have been linked to schizophrenia and other neuropsychiatric disorders[18,35,47]. FGF14 binds to the Nav1.6 intracellular C-terminal domain and promotes localization of Nav1.6 channels to the proximal region of the axon, which is the primary initiation site of the action potential[42,44,50,53,57–61]. It was previously shown that binding of FGF14 to different Nav channel isoforms markedly affected Nav-mediated currents in a Nav isoform-dependent fashion[62–64] and that these changes were distinct from those associated with other FGF isoforms and splice variants[3,43]. Interactions between FGF14 and Nav1.6 are regulated by kinase signaling pathways including glycogen synthase kinase 3 (**GSK3**) and casein kinase 2 (CK2), which directly phosphorylate serine/threonine (S/T) sites on FGF14 and/or Nav1.6. Targeting these kinases with inhibitors or short-hairpin RNA alters protein complex stability, Nav1.6 currents and excitability[43,46,49,57,65], while peptidomimetics targeting the $FGF14^{V160}$ and $FGF14^{Y158}$ residues, which are located at the FGF14:Nav1.6 PPI interface, reduce complex formation, exhibit state-dependent modulation of Nav1.6 currents and suppress excitability of medium spiny neurons in the nucleus accumbens (**NAc**)[50,58]. These findings not only provide evidence for druggability of the FGF14:Nav1.6 complex but also suggest that modulation of cell signaling could provide a strategy for rescuing function of the Nav1.6 channel or FGF14 in related channelopathies.

1.5. FGF14 AS A NAV CHANNEL INTERACTING PROTEIN

While iFGFs share a conserved core β-trefoil region with other FGFs their functions and distributions are distinct from canonical FGFs[66]. Canonical FGFs are normally secreted to activate FGF receptors on the cell surface, however iFGFs lack a secretory sequence, fail to activate or antagonize FGF receptors and are primarily found in the cytoplasm, nucleus or at the axon initial segment (**AIS**), the site of axon potential initiation[67–70]. Initial discoveries using yeast-two-hybrid screening identified FGF12 and FGF13 as direct interactors of Nav channels[64,71,72] and subsequent studies resulted in similar discoveries for the two isoforms of FGF14[43,73,74], aligned in the illustration of Figure 1.1A. To date, the evidence for direct interaction and functional modulation of Nav channels by FGF14 ranges from structural studies and homology models to biochemical in cell assays to animal models and includes recent identification of critical amino acid residues at the FGF14:Nav1.6 channel complex illustrated in Figure 1.1B[43,44,50,57,58,69,73–75].

The N-terminus of FGF14 is alternatively spliced into two isoforms: FGF14-1a and FGF14-1b. FGF14-1a shares sequence homology with FGF12-1a and FGF13-1a, while the amino terminus of FGF14-1b contains a unique 69 amino-acid sequence and is the more prevalent isoform in the CNS[76]. Importantly, the interaction of FGF14 in cells that heterologously express individual Nav isoforms shows that FGF14 is unique, as it results in very distinct isoform-specific Na^+ current phenotypes that are dictated by the two FGF14 splice variants[43,50,73]. In primary hippocampal neurons, overexpression of FGF14-1b increases Na+ current density, causes a hyperpolarizing shift in the voltage-dependence of activation and a depolarizing shifting the voltage-dependence of inactivation, while the F145S, SCA27 dominant negative loss-of-function mutation causes opposite phenotypes,

possibly by disrupting the function of wild-type FGF14[74]. Neurons from *Fgf14*$^{-/-}$ mice exhibit impaired excitability in both the hippocampus and cerebellum[77–80]. The effect of FGF14 on Nav channels and excitability is summarized in **Table 1.2**.

1.6. FGF14 AS A REGULATOR OF EXCITATORY AND INHIBITORY SYNAPTIC TRANSMISSION

Numerous reports describe the effect of genetic deletion of Fgf14 on synaptic transmission. Studies in the cerebellum of *Fgf14−/−* mice revealed decreased excitatory transmission from granule cells to Purkinje cells (parallel fibers, PF), a phenotype that is accompanied by reduced AMPA receptor-mediated excitatory postsynaptic currents and decreased expression of vesicular glutamate transporter 1, a specific presynaptic marker at PF-Purkinje neuron synapses[48]. Presynaptic changes in neurotransmitter release have been also reported at the Schaffer's collaterals to CA1 synapses where deletion of Fgf14 results in reduction in the ready- releasable pool of presynaptic glutamate and diminished expression of synaptobrevin, synaptophysin, syntaxin I[81]. Other changes in presynaptic function have been reported at inhibitory GABAergic terminals onto CA1 pyramidal cells of *Fgf14−/−* mice, which exhibit reduced expression of glutamic acid decarboxylase 67 (GAD67) and vesicular GABA transporter (vGAT), presumably deriving from fast-spiking parvalbumin (PV) interneurons synapses[47]. Additional studies in the same animal model identified selective loss of PV interneurons, reduced γ frequency oscillations and deficits in working memory[47]. Collectively, these results recapitulate some endophenotypes of SZ and are supported by human studies finding significant reduction and co-variation of FGF14, PV, vGAT and GAD67 in post-mortem samples from patients with SZ compared to healthy control individuals[47]. Whether all these changes at presynaptic glutamatergic and GABAergic terminals result from neuroadaptive responses to impaired firing or

represent disruption of a separate function of the FGF14 protein remains to be determined. However, the evidence for genetic links between vGAT, GAD67 and FGF14 might argue for a ‘‘separate function’’ hypothesis of FGF14 that results from a control at the gene level.

1.7. FGF14 IS REQUIRED FOR SYNAPTIC PLASTICITY

Studies have also supported a role of FGF14 in synaptic plasticity in the hippocampus. *Fgf14−/−* mice show impaired long-term potentiation (LTP) at the Schaffer's collaterals to CA1 synapses, which is accompanied by decreased expression of synaptic vesicles docked at the active zone, and fewer miniature excitatory postsynaptic currents in primary hippocampal neurons[81]. Short-term plasticity is also impaired at these *Fgf14−/−* terminals, at which repetitive stimuli causes significant synaptic fatigue, consistent with impaired presynaptic function[81].

Table 1.2: Effect of splice variants in heterologous systems and knockout animals.

Isoforms	FGF14-1a (HEK-293)	FGF14-1b (HEK-cells)	FGF14-1b (Neuronal cell line)	FGF14-1b (Hippocampal neurons)	FGF14 Knockout (Granule neurons and CA1 hippocampal) neurons)
$Na_v1.1$	Depolarizing shift in voltage dependence of activation, depolarizing shift in voltage dependence of inactivation (Lou et al., 2005)	Decreases in current density, depolarizing shift in voltage dependence of inactivation (Lou et al., 2005)	Decreases current density (Laezza et al., 2009)	-	-
$Na_v1.2$	Depolarizing shift in steady state inactivation (Laezza et al., 2009)	-	Decreases current density, small depolarizing shift in steady-state inactivation (Laezza et al., 2009)	-	-
$Na_v1.5$	Decreases current density, depolarizing shift in voltage dependence of inactivation (Lou et al., 2005)	Decreases current density, hyperpolarizing shift in inactivation (Lou et al., 2005)	-	-	-
$Na_v1.6$	Depolarizing shift in steady-state inactivation, slower recovery from inactivation (Laezza et al., 2009)	-	Decreases current density, depolarizing shift in steady-state inactivation (Laezza et al., 2009)	-	-
Native Na_v channels	-	-	-	Increases current density, hyperpolarizing shift in voltage-dependence of activation, depolarizing shift in steady-state inactivation (Laezza et al., 2007)	Reduces evoked repetitive firing (Goldfarb et al., 2007; Hsu et al., 2016)

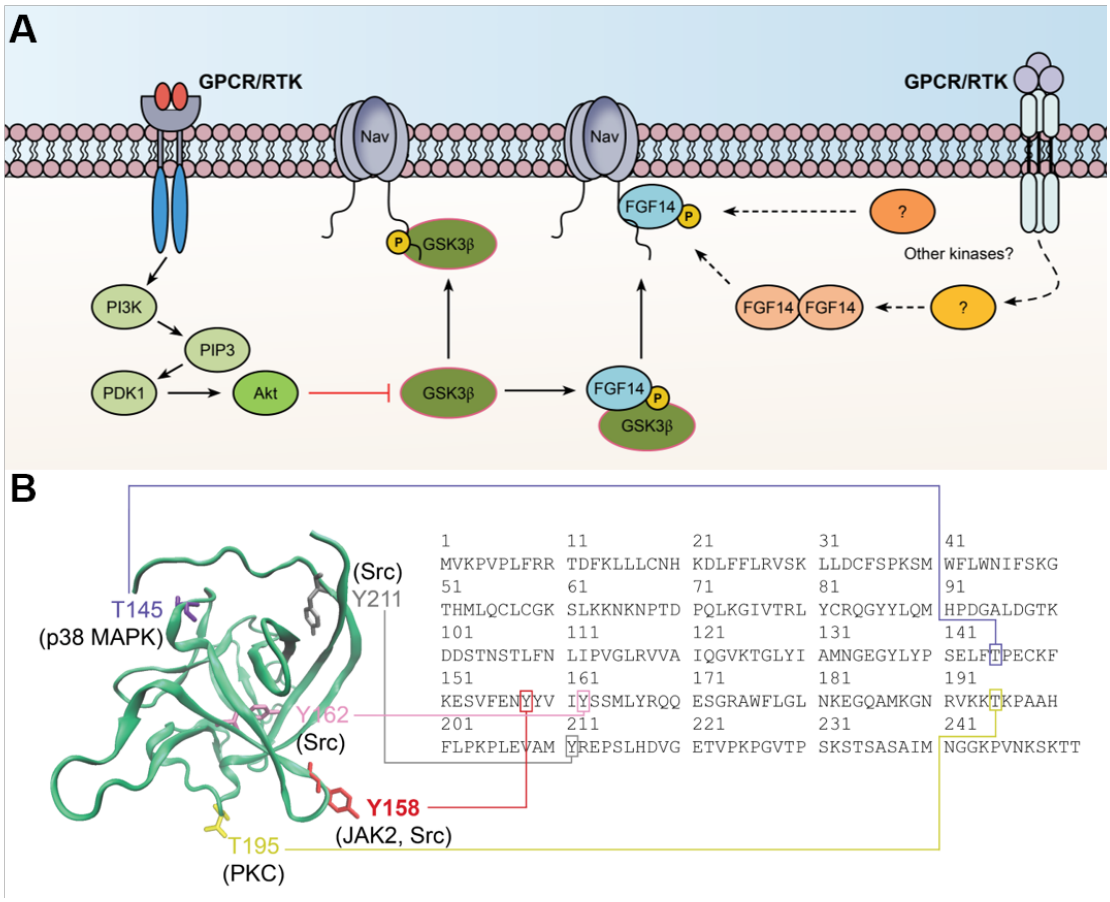

Figure 1.2. Known and predicted regulatory interactions of the FGF14:Nav1.6 complex.
(A) Schematic of some of the known signaling proteins that regulate the FGF14:Nav1.6 complex. **(B)** Homology model of an FGF14 monomer generated using the FGF13:Nav1.5 crystal structure (Protein Data Bank ID: 4DCK) as template. Potential phosphorylation sites and their corresponding motif in the FGF14-1b sequence (accession number NP_787125) are shown. Y158, red, while Y162 is shown as purple. Also showing other predicted phosphorylation sites that are not at the protein:protein interaction interface, including T145, T195, and Y211.

1.8. Regulation of Nav Channel Complexes by Kinases

Due to the critical role of Nav channel complexes, they are understandably subject to intense regulation by accessory proteins including spectrin, ankyrin, and **iFGFs**[35]. In turn, signaling pathways downstream of transmembrane receptors modulate PPI between these accessory proteins and the Nav channel through phosphorylation, which can confer functional specificity to neuronal firing in response to extracellular stimuli. Not only do

these regulatory mechanisms play fundamental roles in neuronal plasticity, but dysregulation of these processes has been associated with increased risk for neuropsychiatric and neurological disorders[18,20,35,82–84] spurring a great interest in searching for novel kinase signaling pathways that control the Nav channel complex.

It has been demonstrated that phosphorylation plays a critical role in regulating Nav channels, particularly for Ser/Thr kinases[85–90]. For example, protein kinase A (**PKA**) and protein kinase C (**PKC**) have been shown to phosphorylate multiple serine residues on the interdomain I-II and III-IV linkers of Nav1.2, significantly reducing current and increasing firing thresholds[89,91,92]. GSK3β phosphorylates the Nav1.2 C-terminal tail at T1966, suppressing Na^+ currents and channel trafficking to the plasma membrane[93], an effect that was found to be opposite for the Nav1.6 channel isoform[65]. Additionally, Nav1.6 is modulated by p38 MAPK via phosphorylation of S533 in the cytoplasmic loop (L1), resulting in reduced peak Nav1.6 current amplitude[94].

However, despite the essential functions that phosphorylation plays in modulating Nav channel functions, a surprisingly limited number of kinases have been identified as regulators of PPI within the Nav channel complex. This is particularly true for Tyr kinases, although some examples are known, such as the protein Tyr kinases (**PTK**) Fyn and Src. These kinases directly phosphorylate Nav channels intracellularly, contributing to synaptic plasticity[95–97]. Recent studies have also added a new dimension to our perspective of FGF14, showing that its interaction with the Nav channel is controlled by selective kinases[45,46,49,57,80]. Initial studies using the luciferase complementation assay (**LCA**) demonstrated that the FGF14:Nav1.6 complex formation is controlled by GSK3[46] (**Fig. 1.2A**), as well as the GSK3 priming kinase CK2 which phosphorylates FGF14 at S228 and

S230[57,98]. Inhibition of GSK3 is sufficient to disrupt FGF14:Nav channel complex formation with consequences for targeting of the two proteins to the AIS and for intrinsic excitability[46,57,80]. We subsequently discovered that GSK3β can phosphorylate FGF14 both *in vitro* and *in vivo* at S226[46] in an experimental model of Alzheimer's disease (**AD**). It is possible that phosphorylation at these kinase specific sites confers functional specificity to FGF14 contributing to regulation of other ion channels (i.e., voltage-gated K^+ and Ca^{2+} channels). More is known about the specific phosphorylation of FGF14 by GSK3 and CK2, but there is some preliminary evidence for other kinases that regulate FGF14:Nav1.6 interactions[45,49]. For instance, GSK3β was found to be the converging node of a signaling network that includes the PI3K/Akt pathway (**Fig 1.2A**), the cell-cycle regulator Wee1 kinase, and PKC as modulators of the FGF14:Nav1.6 complex[49]. However, these signaling cascades are highly complex and the mechanisms for how phosphorylation specifically changes PPI between these complexes is not well understood.

Additionally, the Nav1.6 channel and FGF14 sequences are abundant in predicted phosphorylation sites for both Tyr and Ser/Thr kinases (**Fig. 1.1B**), but evidence for or against phosphorylation of these sites is lacking. Thus, we hypothesized that numerous as-of-yet unidentified kinases regulate the FGF14:Nav1.6 channel complex through mechanisms that may be relevant for neuronal plasticity. This hypothesis is explored in Chapter 4.

1.9. Conclusions and Overall Approach

Altogether, the information described above conveys that the PPI between FGF14 and Nav1.6: *i*) clearly has a functional role in neuronal activity, albeit incompletely understood; *ii*) is dysfunctional in neuropsychiatric diseases; *iii*) is a promising pharmacologic target. However, identifying modulators of PPI between members of ion channel complexes has been hampered by the lack of screening platforms. For most ion channels, expressing their pore-forming subunit in heterologous mammalian cells has now become a routine procedure, but reconstituting protein-channel complexes in near-to-physiological environments is still challenging. This limits our ability to identify regulators and probes that could otherwise lead to more targeted and precise modulation of the channel function.

Therefore, our first goal was to develop and optimize an assay capable of assessing this protein-channel interaction in a high-throughput format. To do this, we created a double stable cell line expressing constructs for the split-luciferase complementation assay (LCA) and sequentially optimized experimental parameters for robust assay performance. This optimized assay was then used for a dual purpose: *i*) to identify cellular regulators of the FGF14:Nav1.6 complex, and *ii*) to discover new chemical probes. These studies were validated by a series of studies ranging from *in vitro* (i.e., biophysics) to *ex vivo* (i.e., brain slices).

THESIS AIMS

Aim 1. Develop a robust high-throughput screening platform to discover new regulators and probes targeting the FGF14:Nav1.6 interaction (**Chapters 3 and 4**)

Aim 2. Identify and characterize the mechanisms by which kinases may regulate the Nav complex via phosphorylation (**Chapter 5**)

Aim 3. Identify new small molecule probes targeting the FGF14:Nav1.6 complex (**Chapters 6 and 7**)

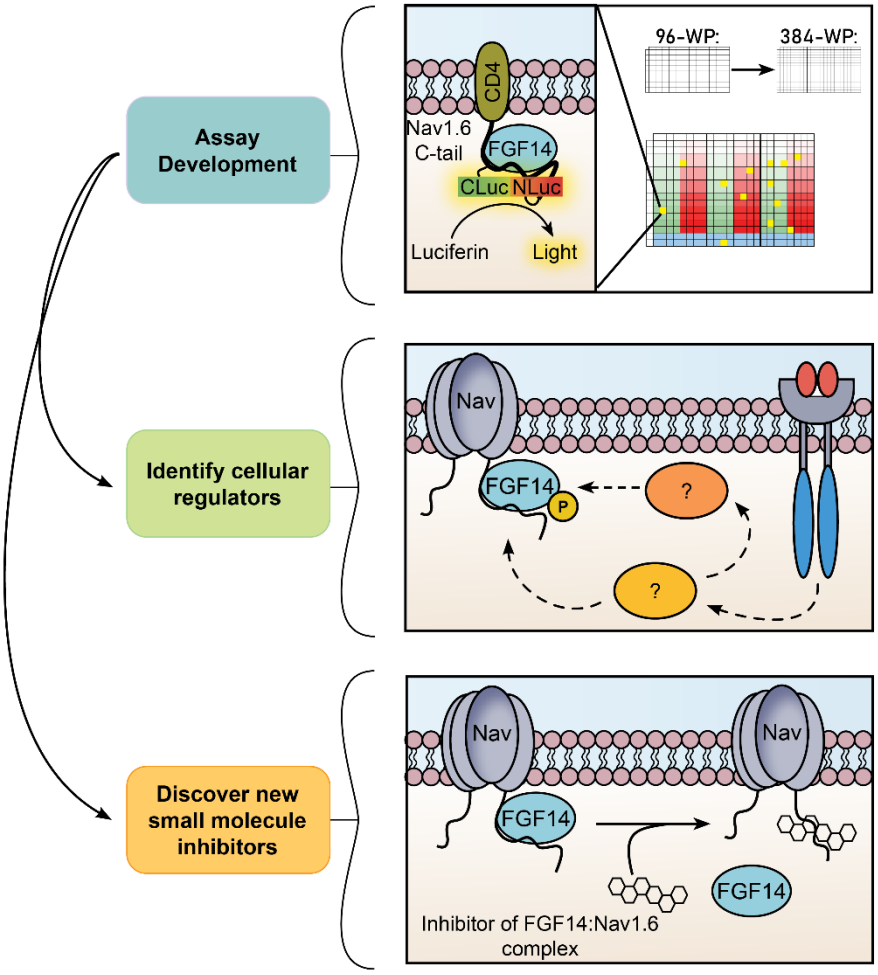

Chapter 2. General Experimental Methods

ABSTRACT: The methods described within this chapter are referred to throughout this dissertation. While a brief description of the luciferase complementation assay is provided in this chapter, a more detailed and technical description is provided in Chapter 3. Additionally, portions of the methods here are published as:

[1] Z. Liu, **P.A. Wadsworth**, A.K. Singh, H. Chen, P. Wang, O. Folorunso, P. Scaduto, S.R. Ali, F. Laezza, J. Zhou, Identification of peptidomimetics as novel chemical probes modulating fibroblast growth factor 14 (FGF14) and voltage-gated sodium channel 16 (Nav16) protein-protein interactions, Bioorganic Med. Chem. Lett., 29 (2019) 413–419.
[2] **P.A. Wadsworth**, O. Folorunso, N. Nguyen, A.K. Singh, D.D. Amico, R.T. Powell, D. Brunell, J. Allen, C. Stephan, F. Laezza, High-throughput screening against protein : protein interaction interfaces reveals anti-cancer therapeutics as potent modulators of the voltage-gated Na + channel complex, Sci. Rep., (2019) 1–15.

2.1. CHEMICALS

D-luciferin was purchased from Gold Biotechnologies. Screened compounds are described below. Repurchased hits, including Momelotinib, TG101209, Fedratinib, Pacritinib, Danusertib, Saracatinib, Ibrutinib, and Bosutinib were obtained from Selleck. For mass spectrometric experiments, LC–MS grade acetonitrile (ACN) and water were from J.T. Baker (Philipsburg, NJ). Formic acid was obtained from Pierce (Rockford, IL) and iodoacetamide (IAA) and dithiothreitol (DTT) were purchased from Sigma-Aldrich (St. Louis, MO). Sequencing grade trypsin was supplied by Promega (Madison, WI). Recombinant human TNF-α was purchased from Abcam and dissolved in PBS containing 0.1 mg/mL BSA and prepared as a 10 μg/mL stock solution. Triciribine and MNS were purchased from Tocris, and ZL181 was developed by the laboratory of Jia Zhou at UTMB; each compound was dissolved in dimethyl sulfoxide (DMSO) as 20 mM stock solutions. HTS compounds were provided by the Gulf Coast Consortium (GCC) as 10 mM stock solutions in DMSO on 384-well plates.

2.2. DNA CONSTRUCTS

The CLuc-FGF14^{WT}, CLuc-FGF14^{Y158A}, CD4-Nav1.6-NLuc, pQBI-FGF14-GFP and pQBI-GFP constructs were engineered and characterized as previously described [44–46,50,58,99–101]. The corresponding gene ID numbers are as follows: NM_175929.2 (human *FGF14-1b*), NT_009759.16 (human *CD4*), and NM_014191.3 (human *Nav1.6*). The choice of using the CD4 chimera fused to Nav1.6 C-tail was based on previous validations of this and other similar constructs in primary hippocampal neurons[102–104]. The plasmid pGL3 expressing full-length firefly (*Photinus pyralis*) luciferase was a gift from Dr. P. Sarkar (Department of Neurology, UTMB). For

protein purification studies, cDNAs encoding FGF14 (accession number NP_787125; aa 64-252) or the C-terminal tail of Nav1.6 (accession number #NP_001171455; aa 1756-1939) were sub-cloned into suitable pET bacterial expression vectors (pET28a-FGF14; pET30a-Nav1.6) with a 6X His-tag at the N-terminal site; these plasmids were a gift of Dr. Moosa Mohammadi (NYU, Langone Medical Center).

2.3. CELL CULTURE

HEK293 cells were incubated at 37 C with 5% CO_2 in medium composed of equal volumes of Dulbecco modified essential medium (DMEM) and F12 (Invitrogen, Carlsbad, CA) supplemented with 10% fetal bovine serum, 100 U/mL penicillin, and 100 mg/mL streptomycin. For transfection, cells were seeded in 24-well CELLSTAR® tissue culture plates (Greiner Bio-One, Monroe, NC) at $4.5x10^5$ cells per well and incubated overnight to give monolayers at 90%–100% confluency. The cells were then transiently transfected with the pair of CLuc-FGF14 and CD4-Nav1.6-C-tail-NLuc constructs or the full-length *Photinus pyralis* luciferase construct (pGL3) using Lipofectamine 2000 (Invitrogen), according to the manufacturer's instructions. 1 µg of each plasmid was used per transfection per well. The double stable HEK293 cell line expressing CD4-Nav1.6C-tail-Nluc and Cluc-FGF14 was described in a previous study[100] and was maintained using selective antibiotics (0.5 mg/mL G418 and 5 µg/mL puromycin). HEK293 cells stably expressing the Nav1.6 channel (HEK-Nav1.6) were maintained under 80 µg/ml G418.

2.4. SPLIT-LUCIFERASE COMPLEMENTATION ASSAY

96-well plate assay: Cells were trypsinized (0.25%), triturated in a medium, and seeded in white, clear-bottom CELLSTAR µClear® 96-well tissue culture plates (Greiner Bio-One)

at ~1x10^5 cells per well in 200 µL of medium. For transiently transfected cells, the trypsinization occurred 48 h post-transfection. The cells were incubated for 24 h, and the growth medium was subsequently replaced with 100 µL of serum-free, phenol red–free DMEM/F12 medium (Invitrogen) containing inhibitors (0.25–50 µM). The final concentration of DMSO was maintained at 0.3% for all wells. Following 2 h incubation at 37 C, the reporter reaction was initiated by injection of 100 µL substrate solution containing 1.5 mg/mL of D-luciferin dissolved in PBS (final concentration = 0.75 mg/mL) by the Synergy™ H4 Multi-Mode Microplate Reader (BioTek, Winooski, VT). Luminescence readings were performed at 2-min intervals for 20-30 min, integration time 0.5 s, and the cells were maintained at 37°C throughout the measurements. Signal intensity for each well was calculated as a mean value of peak luminescence; the calculated values were expressed as percentage of mean signal intensity in the control samples from the same experimental plate.

384-well plate assay: Cells were trypsinized (0.25%), triturated in a medium, and seeded in white, clear-bottom CELLSTAR µClear® 384-well tissue culture plates (Greiner Bio-One) at 3x10^4 cells per well in 40 µL of serum-free, phenol red–free DMEM/F12 medium using the Multidrop Combi (Thermo Fisher). The LabCyte Echo 550 was used to acoustically deliver nanoliter volumes of compounds, TNF-α, and DMSO. The final concentration of DMSO was maintained at 0.3% for all wells excluding the positive control wells containing medium alone. Following 2 h incubation at 37 C, the reporter reaction was initiated by injection of 40 µL substrate solution containing 1.5 mg/mL of D-luciferin (final concentration = 0.75 mg/mL) by the Multidrop Combi. After 1 h incubation, the Tecan Infinite M1000 was used to detect luminescence. Detailed methods for LCA can be

found in previous studies[45,49,50,58,75,100]. Statistical parameters of assay performance were calculated as described previously[100,105] according to the following formulas:

$$Z'\text{factor} = 1 - 3 \times \frac{(\delta_p + \delta_n)}{(\mu_p - \mu_n)} \quad (1)$$

$$S:B = \frac{\mu_p}{\mu_n} \quad (2)$$

$$S:N = \frac{(\mu_p - \mu_n)}{\sqrt{\sigma_p^2 + \sigma_n^2}} \quad (3)$$

$$SW = \frac{\mu_p - \mu_n - 3 \times (\sigma_p + \sigma_n)}{\sigma_p} \quad (4)$$

where δ_p and δ_n are standard deviation of the positive control group p and the negative control group n, and μ_p and μ_n are the arithmetic means of the two groups, respectively; S:B, signal to background; S:N, signal-to-noise; and SW, signal window[105]. For cell-based assays, a Z' of $\geq$ 0.5 signifies that outliers can be reliably identified as statistically significant despite well-to-well and plate-to-plate variability. We calculated Z' using Equation 1, which is based on the mean and standard deviation of positive and negative controls and is calculated in the absence of library compounds[106]. Based on this equation, Z' is improved by greater signal separation between the mean of positive and negative controls, as well as by reducing variance between replicates (i.e., standard deviation). In practical terms, consistency between replicates would improve confidence in a single well outlier being truly significant (i.e., the compound treatment in that single well resulted in significant changes in complex formation, rather than the change in luminescence being due to simple well-to-well variability). Z-scores were calculated for each screened compound using the following formula:

$$\text{Z score} = \frac{\mu_i - \mu_{DMSO}}{\mu_{DMSO}} \quad (5)$$

where μ_i and μ_{DMSO} are the arithmetic means of the sample (i.e., screened compound) and 0.3% DMSO control group, respectively. Dose-response curves were obtained using GraphPad Prism 8 by fitting the data with a non-linear regression:

$$A + \frac{B-A}{1+10^{\log(x_0-x)_H}} \quad (6)$$

where x is log10 of the compound concentration in M, x_0 is the inflection point (EC_{50} or IC_{50}), A is the bottom plateau effect, B is the top plateau effect, and H is the Hill slope. Kinase inhibitors that increased FGF14:Nav1.6 interaction with increasing doses were classified as agonists; inhibitors that decreased FGF14:Nav1.6 interaction were classified as antagonists.

*Screened libraries (**Chapter 5**):* Three libraries provided by the Gulf Coast Consortium (**GCC**) were screened using the LCA, including the Broad Collection, Selleck Bioactive Collection, and UT Austin Combined Kinase Collection (UTKinase), for a total of 3,121 compounds. All compounds were provided as 10 mM in DMSO and were screened at a final concentration of 30 μM. The Broad Collection has been previously described as the "Informer Set,"[107] which targets nearly 250 distinct proteins, encompassing a broad range of cell circuitry relevant to cancer cell line growth and survival. The Informer Set contains all FDA-approved agents, clinical candidates, and small-molecule probes of the Informer Set that were commercially available. The Selleck Bioactive Collection contains some compounds that have been approved by the FDA, have bioactivity and safety confirmed by preclinical research and clinical trials and includes most Selleck inhibitors, active

pharmaceutical ingredients, natural products, and chemotherapeutic agents. The collection is structurally diverse, medicinally active, and cell permeable. The UTKinase collection is comprised of over 1,400 well-characterized, cell permeable, potent and reversible protein kinase inhibitors, the majority of which are ATP-competitive, less cytotoxic, stable in DMSO/H_2O, and structurally diverse. Inhibitors target a broad spectrum of >100 kinases, including but not limited to, RSTK (Receptor Serine/Tyrosine kinase), TK (Tyrosine Kinase), TKL (Tyrosine Kinase like), AGC (PKA, PKG, and PKC family), CMGC (CDK, MAPK, GSK-3, and CLK family), RTP (Receptor Tyrosine Phosphatase), TP (Tyrosine Phosphatase), CAMK (Ca2+/Calmodulin Dependent Protein Kinases), STE (Yeast Sterile Protein Kinases), Atypical, MAPK signaling, PI3-kinase/Atk Signaling, and Transferase. The useful applications of this particular collection are target identification in drug discovery, biochemical pathway analysis, and screening new protein kinases.

2.5. CELL VIABILITY ASSAY

The CellTiter-Blue (CTB) Cell Viability Assay (Promega) was used as a control to detect compounds causing cellular toxicity. Immediately following luminescence reading, 10 µL of 1X CTB reagent was dispensed into 384-well plates, incubated overnight (16 h) at 37 C, and fluorescence was detected using the Tecan Infinite M1000 reader (excitation λ =560 nm, emission λ = 590 nm). Cell viability was expressed as percent mean fluorescent signal intensity in the control samples from the same experimental plate.

2.6. PHOSPHOMOTIF SEARCHES

To search for potential phosphorylation motifs (both S/T and Y) and tyrosine binding motifs, the FGF14-1b (aa 1-252) and Nav1.6 C-tail (aa 1763 – 1968) sequences were input

to the Human Protein Reference Database (HPRD) PhosphoMotif Finder (http://hprd.org/PhosphoMotif_finder)[108], NetPhos 3.1[109], and NetPhorest 2.1[110]. The HPRD PhosphoMotif Finder contains known kinase/phosphatase substrate as well as binding motifs that are curated from the published literature, and this program reports the presence of any literature-derived motif without making any predictions as to whether it will truly exist. NetPhos predicts serine, threonine, and tyrosine phosphorylation sites using a neural network. Note that while NetPhos 3.1 does not currently have the capability to predict JAK2 phosphomotifs, the HPRD PhosphoMotif Finder was able to detect JAK2 consensus motifs. NetPhorest predicts kinase binding sites based on an atlas of consensus sequence motifs for kinases and phosphorylation-dependent binding domains

2.7. Protein Expression and Purification

The two plasmids for protein expression and purification of FGF14 and Nav1.6 C-tail have been previously described [50,65] and were transformed into *E. coli* BL21 (DE3) pLys (Invitrogen). Cells were grown until OD_{600} = 0.7, and the recombinant proteins were expressed after induction with 0.1 mM isopropyl thio-β-D-galacto-pyranoside (IPTG) for 24 h at 16˚C. Cells were harvested and lysed by sonication at 4°C in lysis/binding buffer containing following components (mM): 10 sodium phosphate (prepared from 0.5 M of Na_2HPO_4 and NaH_2PO_4), 25 HEPES, 150 NaCl, phenyl methyl sulphonyl fluoride (PMSF) 0.1, CHAPS 0.1% pH 7.0 (for FGF14), and with glycerol 10% (for Nav1.6 C-tail) pH 7.5. The respective proteins were centrifuged at 40,000 x g for 1 h at 4°C. For purification of FGF14, the supernatant was applied to pre-equilibrated heparin and the proteins were then eluted with NaCl 0.2-2.0 M (sodium phosphate 10 mM, NaCl 0.2-2.0 M, pH 7.0) buffer. For purification of Nav1.6 C-tail, the supernatant was first applied to a cobalt column

(Thermo Fisher Scientific) and eluted with imidazole (200 mM). The Nav1.6 C-tail was further purified using HiTrap QFF-sepharose column (GE Healthcare Bio-Sciences, Pittsburgh, PA) using a buffer containing Tris-HCl 50 mM and eluted with NaCl (10-500 mM) at pH 7.5. Finally, all concentrated proteins were purified on an AKTA FPLC using a Superdex 200 HiLoad 16 x 60 column and equilibrated in Tris-HCl 50 mM + NaCl 150 mM, pH 7.5 (GE Healthcare Bio-Sciences. Protein concentrations were determined using UV absorbance with a Thermo NanoDrop.

2.8. In Vitro Phosphorylation and Sample Preparation

In vitro phosphorylation of the FGF14 peptide [KFKESVFENYYVIYSSMLYR-NH2] (aa149-169) by baculovirus-produced recombinant human JAK2 or Src kinase protein (SignalChem) was performed in the presence of 10 mM Tris-HCl, 25 mM NaCl, 1.5 mM Glutathione, 0.5 mM EDTA, 0.25 mM DTT, 5 mM MOPS, 5 mM $MgCl_2$, 1 mM ATP and 15 ng/μL BSA. Reactions with Src also included 2.5 mM $MnCl_2$.Reactions were incubated at 30 °C for 30 min, followed by overnight incubation at 4 °C. Control studies were performed under identical conditions but lacking the addition of either the kinase or ATP to the reaction solution. Peptide samples for SPR were then buffer exchanged and concentrated into running buffer (HBS-P+ supplemented with 2% DMSO). For *in vitro* phosphorylation of purified recombinant proteins, FGF14 was purified as described above, and phosphorylation by JAK2 or Src was performed identically. To confirm phosphorylation status by mass spectrometry, samples were reduced with 10 mM DTT, alkylated with 5 mM IAA, and digested with modified sequencing grade trypsin 1:50 (w/w) overnight at 37°C.

2.9. MASS SPECTROMETRY

Digested peptide samples were desalted using C18 ZipTips (Millipore) and 1 µl of this solution was combined with 1 µl of a 3 mg/ml α-cyano-4-hydroxycinnamic acid (60% acetonitrile, 1 mM ammonium diphosphate) and spotted onto MALDI targets. All MALDI-MS experiments were performed using a 5800 MALDI-TOF/TOF (Applied Biosystems). The MS data were acquired using the reflectron detector in positive mode (700–4500 Da, 1900 Da focus mass) using 300 laser shots (50 shots per sub-spectrum). Collision induced dissociation tandem MS spectra were acquired on the ions found in the MS1 experiment, using 1 kV of collision energy. Identified phosphopeptide spectra were manually sequenced and annotated using the MS-Product tool on the Protein Prospector website (prospector.ucsf.edu) to generate and compare theoretical m/z values for all fragment ions against observed fragment ions. Phosphorylation sites were identified manually by locating all present site-identifying b and y ions in the sequence.

2.10. MOLECULAR MODELING

The FGF14:FGF14 homodimer model was built with the FGF13 dimer crystal structure (PDB ID: 3HBW)[44] as template, as described previously[75]. The FGF14:Nav1.6 homology model was generated using the FGF13:Nav1.5:CaM ternary complex crystal structure (PDB ID: 4DCK)[111] as template, as described previously[50].

Docking: The docking study of three HTS hits 7647895, 7605086 and 5335477 was performed with Schrödinger Small-Molecule Drug Discovery Suite (Schrödinger Release 2019-4, Schrödinger, LLC, New York, NY,2019) using FGF14:Nav1.6 homology model. First, SiteMap was run on the FGF14:Nav1.6 homology model and individual chain of FGF14 and Nav1.6. Two sites with promising site scores located close to PPI were

identified. One site with a score of 1.041 was selected for FGF14 docking and one site with a score of 0.919 was selected for Nav1.6 docking. The FGF14 chain structure and Nav1.6 chain structure was prepared with Protein Prepared Wizard separately. 7647895, 7605086 and 5335477 were prepared with LigPrep. The grid center was chosen on the predicted sites identified from SiteMap result. FGF14 grid box size was set to 30 × 30 × 30 Å and Nav1.6 grid box size was set to 23 × 23 × 23 Å. 7647895, 7605086 were docked into FGF14 chain and 5335477 was docked into Nav1.6 chain. Grid generating and docking were both employed with Glide using SP-Peptide precision. Docking poses then were incorporated into Schrödinger Maestro for a visualization of ligand-receptor interactions. Overlay analysis was performed with the docked pose of 3 HTS hits and FGF14:Nav1.6 homology model using Schrödinger Maestro.

2.11. Surface Plasmon Resonance Spectroscopy

Surface Plasmon Resonance (SPR) experiments were performed on a Biacore T100 instrument (GE Healthcare, Pittsburgh, PA). Proteins were immobilized on CM5 sensor chips using 10 mM sodium acetate buffer (pH 5.5) with the Amine Coupling Kit (GE Healthcare) as per the manufacturer's instructions. For studies assessing the interaction of recombinant proteins with peptides (**Chapter 5**) and HTS hits (**Chapter 7**), chips with FGF14 bound to final RU values of 16,045 and 17,895 or with Nav1.6 bound to a final RU value of 6,800 were used. For studies assessing the interaction of recombinant proteins, chips with FGF14 or Nav1.6 bound to final values of 930 or 1,130, respectively, were used. No protein was coupled to the control flow channels of the chip (Lanes 1 and 3). The interaction of analytes against FGF14 and Nav1.6 proteins were studied at 25 °C using a flow rate of 50 µl/min.

Small Molecule Binding Studies (**Chapter 7**): Compounds were serially diluted (0.195-200 μM) in PBS supplemented with Tween-20 0.005% and 2% DMSO. Each sample was injected over the chip for 120 s followed by a dissociation period of 150 s and finally chip surface regeneration (600 mM NaCl, 5% DMSO) for 120 s. Compounds were tested with concentrations of 0.195, 0.39, 0.78, 1.56, 3.12, 6.25, 12.5, 25, 50, 100, and 200 μM, including 12.5 μM, 25 μM, and blanks (buffer alone) in duplicate. A DMSO calibration was performed for each experiment 1 [1.5–2.8% (vol/vol) DMSO] to correct for bulk refractive index shifts[112].

PPI Studies (**Chapter 5**): Recombinant protein or peptide samples were serially diluted (10 – 2000 nM or 31 - 6000 nM, respectively) in HBS-P+ (HBS supplemented with Tween-20 0.005%). Each sample was injected over the chip for 60-120 s followed by a dissociation period of 250 s and finally chip surface regeneration (1.5 M NaCl, 3% DMSO) for 120 s. Peptides were tested with concentrations of 31, 62.5, 125, 250, 500, 750, 1000, 1500, 2000, 3000, and 6000 nM. Recombinant proteins were tested with concentrations of 10, 50, 100, 200, 300, 400, 500, 750, 1000, 1500, and 2000 nM. Each sample group also included a minimum of two blanks (buffer prepared similarly to samples). For experiments using protein phosphorylated *in vitro*, recombinant FGF14 protein (50 μM) was incubated with ATP and either 100 nM BSA (control), active JAK2 kinase, or active Src kinase (100 nM) for 30 min at 30 °C, followed by buffer exchange into SPR running buffer (HBS-P+). The serial dilution and buffer exchange concentration was such that the maximal possible concentration of JAK2 or Src in the FGF14 samples for SPR was 4 nM for the highest concentration of FGF14 (2 μM), and thus should yield negligible signal. Additional controls included blanks for each sample group that were prepared identically as the *in*

vitro phosphorylation reaction, but lacking FGF14 protein (i.e., 0 μM FGF14, 4 nM JAK2 or Src). These controls yielded similar or identical response signal (RU) as buffer alone, and thus we ruled out the effects of JAK2 or Src on SPR signal.

SPR Data Analysis: For each sample injection, nonspecific responses (buffer alone) were subtracted from experimental sensorgrams/traces prior to data analysis. Kinetic data were analyzed using the Biacore T100 Analysis software. Following visual inspection of the binding curves, the equilibrium constant (K_D) was calculated using two methods: (1) maximal responses were plotted against compound concentration, and the steady state K_D was calculated from the fitted saturation binding curve; (2) a kinetic analysis of each ligand/analyte interaction was obtained by fitting the response data to the simplest Langmuir 1:1 interaction model ($K_D=k_{off}/k_{on}$). The kinetic constants generated from the fitted binding curves were assessed for accuracy based on the distribution of the residuals (even and near zero to baseline). Graphs were plotted in GraphPad Prism 8 Software (La Jolla, CA).

2.12. ELECTROPHYSIOLOGY

HEK-Nav1.6 cells transiently transfected with GFP or FGF14-GFP were plated at low density on glass cover slips for 3-4 hours and subsequently transferred to the recording chamber. Recordings were performed at room temperature (20-22°C) 24 h post-transfection using a MultiClamp 700B amplifier (Molecular Devices, Sunnyvale, CA). The composition of recording solutions consisted of the following salts; extracellular (mM): 140 NaCl, 3 KCl, 1 $MgCl_2$, 1 $CaCl_2$, 10 HEPES, 10 glucose, pH 7.3; intracellular (mM): 130 CH_3O_3SCs, 1 EGTA, 10 NaCl, 10 HEPES, pH 7.3. Membrane capacitance and series resistance were estimated by the dial settings on the amplifier and compensated for

electronically by 70–75%. Data were acquired at 20 kHz and filtered at 5 kHz prior to digitization and storage. All experimental parameters were controlled by Clampex 9.2 software (Molecular Devices) and interfaced to the electrophysiological equipment using a Digidata 1200 analog-digital interface (Molecular Devices). Voltage-dependent inward currents for HEK-Nav1.6 cells were evoked by depolarization to test potentials between −100 mV and +60 mV from a holding potential of −70 mV followed by a voltage pre-step pulse of −120 mV (Nav1.6). Steady-state (fast) inactivation of Nav channels was measured with a paired-pulse protocol. From the holding potential, cells were stepped to varying test potentials between −120 mV (Nav1.6) and +20 mV (pre-pulse) prior to a test pulse to −20 mV.

Current densities were obtained by dividing Na^+ current (I_{Na}^+) amplitude by membrane capacitance. Current–voltage relationships were generated by plotting current density as a function of the holding potential. Conductance (G_{Na}^+) was calculated by the following equation:

$$G_{Na}^+ = I_{Na}^+/(V_m - E_{rev})$$

where I_{Na}^+ is the current amplitude at voltage V_m, and E_{rev} is the Na^+ reversal potential.

Activation curves were derived by plotting normalized G_{Na}^+ as a function of test potential and fitted using the Boltzmann equation:

$$G_{Na}^+/G_{Na,}^+{}_{Max} = 1 + e[(V_a - E_m)/k]$$

where $G_{Na,}^+{}_{Max}$ is the maximum conductance, V_a is the membrane potential of half-maximal activation, E_m is the membrane voltage and k is the slope factor. For steady-state

inactivation, normalized current amplitude ($I_{Na}^{+}/I_{Na,}^{+}{}_{Max}$) at the test potential was plotted as a function of prepulse potential (Vm) and fitted using the Boltzmann equation:

$$I_{Na}^{+}/I_{Na,}^{+}{}_{Max} = 1/ [1 + e[(V_h - E_m)/k]]$$

where V_h is the potential of half-maximal inactivation, E_m is the membrane voltage, and k is the slope factor.

To determine effects on long-term inactivation (LTI), a four-sweep protocol composed of four 20 ms-long 0 mV pulses separated by 40 ms interpulse recovery phases from a -90 mV holding potential was used. For direct comparison of cells of various size, current densities were calculated by dividing Na+ current (I_{Na}^{+}) amplitude/membrane Capacitance (C_m). For LTI, the fraction of channels recovered after n depolarization cycle was defined as I_{Na}-peak (n + 1) / I_{Na}-peak 1st pulse.

2.13. GENERATION OF B-SCORES FOR SCREENED COMPOUNDS

During screening of the Maybridge and Chembridge compound libraries (Chapter 7), we observed batch effects associated with alterations in the variance in the negative control. For this reason, hit retrieval using a single Z-score cut-off is difficult. In order to account for this issue and minimize the false-detection rate, we prioritized hits using a B-score method with cross-plate smoothing. In general, a B-score is similar to a Z-score however it takes well position and assay chronology into account in addition to activity[113,114]. A critical assumption associated with B-scores is that the majority of wells are in-active on an assay plate, which is generally true for chemical diversity libraries. Inactive wells are then used to fit a local surface using an extension of Tukey's median-polish method. Furthermore, this method can also be applied to correct assay systematic alterations in the noise across assay plates in a larger screening campaign. This effectively

factors in information from well positions across longitudinal plates into the median polishing algorithm. B-score normalization was performed using the Plate Analytics package in Pipeline Pilot (2018 Edition, Biovia). The parameters used to generate B-scores in this data set used a total of 10 iterations of median-polishing across a 20-plate running window with a stringent (0.001) convergence threshold. Results are plotted in plate order and B-score activity is color coded.

2.14. CHEMICAL SIMILARITY EMBEDDING

Chemical similarity was embedded into a two-dimensional graphic by generating stochastic neighborhood embedding from FCFP_6 fingerprints. First, chemical structures are rendered from SMILE stings and 6-connected fingerprints are generated using the molecule fingerprints function in the Chemistry package of Pipeline Pilot. This generates a fixed length vector describing chemical connectivity and has been extensively used in SAR applications. The resulting vector for each molecule was then used an input for a t-distributed stochastic neighborhood embedding (t-SNE) using default settings in the *Rtsne* package in R. This method was used in Chapter 7 to generate the chemical SNE (CSNE) values for all screened compounds in the Maybridge and Chembridge compound libraries, enabling comparison of chemical similarity between identified hits.

2.15. PROTEIN THERMAL SHIFT ASSAY

The protein thermal shift (**PTS**) assay was used to identify compounds that interacted with purified FGF14 and Nav1.6 C-tail protein. Melting (denaturation) of globular proteins exposes hydrophobic regions that interact with the fluorescent dye, resulting in increased fluorescence as detected by the PCR detection system[115]. Changes in protein thermal stability by ligand binding can be detected by shifts in the temperature at which fluorescent

peaks are observed compared to protein in the absence of ligand, enabling the estimation of change in melting temperature (ΔT_M). Reactions were prepared in 96-well PCR plates using the PTS Dye Kit (Applied Biosystems, Life Technologies) as per manufacturer instructions, and the assay was conducted on a QuantStudio 3 rtPCR System. Each well included a total reaction volume of 20 µL comprised of 2 µg of FGF14 or Nav1.6 C-tail protein, 1X dye, and peptidomimetics (50 µM; n = 4 wells per condition) or 0.5% DMSO alone (control; n = 8 wells per plate) in PBS. Additional per plate controls (n = 4 wells per condition) included buffer and dye alone (no protein control) and compounds alone (in the absence of protein) to assess potential interactions between peptidomimetics and fluorescent dye. The plate was heated from 25 to 99 °C at a ramp rate of 0.05°C/s with ROX as the selected reporter. The Boltzmann method was used to obtain protein T_M.

Chapter 3. Methodology for developing an in-cell assay for high-throughput screening against protein:channel interactions

The following chapter is currently IN PRESS with Springer Nature as a chapter in the Methods in Molecular Biology book series:

Wadsworth P.A., Singh A.K., Nguyen N., Stephan C., Laezza F. Bioluminescence methodology for ion channel studies. Patch Clamping: Methods and Protocols. 2020.

Written permission was provided by the editor to use the material as a chapter in this dissertation.

ABSTRACT

As key players in cell function, ion channels are important targets for drug discovery and therapeutic development against a wide range of health conditions. Thus, developing assays to reconstitute ion channel macromolecular complexes in physiological conditions and screen for chemical modifiers of protein:protein interactions within these complexes is timely in drug discovery campaigns. For most ion channels, expressing their pore-forming subunit in heterologous mammalian cells has now become a routine procedure. However, reconstituting protein-channel complexes in physiological environments is still challenging, limiting our ability to identify tools and probes based on allosteric mechanisms, which could lead to more targeted and precise modulation of the channel function. Here, we describe the assay development steps to stably reconstitute the interaction between voltage-gated Na+ (Nav) channel Nav1.6 and its accessory protein, fibroblast growth factor 14 (FGF14) using the split-luciferase complementation assay (LCA), followed by assay miniaturization and optimization in 384-well plates for in cell high-throughput screening (HTS) against protein-channel interactions. This optimized LCA can subsequently be used for rapid estimation of hit potency and efficacy via dose-dependency studies, enabling ranking of hits prior to more labor-intensive validation studies. Lastly, we introduce the methodology for rapid functional hit validation studies using semi-automated planar patch-clamp electrophysiology. Our robust, in-cell HTS platform can be adapted to any suitable ion channel complex to explore regulatory pathways of cellular signaling using kinase inhibitors, to screen for small molecules in light of probe development and drug repurposing toward new targets/areas of medicine. Overall, the flexibility of this assay allows to broadly explore therapeutic options for

channelopathy-associated diseases at a fast pace, enabling rapid hypothesis generation in early phase drug discovery campaigns narrowing down targets prior to more labor-intensive *in vivo* studies.

3.1 INTRODUCTION

Voltage-gated sodium (Nav) channels are the molecular determinant of the action potential, which underlies electrical signaling in the brain [116] and as such are attractive targets for drug development [117,118]. Protein:protein interactions (PPI) between Nav channels and their accessory proteins fine-tune neuronal excitability and are essential in ensuring mechanisms of plasticity and neural adaptations at the cell, circuitry and behavioral level [18,119–122]. Subtle changes in the composition of these ion channel complexes can be disruptive for the entire organism. In addition, mutations in either the channel itself or these regulatory proteins give rise to channelopathies that have few viable treatment options [12,123]. Importantly, PPI interfaces are specific and flexible, making them ideal scaffolds for developing tools and for probe and drug design, especially within the CNS where selectivity and specificity are vital for limiting side effects. The split-luciferase complementation assay (**LCA**) is a robust method for interrogating interactions between ion channels and their regulatory proteins [45,124–126], enabling rapid screening of compounds prior to more labor-intensive orthogonal assays. The LCA can be adapted for high-throughput screening (**HTS**) of large chemical libraries against protein-channel complexes to facilitate hypothesis generation and testing of mechanisms associated with neuronal plasticity and other forms of cellular adaptations. Such endeavors lay the groundwork for medication development against a wide array of diseases associated with ion channel dysfunction.

The goal of this chapter is to: *i*) provide specific technical information for generating a double stable cell line that can be used to assess protein-channel regulators in live cells; *ii)* provide guidance for miniaturizing this assay from 96-well to 384-well plates

with regard to optimization of parameters that both maximize hit detection and selection, and reduce total costs during screening campaigns; *iii)* provide an overview of HTS data analysis to exemplify how this assay lends itself for rapid validation of hits via analysis of in-cell potency and efficacy; and *iv)* explain the methodology for expedited functional validation of hits using the Nanion Port-a-Patch, a portable planar patch-clamp electrophysiology device for rapid functional validation of hits [127].

3.1.1 Development of a robust assay to assess protein-channel interactions in a double stable HEK293 cell line

We have previously introduced the LCA to detect the assembly of FGF14 with the intracellular C-terminal tail of the Nav1.6 channel in live cells using transient transfection [49,50,57,75,126]. The assay was designed with the intent of reconstituting the protein-channel complex in cells using a minimal functional domain (**MFD**) approach, namely restricting the target for screening only to key residues mediating interactions within binding partners. While the MFD approach has been integral to vaccine development strategies in immunology [128], it has been poorly explored in other fields of therapeutic development with few exceptions for G-protein coupled receptors [129], microtubule proteins [130] and the STIM-Orai1 channel complex [131–133]. Thus, MFD represents a novelty in the ion channel drug discovery field. In the LCA, the C-terminal and N-terminal fragments of the *P. pyralis* luciferase are fused, respectively, to FGF14 (CLuc-FGF14), and a chimera expressing CD4 fused to the Nav1.6 C-tail (CD4-Nav1.6-NLuc). Construction of LCA constructs requires cloning of the two interacting partners of interest into suitable mammalian expression vectors. The vectors are designed to express the target proteins in frame with complementary luciferase fragments spaced by a flexible linker region [126]. Following co-

expression of these constructs in transiently transfected HEK293 cells, FGF14:Nav1.6 C-terminal tail complex formation can be detected in the presence of the luciferase substrate, D-luciferin, with light production as a read-out of relative binding of the two proteins. However, while transient transfection is suitable for establishing new assays and is still the preferred mode for directly comparing the impact of mutations on protein-channel interactions, stable cell lines are vastly superior, if not necessary, for large screening campaigns against a unique target. Thus, with the intent of developing an assay suitable for HTS, the first goal is to develop a double stable cell line to circumvent the need for high volume transient transfections, reducing variability and labor-related costs. A double stable HEK293 cell line can be generated using linearized CLuc- and -NLuc constructs under the control of selective antibiotics, such as neomycin and puromycin, as for CLuc-FGF14 and CD4-Nav1.6-NLuc, respectively.

3.1.2 Miniaturization and optimization of assay in 384-well plates

This assay should be adapted from a 96-well to 384-well plate format with the intent of achieving a satisfactory Z'-factor (≥ 0.5 for in cell assays) and the minimal resource consumption required for maintaining robust assay performance. The Z'- factor (also known more simply as Z') is a well-accepted statistical parameter utilized to determine assay performance; it is defined as the ratio between the sum of the standard deviation of the positive and the negative control groups, and the difference between the arithmetic means of the two groups, respectively [134]. An overall Z' of ≥ 0.5 signifies that the assay is sufficiently robust for hits to be reliably identified as statistically significant despite well-to-well and plate-to-plate variability. With this in mind, we explored two criteria to maximize Z'; cell density and efficacy of positive controls. Greater signal separation

between these controls compared to the vehicle (i.e., DMSO which is used to dissolve compounds) improves Z' and increases confidence in hit detection. Finding reliable and robust positive and negative controls can be a challenge, especially when little is known about a given target. For instance, for our target, positive controls were selected from kinase inhibitors, which presumably affect the FGF14:Nav1.6 complex formation indirectly through posttranslational modifications (no changes are observed in protein expression). Even when the ultimate goal of the screening campaign is to identify small molecules that modify the PPI interface of a protein complex directly, it may be necessary to select positive controls from separate classes of compounds, if no chemical modifiers of the desired group are available at the time.

MINIATURIZATION

To miniaturize the assay from 96-well to 384- or 1536-well plates, parameters for optimization should include cell density, positive and negative controls, reagent volumes, substrate incubation times, cell adhesion, and media composition. In previous versions of our LCA, based on transient expression of cDNA plasmids, transfected cells were transferred from the original 24-well plate format, chosen for optimal transfection efficiency, into either 96-well or 384-well plates 24 h prior to the assay. We found that to be necessary to facilitate protein production, as well as maximizing cell adhesion prior to exchange of media for compound treatments [45]. However, plating cells in advance (> 18 h) necessitates the use of complete cell culturing medium including 10% FBS and phenol red, which we found reduce compound effectiveness and inhibit luminescence signal, respectively. Thus, to limit interference with LCA performance, cells need to be washed and medium replaced with serum-free/phenol red-free medium prior to the assay. We

attempted washing cells (in 384-well plates) with either warm medium or saline phosphate buffer but observed significant and highly variable levels of cell loss (i.e., large patches of detached cells) during aspiration with the automated Multidrop Combi reagent dispenser on the slowest dispensing speed settings, and also found that ~5-10 µL of medium (final volume per well=40 µL) remained in each well following aspiration. Though deviations from the desired volume by 5% [135] are commonly accepted for liquid handling devices, any residual volume from washes constitutes an additional source of variation. Furthermore, it is not feasible for liquid handling devices to completely aspirate all reagent in 384-wells, leading to dilution of the fresh 40 µL of serum-free media by ~20% (10 µL) and resulting in variable compound concentrations during screening (final concentration >30 µM in a volume of >40 µL). We tested the assay using cells in suspension (cells plated 1-4 h prior to plate reading) and observed superior raw luminescence values compared to adherent cells, with positive controls exerting similar effects. Thus, for the assay presented here, we recommend using cells in suspension to increase reliability and reduce costs during HTS campaigns.

OPTIMIZATION

The primary criterion to consider for optimization of LCA is cell density per well, which should be evaluated with respect to signal-background (S:B) ratio and Z' when treated with the positive controls. We observed that Z' improves with increasing cell density and extended D-luciferin incubation (≥ 45 min) due to greater signal separation between positive and negative controls, and thus recommend reading plate luminescence for a sustained duration to identify optimal plate reading time-points for subsequent screening campaigns. Additionally, we have observed a significant relationship between

cell density and dose of the inhibitory positive control MNS: the inhibitor dose-response curve shifts to the left with decreasing cell density, indicating increased drug efficacy. This is an extremely useful point, as during compound screening, each plate should include an 8-point dose-response of the positive control, enabling evaluation of plate-to-plate variability and rapid identification of faulty experiments. For instance, errors in cell plating that lead to excess cells per well can be recognized by reduced potency of the negative control (dose-response curve rightward-shift). Potency of screened compounds can be extrapolated by mapping their respective well's luminescence against this curve, thereby improving hit detection due to an additional layer of "normalization" with respect to changes in cell density.

Users should also be aware that Z' will likely increase with increasing cell density, largely due to greater S:B. However, we recommend using the absolute minimum cell density that demonstrates satisfactory assay sensitivity for two reasons: *i)* during compound screening, lower cell density translates into increased probability of a potent inhibitor to cross the hit threshold due to increased efficacy and *ii)* a 25% reduction in cell density significantly cuts cell culture resource requirements when large volumes are required for HTS. Thus, if two cell densities yield similar Z' values, the lesser density should be used. A similar rationale should also be applied when optimizing other variables, such as volume per well.

3.1.3 Limitations of the LCA system for screening ion channel regulators, and possible solutions

One major drawback of LCA and other luminescence-based screenings is the relatively high number of false positives compared to other screening modalities, a

phenomenon that has been attributed in some cases to the spurious activity of compounds on the reporter (luciferase). In the LCA, a false positive hit could bind to the reconstituted luciferase interfering with the enzyme's ability to emit light leading to target-unrelated signal reduction. It is necessary to control for this by including counter-screenings by which putative hits are tested against the full luciferase enzyme. However, our experience is that counter-screenings can eliminate valuable compounds. In an early screening campaign aimed at identifying kinase pathways regulating the FGF14:Nav1.6 channel complex, we triaged the casein kinase 2 (CK2) inhibitor 4,5,6,7-tetrabromobenzotriazole (TBB) on the basis of full luciferase-based counter-screening [46]. A subsequent analysis of the FGF14 coding sequence identified a putative CK2 sequence recognition motif and spurred further evaluation of structurally diverse CK2 inhibitors. Not only did these follow-up studies reveal potent regulation of the FGF14:Nav1.6 complex by the CK2 enzyme [57], but they also enabled integration of the results with a broader signaling pathway analysis that revealed convergence of CK2 and the enzyme glycogen-synthase kinase 3 (GSK3) on the same region (aa226-231) of FGF14 [49]. Thus, although we recognize the need for counter-screenings, we advise making hit selection an integrated process encompassing chemoinformatic as well as domain-expert and pathway analysis. Another limitation of the LCA is that it does not allow for identification of toxic compounds nor selection of hits based on functional activity. In both cases, these limitations can be overcome by integrating counter-screenings for cell toxicity and orthogonal assays, such as manual or planar patch-clamp electrophysiology, for functional validation of hits.

3.1.4 Advantages of the cell-based LCA approach to discovering new ion channel regulators

The foremost advantages of the LCA are its flexibility for choosing what targets will be used, as well as its ability to be implemented in live cells, allowing reconstitution of protein-channel interactions in a physiological environment (i.e., maintaining channel domains at the cell membrane where specific ionic concentrations or presence of region-specific signaling mediators may have a significant impact on protein conformation).

Additionally, conducting a primary screening using cell-based assays such as the LCA enable simultaneous filtering out of poorly permeable and cytotoxic compounds, providing initial ADMET information for hits at an early phase of the drug discovery campaign. Another advantage is the microplate format of the LCA that enables multiplexing by which following luminescence reading, cells can be assayed with other screening modalities, such as in-cell Western and imaging-based high-content phenotypic screenings [136,137], providing a comprehensive read-out of any given compound performance. For screening campaigns of 2,000-100,000 compounds where there is interest for multiple assays, we recommend using a 384-well plate format (working volume per well of 15-110 μL). In the 384-well format, the final volume of the LCA can range between 40-80 μL depending on optimized conditions, leaving room for 30-70 μL of additional reagents, such as a fluorescent-based cell viability assay (i.e., CellTiter-Blue) or high-content screening dyes. Furthermore, the optimized LCA used for HTS can subsequently be used for rapid validation of hits via dose-dependency studies, enabling ranking of hits by potency and efficacy prior to more labor-intensive validation studies. Using conditions identical to that of the primary screening, 8-20 hits can be tested per 384-well plate using 8-10 doses with n=2-4 replicates per concentration. During follow-up studies, this system also facilitates confirmation of repurchased hit potency, preliminary

evaluation and comparison of analogs to parent compounds, as well as mechanistic investigations through transient transfection with LCA constructs containing rationally-guided point mutations.

3.2 MATERIALS

Prepare all solutions using ultrapure water (18 MΩ-cm at 25 °C) and analytical grade reagents. Prepare and store all reagents at 4 °C (unless indicated otherwise). Diligently follow all waste disposal regulations when disposing waste materials. We do not add sodium azide to reagents as it might interfere with the assay results.

3.2.1 Cell Lines and Bacterial Strains

1. HEK-293 cells
2. Chemically competent *E. coli* (such as One Shot TOP10 Chemically Competent *E. coli*, Invitrogen).

3.2.2 Tissue Culture

1. *Complete medium*: Dulbecco's Modified Eagle's Medium (DMEM) and F12 (Ham's) nutrient mixture in 1:1 ratio supplemented with 10% Fetal bovine serum (FBS), 100U/mL penicillin and 100ug/mL streptomycin. To prepare ~500 mL, combine 220 mL DMEM, 220 mL F12, 50 mL FBS, and 5 mL of 1000X Penicillin–Streptomycin solution. Store 50 mL aliquots at 4 °C for up to 4 weeks.
2. *Preconditioned medium*: complete medium (fresh) supplemented with 10-40% complete medium collected from healthy HEK293 cells maintained in dishes or flasks. The cells used for generating preconditioned medium should be washed and medium replaced no less than every 48 hrs. Pass through sterile 0.22 μm filters to remove cells and other contaminants.

3. 1X phosphate-buffered saline (PBS): 0.02 M phosphate (0.0038 M NaH_2PO_4, 0.0162 M Na_2HPO_4), 0.15 M NaCl, pH 7.4, titrated with HCl.
4. 0.25 % Trypsin–EDTA, diluted at a ratio of 1:6 for 0.25% trypsin-EDTA to PBS.
5. 75 cm^2 and 150 cm^2 cell culture flasks.
6. 10 cm^2 tissue culture dishes.
7. 6-well and 24-well tissue culture plates.
8. 96-well and 384-well tissue culture white/μClear® plates with lid (Greiner Bio-One).
9. Transfection reagent (such as Lipofectamine 3000, Invitrogen).
10. Geneticin (G418), 100 mg/mL, dissolved in sterile water or PBS.
11. Puromycin, 1 mg/mL, dissolved in sterile water or PBS.
12. 150 μL cloning cylinders, glass (Millipore Sigma, C1059)
13. Trypan blue.

3.2.3 Cloning and DNA Preparation

1. pcDNA3.1-CD4-Nav1.6 C-tail-NLuc [126].
2. pEF6-CLuc-FGF14 [126].
3. pcDNA4-TO-Puromycin-mVenus-MAP (ECFP variant; Addgene, plasmid # 44118).
4. pGL3 firefly luciferase plasmid (Promega).
5. Phusion High-Fidelity DNA Polymerase (New England Biolabs).
6. High Fidelity BamHI, NotI, and XbaI restriction enzymes (New England Biolabs).
7. Custom cDNA Primers (Integrated DNA technologies).
8. T4 DNA ligase (New England Biolabs).

9. Gel Extraction Kit (Qiagen)
10. Luria broth (LB): 10 g of Bacto-Tryptone, 5 g of yeast extract, 10 g of NaCl dissolved in 1 L of distilled or deionized H2O and sterilized by autoclaving.
11. Luria agar: 10 g of Bacto-Tryptone, 5 g of yeast extract, 10 g of NaCl, 15 g of agar dissolved in 1 L of distilled or deionized H2O with heating and sterilized by autoclaving.
12. Ampicillin.
13. Selection media: LB agar plates supplemented with 100 μg/mL ampicillin.
14. QIAprep Spin Miniprep Kit (Qiagen).
15. EndoFree Plasmid Maxi Kit (Qiagen).

3.2.4 Luciferase Assay

1. *LCA cell medium*: combine 245 mL of DMEM without Phenol Red with 245 mL of F12, 5 mL of 1000X non-essential amino acids, and 5 mL of 1 M HEPES. Store 50 mL aliquots at 4 °C. HEPES is added to prevent pH changes during long periods outside of CO2 atmosphere (i.e., while reading plate luminescence for >1 hr).Presence of phenol red may reduce luminescence signal, and FBS may interfere with compound effects during screening, and thus are not recommended as components of medium for assaying.
2. *30 mg/mL D-luciferin stock solution*: dissolve 1 g of D-luciferin (potassium salt, GoldBio) in 33.33 mL of cold PBS. Store 1.25 mL aliquots at -20 °C. Keep solutions containing luciferin protected from light.
3. *50 mM Coenzyme A stock solution*: dissolve 100 mg of Coenzyme A (trilithium salt, Sigma) (**Note 1**) in 2,547 μL of cold PBS. Store 75 μL aliquots at -20 °C.

4. *LCA substrate solution (2X)*: For one 96-well plate (minimum required volume of 9.6 mL for 100 µL /well), combine 1.25 mL of 30 mg/mL D-luciferin, 75µLof 50 mM Coenzyme A, and 11.2 mL of warmed (37 °C) PBS (**Note 2**) to yield a final concentration (2X) of 3 mg/mL D-luciferin and 0.3 mM Coenzyme A. For one 384-well plate (minimum required volume 15.36 mL for 40 µL /well), scale up volume for one 96-well plate by 1.5X (1.875 mL of 30 mg/mL D-luciferin, 112µLof 50 mM Coenzyme A, and 16.8 of mL PBS). Thoroughly mix and keep protected from light. Solutions should be used within 1 hr. Volumes can be scaled up proportionally. Prepare an additional half recipe for priming if using an automated liquid dispenser. Dispense an equal volume of this 2X solution to wells prior to luminescence reading; final well concentration (1X) during luminescence reading: 1.5 mg/mL D-luciferin and 0.15 mM Coenzyme A.
5. Dimethyl sulfoxide (DMSO).
6. *Positive control (inhibitor):* Dissolve 4 mg of MNS (3,4-Methylenedioxy-beta-nitrostyrene) in 518 µL of DMSO to yield a 20 mM stock. Store 20 µL aliquots at -20 °C.
7. *Positive control (enhancer):* Dissolve 10 ug of recombinant human tumor necrosis factor- α (TNF-α) protein in 995 µL of cold PBS and supplement with 5 µL of 20 mg/mL BSA to yield a final concentration of 10 ug/mL TNF-α with 0.1 mg/mL BSA. Store 20 µL aliquots at -20 °C.
8. White plate bottom tape seals (**Note 3**).
9. Targeted compound libraries resuspended in 100% DMSO (**Note 4**)

3.2.5 Cell Viability Assay

1. Cell Proliferation Assay Kit (such as CellTiter-Blue, Promega).

3.2.6 Electrophysiology

1. *Nanion standard Intracellular (internal) solution for Na^+ channels:* 50 mM CsCl, 10 mM NaCl, 60 mM Cs-Fluoride 20 mM EGTA, 10 mM HEPES; osmolarity: 285 mOsmol. Adjust pH to 7.2 using CsOH. Sterilize using 0.22 μm filters, and store 1 mL aliquots at 4 °C for up to 1 week or at -20 °C for up to 6 months.
2. *Nanion standard extracellular (external) solution for Na^+ channels:* 140 mM NaCl, 4 mM KCl, 1 mM $MgCl_2$, 2 mM $CaCl_2$, 5 mM D-Glucose monohydrate, 10 mM HEPES; osmolarity: 298 mOsmol, or at least 10 mOsmol greater than the intracellular solution. Adjust pH to 7.4 using NaOH. Sterilize using 0.22 μm filters, and store 10-50 mL aliquots at 4 °C for up to 1 week or at -20 °C for up to 6 months.
3. *Seal enhancing solution (SES):* 80 mM NaCl, 3 mM KCl, 10 mM $MgCl_2$, 35 mM $CaCl_2$, 10 mM HEPES; osmolarity: 298 mOsmol. Adjust pH to 7.2 using HCl. Sterilize using 0.22 μm filters, and store 1 mL aliquots at 4 °C for up to 1 week or at -20 °C for up to 6 months.
4. *Suspension medium:* DMEM and F12 (Ham's) nutrient mixture in 1:1 ratio supplemented with 15 mM HEPES. Combine 246 mL of DMEM, 246 mL of F12, and 7.5 mL of 1 M HEPES. Store 50 mL aliquots at 4 °C.
5. TrypLE Express Enzyme (1X).
6. NPC-1, 3-5 MOhm Chips (Nanion #061103)

3.2.7 Instrumentation

1. Thermal cycler.
2. Gel imaging system (i.e., Alpha Imager).

3. UV/Vis spectrophotometer (i.e., Nanodrop).
4. Multimode microplate reader (i.e., Tecan Infinite M1000 or Biotek Synergy Neo2).
5. Liquid dispenser, preferably automated (i.e., Multidrop Combi); alternatively, a multichannel pipet (12 channels) may be used.
6. LabCyte Echo 550 acoustic liquid handler.
7. Hemocytometer, preferably automated (i.e., Bio-Rad TC 10).
8. Port-a-Patch (Nanion).

Figure 3.1: Overview of procedure for generating a double stable cell line.
Plasmids for expression of the luciferase constructs are linearized prior to sequential

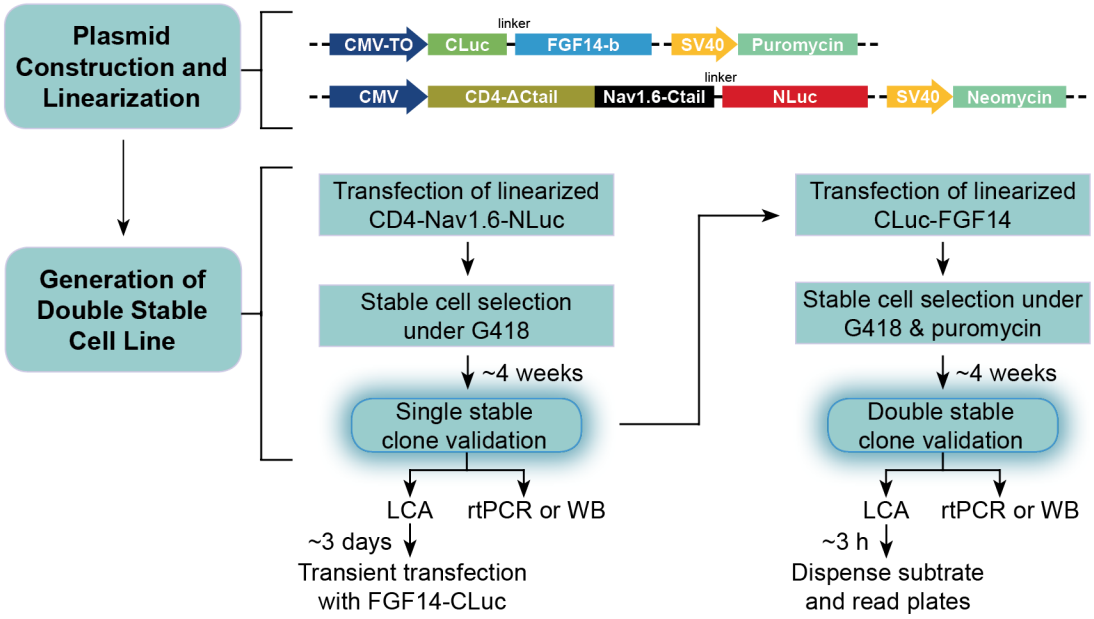

transfection in HEK293 cells (Step 3.1), and cells are selected using the antibiotics G418 (resistance encoded by the Neomycin gene) and puromycin. Following successful insertion of the first expression vector (encoding CD4-Nav1.6-NLuc), cells are validated using either rtPCR or WB (to confirm presence of recombinant protein), as well as by LCA, whereby the single stable cells are transiently transfected with CLuc-FGF14. In contrast, double stable cells can be rapidly validated by administration of the substrate solution and reading luminescence. Lack of luminescence indicates a non-usable cell line, and alternate clones should be selected. Abbreviations: LCA, luciferase complementation assay; WB, Western blot

3.3 METHODS

Described below are (1) the steps to create a double stable cell line using linearized vectors and (2) how to optimize an assay in 384-well plates for HTS to screen regulators of Nav channels. The previously known interacting pair of FGF14 and Nav1.6 intracellular C-terminal tail will be used to demonstrate the use of this assay to screen regulators or small molecule probes, but this system is well suited for investigating other similar targets (i.e., binding between an ion channel and other regulatory proteins, such as CaMKII). For those intending to screen relatively small libraries (<5,000 compounds), transient transfection may be adequate, and Steps 3.2 may be skipped. However, the use of a stable cell line will significantly reduce plate-to-plate variability and allow for lower cell densities/well, enabling more robust hit detection.

3.3.1. DNA Cloning and Linearization of Constructs

First, coding regions for proteins of interest are cloned in frame with the CLuc or NLuc fragments and must be inserted into vectors containing resistance genes for the selective antibiotics puromycin or G418. The methodology for the initial generation of both the pcDNA3.1-CD4-Nav1.6-NLuc and pEF6-CLuc-FGF14 constructs has been described previously [126]; the pcDNA3.1 vector contains the neomycin gene, which enables resistance to G418. However, the CLuc-FGF14 fragment must be excised from pEF6 and inserted in the pcDNA4-TO-Puromycin-mVenus-MAP vector to enable resistance to puromycin. Additionally, we recommend excision of the ECFP component through addition of a single XbaI restriction site. Finally, the two constructs are linearized prior to transfection to improve integration of DNA into the cell genome for stable cell creation (**Fig. 3.1**).

3.3.1.1 Excise ECFP from pcDNA4-TO-Puromycin-mVenus-MAP

1. To excise ECFP from pcDNA4-TO-Puromycin-mVenus-MAP, first insert an additional XbaI restriction site at the N-terminus of ECFP using two site-directed mutagenesis steps with the following primers:
    i. Forward pcDNA4.XbaI.1FW: 5'- GGCGGCCGCGTCTGCAGCAT - 3'
    ii. Reverse pcDNA4.XbaI.1RV: 5'- CCGCCGGCGCAGTCGTCGTA – 3'
    iii. Forward pcDNA4.XbaI.2FW: 5'- GCGGCCGCGTCTAGAGCATGG – 3'
    iv. Reverse pcDNA4.XbaI.2FW: 5'- GCGGCCGCGTCTAGAGCATGG – 3'.
2. Digest pcDNA4-TO-Puromycin-mVenus-MAP (~5-10 µg) using XbaI (1 µL or ~10 Units) to excise the ECFP fragment and yield linearized DNA with sticky ends. Perform in triplicate with a final volume of 50 µL per reaction, and incubate at 37 °C for 1 h.
3. Re-ligate the vector using T4-DNA ligase (100 ng in 20 µL volume), and incubate for 16 h at 16 °C.

3.3.1.2 Insert CLuc-FGF14 into pcDNA4-TO-Puromycin-mVenus-MAP

1. Excise the cDNA fragment corresponding to the coding sequence for the CLuc-FGF14 from pEF6-CLuc-FGF14 using the BamHI and NotI restriction enzymes: combine 10 µg of pEF6-CLuc-FGF14 plasmid DNA and 1 µL of each enzyme with their respective 1X reaction buffers for a final reaction volume of 50 µL. Incubate at 37 °C for 1 h. Perform this reaction in triplicate. Resolve products by electrophoresis using a 1% agarose gel and purify using a gel extraction kit according to the manufacturer's instructions.

2. A directional cloning strategy can be used to insert the excised and purified CLuc-FGF14 fragment into the cDNA4-TO-Puromycin-mVenus-MAP vector at 5' BamHI and 3' NotI sites. Ligate the purified CLuc-FGF14 fragment (insert) into the pcDNA4-TO-Puromycin-mVenus-MAP vector at 5' BamHI and 3' NotI sites, with a 1:3 molar ratio of vector to insert, using T4 DNA ligase, and incubate for 16 h at 16 °C.
3. Use 0.5–5 µL of the ligation reaction mixture to transform 50 µL of high efficiency DH5α *E. coli* cells. Add 450 µL of LB broth to transformation reaction and incubate at 37 °C for 1 h prior to plating on selective LB agar plates supplemented with 100 µg/ml ampicillin.
4. Select individual colonies and grow 5 mL overnight cultures in LB broth containing 100 µg/ml ampicillin.
5. Purify plasmid DNA using a Miniprep Kit and confirm the identity of the recombinant plasmid by restriction digestion using BamHI and NotI restriction enzymes.
6. Finally, verify the construct pcDNA4-TO-Puro-CLuc-FGF14 by DNA sequencing with the following primers:
    i. Sequencing primer 1: 5' – GACCTCCATAGAAGACACCGG – 3'
    ii. Sequencing primer 2: 5' – GCAGGCAAGGCTACTACTTG – 3').
7. Select colonies which yielded correct recombinant plasmids and grow 100 mL cultures in LB broth containing 100 µg/ml ampicillin using the verified clones and purify plasmid DNA using an EndoFree Plasmid Maxi Kit.

8. Quantify the purified constructs by UV spectrophotometry (i.e., optical density at 260 nm using the Nanodrop).

3.3.1.3 Linearize the constructs containing CLuc-FGF14 and CD4-Nav1.6-NLuc

1. Linearize the pcDNA3.1-CD4-Nav1.6 C-tail-NLuc and pcDNA4-TO-Puromycin-CLuc-FGF14 constructs with single cutter restriction enzyme NotI and XbaI, respectively, according to the manufacturer's instructions.
2. Resolve the digested reaction mix by electrophoresis using a 1% agarose gel, and visualize linear bands using a gel imaging system. Purify linear bands using a gel extraction kit according to the manufacturer's instructions. Elute the linearized DNA fragments in 30 µL of sterile, molecular biology grade water to obtain an expected final yield of ~300-500 ng/µL.

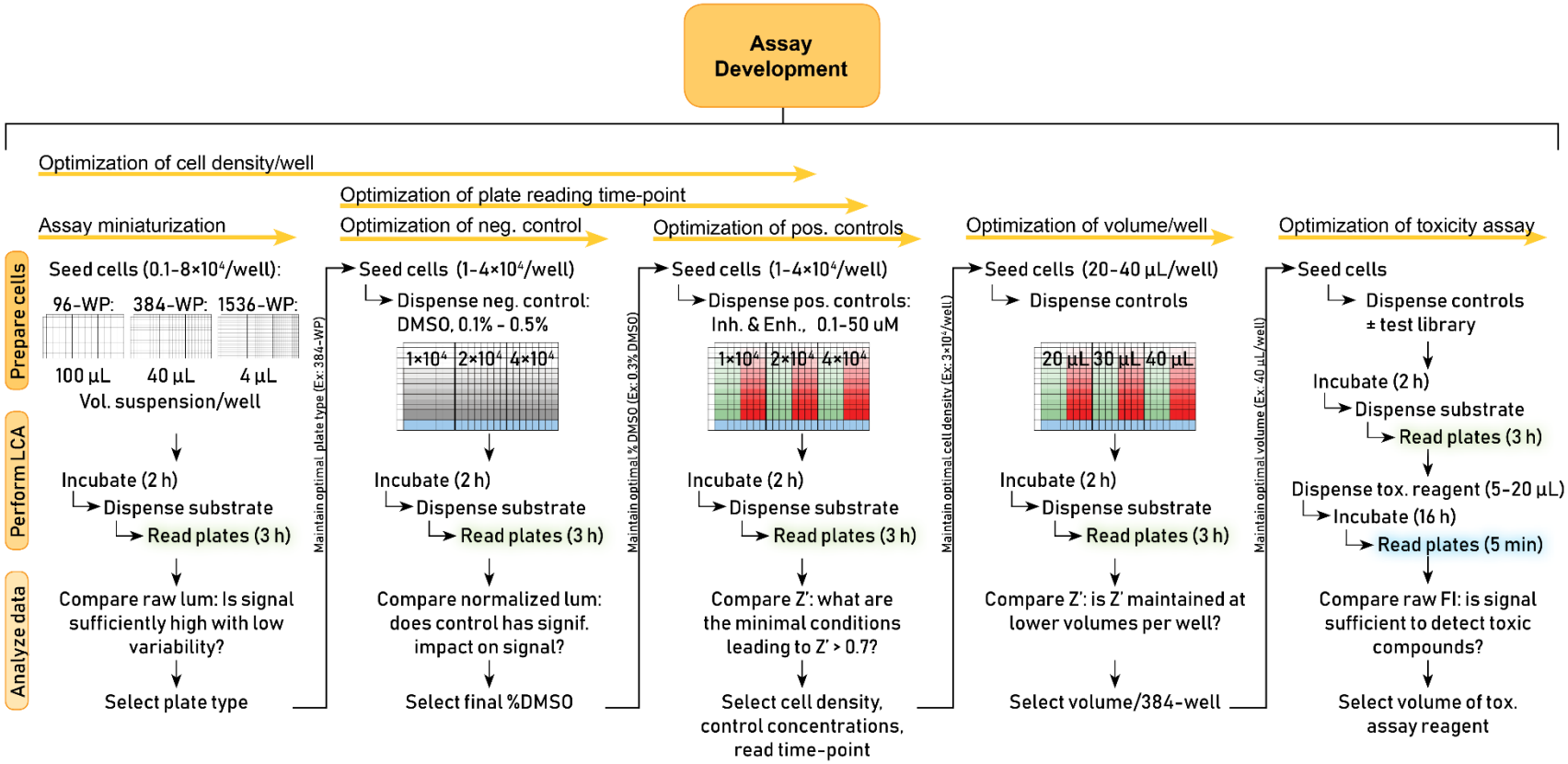

Figure 3.2: Assay development.

Schematic of the procedure for developing an assay to screen compounds against protein-channel interactions in a high-throughput format, representing the methodological procedure discussed in Step 3.3. Abbreviations: FI, fluorescence intensity; LCA, luciferase complementation assay; WP, well-plate.

3.3.2. HEK293 Cell Transfection and Selection of Stable Clones

The primary goal of this section is to generate a monoclonal cell line that expresses both recombinant LCA constructs. First, one linearized construct will be transfected into HEK293 cells and clones will be selected using G418 over 3-5 weeks, and then validated by LCA, as well as WB and/or rtPCR (**Fig 3.1**). These single stable clones should be expanded and used for transfection of the second linearized construct, and the clone selection process repeated using both G418 and puromycin. Due to slow cell growth in the presence of these antibiotics, this process may take between 3-6 months.

1. Maintain HEK293 cells in 75 cm^2-tissue culture flasks in a 5% CO_2 incubator at 37 ºC using complete medium. These flasks must be maintained to provide preconditioned medium for generation of the first single stable clones.
2. Plate $3.5x10^5$ HEK293 cells per well (6 wells total) of a 24-well tissue culture plate and incubate overnight to give monolayers at ~80 % confluency.
3. The next day, gently wash the HEK293 cells two times with prewarmed DMEM/F12 without serum or antibiotics and transfect (with Lipofectamine 3000) using either 1 or 2 µg of linearized pcDNA3.1-CD4-Nav1.6 C-tail-NLuc plasmid DNA, at least two 24-wells per transfection (**Note 5**). Use 1 µl of the transfection reagent per 1 µg of plasmid DNA, with a final transfection volume of 200 µl per well, as described previously [126]. Leave two wells non-transfected as controls (for when media with antibiotics is added, to make sure non-transfected cells die).
4. After 24 h, aspirate media, wash cells with 400 µl PBS, and dispense 1 mL of 30% preconditioned medium (**Note 6**) supplemented with 0.5 mg/mL G418 to all wells (including two control wells). Allow cells to grow for 24 h.

5. After 24 h, wash each well briefly with 400 µl of PBS and dispense 100 µl of 0.04 % trypsin solution (0.25 % trypsin diluted with PBS) per well. Stop trypsinization using 800 µL of complete medium, and carefully wash the cells off the plate and dispense all wells for each transfection ratio into separate 15 mL tubes. Centrifuge for 5 min at 800 x *g* and resuspend in 5 mL complete medium.
6. Plate cells at a low density (~20% confluency) in 6-well plates using a final volume of 4 mL of 30% preconditioned medium (supplemented with G418) per well.
7. Replace medium every 2-3 days to remove dead cells, provide fresh nutrients, and replace degraded antibiotic. When few to no viable cells are observed in control wells (non-transfected cells in medium containing antibiotics) or when wells contain healthy stable cells that have grown to ≥30% confluency, wash and split cells to new 6-well plates or 6 cm^2 dishes.
8. After 2-3 weeks, wash and split wells containing healthy cells to 10 cm^2 dishes at an extremely low density (**Note 7**) using a final volume of 8 mL of 20% preconditioned medium (supplemented with G418) per dish.
9. After 1-2 days, use an inverted light microscope to identify the healthiest cells. Gently mark their location on the dish bottom using a permanent marker. Use cloning cylinders to isolate ≥ 5-10 single cells as follows:
    a. Place cloning cylinders (glue side down) onto marked colonies on plate
    b. Using a gloved, sterile hand press gently on top of the cylinders to secure them around the colonies.
    c. Add 50 µL Trypsin-EDTA:PBS (1:6) to each cylinder and incubate for 1-3 min.

d. Add 50 µL complete medium to each cylinder and use a 1000 µL tip pipette to triturate and disperse cells.

e. Transfer 100 µL from cylinder into 24-well plates, and dispense 1 mL of 20% preconditioned medium (supplemented with G418) to each well.

10. Grow for ~1 week or until cells reach >70% confluency, *gently* changing media (take care to not detach cells) every 3 days.

11. Validate clones using LCA, in addition to either WB [126] or rtPCR [138]. For LCA, split each clone into 4 wells of a 24-well plate, and subsequently transfect with 1 ug of pEF6-CLuc-FGF14 per well. After 24 h, split into 96-well plate and read plate luminescence, as described previously [126]. Expand 1-2 clones (**Note 8**) that yield the highest luminescence, as well as exhibit presence of the CD4-Nav1.6-NLuc construct (by WB or rtPCR).

12. Using single stable clones, repeat Steps 3.2.1 - 3.2.10. At this stage, medium should always contain 0.5 mg/mL G418, and should be supplemented with 1 µg/mL puromycin following transfection with linearized pcDNA4-TO-Puromycin-CLuc-FGF14 plasmid DNA.

13. Validate clones using LCA, in addition to either WB [126] or rtPCR [138]. To validate double stable clones by LCA:

    a. Expand each clone in at least two wells of 24-well plates.

    b. Trypsinize cells as in Step 3.2.5. Resuspend cells from one 24-well in 450 µL of LCA medium and dispense 100 µL to four 96-wells. Incubate at 37ºC for 2 h.

c. Dispense 100 μL of LCA substrate solution to each 96-well, and read plate luminescence for ≥ 30 min, as described previously [126].

14. Expand 1-2 clones that yield the highest luminescence, as well as exhibit presence of both the CD4-Nav1.6-NLuc and CLuc-FGF14 constructs (by WB or rtPCR). Proceed to Section 3.3 using a single clone, and store alternate clones at -80ºC.

3.3.3. Assay Miniaturization and Optimization in 384-well Plates

For the purpose of screening large chemical libraries in a high-throughput and economically viable manner, the assay must be scaled from a 96-well to 384- or 1536-well plate format (**Fig. 3.2**). Assay parameters should then be finely tuned in a manner that leads to satisfactory assay performance while minimally impacting assay sensitivity. This is assessed by measuring the signal separation between the mean of positive and negative controls and the variance between replicates to calculate Z'. Thus, to improve Z', the inhibitory positive control should reduce the signal to as close to zero percent as possible, while the enhancer control should increase the signal by ≥2-fold and ≥3 SDs (i.e., ≥ 200% luminescence when normalized to DMSO controls). For more in-depth understanding of this and related concepts during optimization, we recommend consulting the Assay Guidance Manual [105].

The positive controls MNS and TNF-α are used here due to their effects on the FGF14:Nav1.6 interaction, but these compounds may not work for other ion channel interactions. Additionally, while our assay optimization experiments led us to select 384-well plates containing 3×10^4 cells per 40 μL per well, these conditions may not work for others and are described here with the sole purpose of exemplifying the technical details involved with each step.

All optimization experiments should be tested in triplicate (i.e., three independent 384-well plates with identical conditions) to ensure that plate-to-plate variability can be monitored (through calculation of Z'-factor standard error). The order of steps mentioned here should not be taken as absolute. All components of assay development are deeply intertwined, and thus it may not always be practical to separate optimization into discrete, consecutive experiments as described here. Additionally, it may be necessary to retest previous optimization experiments following significant downstream modifications (i.e., more potent positive control identified, change in volume per well, new brand of substrate reagents).

3.3.3.1. Cell Culture

Cell health is fundamental to any in cell screening campaign. Cell culture conditions (flask type, media composition, cell handling, and schedule for passing cells) must be kept constant to reduce variability during assay development and screening.

1. Expand double stable cells to ~90% confluency in 150 cm^2 cell culture flasks. Wash cells with 10 mL of warm PBS and provide 25-30 mL of complete medium (supplemented with appropriate antibiotics) every other day. To ensure cells do not reach >95% confluency (may change gene expression), pass cells every 3-4 days using the following protocol:
    a. Aspirate media
    b. Dispense 10 mL warm PBS to wash *briefly* (<5 sec); aspirate PBS.
    c. Dispense 4 mL of trypsin-EDTA (1:6) and incubate at 37C for 1-2 min; observe cells under microscope to ensure all cells are detached and in solution.

d. Dispense 8 mL of complete medium, collect all cells in a 15 mL tube, and centrifuge.

e. Aspirate supernatant and resuspend in complete medium.

2. To prepare cells on the day of assaying, trypsinize 3-5 flasks with cells at ~75-90% confluency following Steps 3.3.1.1A-D but using a 50 mL tube to collect cells from all flasks (of similar passage number). Resuspend cells initially using ~6 mL of LCA medium and thoroughly triturate using a 5 mL serological pipette. Ensure all cell clumps have been removed using a light microscope or cell counter, then add ~40 mL of LCA medium and incubate at RT for 30 min (or no more than 5 h) prior to counting and dispensing cells for assaying.

3.3.3.2. Assay Miniaturization

Following generation of the stable cell line, the assay can be scaled down depending on 1) the intended volume of the screening campaign, and 2) the basal luminescence that can be generated by the stable cell line. Luminescence increases approximately linearly with cell density, and a minimum of ~0.5-1×10^4 cells may be required to detect appreciable signal (Fig. 3), although surface area per well may also play a role. Additionally, the required cell concentration to achieve a cell density in smaller wells may be prohibitive; suspensions with high cell concentrations to dispense a large number of cells in a very low volume (i.e., 5 µL per 1536-well) may result in excessive variability due to fluctuations in cell concentration throughout the suspension being dispensed. This may occur when dispensing cells at a concentration ≥ ~1,000 cells/µL. We recommend beginning with at least 3 cell densities covering a broad range per plate format. This step will serve as an initial guide for subsequent steps where cell density per well can be further refined.

1. Quantify cell viability (using trypan blue) and cell density using a cell counter to ensure there is sufficient cell suspension volume (**Note 9**) containing > 90% live cells.
2. For each plate format, serially dilute cells into equal volumes of 3-6 different densities (**Note 10)**. Dispense each cell suspension across 4, 8, or 16 columns of 96-, 384-, or 1536-well plates, respectively, either manually or with an automated liquid dispenser using the following conditions (**Note 11)**:
    a. 96-well plates: 0.5-1.5×10^5 cells/well using 100 µL of cell suspension/well
    b. 384-well plates: 1-4×10^4 cells/well using 40 µL of cell suspension/well
    c. 1536-well plates: 1-10×10^3 cells/well using 4 µL of cell suspension/well
3. Set up the experimental protocol for the Microplate Reader with the following parameters (**Note 12**):
    a. Maintain temperature at 37 C.
    b. End Point Assay: perform kinetic reading (luminescence) at 5 min intervals for 3 h.
4. Prepare LCA substrate solution (2X), dispense to wells using a 1:1 ratio of cell suspension to substrate solution, and immediately begin reading plates.
5. Plot luminescence over time (as in Fig 2C) for each condition to determine when the signal peaks and plateaus.
6. Choose the plate format that had a reasonable and feasible cell density that output an appreciable luminescence signal with low variability (SD<20% when normalized to the mean luminescence for all wells).

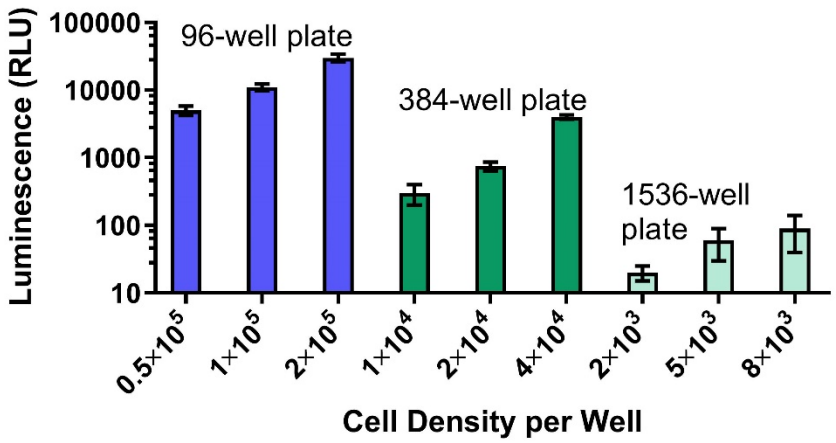

Figure 3.3: LCA signal strength and variability in 96, 384, or 1536-well plates.
Plot of luminescence (RLU, relative luminescence units) by cell density in 96, 384, or 1536-well plates. Luminescence was detected after 1 h incubation with luciferin. While luminescence output has an approximately linear relationship with cell density, numerous other factors also play a role, including surface area per well and volume of cell suspension dispensed per well (60-120 uL/well, 20-50 uL/well, or 3-8 uL/well for 96, 384, or 1536-well plates, respectively). There is often a balance between cell density and volume per well that results in optimal luminescence values with low SD. In our experience, variability increases when too minimal of volumes are used or cell density is too low, leading to inconsistency in actual number of cells dispensed per well.

3.3.3.3. Selection of the Negative Control

Following plate selection, the negative control type and concentration must be selected prior to optimization of positive controls (which require a negative control for comparison). For most ion channel studies, DMSO is the natural choice, as compound libraries (both drug-like scaffolds and kinase inhibitors) are generally dissolved in DMSO. Alternative negative controls may be required for screening of other library types (RNA, etc.). At this stage, it is also necessary to have a general idea of the desired compound screening concentration, which may govern the minimum DMSO concentration needed: the stock concentration of commercially available compound libraries is generally 10 mM. A screening concentration of 20 μM will yield 0.2% DMSO following dispensing a compound to cells, thus this is the minimum concentration of DMSO that should be used

for negative controls. If higher concentrations may be desired for either screening or subsequent validation studies, then use this test to determine the maximal dose that has no significant impact on either cell health or luminescence signal. Concentrations greater than 0.5-1% DMSO may be toxic.

Additionally, this test can be used to further refine an optimal cell density range that generates a sufficiently high signal with low variability. Based on the signal from cell densities in the plate type from Step 3.3.2 (Assay Miniaturization), those densities with low signal should be eliminated. Use the cell density that resulted in sufficient signal, as well as densities with either 50% fewer and 50% greater cells per well. As an example, we describe using 384-well plates.

1. Quantify cell viability (using trypan blue) and cell density using a cell counter.
2. Dilute cells into 3 different densities from 1×10^4 cells/40µL/well to 4×10^4cells/40µL/well (**Note 13**). Dispense 40 µL of each cell suspension across 8 columns of a 384-well plate manually or using an automated liquid dispenser.
3. Prepare 100% DMSO solution in 384-wells of the source plate for an acoustic liquid dispenser. Test the effect of 0.05% to 0.5% DMSO (**Note 14**) for each cell density by dispensing 20 nL to 200 nL of DMSO per well using n≥4 wells per condition; leave one column of cells with no DMSO (cells in media alone) as a negative control.
4. Set up the experimental protocol for the Microplate Reader with the following parameters:
    a. Maintain temperature at 37 ºC.

b. End Point Assay: perform kinetic reading (luminescence) at 5 minute intervals for 3 h.

5. Prepare LCA substrate solution (see Section 2.4), dispense 40 µL per well, and immediately begin reading plates.
6. Plot luminescence over time (as in Fig 2C) for each condition to determine when the signal peaks and plateaus, and whether DMSO had a significant impact.
7. Proceed to the next optimization experiment using the maximum required concentration of DMSO that had minimal impact on luminescence.

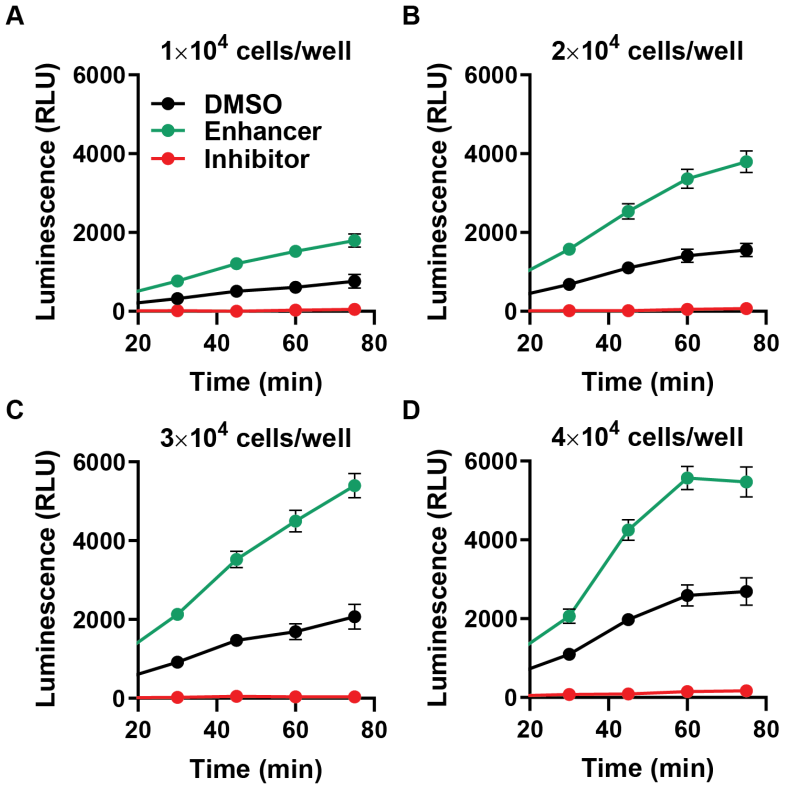

Figure 3.4: Signal separation for positive controls varies with time and cell density per well.
Signal separation for positive controls varies with time and cell density per well. (**a-d**) Plot of luminescence (RLU, relative luminescence units) signal in 384-well plates for 1-4×10^4 cells per well over 30 to 75 minutes following dispensing of the LCA substrate solution containing D-luciferin. Luminescence increases over time and with increasing cell density. The S:B ratio and corresponding Z' values calculated at each time-point also tend increase over time but not necessarily proportionally with either time or cell density. Thus, optimization of the luminescence reading time-point should be thoroughly explored throughout assay development.

3.3.3.4. Optimization of Assay Positive Controls and Cell Density per Well

Following selection of the negative control concentration, the cell density per well should be optimized with respect to the positive controls (**Fig. 3.4**), as assessed by calculation of Z'. As an example, we use a final concentration of 0.3% DMSO, which is maintained for all wells including positive controls.

1. Quantify cell viability and cell density using a cell counter.
2. Dilute cells into 3 different densities from 1×10^4 cells/40μL/well to 1×10^4cells/40μL/well. Dispense 40 μL of each suspension across 8 columns of a 384-well plate manually or using automated liquid dispenser.
3. Prepare positive assay control compounds in 384-wells of the source plate to test an appropriate concentration range for each cell density. For example, for the inhibitor MNS and enhancer TNF-α, we recommend using 8 concentrations (0.1, 0.5, 1, 2.5, 5, 10, 20, and 30 μM for MNS; 0.1, 0.5, 1, 5, 10, 20, 30, 40, and 50 ng/mL for TNF-α) with n≥4 wells per concentration per cell density; additionally, include two columns of negative controls for every cell density (**Note 15**). The final concentration of DMSO should be maintained at 0.3% for all wells (excluding those containing cells with medium alone) by using the acoustic liquid dispenser to backfill with 100% DMSO (i.e., for 20 μM MNS, dispense 40 nL of 20 mM MNS and backfill with 80 nL of 100% DMSO).
4. Set up the experimental protocol for the Microplate Reader as in Step 4 in section 3.3.2.
5. Prepare LCA substrate solution, dispense 40 μL per well, and immediately begin reading plates.

6. Data analysis:
    a. Export relative luminescence values into Microsoft Excel.
    b. Plot luminescence over time (as in Fig. 4) for each condition to determine when the signal peaks and plateaus (**Note 16**).
    c. For each time point, plot the raw luminescence values for all replicates of each condition (0.3% DMSO, MNS, and TNF-α) using a scattered dot plot (**Note 17**)
    d. Plot the individual values of TNF-α compared to control by cell density (Fig 2A); the effect of TNF-α increases with increasing cell density, yielding higher Z' values.
    e. Plot the dose-response of the MNS by cell density (Fig 2B); the dose-response curve shifts to the left with decreasing cell density, indicating increased drug potency.
        i. Maintaining a dose response of control compounds on every screening plate may be beneficial to compare screened compound potency to that of the control dose response curve.
    f. Identify the concentration
    g. The positive control concentration yielding the greatest potency and lowest standard deviation should be used for all subsequent studies
    h. Using the most potent MNS and TNF-α concentration, calculate the following (**Note 18**):

$$Z'\text{factor} = 1 - 3 \times \frac{(\delta_p + \delta_n)}{(\mu_p - \mu_n)} \quad (1)$$

$$S : B = \frac{\mu_p}{\mu_n} \quad (2)$$

$$S:N = \frac{(\mu_p - \mu_n)}{\sqrt{\sigma_p^2 + \sigma_n^2}} \quad (3)$$

$$SW = \frac{\mu_p - \mu_n - 3 \times (\sigma_p + \sigma_n)}{\sigma_p} \quad (4)$$

7. We recommend selecting a final assay cell density based on the following criteria:
    a. Z'-factor > 0.5-0.7 (**Note 19**)
    b. Reproducibility (similar Z'-factor between independent runs/plates).
    c. Minimum necessary cell density (i.e., if two densities have similar Z'-factors and reproducibility, choose the lower cell density to reduce costs and increase apparent potency of screened compounds).

3.3.3.5. Optimization of Assay Volume per Well

Following selection of cell density and optimization of controls, total reagent volume per 384-well can be optimized. For large screening campaigns, smaller volumes can translate to large cost reductions. For example, reducing the volume of cell suspension by 25% (to 30 µL/384-well) would similarly reduce the volume of LCA substrate solution (2X) to 30 µL/384-well, as well as potentially the toxicity assay reagent, which constitutes one of the highest cost reagents. Additionally, a volume reduction would allow greater flexibility for multiplexing of additional assays that may require additional reagents, such as high-content imaging dyes.

1. Quantify cell viability and cell density using a cell counter.
2. Dilute cells into 3 different cell concentrations such that dispensing either 20, 30, or 40 µL of cell suspension per 384-well results in the same cell density per well based on Step 3.3.2 (i.e., all wells in the plate contain 3×10^4 cells, but the final volume of media in each well is 20, 30, or 40 µL. Dispense 20, 30, or 40 µL of each

suspension across 8 columns of a 384-well plate manually or using automated liquid dispenser.

3. For each of the 3 groups (20, 30, or 40 µL), dispense positive controls as in Step 3 in section 3.3.3, with compound volumes appropriately adjusted.
4. Set up the experimental protocol for the Microplate Reader as in Step 4 in section 3.3.2.
5. Prepare LCA substrate solution, dispense 20, 30, or 40 µL per well, and immediately begin reading plates.
6. Analyze data similarly to Step 6 in section 3.3.3.
7. We recommend reducing the assay volume per 384-well if the following criteria are met compared to control (40 µL per well):
    a. Z'-factor is not significantly reduced.
    b. Z'-factor standard error is not significantly increased.
    c. Luminescence peak and plateau timepoints are not significantly extended.

3.3.3.6. Optimization of additional assay variables

There are many variables in every assay that can be similarly optimized, and a fraction of these are briefly described here. While the order of steps and conditions exampled here worked optimally for our assay, we encourage the testing of many conditions to further improve an assay on a case-to-case basis. When assessing any condition, always maintain a full spectrum of controls (negative and positive, multiple doses), sufficient biological replicates (independent plates) and technical replicates (independent wells, consecutive luminescence readings), and consistency of other conditions to enable comparison of runs.

1. Repeat Steps 3.3.5, substituting the following for change in final volume per well:

a. *Volume of substrate solution per well*. Keep cell suspension volume per well constant. Dispense a reduced volume of substrate solution with proportionally increased stock concentrations.

b. *Substrate brand*. Alternate sources of luciferin are available (at potentially increased cost) that may have features such as increased stability/longevity, greater output, or not impaired by phenol red.

c. *Multiplexing*. The LCA lends itself to multiplexing with other tests using a single well. For instance, cytotoxicity can be assessed directly following LCA luminescence reading (discussed in Step 3.3.8). However, morphological effects of compounds can also be assessed by imaging of plates in a high-throughput manner [137,139]. Brightfield imaging can be used alone, or dyes/stains (i.e., DAPI or high-content imaging dyes) can be dispensed for high-content analysis, which monitors phenotypic changes such as morphology and organelle localization that can be both visualized and quantified and in real time.

3.3.3.7. Troubleshooting: Assessment of well-to-well variability, plate effects and streaking

For optimal results, the effect of well position on luminescence output for a given plate reader should be tested to ensure that plate location does not impact results. Additionally, high well-to-well variability will result in an inability to accurately detect hits during compound screening, and this will be apparent by low Z' values.

1. To determine if poor assay performance (low Z') is due to high well-to-well variability, trypsinize cells from 3 independent flasks and keep cell suspensions

separate. Count cells and seed into three 384-well plates (one plate per cell suspension) using a single cell density and no treatment (40 µL of cells in media alone per well). Perform LCA. If the normalized SD for all wells exceeds ~10-15%, examine the following:

a. Cell clumping; check by visualizing cells using cell counter. Cell clumping may occur due to microbial contamination or excessive swirling/tapping of flasks during trypsinization. Use syringe (i.e., 18-20 gauge) to triturate cells prior to cell seeding.
b. Gain/sensitivity setting too high during luminescence reading; systematically reduce gain in small intervals (**Note 12**).

2. To test the effect of well position, seed cells into all wells of 96- or 384-well plates in triplicate using a single cell density with no treatment (40 µL of cells in media alone per well), and perform LCA.
    a. If streaking (i.e., odd rows have decreased luminescence compared to even rows) or other row effects are observed, the issue likely originates with the automated liquid dispenser used for cell dispensing.
    b. If a particular region on the plate is affected, such as plate sides, center, or bottom right, the issue likely originates with the plate reader.

3.3.3.8. Cell Viability Testing

To ensure that change in luminescence signal is not a result of compound cytotoxicity, a cell viability assay should be run in parallel with screening campaigns to quickly eliminate potential false positives. One major advantage of the in-cell LCA in 384-well plates is its ease of use for multiplexing additional assays. Immediately following luminescence

reading, the cell viability assay reagent can be dispensed without aspiration of existing media. The CTB cell viability assay is used as an example; this assay measures fluorescence produced when resazurin is reduced (by NADH) to resorufin in cells. Cell cytotoxicity (i.e., induced by drugs) leads to decreased NADH production (and thereby, the capacity to reduce resazurin), which is then detected as a drop fluorescence intensity. At this stage of development, we recommend introducing additional compounds of interest for testing with LCA that can be used as guides to select cut-offs for cell viability. For instance, use a known cytotoxic compound (i.e., tamoxifen) and possibly other compounds that do not adversely affect cell viability.

1. Perform LCA identically to Step 3.3.4 using the optimized cell density and reagent volume for all wells; however, dispense LCA medium without cells and substrate solution for one column in each 8-column set (i.e., columns 1, 9, and 17). Treat cells with positive controls as well as known cytotoxic compounds (**Note 20**).
2. Immediately following luminescence reading, dispense either 5, 10, or 20 µL of CTB reagent across 8-column sets in the 384-well plates.
3. Incubate plates for 10-16 h at 37 °C with 5% CO_2 and subsequently detect fluorescence signal intensity (FI) using a plate reader with the following settings:
    a. Excitation λ =560 nm; emission λ = 590 nm
    b. Gain 100 (or use optimal gain)
4. Data analysis to determine compound toxicity:
    a. Plot all individual wells on a scatterplot in order of well number to ensure there are no plate effects.

b. To obtain the corrected fluorescence intensity for viable cells, subtract the mean fluorescent signal intensity of wells with no cells (background fluorescence) from the mean of negative controls (cells treated with 0.3% DMSO alone). Next, use this value to normalize sample fluorescent signal intensity for each set.

c. The toxicity cut-off can be set as:

    i. Compounds that cause a reduction in fluorescence by ≥ 50% compared to negative controls.

    ii. Compounds that cause a reduction in fluorescence by ≥ 3 SDs (Z-score > 3) compared to negative controls (**Note 21**).

    iii. Set the fluorescence of the known cytotoxic compound as 0%, and the negative control as 100%. Choose a cut-off in this range depending on the target application. Note that this method should yield a similar result as subtracting the background fluorescence.

d. Compare the mean and standard error of raw fluorescence signal intensities for each volume of CTB reagent. For screening, use the lowest volume of CTB reagent that had sufficient signal and low error to accurately identify toxic compounds in a single well (one replicate). High fluorescence values are less important than the well-to-well variability.

3.3.4. High-throughput screening of small molecule libraries and hit selection using Z-scores

Following completion of assay development in 384-well plates, the assay is ready to be used for screening of large chemical libraries in 384-well plates. Depending on the selected

incubation times, up to 10-20 plates containing can be screened per day, yielding a total of 3200-6400 compounds screened per day (320 compounds per plate). If no plate effects were observed in Step 3.3.5 (i.e., lower luminescence along plate sides), then we recommend using a screening plate layout with 320 experimental compounds in columns 3-22 and all controls in columns 1-2 and 23-24 (**Note 22**).

1. Dispense screening compounds, DMSO, and positive controls into 384-well plates using an acoustic liquid dispenser (**Note 23**).
2. Quantify cell viability and cell density using a cell counter and dispense cells into pre-pinged plates according to the optimized cell density and reagent volumes. Incubate plates for 2 h at 37 °C with 5% CO_2, dispense LCA substrate solution, and read plate luminescence after 1 h.
3. Immediately following luminescence reading, dispense 5-10 μL of CTB reagent. Incubate for ~16 h at 37 °C with 5% CO_2 and read plate fluorescence (excitation λ =560 nm, emission λ = 590 nm).
4. Data analysis:
    a. Calculate Z' for each plate. Plates with Z'<0.5 should be thoroughly reviewed for potential problems and repeated if results appear spurious.
    b. Plot the MNS dose response (mean normalized luminescence vs log [M]) for each plate. Plates with significant shifts in the dose response should be thoroughly reviewed for potential problems and repeated if results appear spurious.
    c. To determine compound toxicity, normalize sample fluorescent signal intensity to the mean fluorescence of per plate negative controls. Exclude

compounds from further analysis based on cut-offs determined in Step 3.3.6.

d. Calculate Z-scores for all screened compounds according to the following formula:

$$\text{Z score} = \frac{\mu_i - \mu_{DMSO}}{\delta_{\text{DMSO}}} \quad (5)$$

where μ_i and μ_{DMSO} are the arithmetic means of the sample (i.e., screened compound) and 0.3% DMSO control group, respectively.

e. Examine the distribution of screening results and select hits. Traditionally, hits are those compounds with Z-scores > 3 or < -3. However, thresholds can be adjusted based on the Z-score distribution, which is dependent on the compound library and system of interest.

5. Counter-screen hits against the full-length luciferase to identify false positives using transiently transfected HEK293 cells in 96-well plates (**Note 24**) as described previously [45,126].

3.3.5. High-throughput hit validation via dose-dependency studies

Once selected, hits should be repurchased to confirm compound identity and to assess dose-dependency. Using the newly optimized assay, this can be rapidly achieved under conditions identical to that of the primary screening. Here, expanded dose-responses of compounds can be rapidly tested in variable formats depending on the number of hits. Each hit should be validated using ≥ 8 doses over ≥ 2 log dilutions (i.e., 0.1 μM – 30 μM). For larger sets of hits, 20 compounds can be tested per 384-well plate using 8-concentrations

of n=2 replicates per concentration (each hit in separate columns). For smaller sets, 8 compounds can be tested using 10 concentrations with n=4 replicates per concentration.

1. Dispense compounds, DMSO, and positive controls into 384-well plates using an acoustic liquid dispenser and perform LCA as in Step 3.4.
2. Data analysis to determine hit dose-dependency:
    a. Plot mean normalized luminescence vs log [M] for each compound concentration.
    b. Fit the data using a non-linear regression (using software such as GraphPad Prism):

$$A + \frac{B-A}{1+10^{loglog\,(x_0-x)\,H}} \quad (6)$$

where x is log10 of the compound concentration in M, x_0 is the inflection point (EC_{50} or IC_{50}), A is the bottom plateau effect, B is the top plateau effect, and H is the Hill slope.

    c. Compound potency is defined by the EC_{50}/IC_{50}, whereas the compound efficacy is defined by the maximal compound effect (bottom plateau effect).
    d. Kinase inhibitors that increase the FGF14:Nav1.6 interaction with increasing doses are classified as agonists; kinase inhibitors that decrease FGF14:Nav1.6 interaction with increasing doses are classified as inverse agonists [49].

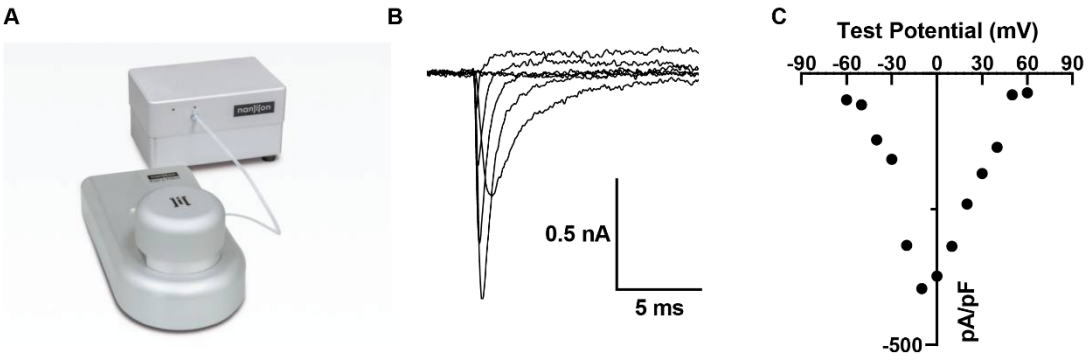

Figure 3.5: Planar patch-clamp electrophysiology using the Port-a-Patch.

Planar patch-clamp electrophysiology using the Port-a-Patch. (**a**) The small, yet highly versatile Port-a-Patch connected to the Suction Control Unit. (**b**) Raw Na^+ transient current traces of a HEK293 cell expressing the human Nav1.6 recorded on the Port-a-Patch. Currents were elicited using a voltage step protocol from a holding potential of -80 mV to -60 mV increasing in 10 mV steps up to 60 mV. (**c**) Corresponding IV activation plot for a single cell.

3.3.6. Functional hit validation via planar patch-clamp electrophysiology.

Hits discovered using LCA can be rapidly validated using the Port-a-Patch to conduct planar patch-clamp electrophysiology [127] with cell lines stably expressing the ion channel of interest, such as Nav channels [140,141] (**Fig. 3.5**). The only required equipment includes the Port-a-Patch with Suction Control Unit (**Fig. 3.5**), an amplifier, and a computer to operate the included PatchControl software. Multiple add-ons are also available to increase functionality or automation, such as internal and external perfusion systems, temperature control, a low capacitance holder to reduce noise, and a microscope slide kit to simultaneously visualize (i.e., fluorescence) and record cells. Overall, the ease-of-use of this instrument makes functional validation of hits possible even to those laboratories without extensive experience in electrophysiology. Once proficient, 25-50 cells can be patched in a single day, enabling testing of relatively large sets of hits (~10-20) in a short period.

1. Culture HEK293 cells stably expressing both the human Nav1.6 channel and FGF14-1b (**Note 25**) in 75 cm^2 flasks using complete medium supplemented with 100 mg/mL G418. Cells should not be grown above ~80% confluency.
2. Harvest one 75 cm^2 flask at 60-80% confluency using the following protocol (**Note 26**) to obtain a cell suspension that can be used for 2-4 hours (**Note 27**). The optimal cell density is ≥ 1 million cells/mL, but only 5 µL of cell suspension is used per experiment (one cell).
    a. Gently wash the cells 2X using 5 mL of warmed PBS.
    b. Dispense 5 mL of TrypLE and tilt the dish/flask gently to distribute the enzyme evenly. Immediately aspirate ~3 mL to leave only a thin coating but ensure that all cells remain moist.
    c. Incubate for 3-5 min at 37 °C. Observe cells using light microscope to confirm that cells have detached and are loose in media. If cells are not yet detached, incubate for ~1-2 min longer.
    d. Dispense 5 mL of resuspension medium and centrifuge cells at 500 x *g* for 4 minutes.
    e. Aspirate supernatant and triturate cells in 0.5 mL of resuspension medium and 0.5 mL of extracellular solution.
    f. Allow cells to recover for 10-20 min at 4-10°C before use. During patching, cells should be kept on a gentle shaking or rotating platform at very low speed to prevent formation of a cell pellet.
3. Launch the PatchControl software and load the appropriate suction protocol (i.e., intermediate.ppf for cells with typical membrane quality/robustness).

4. Fill the inside of an NPC-1 chip with 5 µL of intracellular solution (**Note 28**).
5. Screw chip onto mount of the Port-a-Patch, ensuring that the internal solution is in contact with the internal electrode (**Note 29**).
6. Place the Faraday shielding unit on top.
7. Dispense 5 µL of extracellular solution onto the chip and ensure that it is in contact with the external electrode. In PatchControl, press the "Play" button.
8. Gently rotate cell suspension to mix, and aspirate 5 µL. In a separate pipette, aspirate 20 µL of SES.
9. When the "Add Cells!" button appears, click the button and dispense the 5 µL of cell suspension directly over the center of the chip.
10. When the resistance has increased to 20-40 MOhm (indicating cell attachment; **Note 30**), gently dispense 20 µL of SES with the pipette tip facing *away* from the center.
11. Once sealing procedure is complete (i.e., R > 1 GOhm), gently wash off SES by pipetting 20 µL of external solution on one side of the chip (ie, right side) with pipette tip facing *away* from the cell. Then, slowly aspirate 20 µL from the other side (ie, left side), again with the tip facing *away* from the cell. Repeat 3 more times to ensure that solution is completely washed.
12. Start the experiment using the following pre-loaded protocols:
    a. NaPharmP4leak
    b. Na-IV-P4leak
    c. Na_Inact

13. Repeat Steps 4-11 using extracellular solution containing the compound of interest at a concentration based on the IC/EC_{50} calculated from dose-responses in Step 3.5. Use $n \geq 10$ cells per condition.
14. Analyze data:
    a. Export data from PatchMaster using the ASCII format.
    b. Open in Microsoft Excel.
    c. Calculate the mean and standard error for corresponding data values from each cell.
    d. Fit the averaged data for both the IV and inactivation IV using the Boltzmann equation using Igor (or an equivalent electrophysiological data analysis software).

3.4 NOTES

1. Coenzyme A is useful for increasing the signal, as well as increasing the length of time that the signal plateaus. This may be useful when reading a large number of plates in a single day during screening, especially where it is not feasible to read every plate at an extremely precise time-point.

2. LCA cell medium supplemented with HEPES can be used as an alternative to PBS when plates will be read for an extended period without the presence of CO_2 to maintain a more stable pH. We have observed that use of LCA cell medium for substrate solution yields moderately higher raw luminescence values without significantly affecting drug effects on normalized luminescence.

3. We recommend using clear bottom plates to visualize cells throughout assay development (i.e., ensure that no odd cell morphology is observed, cells are not in clumps, cells appear evenly distributed across wells). However, using solid white bottom plates (Greiner #781080) or sealing plates with white tape seals prior to reading will significantly increase raw luminescence values and decrease the apparent well-to-well variation due to reduced backscatter of light through the plate bottom.

4. During assay development, we recommend using a small library (<320 compounds on a single 384-well plate) to assess how assay parameters (i.e., varying cell density or reagent volumes) impact compound effectiveness (i.e., relative Z-scores), as well as to determine reproducibility between independent experiments. Libraries should contain well-annotated compounds, such as targeted kinase inhibitors or FDA-approved drugs, such as the Broad Institute Collection.

5. Especially when attempting transfection of new plasmid DNA, it is wise to test multiple quantities of plasmid DNA (i.e., 0.5, 1, 2, or 3 μg). As the goal is to generate a single, healthy clone that stably expresses the cDNA constructs of interest, multiple conditions should be tested to find the optimal method.

6. To prepare 50 mL of 20% preconditioned media, combine 40 mL complete medium supplemented with appropriate antibiotics (i.e., 500 μg/mL G418 for the first stable transfection) with 10 mL of sterile filtered medium from subculture of HEK293 cells. The final concentration of selective antibiotics is reduced by the same percentage as it is comprised of preconditioned medium. By slowly increasing the antibiotic concentration over 3 weeks (30%, 20%, and finally 10% during week 3), the initial

stress to transfected cells is reduced to promote faster and healthier growth for stable cells while simultaneously preventing growth of non-stable cells.

7. Cells should be seeded extremely sparsely in dishes such that individual clones can be discretely selected (i.e., only one cell visible at a given location when observed with a light microscope). Over-seeding cells can occur easily and will necessitate subsequent splitting and reseeding at lower density.

8. At this stage, the single stable cell line should be immediately expanded, and aliquots frozen at -80ºC. These cells can be used for subsequent generation of multiple double stable cell lines expressing alternative complementary cDNA plasmids expressing protein pairs of interest (i.e., numerous regulators of a single ion channel, such as FGF13 or spectrins). For instance, while this chapter describes the subsequent insertion of CLuc-FGF14, other regulatory proteins fused to CLuc could be used to generate alternative double stable cell lines. This would enable rapid cross-screening of small molecules against multiple related protein complexes to discover highly specific probes against a single target of interest.

9. Cell suspensions need to be continually mixed by gentle pipetting/swirling prior to counting and plating, and all solutions should always have at least 20% dead volume, or a minimum of 4 mL when dispensing with a multichannel pipette from reagent reservoir, or a minimum of 15-20 mL dead volume when dispensing with an automated dispenser to account for priming. The minimum volume for 128 wells of a 384-well plate (8 columns) is 5,120 µL but should be brought to ~10 mL to account for dead volume if using a multichannel pipette. The use of insufficient dead volumes can significantly impact results and lead to higher well-to-well variability, for instance due

to plate streaking (every other row having reduced cells, causing reduced signal output; results from such plates must be discarded).

10. For example, to obtain a density of 4×10^4 in 40 µL/384-well, the cell suspension will need to have a concentration of 1×10^6 cells/mL (1,000,000 cells/mL × 0.04 mL = 40,000 cells) with sufficient volume for n=128 wells (8 columns) using 40 µL per well accounting for dead volumes. Obtain a cell suspension volume of 100 mL with a density of 1×10^6 cells/mL. Use 25 mL of this suspension for seeding the first 8 columns. Dilute the remaining 75 mL of suspension by 25% by adding 25 mL of media, mix, and use 25 mL of this suspension for seeding 3×10^4 cells into the second 8 columns. Repeat as necessary. See table below for examples of the necessary cell concentrations to achieve a particular cell density for a given volume:

	Cell Suspension Concentration needed for a volume of:	
Cell #/Well	**30 µL/well**	**40 µL/well**
1000	~3.3×10^4	2.5×10^4
10000	~3.3×10^5	2.5×10^5
30000	1×10^6	7.5×10^5
40000	1.25×10^6	1×10^6
50000	1.5×10^6	1.25×10^6

11. We recommend starting with these volumes for each plate type, but this step is also amenable to testing several volumes of suspension per well in addition to multiple cell densities. However, bear in mind that the volume of cell suspension dispensed is only half of the final working volume (an equal volume of LCA substrate solution (2X) will be dispensed prior to reading plates). We have found that increasing the substrate solution concentration to 4X yielded reduced luminescent signal.

12. Recommended initial settings for luminescence reading using various plate readers:

    a. Synergy H1: open hole; integration time 0.5 s, gain 200

b. Tecan Infinite M1000: open hole; integration time 0.1 s, settle time 0.01 s

Please note that while increasing the gain/sensitivity setting will increase the raw luminescence values, an excessively high gain setting may result in high well-to-well variability. In this case, the apparent high standard deviation between replicates within a given plate is a result of technical errors rather than biological problems. Low raw luminescence values (i.e., <500 in a 384-well plate or <2000 in a 96-well plate) may not be cause for concern if the well-to-well variability is low. If luminescence appears low, multiple gain settings should be tested to find an optimal assay sensitivity prior to troubleshooting the biological experimental parameters

13. Depending on the baseline luminescence generated by the stable cell line and results from Step 3.3.2, plate cell densities ranging from 1×10^3 to 1×10^5 with each cell density having 8 columns of the plate (thus, a maximum of 3 different cell densities per 384-well plate). The expected optimal cell density will likely range from 2×10^4 to 4×10^4.
14. Test at least the maximum DMSO concentration that will be required for the assay, which depends on the stock concentration of library drugs (generally 10 mM). Thus, if the screening concentration will be 20 μM, then the DMSO concentration can be no less than 0.2%. Concentrations greater than 0.5-1% DMSO may be toxic.
15. This includes one column of cells treated with media alone and one column of cells treated with media and DMSO alone. Especially during assay development, maintain an excess of negative controls on every plate to monitor well-to-well variation and to ensure that the parameters being optimized are not misrepresented by normalization to outlier controls.

16. The time required for signal peak and plateau is also useful for determining how long plates can be incubated prior to plate reading, which is one limiting factor for the number of plates that can reasonably be assayed in a single day during HTS.
17. Plotting all individual replicate values, rather than mean ± SD alone, enables rapid visualize of the spread between wells.
18. δ_p and δ_n are standard deviation of the positive control group p and the negative control group n, and μ_p and μ_n are the arithmetic means of the two groups, respectively; S:B, signal to background; S:N, signal-to-noise; and SW, signal window. For cell-based assays, a Z' of ≥ 0.5 signifies that outliers can be reliably identified as statistically significant despite well-to-well and plate-to-plate variability. Based on Equation 1, Z' is improved by greater signal separation between the mean of positive and negative controls, as well as by reducing variance between replicates (i.e., standard deviation). In practical terms, consistency between replicates would improve confidence in a single well outlier being truly significant (i.e., the compound treatment in single well resulted in significant changes in complex formation, rather than the change in luminescence being due to well-to-well variability). Z' can be calculated separately using the enhancer and inhibitor positive controls, demonstrating the assay sensitivity for essentially two separate assays (one to detect FGF14:Nav1.6 enhancers, one to detect inhibitors) using a single system.
19. If Z' is low, we recommend the following for these potential causes:
    a. High well-to-well variability: repeat experiment; ensure that cell viability is > 90% and that cells do not form clumps prior to seeding cells.

b. Lack of potent controls: repeat experiment using fresh controls; dissolve controls in DMSO rather than water-based solvents to ensure sample viscosity is not an issue for acoustic liquid dispenser; search literature for more potent modulators of the ion channel target of interest.

20. The dose makes the poison: all compounds may be cytotoxic at high concentrations. Test multiple doses of suspected cytotoxic compounds to confirm cytotoxicity (or lack of).
21. Using SDs as a threshold for toxicity may not be advisable due to typically relatively low SD (~3-6%) in negative controls. Thus, a compound that reduces fluorescence by only 20% may have a Z-score of -6. Small reductions in fluorescence may indicate an outlier, or cytotoxicity due to high concentrations (i.e., if screening concentration is high). Furthermore, if the negative control SD is low for the toxicity assay, then experimental compound Z-scores may be less relevant than normalized mean change in fluorescence.
22. Controls should include a minimum of n=8 wells for cells treated with media alone (negative control as quality check for DMSO), and n=16 wells for cells treated with 0.3% DMSO or positive controls (n=8 wells for each condition on each side of the plate). Alternatively, the positive controls can be split into n=8 wells of the maximal concentration and n=8-16 wells of the positive control dose response (n=2 wells per concentration). This will enable mapping of screened compounds against a standard curve for either inhibition or stimulation.
23. Depending on the acoustic liquid dispenser's processing speed and number of screening plates, it may be necessary to "pre-ping" dissolved screening compounds, DMSO, and

positive controls into 384-well plates in advance. Seal plates with foil to prevent evaporation and store at -20 °C until ready for use. Warm to room temperature prior to dispensing cells.

24. This assay can be scaled up to 384-well plates using conditions similar or identical to those optimized in Step 3.3. To identify false positives in this assay, calculate Z-scores using negative controls as in Step 3.4.4d. Exclude those compounds with Z-scores of > 3 or < -3.
25. HEK293 cells stably expressing the Nav1.6 channel are commercially available. These cells can be used to create a double stable cell line expressing the protein of interest by following a protocol similar to Step 3.2. Stable cells should be validated using WB and/or rtPCR, as well as patch-clamp electrophysiology (rather than LCA).
26. This relatively quick procedure should be viable for most cell lines. However, if poor seals are obtained, it may be caused by excess stress during cell harvesting. Nanion has optimized the following procedure has been optimized for gently harvesting cells to achieve improved seals for patching:
    a. Pre-warm 10 ml HBSS to 37°C and 5 mL 30% Accutase to RT.
    b. Aspirate medium and dispense 5 mL of 37°C HBSS and incubate for 1 min at RT. Aspirate HBSS and repeat.
    c. Dispense 5 mL of 30% Accutase (pre-warmed to RT), and quickly remove 4 mL. Incubate at 37°C for ~10 min.
    d. Observe cells using light microscope to confirm that cells have detached and are loose in media. If cells are not yet detached, incubate for ~1-5 min longer.

e. Add 8 mL of cold (4-8°C) HBSS-EDTA and gently pipette cells using a large pipette (i.e., 5 mL serological pipette), and incubate at 4-8°C for 10 min to allow cells to recover

f. Carefully aspirate off 8 ml medium, add fresh 4-8°C 8 ml BHK-HEPES, and incubate 5 min at RT. Carefully aspirate off 8 ml medium.

g. Add 3 ml external solution, and transfer the cells to Eppendorf low-binding tubes (1 mL/tube) and keep at 4-10°C. Let cells recover for 15-30 min.

27. Additional flasks can be harvested as needed to continue patching in a single day, but cells should not be used after 4 hours of incubation in extracellular solution. To patch for an extended duration, you may alternatively triturate centrifuged cells in 4 mL of resuspension medium and aliquot into 4 separate Eppendorf tubes to maintain sterility. Medium can be aspirated and changed to extracellular solution immediately prior to patching.
28. Hold chips by grasping only the sides (do not touch the surface) to avoid contamination by grease or dust, which could compromise cell sealing or data quality.
29. Ensure that both the internal and external electrodes are well chlorided. Depending on frequency of usage, we recommend rechloriding electrodes at least once per week.
30. It may be necessary to optimize the suction protocol depending on the particular cell type and overall health; if the suction is too strong (i.e., weaker membrane breaks too early using intermediate.ppf) or too weak, adjust the suction protocol to weak.ppf or strong.ppf, respectively.

Chapter 4. Assay development reveals FDA-approved therapeutics as potent modulators of the voltage-gated Na^+ channel complex

Portions of the following chapter were published in *Scientific Reports* (Open Access) as:

High-throughput screening against protein:protein interaction interfaces reveals anti-cancer therapeutics as potent modulators of the voltage-gated Na^+ channel complex

Paul A. Wadsworth, Oluwarotimi Folorunso, Nghi Nguyen, Aditya K. Singh, Daniela D'Amico, Reid T. Powell, David Brunell, John Allen, Clifford Stephan, Fernanda Laezza

ABSTRACT

Multiple voltage-gated Na^+ (Nav) channelopathies can be ascribed to subtle changes in the Nav macromolecular complex. Fibroblast growth factor 14 (FGF14) is a functionally relevant component of the Nav1.6 channel complex, a causative link to spinocerebellar ataxia 27 (SCA27) and an emerging risk factor for neuropsychiatric disorders. Yet, how this protein:channel complex is regulated in the cell is still poorly understood. To search for key cellular pathways upstream of the FGF14:Nav1.6 complex, we have developed, miniaturized and optimized an in-cell assay in 384-well plates by stably reconstituting the FGF14:Nav1.6 complex using the split-luciferase complementation assay. We then conducted an HTS of 267 FDA-approved compounds targeting known mediators of cellular signaling. Of the 65 hits initially detected, 24 were excluded based on counter-screening and cellular toxicity. Based on target analysis, potency and dose-response relationships, 5 compounds were subsequently repurchased for validation and confirmed as hits. Among those, the tyrosine kinase inhibitor lestaurtinib was highest ranked, exhibiting submicromolar inhibition of FGF14:Nav1.6 assembly. While providing evidence for a robust in-cell HTS platform that can be adapted to search for any channelopathy-associated regulatory proteins, these results lay the potential groundwork for repurposing cancer drugs for neuropsychopharmacology.

4.1 INTRODUCTION

As described in Chapters 1 and 2, PPI between Nav channels and their accessory proteins fine-tune neuronal excitability. Mutations in either the channel itself[32,33] or these regulatory proteins[18,34–38] give rise to channelopathies that have few viable treatment options. Identifying new modulators of PPI within ion channel complexes has been hampered by the lack of robust in-cell assays and screening platforms. To address this need, this Chapter presents the results for the development and optimization of the LCA for HTS in 384-well plates using the methodology described in Chapter 3. Further, we present the screening results from the Custom Clinical and National Cancer Institute (**CC_NCI**) collection of 267 FDA-approved drugs targeting known cellular signaling pathways, which was used as a test library for our assay. Our study not only provides a new practical tool to accelerate drug discovery for ion channels, but also identifies the tyrosine kinase inhibitor lestaurtinib, an FDA approved anti-cancer drug, as a potential compound for repurposing toward CNS-related channelopathies.

4.2. RESULTS

4.2.1. Construction of a robust double stable HEK293 cell line for LCA

We have previously introduced the LCA to detect interactions between FGF14 and the Nav1.6 C-tail in transiently transfected cells[45,46,49]. The C- and N-terminal fragments of the P. Pyralis luciferase are fused, respectively, to FGF14 (CLuc-FGF14) and a chimera expressing CD4 fused to the Nav1.6 C-tail (CD4-Nav1.6-NLuc), and FGF14:Nav1.6 C-tail complex formation can be detected in the presence of the luciferase substrate, D-

luciferin (**Fig. 4.1A-C**). In order to utilize this system for HTS, we developed a double stable cell line that increased signal-to-noise ratio, decreased well-to-well variability, and circumvented the need for high volume transient transfections, which are labor-intensive and uneconomical. We generated a monoclonal double stable cell line by sequentially transfecting HEK293 cells with linearized CLuc-FGF14 and CD4-Nav1.6C-tail-NLuc constructs (**Fig. 4.1B**) under the control of puromycin and neomycin, respectively.

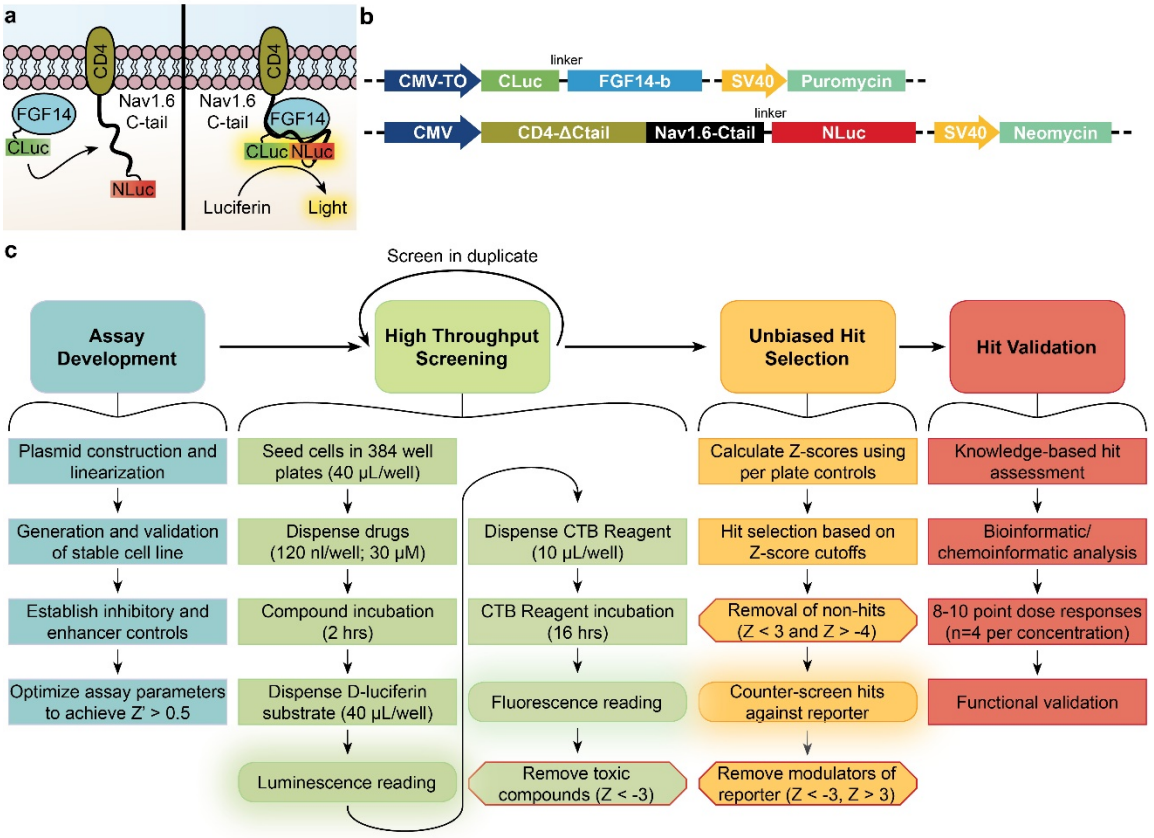

Figure 4.1. Overview of the cell-based LCA for HTS against the FGF14:Nav1.6 C-tail complex.

(A) Theory of LCA in live cells. Assembly of the CLuc-FGF14:CD4-Nav1.6-NLuc complex results in reconstitution of the luciferase enzymatic activity, which produces light in the presence of its substrate D-luciferin. (B) Linearized constructs encoding CLuc-FGF14-1b and CD4-Nav1.6-NLuc under the control of Neomycin and Puromycin, respectively, were sequentially transfected into HEK293 cells to create the double stable cell line. (C) Workflow for HTS using a cell-based assay. The work presented here describes assay development, screening and counter-screening of a test library of kinase inhibitors, and preliminary dose response hit validation. Z' was used to measure the assay's ability to detect hits, whereas Z-scores were calculated for experimental compounds based on per plate controls.

Next, we compared the double stable cell line, hereafter referred to as Clone V, to transiently transfected HEK293 cells after treatment with the peptidomimetic ZL181 (negative control 1), a rationally designed inhibitor of the FGF14:Nav1.6 interaction[58], and the Akt inhibitor triciribine (positive control 1), which enhances the interaction of this complex presumably by increasing GSK3-dependent phosphorylation of the complex[49,65]. Treatment with 50 μM ZL181 caused a similar inhibitory effect (23.9 vs. 25% luminescence compared to DMSO control), and treatment with 25 μM triciribine resulted in a similar increase in FGF14:Nav1.6 C-tail assembly (144.0% vs. 166.9% luminescence) in transiently transfected cells compared to Clone V cells (**Fig. 4.2A,B**). At this stage, our use of ZL181 and triciribine as controls was to validate that Clone V behaved similar to transiently transfected cells as shown previously[49,58,65]. While an enhancer acting through more direct means may be preferable, this limitation arises from the very problem that this HTS project aims to solve; namely, to discover specific and potent modulators of the FGF14:Nav1.6 complex.

4.2.2 Selection of potent inhibitory and enhancer controls suitable for an HTS format

Following validation of Clone V, we scaled our assay from a 96-well to 384-well plate format to economically support high-throughput drug screening. We chose conditions leading to satisfactory assay performance that minimally impacted assay sensitivity, and we calculated Z'-factor (**Equation 1**) to evaluate the robustness of our assay. Z'-factor measures the signal separation between the mean of positive and negative controls and the variance between replicates. To improve Z'-factor, the inhibitory (negative) control should reduce the signal to as close to zero percent as possible, while an enhancer (positive) control

should increase the signal by ≥2-fold and ≥3 SDs (i.e., ≥ 200% luminescence when normalized to DMSO controls). However, ZL181 plateaus at ~25% luminescence[58], while the enhancing effect of triciribine plateaus at ~150% luminescence[49]. Thus, we searched for controls with greater potency and efficacy than that of ZL181 and triciribine.

Parallel studies lead us to explore the effect of TNF-α (positive control 2) on the FGF14:Nav1.6 complex, and we found that it is a more efficacious enhancer of the complex (mean and SD: TNF-α, 210.8% ± 18.6%; triciribine, 142.5% ± 10.7%; triciribine, 142.5% ± 10.7%; Fig. 2A-D); despite moderately higher variance, the mean effect of TNF-α is over 2-fold greater than that of triciribine. Additionally, we found that the tyrosine kinase inhibitor MNS (30 μM; negative control 2) significantly reduces FGF14:Nav1.6 interaction, and the effect was greater with lower variance than that of ZL181 (one-way ANOVA; normalized mean and SD: MNS, 10.8% ± 3.1%; ZL181, 25.0% ± 7.3%; $p<0.0001$) (**Fig. 4.2**).

The concentration range of MNS and TNF-α was selected based on a preliminary dose response (**Fig. 4.3**). TNF-α protein supplemented with 0.1 mg/mL BSA (manufacturer suggestion) improves protein stability, increases efficacy, and minimizes variance (**Fig. 4.3**). However, the increased viscosity of this solution was problematic for dispensing using the LabCyte Echo 550. Thus, using a higher concentration of TNF-α without BSA (50 ng/mL) reproduced the effects observed for lower TNF-α concentrations (5 and 25 ng/mL) supplemented with BSA.

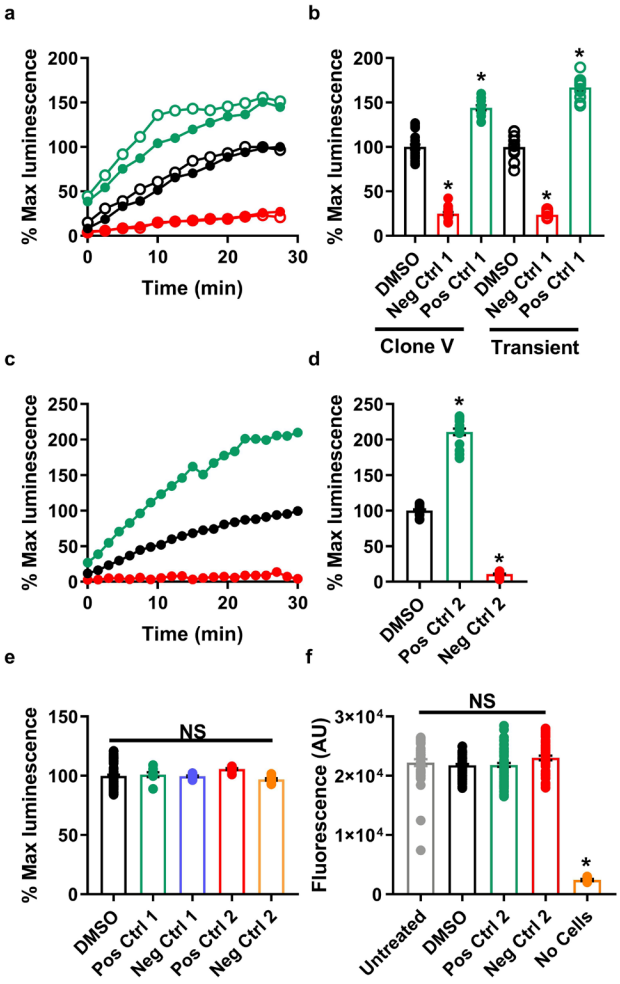

Figure 4.2. Validation of double stable cell line and selection of inhibitory and enhancer controls.

(A, B) Clone V cells (filled circles) stably expressing CLuc-FGF14 and CD4-Nav1.6-C-tail-NLuc constructs were compared with transiently transfected HEK293 cells (empty circles) treated with the Akt inhibitor triciribine (positive control 1, green) or the peptidomimetic ZL181 (negative control 1, red). (**A**) Percent luminescence (normalized to 0.3% DMSO controls, n=16) is measured over 30 minutes following dispensing of luciferin substrate in 96-well plates, and (**B**) percent of maximal luminescence for each group shown in (**A**). **(C,D)** TNF-α (positive control 2, green) and MNS (negative control 2, red) are more potent than original positive and negative controls (triciribine and ZL181 in (A,B)) and demonstrate the high performance capabilities of LCA as an HTS assay. (**C**) Percent luminescence over time and (**D**) percent maximal luminescence of Clone V cells after treatment with 50 ng/mL TNF-α (positive control 2, green) or 25 µM MNS (negative control 2, red) in 96-well plates. (**E**) HEK293 cells were transiently transfected with full-length *P. pyralis* luciferase to rule out effects on luciferase following treatment with triciribine (positive control 1, green), ZL181 (negative control 1, purple), 50 ng/mL TNF-α (positive control 2, red) or 30 µM MNS (negative control 2, orange) in 96-well plates. Percent maximal luminescence (normalized to 0.3% DMSO controls, n=16) is shown for each treatment (n=8 per treatment), and no significant effects were observed. **(F)** Cell titer blue (CTB) assay was initiated on Clone V cells or wells containing media alone immediately following luminescence reading in 384-well plates (n=16 per group). Fluorescence intensities were subsequently read after approximately 18 hours. Untreated cells (white), 0.3% DMSO (gray), 25 µM MNS (red), 50 ng/mL TNF-α (green), or media and luciferin mixture with no cells (orange). Data are mean for real-time graphs (A,C) and values measured from individual replicate wells are plotted for graphs showing % maximal luminescence (B,D,E) or fluorescence (F). One-way ANOVA with post-hoc Dunnett's multiple comparisons test was used to determine significance; *, $p<0.0001$.

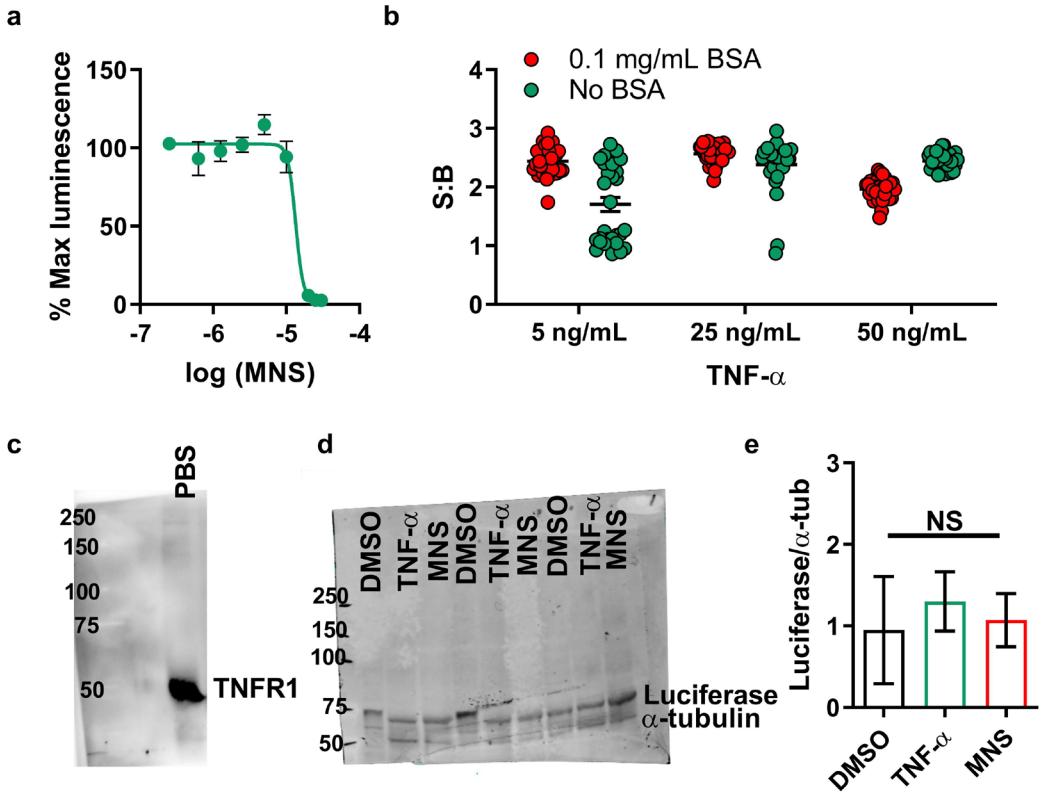

Figure 4.3. Validation of TNF-α and MNS as LCA controls and confirmation of TNFR1 expression in HEK293 cells.

(**A**) Plot of percent luminescence (normalized to DMSO controls) from Clone V cells treated with MNS in 384-well plates versus compound concentration (range: 0.625 - 25 µM, *n*=16 per concentration) with nonlinear regression curve fitting using Graphpad Prism 8. Estimated IC_{50} = 13.35 µM. Based on these results, we used a final concentration of 30 µM for the 384-well plate inhibitory controls that were used to calculate Z'. (**B**) Plot of signal to background (S:B) ratio from Clone V cells treated with recombinant human TNF-α (positive control 2) in 384-well plates (*n*=32 per treatment group), calculated using DMSO controls as the background signal. The manufacturer recommends to supplement TNF-α with 0.1 mg/mL BSA to improve stability; however, the increased viscosity of this solution was problematic for dispensing using the LabCyte Echo 550. We found that BSA decreased the variance between replicates at lower concentrations of TNF-α (5 and 25 ng/mL), but that using a higher concentration of TNF-α without BSA could replicate this result. This point highlights the necessity of carefully examining practical concerns such as solution viscosity for high-throughput screening. (**C**) Immunoblot with antibody against human TNFR1 on lysate of double stable HEK293 cells. Blot was cropped to remove bands not pertaining to this paper (**D,E**) Immunoblot with anti-Luciferase (251-550 aa) and α-tubulin (as control for protein loading) on lysate of double stable HEK293 cells treated with 50 ng/mL TNF-α (positive control 2) or 30 µM MNS for 2 hrs. (**E**) Quantification of bands in (**D**); data are mean ± SD (*n*=3 per treatment group). One-way ANOVA with post-hoc Dunnett's multiple comparisons test was used to determine significance.

These new positive and negative controls were subsequently validated to ensure that their respective effects on luminescence arose due to modulation of PPI between FGF14 and the Nav1.6 C-tail rather than confounding factors. To rule out that the observed luminescence change by these compounds was a result of interference with luciferase enzymatic activity, a common side-effect in luminescence-based assays, HEK293 cells transfected with the full-length *P. pyralis* luciferase were similarly treated with MNS (30 μM) or TNF-α (50 ng/mL) in 96-well plates (DMSO, n=32; MNS and TNF-α, n=4 per group). There was no significant effect observed (one-way ANOVA; normalized mean and SD: DMSO, 100 ± 10.3%; triciribine, 101.0 ± 5.8%; ZL181, 99.58 ± 1.8%; MNS, 96.8% ± 2.8%; TNF-α, 105.7% ± 2.5%; Fig. 2F). Next, we used western blot to confirm that Clone V cells expressed TNF receptor 1 (TNFR1), the primary receptor that initiates TNF-α signaling cascades [142,143] (**Fig. 4.3**). Additionally, we used western blot to rule out changes in expression of recombinant CLuc-FGF14 or CD4-Nav1.6-NLuc protein as a potential mediator of changes in luminescence from Clone V cells treated with MNS or TNF-α (Supplementary Fig. S1). Finally, the CellTiter Blue (CTB) cell viability assay was used as a counter screen to eliminate drug toxicity as a confounding variable for luminescence signal intensity. The CTB reagent was dispensed into 384-wells immediately after LCA luminescence reading, and fluorescence was read after 16 hrs. We observed no significant difference in cell viability between untreated cells (media alone) or cells treated with 0.3% DMSO, 25 μM MNS, or 50 ng/mL TNF-α (**Fig. 4.2**). These new control compounds demonstrate that our modified LCA is capable of detecting agents that greatly increase or decrease FGF14:Nav1.6 complex formation without modifying the assay output

(luminescence) through non-specific effects (i.e., luciferase modulation or changes in protein expression).

4.2.3 Optimization of assay parameters in 384-well plates

These controls were subsequently used as guides as we miniaturized the assay format from 96-well to 384-well plates. We first optimized cell plating time and media composition, and subsequently used these conditions to explore the effects of cell density and substrate incubation times on assay sensitivity (Z'-factor).

Previously, transiently transfected cells were plated 24 hrs prior to reading in order to facilitate protein production and cell adhesion prior to compound treatment[45,99]. However, overnight incubation necessitates the use of medium supplemented with 10% FBS, which may reduce compound effectiveness (**Fig. 4.4**) and inhibit luminescence signal, respectively. The presence of FBS completely prevented triciribine from enhancing FGF14:Nav1.6 complementation (10% FBS: 103.1 ± 8.9%, n=8; 5% FBS: 97.6 ± 8.1%, n=8; no FBS: 142.5% ± 10.7%, n=8, p<0.0001), and a higher concentration of FBS significantly reduced the potency of ZL181 (21.2 ± 2.8%, n=8, p<0.0001) compared to media with no FBS (11.2 ± 1.5%, n=8, p<0.0001). To circumvent this issue, as well as minimize potential variance associated with multiple liquid handling steps[135], we attempted using cells in suspension by dispensing immediately prior to screening (cell-based homogeneous assay). Superior raw luminescence values (10446 ± 233.2 RLU, n=8) were observed compared to adherent cells (8692 ± 78.7 RLU, n=8, p<0.0001, Supplementary Fig. S2). For these reasons, we find the use of cells in suspension to be superior to adherent cells for the purpose of increasing reliability and reducing costs. Additionally, we

examined the effect of DMSO at varying concentrations (0.2-0.5% DMSO) on all cell densities and observed minimal effects at higher cell densities (**Fig. 4.4**). Importantly, lower volumes reduce resource consumption, as well as increase well-capacity for subsequent assays (i.e., capacity for CTB assay reagent following LCA luminescence reading). We attempted to reduce the final 384-well volume by dispensing 20 µL of a 2X (6 mg/mL) luciferin solution, however higher luminescence and signal-background (S:B) separation was observed for those wells with 40 µL of 1X (3 mg/mL) luciferin.

Next, we optimized cell density per 384-well with respect to S:B ratio when treated with TNF-α. Cells were seeded at densities ranging from 1×10^4 – 4×10^4 cells per well, and luminescence was read following luciferin dispensing for up to 75-minutes, after which point the signal plateaus. We observed a positive linear relationship between luminescence and cell density for treatment with either 0.3% DMSO or 50 ng/mL TNF-α (**Fig. 4.5A**). The signal-background (**S:B**) ratio was significantly greater for a density of 3×10^4 cells per well compared to densities of 1×10^4, 2×10^4, and 4×10^4 cells per well (mean and SD: 2.60 ± 0.14 followed by 2.05 ± 0.11, 2.26 ± 0.18, and 2.12 ± 0.16X background signal, respectively; n=16; $p<0.0001$ using one-way ANOVA with post-hoc Tukey's multiple comparisons). Additionally, we investigated the relationship between cell density and different doses (0.625, 1.25, 2.5, 5, 10, 20, 25, and 30 µM, n=8 per concentration) of the negative control MNS (**Fig. 4.5B**). As expected, the dose-response curve shifts to the left with decreasing cell density, indicating increased drug potency (MNS IC_{50}: 1×10^4, 3.96 µM; 2×10^4, 7.49 µM; 3×10^4, 9.82 µM; 4×10^4, 13.3 µM). For compound screening, each 384-well plate contains an 8-point dose-response of the negative control, enabling evaluation of plate-to-plate variability and rapid identification of faulty experiments. For

instance, errors in cell plating leading to excess cells per well can be recognized by reduced potency of the negative control (dose-response curve shifted to the right).

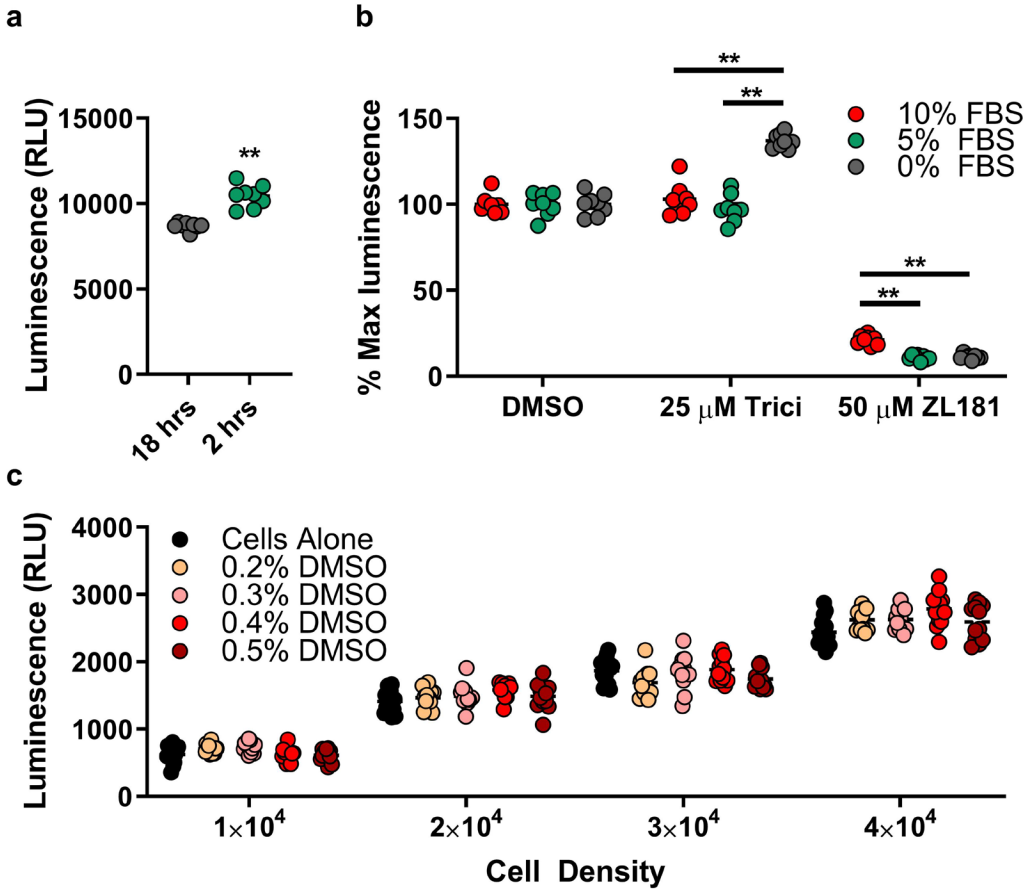

Figure 4.4. Effect of cell adhesion, FBS, and DMSO on assay performance. (

A) Raw luminescence from Clone V cells plated either 18 hrs (adherent) or 2 hrs (suspension) prior to luminescence reading. The luminescence was significantly higher for cells in suspension, indicating that successful luciferase complementation does not require complete cell adherence. Unpaired t test was used to determine significance; $p<0.0001$. (**B**) Stable cells in plated 2 hrs prior to plate reading in media containing either 10%, 5%, or no FBS were treated with either 0.3% DMSO (control), 25 uM triciribine, or 50 uM ZL181. The effect of triciribine was abolished in media containing FBS, while the effect of ZL181 was similar in 5% FBS but reduced in 10% FBS. $n=8$ per treatment group. Two-way ANOVA with post-hoc Tukey's multiple comparisons test was used to determine significance; $p<0.0001$. (**C**) Raw luminescence from Clone V cells in 384-well plates in media containing 0.2%, 0.3%, 0.4%, or 0.5% DMSO or without DMSO. $n=12$ per treatment group.

Finally, we examined the effect of luciferin incubation time (**Fig. 4.5A**) on Z' for cell densities ranging from 1×10^4 – 4×10^4 cells per 384-well. We observed that Z' improves with increasing cell density (**Table 4.1**) and longer luciferin incubation (60 min; **Fig. 4.5C**) compared to earlier time points due to greater signal separation between positive and negative controls. However, Z' stabilizes or decreases at later timepoints (75 min) due to increased SD of DMSO and TNF-α. Both 3×10^4 and 4×10^4 cells/well were sufficient to achieve a Z' of 0.7 (**Table 4.1**); however, during compound screening, lower cell density translates into increased probability of a potent inhibitor to cross the hit threshold due to increased efficacy (**Fig. 4.5B**). Additionally, a 25% reduction in cell density substantially diminishes cell culture resource requirements when large volumes are required for HTS. Thus, the final optimized conditions for the assay in 384-well plates were as follows: cell density, 3×10^4 per well; luciferin incubation time: 60 min; background control: 0.3% DMSO alone; positive control: 50 ng/mL TNF-α; and negative control: 25 μM MNS (**Fig. 4.5C, Table 4.1**).

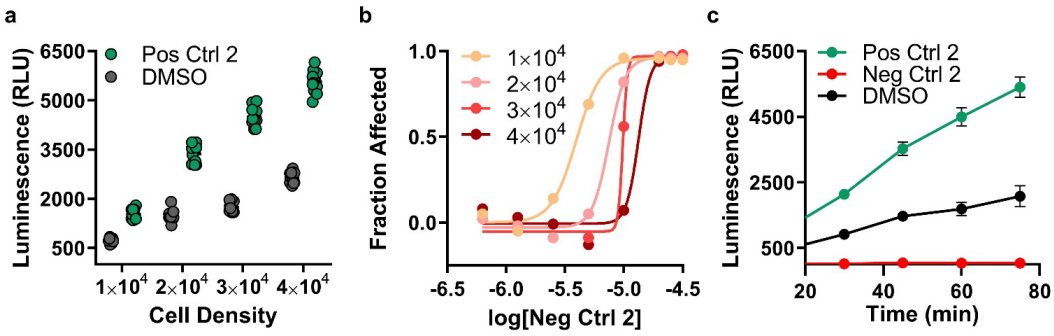

Figure 4.5. Cell density optimization in 384-well plates.

(A) Luminescence values from Clone V cells treated with 0.3% DMSO (vehicle) or Positive Control 2 (50 ng/mL TNF-α) in 384-well plates containing cell densities ranging from 1-4×104 cells/well. (B) Dose-response curves for Negative Control 2 (8 concentrations: 0.625, 1.25, 2.5, 5, 10, 20, 25, and 30 µM, n=6 per concentration) versus fraction affected, which corresponds to the proportion of Clone V cells that are inhibited by MNS treatment. The curve shifts to the left with decreasing cell density, indicating increased drug potency (MNS IC50: 1×104, 3.96 µM; 2×104, 7.49 µM; 3×104, 9.82 µM; 4×104, 13.3 µM). (C) Luminescence values from Clone V cells in 384-well plates (3×104 per well) treated with either Positive Control 2 or Negative Control 2. Plate luminescence read in 15minute intervals beginning 30 minutes after dispensing of luciferin substrate. Z' was greatest for the 60minute reading due to greater S:B ratio compared to earlier timepoints and lower SD compared to 75-minutes. Data shown are mean ± SD (n=12 per treatment group).

	Z'-factor					
Cell Density	MNS-DMSO		TNF-DMSO		TNF-MNS	
	45 min	60 min	45 min	60 min	45 min	60 min
1×10^4	0.41	0.43	-0.23	0.21	0.59	0.70
2×10^4	0.63	0.51	0.36	0.37	0.75	0.75
3×10^4	0.68	0.72	0.54	0.54	0.80	0.80
4×10^4	0.58	0.62	0.54	0.54	0.82	0.82

Table 4.1. Z'-factor calculated for varying cell density and luminescence read timepoint.

Z' values calculated (Equation 1) for different cell densities (1-4×10^4 cells per 384-well) at either 45- or 60-minutes following dispensing of luciferin substrate. For column 1 (MNS-DMSO), MNS was used as the positive control and DMSO as the negative control. For column 2 (TNF-DMSO), TNF-α was used as the positive control and DMSO as the negative control. For column 3 (TNF-MNS), TNF-α was used as the positive control and MNS as the negative control. Overall, the LCA is most robust across all categories using a cell density of 3×10^4.

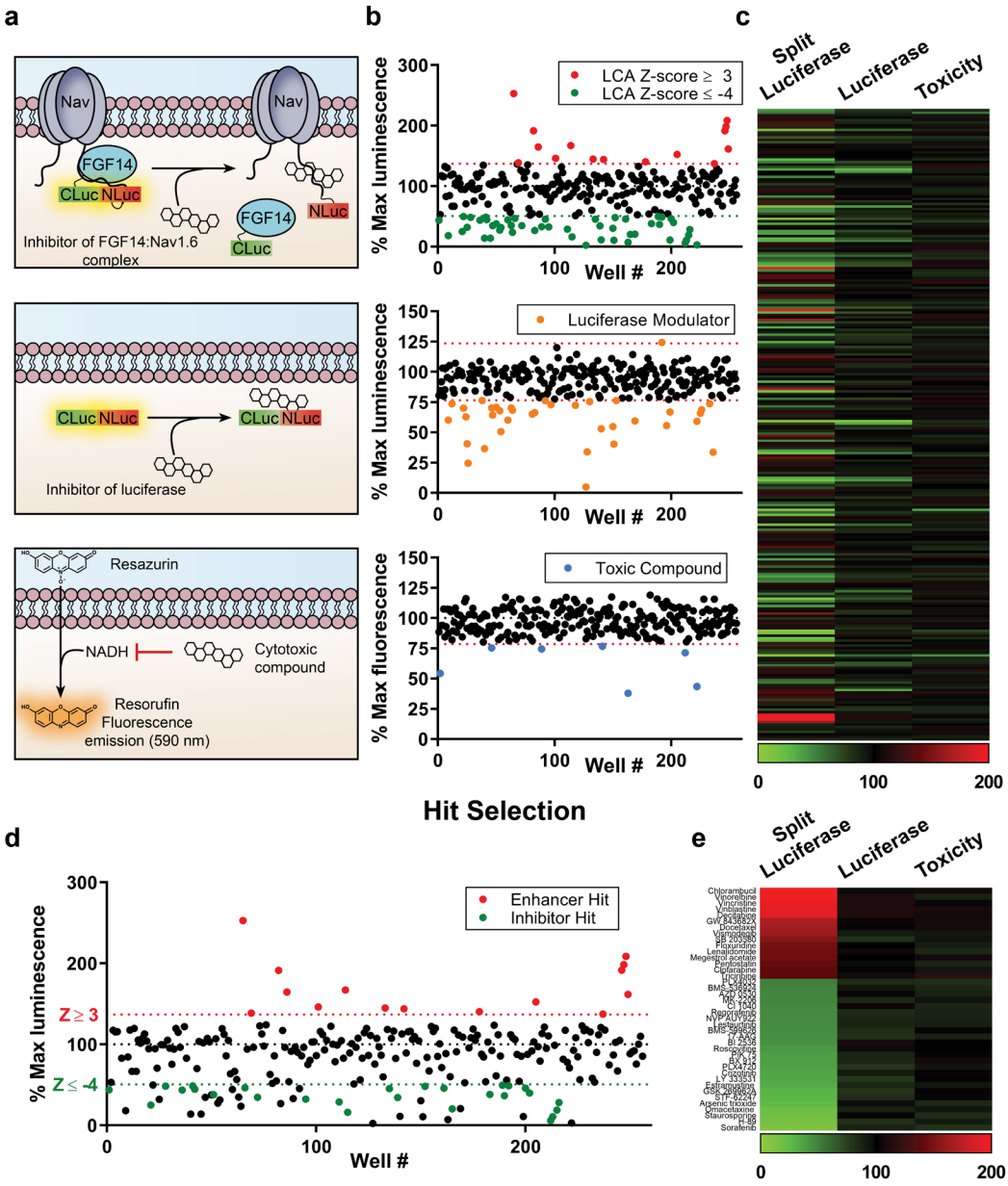

Figure 4.6. Identification of hits from the CC_NCI test library.
(**A**) Cartoon representations of the primary assay and counter-screening assays used to identify false positives. Top: example of a compound that binds the Nav1.6 C-tail, preventing FGF14 binding and resulting in reduced complementation of luciferase fragments. Alternative mechanisms (not shown) include direct FGF14 binding or modulation of signaling pathways that regulate FGF14 or Nav1.6 through phosphorylation. Middle: example of a compound that reduces luminescence through direct inhibition of the luciferase enzyme, which could lead to false positives in the LCA. Bottom: example of a cytotoxic compound, leading to decreased NADH production and resulting in reduced fluorescence in the CTB cell viability assay. (**B**) Scatter plot of all compounds tested from the CC_NCI library showing % maximal luminescence or fluorescence (normalized to DMSO). Top: LCA results with preliminary hits highlighted as green (50 inhibitors; $Z \leq -4$ and % max luminescence $\leq 50.7\%$) or red (15 enhancers; $Z \geq 3$ and % max luminescence $\geq 137.0\%$). Middle: full-length luciferase assay in-cells used to identify false positives ($Z \geq \pm 3$, equivalent to % max luminescence cut-offs of 76.6% and 123.4%, respectively); 1 enhancer and 36 inhibitors were identified, 22 of which were in the initial set of hits. Bottom: cell viability assay identified 7 toxic compounds, 5 of which were in the initial set of hits ($Z \geq \pm 3$, equivalent to % fluorescence cut-offs of 78.54% or 121.46%).

Note: 2 of these toxic compounds were also inhibitors of the full-length luciferase. (**C**) Heat map representation of LCA, luciferase, and cell viability assay results. (**D,E**) Final hits were selected following exclusion of false positives and toxic compounds, resulting in a final set of hits including 14 enhancers and 26 inhibitors. (**D**) Scatter plot with final hits highlighted as green (inhibitors) or red (enhancers). (**E**) Heat map representation of final hits.

Rank	Antagonist	Target(s)	% Lum	Z-score	IC_{50} (μM)
1	Sorafenib	RAF, PDGFR, VEGFR2/3	5.98	-7.62	3.98
2	H-89	PKA	16.07	-6.81	12.16
3	Staurosporine	PKA/C/G	18.86	-6.58	0.54
4	GSK 269962A	ROCK1	28.81	-5.77	24.66
5	LY 333531	PKCβ	34.34	-5.33	12.19
6	Crizotinib	ALK	34.72	-5.29	12.19
7	PLX4720	B-RafV600E	36.71	-5.13	2.14
8	BX 912	PDK1	37.84	-5.04	9.23
9	PIK 75	PI3Kα	38.11	-5.01	1.63
10	BI 2536	PLK1, BRD4	43.68	-4.57	8.71
11	Lestaurtinib	FLT3, JAK2	45.45	-4.42	1.22
12	CI 1040	MEK1/2	46.49	-4.34	14.85

Rank	Agonist	Target(s)	% Lum	Z-score	EC_{50} (μM)
1	Chlorambucil	Alkylating agent	252.88	12.39	16.41
2	Vinorelbine	Microtubules	208.53	8.79	1.55
3	Vincristine	Microtubules	198.49	7.99	0.27
4	Vinblastine	Microtubules	191.58	7.42	20.56
5	Decitabine	DNA synthesis inhibitor	191.40	7.41	28.77
6	Vismodegib	SMO	161.54	4.99	1.91
7	SB 203580	p38 MAPK	152.42	4.25	3.56
8	Floxuridine	Antimetabolite	146.01	3.73	2.46

Table 4.2. Target-based hit assessment.
Hits are ranked by average Z-score from the primary screening (n=2). Estimated IC_{50} and EC_{50} values are calculated from data represented in Figure 5.

4.2.4. Identification of novel regulators of the FGF14:Nav1.6 complex

We next tested this optimized system by screening a library comprised of 267 experimental or FDA-approved drugs from the Custom Clinical and National Cancer Institute (**CC_NCI**) collection. The compounds contained in this library have established toxicity profiles, are tolerable in humans, have well-established mechanisms of action and have been internally annotated with targets and cellular signaling pathways. Importantly, a subset of these compound's targets overlap with pathways that our lab has previously explored using the transiently transfected FGF14:Nav1.6 system[46,49], enabling us to directly compare and reconfirm previous results with this new assay.

An overview of the protocol used for our screening is shown in **Figure 4.1C**. Clone V cells were seeded in plates containing 0.3% DMSO (n=16), cells alone (n=8), 30 μM MNS (n=8), MNS dose response (1.25, 2.5, 5, 7.5, 10, 15, 20, and 25 μM, n=2 per concentration), and 50 ng/mL TNF-α (n=16) controls and experimental compounds (30 μM; 1 compound per well). Z-scores (Equation 5) were calculated for each compound using the mean and standard deviation of on-plate negative controls (0.3% DMSO). Immediately following luminescence reading, the cell viability assay was initiated by dispensing 10 μL of CTB reagent per well. Fluorescence was then read after 16 hrs, and cut-offs were set at a Z-score of < -3 to identify and exclude toxic compounds. This library was screened in duplicate, and the results are presented in Figure 4. Initially, a total of 50 inhibitors and 15 enhancers were detected using Z-score cutoffs of +3 for enhancers and -4 for inhibitors, respectively. The cutoff for inhibitors was set such that no more than 50 candidate inhibitors were selected, which corresponds to Z-score < -4 and % maximal luminescence of 50.7%. Due to challenges in finding enhancers of Nav channels, a less

stringent cutoff of Z-score > 3 was selected (corresponding to % max luminescence of 137%), resulting in 15 enhancers. Of these preliminary hits, 5 were excluded due to effects on cell viability (Z-score ≤ -3, equivalent to % fluorescence ≤ 78.54% of DMSO controls). Additionally, the library was counter-screened against the full-length luciferase (to identify potential false-positives) using transiently transfected HEK293 cells in 384-well plates under identical conditions as the primary assay. One luciferase enhancer and 36 luciferase inhibitors were identified in total, 22 of which were in the preliminary set of hits and excluded from further analysis. Interestingly, only one compound, PP121, significantly enhanced luminescence in the full-length luciferase assay (Z-score = 3.11), while inhibiting luminescence in the LCA (Z-score = -4.14). The effects of all compounds on the primary LCA, as well as the full-length luciferase and cell toxicity counter-screening assays are presented in Figure 4 as percent luminescence (LCA and full-length luciferase assay) or fluorescence (cell viability assay) normalized to per plate DMSO controls (n=16 per plate). To provide an integrated snapshot of the screening campaign, we represent the normalized response values in a heat-map (**Fig. 4.6C,E**). Following exclusion of false positives identified in the counter screens (**Fig. 4.6D**), the set of hits included 15 enhancers and 25 inhibitors (**Fig. 4.6E**). From this initial set, 20 hits (12 inhibitors, 8 enhancers) were subsequently selected for follow-up based on LCA ranking and relevance of the drug target (**Table 4.2**). Hits were confirmed through an 8-point dose response (0.25, 0.5, 0.95, 1.88, 3.75, 7.5, 15, and 30 μM, n=2 per concentration) in duplicate (20 hits per 384-well plate, n=4 per concentration over two plates) (Fig. 5). Average normalized luminescence for each concentration and nonlinear curve fitting are shown in Figure 5, and estimated IC/EC_{50} concentrations are provided in **Table 4.2**.

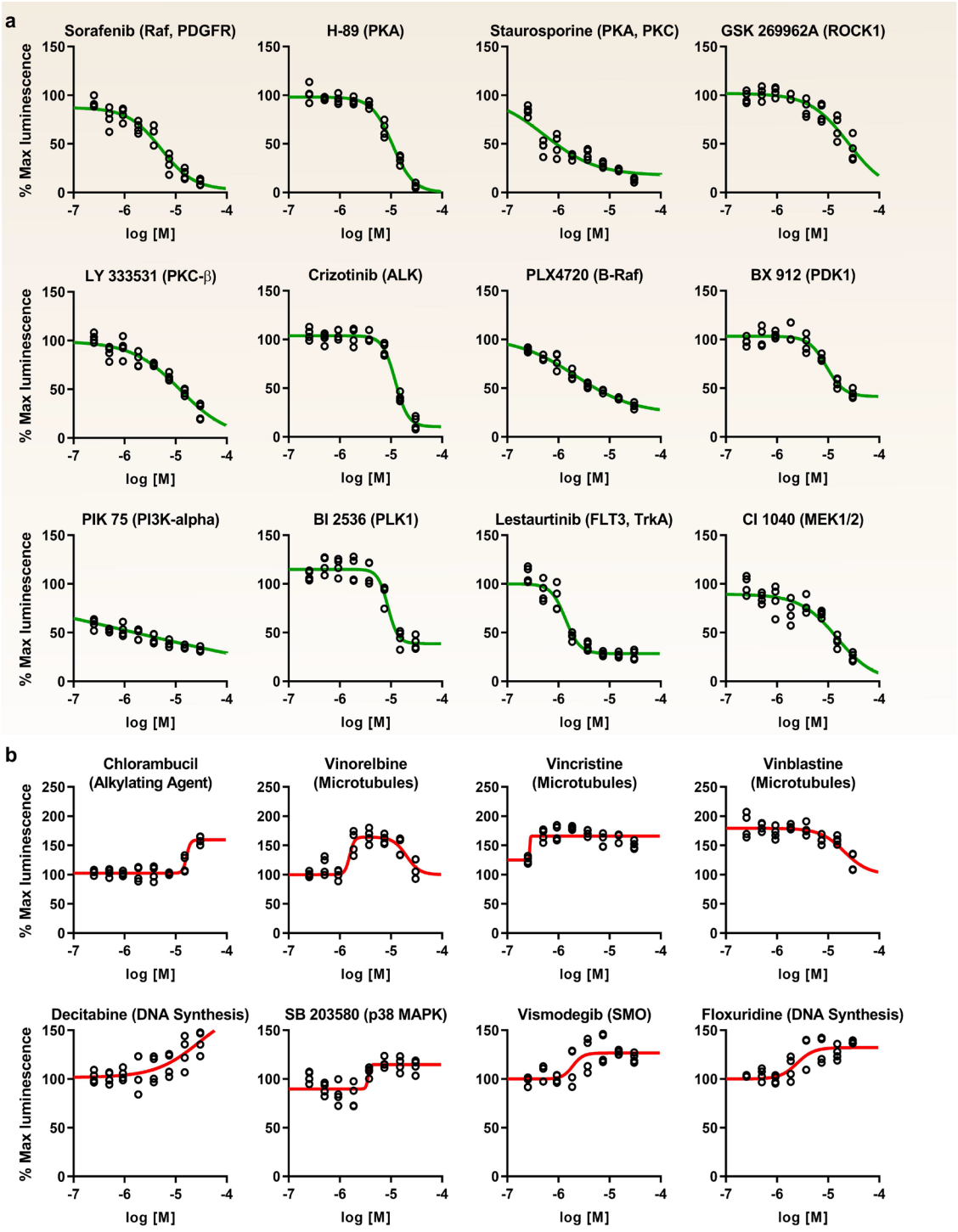

Figure 4.7. Initial dose-response validation of identified HTS hits.

Percent maximal luminescence from treated Clone V cells (normalized to DMSO controls) versus compound concentration with nonlinear regression curve fitting. (**A**) Antagonists and (**B**) agonists are listed in order of efficacy as determined in the primary screening. Antagonists were defined as those compounds that inhibit FGF14:Nav1.6 complementation with increasing dose, while agonists were defined as those compounds which increase FGF14:Nav1.6 complementation with increasing dose. Estimated IC_{50} and EC_{50} values are provided in Table 2. Doses range from 0.25 µM - 30 µM and were tested under identical conditions as the primary screening

We found that the FGF14:Nav1.6 C-tail interaction was indirectly inhibited (i.e., the relevant kinase inhibitor acts as antagonist) through targeting S/T kinases including rapidly accelerated fibrosarcoma (**c-RAF**), protein kinases A, C, and G (**PKA, PKC, PKG**), rho-associated coiled-coil-containing protein kinase 1 (**ROCK1**), pyruvate dehydrogenase kinase 1 (**PDK1**), phosphoinositide 3-kinases (**PI3K**), polo-like kinase 1 (**PLK1**), and mitogen-activated protein kinase kinase (**MEK1**, aka **MAP2K1**). RAF kinases participate in the RAS-RAF-MEK-ERK signal transduction cascade[144]; this pathway likely stimulates the FGF14:Nav1.6 interaction, as inhibition of RAF, MEK1, and p38 MAPK (lower doses of SB 203580, **Figure 5**) all reduced this interaction in our assay. While non-specificity (i.e., off-target effects) is a common issue for experiments involving kinase inhibitors, the observation of multiple inhibitors targeting numerous kinases in the same pathway lends support to these results. Additionally, inhibition of the following protein or receptor tyrosine kinases (**RTKs**) reduces PPI between FGF14 and Nav1.6 C-tail: platelet-derived growth factor receptor (**PDGFR**), vascular endothelial growth factor receptor (**VEGFR**) 2 and 3, anaplastic lymphoma kinase (**ALK**), FMS-like tyrosine kinase 3 (**FLT3**), Tropomyosin receptor kinase A (**TrkA**), and janus kinase 2 (**JAK2**). Interestingly, numerous DNA synthesis inhibitors (anti-metabolites), alkylating agents, and microtubule inhibitors enhanced the FGF14:Nav1.6 interaction; while exploration of possible mechanisms for these compounds are subjects for future investigation, the results may not be biologically relevant for neuronal Nav channel function. The p38 MAPK inhibitor SB 203580 was initially found to enhance the FGF14:Nav1.6 interaction in the primary screening (30 μM), but evaluation of dose-dependent behavior (**Fig. 4.7**) revealed

mild inhibition at lower concentrations (0.5 – 2 μM) and stimulation at higher concentrations, indicative of off-target effects. ROCK1 is a is a regulator of the actomyosin cytoskeleton which promotes contractile force generation[145]; this finding in combination with the numerous microtubule hits observed in our assay serves to reinforce the idea that the cytoskeleton may play a role in controlling FGF14:Nav1.6 interactions.

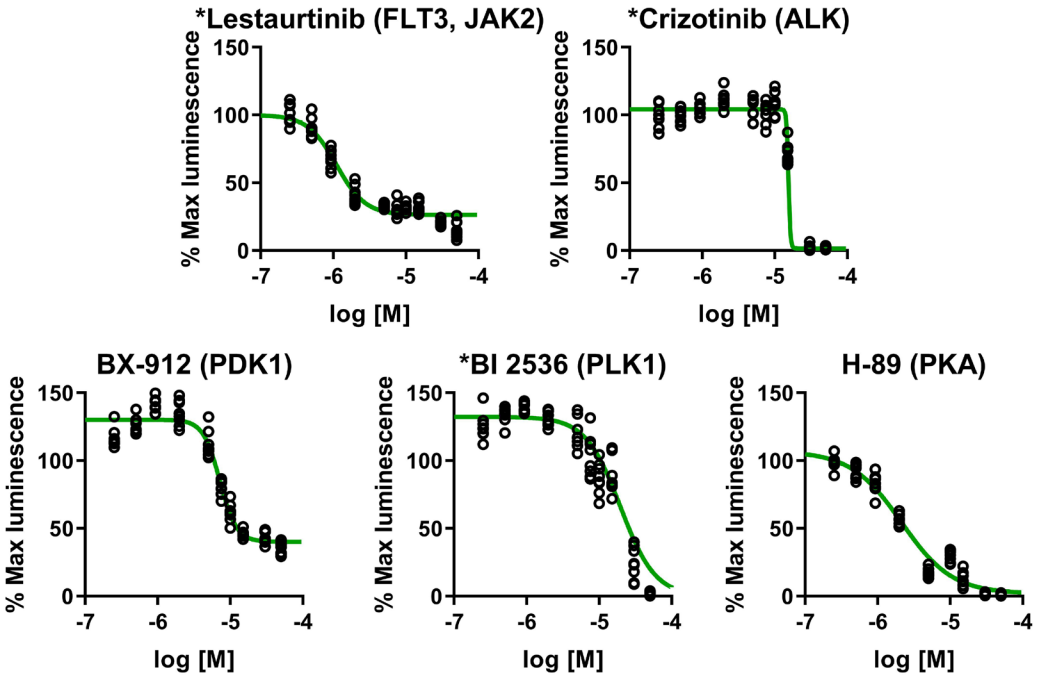

Figure 4.8. Second validation of prioritized hits using repurchased compounds.

Based on initial dose responses (potency, efficacy, and curve shape) as well as target information, the tyrosine kinase inhibitors Lestaurtinib and Crizotinib, as well as the S/T kinase inhibitors H-89, BX-912, and BI 2536, were repurchased to confirm compound identity and potency. Fresh compounds were tested by 10-point dose responses (range: 0.25 μM - 50 μM) in Clone V cells under identical conditions as the primary screening. All compounds demonstrated results similar to the original. While Lestaurtinib, Crizotinib, and H-89 appear to have purely inhibitory effects, BX-912 and BI 2536 act as enhancers at lower concentrations. Estimated IC_{50}: Lestaurtinib, 0.95 μM; Crizotinib, 15.5 μM; H-89, 1.9 μM; BX-912, 6.8 μM; BI 2536, 17.4 μM. *Drug has completed and/or on-going clinical trials, including for PNS or CNS-related cancers.

Based on initial dose responses (potency, efficacy, and curve shape) as well as target information, 5 compounds (Lestaurtinib, Crizotinib, H-89, BX-912, and BI 2536) were repurchased to confirm compound identity and establish potency. The freshly acquired compounds were retested in Clone V cells using 10 doses (0.25, 0.5, 1, 2.5, 5, 7.5, 10, 15, 30, and 50 μM, n=8 per concentration) in duplicate (10 compounds per 384-well plate, n=8 per concentration over two plates). Results confirm the dose-dependent activity of all compounds, which are similar to the primary screen (**Fig. 4.8**). The most potent inhibitor identified by this screen was Lestaurtinib, with an in-cell IC_{50} of 0.95 μM, followed by H-89 (1.9 μM), BX-912 (6.8 μM), Crizotinib (15.5 μM), and BI 2536 (17.4 μM). While Lestaurtinib, Crizotinib, and H-89 appear to have purely inhibitory effects, BX-912 and BI 2536 display counter acting activity as a function of dosage. However, the sigmoidal appearance of dose-response curves is promising. Based on this data, we identify these five inhibitors as top hits from our screening against the FGF14:Nav1.6 complex and recommend follow-up functional studies to determine the effects of the relevant kinase targets on neuronal excitability. Overall, these results demonstrate that: (1) our assay is capable of reliably detecting both inhibitors and enhancers of the FGF14:Nav1.6 complex from a background signal with low variability; (2) initial effects of identified hits can be reproduced in subsequent studies; and (3) that the screening system is capable of follow-up dose-dependency studies using an identical 384-well plate format with additional replicates for each concentration.

4.3. DISCUSSION

Despite extensive interest in pharmacologically targeting protein-channel complexes[41,146–149], the lack of adequate platforms to rapidly screen compounds in physiologically relevant models[140,150] has significantly hampered discovery of compounds targeting these interfaces. Growing appreciation of how ion channels and receptors operate as macromolecular complexes, rather than isolated entities within the lipid bilayer, necessitates drug development strategies beyond conventional agonists and antagonists targeting voltage-sensitive domains or ligand binding pockets[151,152]. Mutations that impact the intracellular portions of the Na^+, K^+, and Ca^{2+} channel's pore-forming alpha subunits or their accessory proteins are associated with genetically inherited epilepsies[153]. However, given that the effects of these mutations are heterogenous and have variable impact on patients, there is a dearth of uniform or efficacious treatments. Increasing evidence suggests that specific microdomains separate from the ion permeating region of these channels are associated with physiologically- and disease-relevant effects and could possibly be targeted as allosteric surfaces for drug development. It is therefore necessary to develop strategies to study these ancillary portions of the primary channel with precise and targeted methods.

One of the challenges in searching for ion channel regulators is that these protein complexes, particularly for Nav channels, are large and difficult to reliably express in heterologous cells using lipid-based transfection. Traditionally, whole cell patch-clamp has been used as a functional readout of channel activity; however, this technique does not easily transition to HTS when the channel is assessed in the presence of an accessory protein. This is in part due to the lack of ability to control protein-channel interactions

during the channel cycle within multi-well plates[105] and to specifically isolate these interactions from the rest of the channel.

Here, we have applied a minimal functional domain (**MFD**) approach to isolate specific regions within Nav channels[154]. Our strategy isolates the MFD within the FGF14:Nav1.6 channel complex, reconstitutes this domain in a heterologous cell system, and uses LCA to investigate specific interactions while maintaining the protein:channel domain near-to-physiological conditions. The design of the CD4-Nav1.6 C-tail chimera anchors the C-tail to the inner leaf of the plasma membrane, enabling closer to native presentation of the FGF14:Nav1.6 interacting domain compared to diffuse and freely floating cytosolic Nav1.6 C-tail. For screening modulators of cell signaling, maintaining these interacting proteins in membrane microdomains increases the likelihood of identifying the most physiologically relevant Nav1.6 regulatory pathways.

Building on previous studies in which LCA was conducted using transient transfection, here we created a double stable cell line that expresses the FGF14:Nav1.6 C-tail complex and miniaturized this assay from 96- to 384-well plates to be amenable for HTS of large chemical libraries. Our new assay platform implements liquid-handling robotic systems, enabling rigorous counter-screens to be conducted in parallel with LCA, which drastically reduces false positives while simultaneously allowing for expedient hit validation studies. Using 3×10^4 cells per 384-well in suspension and 1 hr reporter substrate incubation, our assay achieved $Z' > 0.5$ for both inhibitory and enhancer-type assays (**Table 1, columns 1 and 2**) and exhibited a robust ability ($Z' > 0.8$) to distinguish agonist from antagonist (**Table 1, column 3**). Thus, this miniaturized LCA is capable of reliably distinguishing significant FGF14:Nav1.6 modulators from background signal.

Using this new miniaturized assay, we screened a test library of 267 FDA-approved and clinical oncology drugs and identified potent agonists and antagonists of the FGF14:Nav1.6 interaction (**Table 4.2**). The rationale for selecting this library was two-fold. First, the compounds target a broad range of cell signaling pathways potentially important for regulation of the Nav channel complex while simultaneously screening clinically relevant compounds that could be repurposed for CNS disorders and channelopathies. Second, the economical size of the library (one 384-well plate including controls) facilitated duplicate screening under numerous conditions throughout development, enabling extensive assay optimization prior to larger campaigns. The initial hit selection criteria were based on previously identified challenges in detecting potent enhancers of the FGF14:Nav1.6 C-tail interaction[46,49], and the target profile and chemical attributes of compounds were subsequently analyzed to determine top hits for validation studies (Fig. 1C and Table 2). These data show that many of the hits target kinases that are known to play an important role in regulating PPI that affect electrical activity of neurons[18]. The PI3K/Akt pathway, which converges on GSK3, has been identified as a prospective regulatory node of neuronal excitability through modulation of the FGF14:Nav1.6 complex19. GSK3β directly phosphorylates FGF14 at S226 and Nav1.6 at T1936, two sites that were found to be disease-related in experimental models of neurodegeneration and of vulnerability to stress and depression, respectively [57,65]. Clusters of S/T kinase inhibitors, including those targeting casein kinase 2 (**CK2**), PKC and Wee1 kinase, have been found to converge on the FGF14:Nav1.6 complex through the GSK3 pathway[49]. For example, inhibitors of CK2, which serves as a priming kinase for GSK3 in neurons and has been shown to phosphorylate FGF14 at S228 and S230, are strong suppressors of the

FGF14:Nav1.6 interaction and decrease excitability in hippocampal neurons[57]. Thus, it is possible that hits identified in this study would modulate the FGF14:Nav1.6 complex through finely-tuned regulation of phosphorylation at these sites. Based on this information, we selected five 'hit' kinase inhibitors for extensive dose-dependency validation studies using fresh compound samples, including H-90, Critzotinib, BX913, Lestaurtinib, and BI2537, which all acted as antagonists toward the FGF14:Nav1.6 C-tail interaction. These kinases also converge on the Akt/GSK3 pathway, which alters Nav1.6 current[49] and modulates neuronal excitability and leads to various behavioral outcomes[65]. For example, activation of PKA reduces Nav1.6 currents in heterologous cell systems[155], and disruption of the PDK1–Akt pathway leads to cognitive deficits and diminished motivation[156]. Additionally, ALK-PI3K pathway plays a role in learning, memory and neurogenesis[157] and synaptic plasticity in the nucleus accumbens[158].

Importantly, we show that the FDA-approved drug lestaurtinib might be of interest for regulating excitability in CNS disorders. This tyrosine kinase inhibitor targets the JAK2[159], FLT3, and TrkA pathways and is the most potent inhibitor (IC50 = 0.95 μM) of the FGF14:Nav1.6 interaction that we have identified to date. There are currently 14 ongoing or completed clinical trials using lestaurtinib for the treatment of various cancers including myelofibrosis, leukemia, prostate cancer, and neuroblastoma, and the TrkA pathway is a target for neuroblastoma therapy[160]. Furthermore, the brain-derived neurotrophic factor (**BDNF**)-TrkB pathway has been implicated in channelopathies[161], and inhibition of this pathway by lestaurtinib prevents epileptogenesis in immature brains[162] and hyperexcitability-induced emotional and cognitive behavioral dysfunction after hypoxic seizures[163]. These results indicate that this FDA-approved drug might be of interest

for CNS activity in diseases characterized by dysfunction of Trk receptor signaling. Our results suggest that lestaurtinib could be potentially repurposed toward channelopathies and other CNS diseases characterized by dysfunction of neuronal excitability mediated by Nav1.6. However, these results await functional validation studies, such as electrophysiology *ex vivo*, as well as extensive *in vivo* evaluation.

In summary, here we report a robust assay for HTS of small molecules based on split-luciferase complementation that could be applied to search for mechanisms regulating ion channel complexes and develop targeted treatments for channelopathies associated with changes in protein:channel interactions in cells.

Chapter 5. JAK2 regulates Nav1.6 channel function via FGF14^{Y158} phosphorylation

Portions of the following chapter are currently under review by *Biochimica et Biophysica Acta (BBA) - Molecular Cell Research* as:

JAK2 regulates Nav1.6 channel function via FGF14^{Y158} phosphorylation

Paul A. Wadsworth, Oluwarotimi Folorunso, Nghi Nguyen, Aditya K. Singh, Daniela D'Amico, Reid T. Powell, David Brunell, John Allen, Clifford Stephan, Fernanda Laezza

ABSTRACT

Background: Despite the essential function of the voltage-gated Na^+ (Nav) channel complex in controlling neuronal firing and plasticity, a surprisingly limited number of kinases have been identified as regulators of this molecular complex. We hypothesized that numerous as-of-yet unidentified kinases indirectly regulate the Nav channel via modulation of the intracellular fibroblast growth factor 14 (FGF14), an accessory protein with numerous unexplored phosphomotifs and required for channel function in neurons.

Methods: Here we present results from an in-cell high-throughput screening (HTS) against the FGF14:Nav1.6 complex using >3,000 well-characterized and structurally diverse compounds targeting an extensive range of signaling pathways. Studies were complemented by *in vitro* phosphorylation, biophysics, mass-spectrometry and patch-clamp electrophysiology.

Results: We found that hits targeting Janus kinase 2 (JAK2) were over-represented. Phosphomotif scans supported by *in vitro* phosphorylation revealed FGF14^{Y158}, a site previously shown to mediate both FGF14 homodimerization and monomer interaction with

Nav1.6, as a JAK2 phosphorylation site. Following inhibition of JAK2, FGF14 homodimerization increased in a manner directly inverse to FGF14:Nav1.6 complex formation and these effects were abolished in the presence of the FGF14^{Y158A} mutant. Patch-clamp electrophysiology revealed that the JAK2 inhibitor Fedratinib abolishes FGF14-dependent modulation of Nav1.6 currents, eliciting phenotypes previously shown to depend on Y158 and consistent with regulatory mechanisms of Nav1.6 long-term inactivation.

Conclusions: These studies point toward a novel mechanism by which levels of JAK2 in neurons could directly influence firing and plasticity by controlling the FGF14 dimerization equilibrium, and thereby the availability of monomeric species for interaction with Nav1.6.

5.1. INTRODUCTION

The voltage-gated Na^+ (**Nav**) channel forms the basis of neuronal excitability[116]. As molecular determinant of the action potential, the Nav channel underlies the major electrical signaling in the brain mediating neuronal firing, synaptic transmission and plasticity[164]. Due to the critical role they play, Nav channels are understandably subject to intense regulation by accessory proteins including β-IV spectrin, ankyrin, and intracellular fibroblast growth factors (**iFGFs**)[35]. In turn, signaling pathways downstream of transmembrane receptors modulate PPI between these accessory proteins and the Nav channel through phosphorylation, which can confer functional specificity to neuronal firing in response to extracellular stimuli. Not only do these regulatory mechanisms play fundamental roles in neuronal plasticity, but dysregulation of these processes has been associated with increased risk for neuropsychiatric and neurological disorders[18,20,35,82–84] spurring a great interest in searching for novel kinase signaling pathways that control the Nav channel complex.

As described in **Chapter 1**, phosphorylation is a key form of Nav channel regulation, particularly for Ser/Thr kinases[85–90]. For instance, **PKA** and **PKC** phosphorylate multiple serine residues on intracellular domains of Nav1.2, significantly reducing current and increasing firing thresholds[89,91,92]. Our laboratory has previously demonstrated that **GSK3β** phosphorylates T1966 on the Nav1.2 C-terminal tail, suppressing Na^+ currents and channel trafficking to the plasma membrane[93]. In addition, GSK3β was identified as the converging node of a signaling network that modulates the FGF14:Nav1.6 complex via interactions between the PI3K/Akt pathway, NF-kB, Wee1

kinase, and PKC[49]. However, the mechanisms for how phosphorylation or other signaling events specifically change PPI between these complexes is not known.

Additionally, despite the essential function of phosphorylation in modulating Nav channel functions, a surprisingly limited number of kinases have been verified as regulators of Nav channel complexes. The Nav1.6 channel and FGF14 sequences are rich in predicted Tyr and Ser/Thr phosphorylation sites, but evidence supporting phosphorylation or other means of regulation at these sites is lacking. Thus, we hypothesized that numerous as-of-yet unidentified kinases regulate the FGF14:Nav1.6 channel complex through mechanisms that are relevant for neuronal plasticity. We sought to discover new regulators and explore potential phosphorylation networks regulating the FGF14:Nav1.6 complex by first conducting an expanded high-throughput screening (**HTS**) campaign of diverse chemical libraries compared to previous studies[46,49]. We have recently developed and optimized an in-cell, luminescence-based assay for HTS against PPI at the FGF14:Nav1.6 complex for this purpose, and have validated its ability to detect potent inhibitors and enhancers of this interaction[100]. Using this robust form of the split-luciferase complementation assay (**LCA**), here we screened three libraries comprising a total of ~3,000 well-characterized kinase inhibitors, FDA-approved drugs, and natural products. As promiscuity of kinase inhibitors is a well-known phenomenon, observing multiple structurally diverse hits with a common kinase target provides stronger evidence for target relevance. Thus, we selected libraries to provide coverage for a comprehensive array of targets representative of the known "kinome," while also including a high degree of target overlap to ensure confidence and reproducibility in preliminary screening results (i.e., validation studies not based on a single hit kinase inhibitor).

Following exclusion of toxic compounds identified through cell viability screening run in parallel, we discovered that inhibitors of Janus kinase 2 (**JAK2**), a Tyr kinase downstream of transmembrane receptors[165], were over-represented among hits. Phosphomotif scans, molecular modeling, and in-cell counter-screening suggested a regulatory mechanism dependent on changes affecting residues at the PPI interface that were common to both the FGF14:Nav1.6 and FGF14:FGF14 homodimer complexes[50,75]. Subsequent biophysical studies including mass-spectrometry (MS) and surface plasmon resonance (SPR) revealed that JAK2 phosphorylates FGF14 at Y158, a site critical in mediating high-affinity dimerization[44,50]. Functionally, JAK2 inhibition prevents FGF14-dependent regulation of Na^+ currents. Based on these results, we concluded that by regulating the equilibrium between FGF14 homodimerization, activation of JAK2 might enable neurons to dynamically adjust firing in response to JAK2-mediated receptor signaling.

5.2. RESULTS

5.2.1. High-throughput screening of kinase inhibitors to discover new regulators

We have previously developed and reported an in-cell, high-throughput assay that can be used to identify targets that inhibit and/or enhance the FGF14:Nav1.6 complex assembly[100]. This adapted form of the luciferase complementation assay (LCA) is based on a double stable HEK293 cell line expressing CLuc-FGF14 and CD4-Nav1.6 C-tail-NLuc recombinant proteins that, upon binding, produce luminescence in the presence of the substrate luciferin[45,166]. Based on this assay, we sought to identify potential regulators of the FGF14:Nav1.6 complex by screening a large library of well-characterized and structurally diverse kinase inhibitors targeting an extensive range of cell signaling

pathways. Compound screening was subsequently validated using previously established orthogonal screening methods (i.e., cell viability and full-length luciferase assays)[100] to identify artifacts, followed by target-based hit selection (**Figure 5.1A**). Top ranking targets were then counter-screened against the FGF14:FGF14 homodimer to identify pathways of biological relevance for FGF14 signaling.

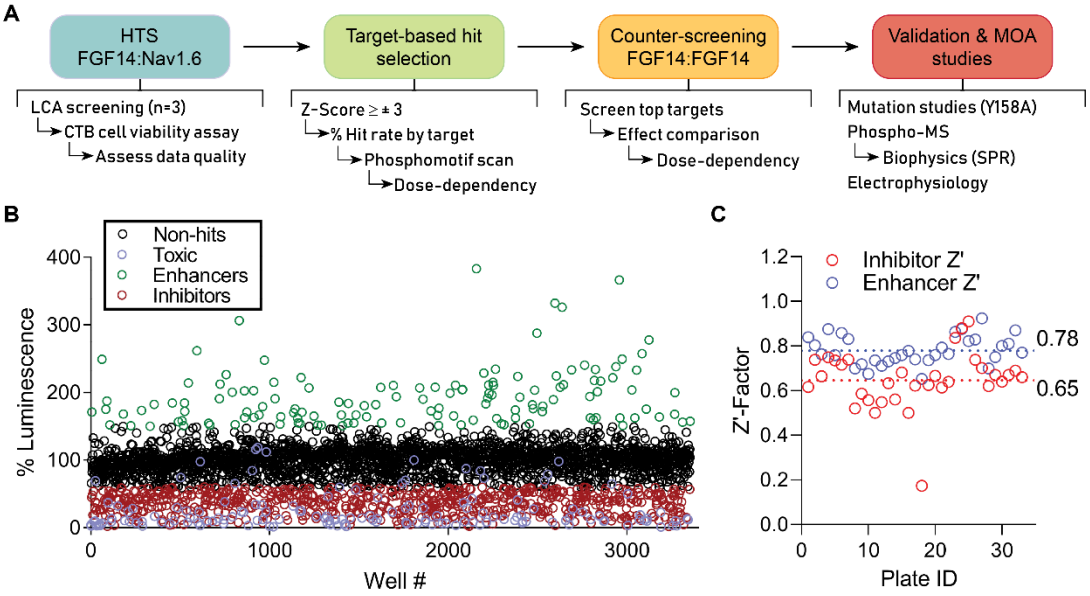

Figure 5.1. HTS pipeline and results for discerning mechanisms of Nav channel complex regulation by kinases.

(A) Screening and validation pipeline. (**B**) Double stable HEK293 cells expressing CLuc-FGF14 and CD4-Nav1.6-NLuc were plated in 384-well plates and treated with kinase inhibitors (n = 1 compound/well) from the Broad, Selleck, and UTKinase collections, with each plate screened in triplicate. The mean percent luminescence (normalized to on-plate 0.3% DMSO controls) is shown for each compound. Following exclusion of toxic compounds (purple), hits were initially selected using unbiased criteria of change in FGF14:Nav1.6 complex assembly by at least 40% (i.e., % luminescence > 140% or < 60%) and Z-score ≥ 3 (enhancers, green) or Z-score ≤ -5 (inhibitors, red). (**C**) Z'-Factor (Z') for each screened library plate, calculated using either the inhibitor (red) or enhancer (blue) positive controls as described previously[100]. A total of 33 plates were screened, including 6 from Broad, 12 from Selleck, and 15 from UTKinase, for a total of 3,120 compounds.

With this identification and validation pipeline, we screened three libraries: the Broad Institute Collection (407 compounds), the Selleck Bioactive Collection (1,280 compounds), and the UT Austin Combined Kinase Collection (1,434 compounds) (Figure 1B). This library included a high degree of overlap between kinase targets to ensure broad "kinome" coverage and to increase confidence in results (i.e., rule out promiscuity by observing multiple hits with a common target). Cells were seeded in 384-well plates containing compounds at a screening concentration of 30 μM (n = 1 compound per well; 320 compounds/plate), as well as negative controls (0.3% DMSO, n = 16; cells alone, n = 8 wells), and previously established[100] inhibitory positive controls (MNS, concentration range: 2.5 – 30 μM [Fig. 5.2B], n = 24), and enhancer positive controls (TNF-α, n = 16) that were used to calculate Z'-factor to assess assay robustness throughout the screening campaign. Each plate of compounds was screened in triplicate. Immediately following luminescence reading, the CellTiter-Blue® (CTB) cell viability assay was initiated by dispensing 10 μL of CTB reagent per well. Fluorescence was read after 16 hrs, and cut-offs were set at a Z-score of < -3 (relative to DMSO controls) to identify and exclude toxic compounds. The coefficient of variation (CV) and Z' factor for our in-cell HTS assay were found to be within acceptable range (Broad (n = 6 plates): CV = 0.09 ± 0.005; inhibitor Z' = 0.66 ± 0.02; enhancer Z' = 0.78 ± 0.05; Selleck (n = 12 plates): CV = 0.08 ± 0.02; inhibitor Z' = 0.64 ± 0.09; enhancer Z' = 0.77 ± 0.06; UTKinase (n = 15 plates): CV = 0.07 ± 0.02; inhibitor Z' = 0.65 ± 0.17; enhancer Z' = 0.78 ± 0.07;

	Z'-Factor		
Plate	Inhibitor	Enhancer	CV
Broad-1A	0.621	0.698	0.102
Broad-2A	0.674	0.746	0.088
Broad-1B	0.638	0.797	0.086
Broad-2B	0.671	0.808	0.096
Broad-1C	0.694	0.866	0.089
Broad-2C	0.658	0.765	0.093
SEL-1A	0.616	0.839	0.100
SEL-2A	0.738	0.803	0.065
SEL-3A	0.664	0.763	0.069
SEL-4A	0.749	0.875	0.060
SEL-1B	0.735	0.759	0.060
SEL-2B	0.716	0.858	0.072
SEL-3B	0.739	0.831	0.062
SEL-4B	0.520	0.700	0.070
SEL-1C	0.586	0.718	0.092
SEL-2C	0.557	0.675	0.106
SEL-3C	0.500	0.735	0.126
SEL-4C	0.548	0.711	0.120
UTK1A	0.633	0.731	0.070
UTK2A	0.560	0.746	0.093
UTK3A	0.681	0.759	0.064
UTK4A	0.500	0.778	0.057
UTK5A	0.622	0.740	0.087
UTK1B	0.174	0.652	0.099
UTK2B	0.625	0.736	0.063
UTK3B	0.666	0.759	0.073
UTK4B	0.614	0.792	0.092
UTK5B	0.639	0.764	0.068
UTK1C	0.836	0.863	0.050
UTK2C	0.880	0.876	0.033
UTK3C	0.910	0.823	0.023
UTK4C	0.738	0.830	0.071
UTK5C	0.702	0.924	0.085

Table 5.1. Z'-factor and coefficient of variation (CV) for all screened plates.

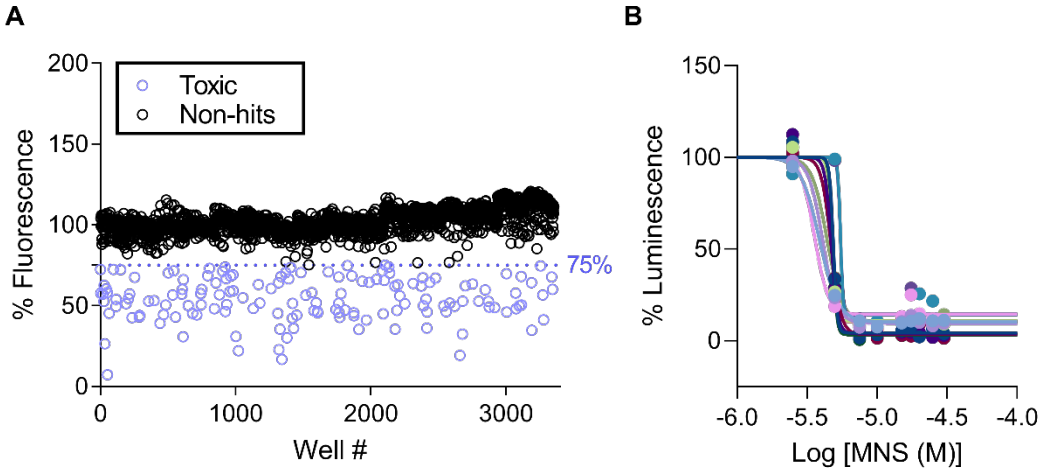

Figure 5.2. HTS assay controls and toxicity counter-screen.

(**A**) Cell viability assay results for the Broad, Selleck and UTKinase libraries. Cut-offs for compound toxicity were set at 75% fluorescence (relative to the mean for 0.3% DMSO controls). (**B**) Per plate inhibitor control dose response to verify reproducibility between screened plates, ensuring that there were not changes in cell density or other cell behaviors, which often can be detected through changes in the concentration dependency.

data are mean ± SD) (**Fig 4.1C and Table 5.1**) [100]. Following exclusion of toxic compounds (**Figure 5.1**), hits were initially selected using unbiased criteria of change in FGF14:Nav1.6 complex assembly by at least 40% (i.e., % luminescence > 140% or < 60%) and Z-score ≥ 3 (enhancers, green) or Z-score ≤ -4 (inhibitors, red). Note that this combination of Z-scores and % luminescence was used to ensure that hits were not preferentially selected from plates with lower control standard deviation, which could artificially over-inflate a given compound's rank despite lack of biological relevance[100].

We observed clusters of hits targeting kinases including Akt, GSK3, PKC, PI3K, MEK, p38 MAPK, and NF-kB, supporting findings of previous smaller scale studies[46,49]. However, this expanded screening campaign identified two previously unobserved targets that were highly over-represented among hits: the JAK2 (26 hits) and Src (18 hits) tyrosine kinases (**Table 5.2**). Phosphomotif scans (**Table 5.3**) using the HPRD PhosphoFinder and NetPhos 3.1 revealed that the FGF14 sequence contains possible phosphorylation sites for

Target	# Screened Compounds	# Hits	Hit %
Src	31	20	0.65
JAK	47	28	0.60
PKC	21	12	0.57
VEGFR	64	34	0.53
GSK3	33	17	0.52
NF-kB	36	18	0.50
Raf	24	11	0.46
FLT3	11	5	0.45
STAT3	7	3	0.43
Akt	29	11	0.38
p38 MAPK	27	10	0.37
MEK	28	9	0.32
Raf	23	7	0.30
Wee1	7	2	0.29
Syk	18	5	0.28
PI3K	64	16	0.25
EGFR	75	13	0.17
mTOR	37	6	0.16

Table 5.2. Top HTS kinase targets.
Total number of HTS hits compared with total number of compounds screened by kinase target.

several of these kinases, including GSK3, PI3K, PKC, p38 MAPK, JAK2, and Src. Additionally, NetPhorest 2.1 identified probable Src homology 2 (**SH2**) domains at residues 155-164 (corresponding to the FGF14 sequence VFENYYVIYSS) and residues 206-216 (LEVAMpYREPSL).

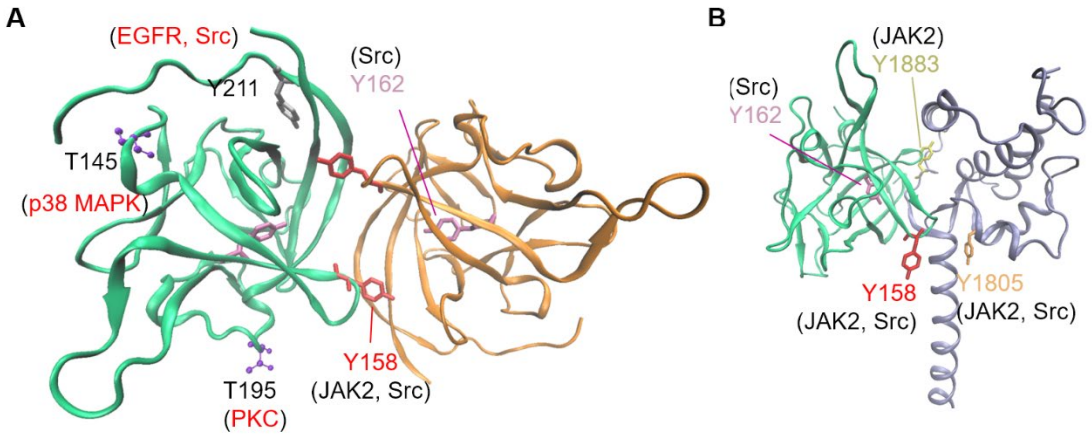

Figure 5.3. Structural relationship of potential phosphorylation sites to the PPI interfaces of the FGF14:FGF14 homodimer and FGF14:Nav1.6 complex.

(A) Model of the FGF14:FGF14 homodimer homology model, based on the FGF13 homodimer crystal structure (PDB ID: 3HBW) with monomer #1 as teal and monomer #2 as orange. Y158 on each is shown as red, while Y162 is shown as pink. Y162 is > 10Å from the PPI surface, and is unlikely to contribute to dimerization. On monomer #1 (teal), also showing other predicted phosphorylation sites that are not at the dimer interface, including T145, T195, and Y211. (**B**) Model of the FGF14:Nav1.6 C-tail complex, based on the FGF13:Nav1.5:CaM ternary complex crystal structure (PDB ID: 4DCK). Predicted Src and JAK2 phosphorylation sites on both FGF14 and Nav1.6 C-tail are shown.

FGF14 Position	FGF14 Sequence	Kinase or Phosphatase	FGF14 Position	FGF14 Sequence	Tyrosine Binding Motifs
81 - 86	YCRQGY	ALK	81 - 84	pYCRQ	STAT3
145 - 147	TPE	p38 MAPK	86 - 89	pYYLQ	STAT3
158 - 161	YYVI	JAK2	129 - 132	pYIAM	PI3K p85
162 - 163	YS	Src	156 – 161	SVFENpYYVIYS	SHC, SH2
162 - 167	YSSMLY	ALK, INSR	154 - 165	VFENYpYVIYSS	SH2, PTP
193 - 195	KKT	PKC	162 - 165	pYSSM	PI3K p85
211 – 212	YR	Src	167 - 170	pYRQQ	STAT3
226 – 230	SKSTS	GSK3	206 – 216	LEVAMpYREPSL	SH2, PTP

Table 5.3. FGF14 phosphomotifs correspond to hit targets identified by HTS.
FGF14 phosphomotifs correspond to hit targets identified by HTS. Subsequent investigation using the HPRD PhosphoMotif Finder, NetPhos 3.1, and NetPhorest 2.1 revealed potential JAK2 and Src phosphorylation sites at Y158 and Y162, respectively, as well as other sites for kinases identified in the HTS. The identified JAK2 and Src phosphorylation sites are in line with the observed screening data, as well as previous studies showing the importance of Y158 and other nearby residues in mediating both FGF14 dimerization and binding to the Nav1.6 C-terminal tail.

Despite there being a disproportionately high number of PI3K inhibitors (64) in the screening set, only 16 compounds ranked as hits, and the primary target IP3K isoform was distributed between hits, reducing our interest in this target/suggesting this was due to off-target effects/more complex mechanism.

The GSK3 and CK2 sites have previously been thoroughly explored[46,57], the identified JAK2 and Src phosphorylation and binding sites, Y158 and Y162, are in line with the observed screening data. Previous studies have shown the importance of Y158 in mediating both FGF14 dimerization and binding to the Nav1.6 C-terminal tail[50,75], and Y158 was found at the PPI interface for both the FGF14 dimer and the FGF14:Nav1.6 complex[50,75] (**Fig. 5.3**). Conversely, despite its relative vicinity to Y158, Y162 is more buried in the complex at a location that may render kinase binding and phosphorylation at this site more challenging. Thus, Y162 is less likely to be involved in structurally relevant regulation of the PPI interface (> 10Å from the PPI surfaces).

Primary hits that fulfilled the following two criteria were promoted for further studies: (1) inhibition or stimulation of the FGF14:Nav1.6 complex by at least 40% (equivalent to 60% or 140% luminescence when normalized to DMSO controls,

respectively) and Z-score ≥ 3 for enhancers or ≤ -5 for inhibitors, and (2) the primary kinase target was targeted by two or more compounds meeting the prior hit selection criteria (i.e., at least two inhibitors of JAK2 observed to modulate FGF14:Nav1.6 complex assembly by ≥ 40%). Compounds with known promiscuity were avoided where possible (alternative hit inhibitors of the same target).

5.2.2. Initial validation of hits

Prior to further mechanistic studies, we conducted dose response validation of selected hits targeting JAK2 and Src against the double stable cell line using screening library compounds to determine which to proceed with for additional testing. These studies confirmed initial findings, revealing low micromolar potencies (1-15 μM), and validated JAK2 and Src inhibitors from structurally distinct families (**Figure 5.4**). JAK inhibitors with a preference for the JAK3 isoform had varied effects by LCA, and the most significant JAK3 inhibitors, such as 420121, have numerous additional targets. This combined with the observation that the JAK3 inhibitor 420126 failed to validate during initial dose dependency studies (**Fig. 5.4**), suggested that JAK3 was unlikely to be a key regulator of the FGF14:Nav1.6 complex. Additionally, the enhancing effect of JAK inhibitors with a preference toward JAK1 (INCB424, XL019) may suggest a different role for JAK1-mediated regulation of the FGF14:Nav1.6 complex.

As to whether the effects of JAK inhibitors are driven in part by signal transducer and the activator of transcription 3 (STAT3) signaling, a pathway that often co-exists with JAK2 in cell regulatory mechanisms[165], we also identified several STAT3 inhibitors in the screening (**Table 5.2**), and STAT3 tyrosine binding motifs were identified in the FGF14 sequence (**Table 5.3**). From the Selleck library, two STAT3 inhibitors (S3I-201 and Ursolic Acid) had minimal impact (115.3% and 103.5% luminescence, respectively), while the inhibitor Stattic resulted in almost complete inhibition of the FGF14:Nav1.6 complex (6.0% luminescence), but was excluded due to cell toxicity (57.2% fluorescence from the

CTB assay). In the Broad library, two top scoring STAT3 inhibitors Cucurbitacin I and Niclosamide (5.6% and 18.7% luminescence, respectively) were identified. Initial dose-dependency studies for the natural product Cucurbitacin I revealed highly potent but

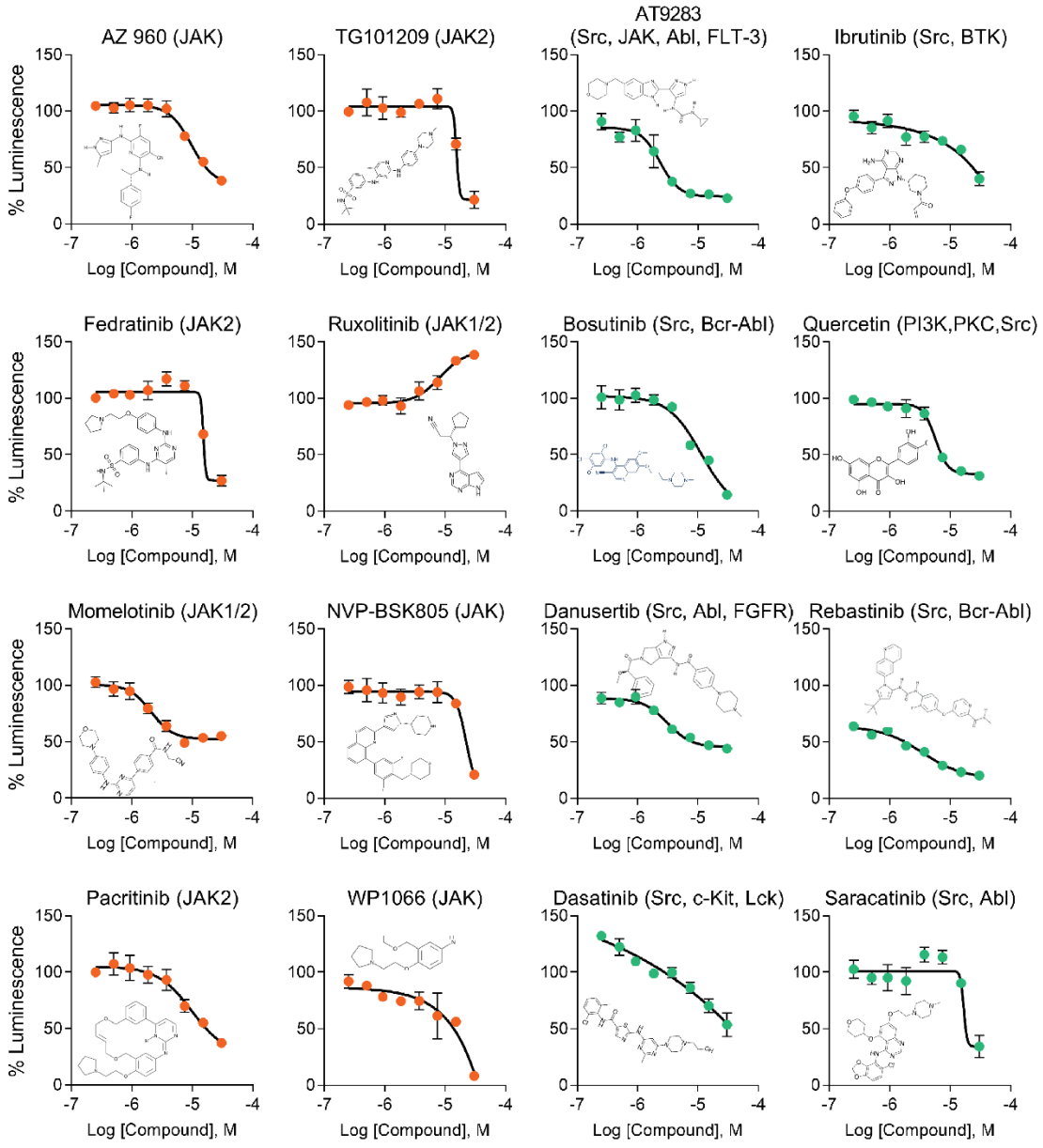

Figure 5.4. Identification of JAK and Src as regulators of the Nav1.6 complex by HTS.

JAK and Src kinase inhibitors were consistently ranked among the highest scoring non-toxic compounds from an HTS of kinase inhibitors against the FGF14:Nav1.6 complex. Dose response plots are shown using original library compound for the top eight inhibitors targeting JAK2 (orange) or Src (teal). Each compound's structure is inlaid into its respective plot, demonstrating structural diversity among hits. Data are mean percent luminescence ± SD with a non-linear regression curve fitting.

undesirable curve shape (linear decrease in luminescence) (**Fig. 5.5**), possibly due to additional inhibition of the NF-kB pathway[167]. Although this odd behavior for the FGF14:Nav1.6 complex was less prevalent in follow-up studies with repurchased compound, a similar pattern of linear direction for enhancing the FGF14:FGF14 dimer was observed using Cucurcitabine I, but not S3I-201, which had minimal effect against FGF14:Nav1.6. Altogether, the results suggest that STAT3 may be involved, but further studies would be required to fully discern the mechanism. One possible reason for the less clear patterns observed may be due to fewer available inhibitors specific for STAT3, as well as that changes in STAT3 regulation of the FGF14:Nav1.6 complex may be a less potent form of regulation (i.e. indirect) than that of phosphorylation by JAK2.

Inhibitors of other Src-family kinases were also identified as hits. Five out of 18 inhibitors targeting Lck kinase were hit inhibitors, including PRT062607, Syk Inhibitor III, and ER 27319, with % luminescence ranging from 22.2 to 50.5%. Two out of three compounds targeting Lck, were also hits, including AMG-47a and 428205. Of these, PRT062607 and 428205 demonstrated promising concentration dependency (**Fig. 5.5**), but ER 27319 was less ideal. Although these findings support the role of Src family kinases in regulation of the FGF14:Nav1.6 complex, Lck and Syk were not further pursued due to both proportionately low number of hits (relative to total # screened compounds targeting that kinase), as well as lack of observed phosphorylation motifs in FGF14.

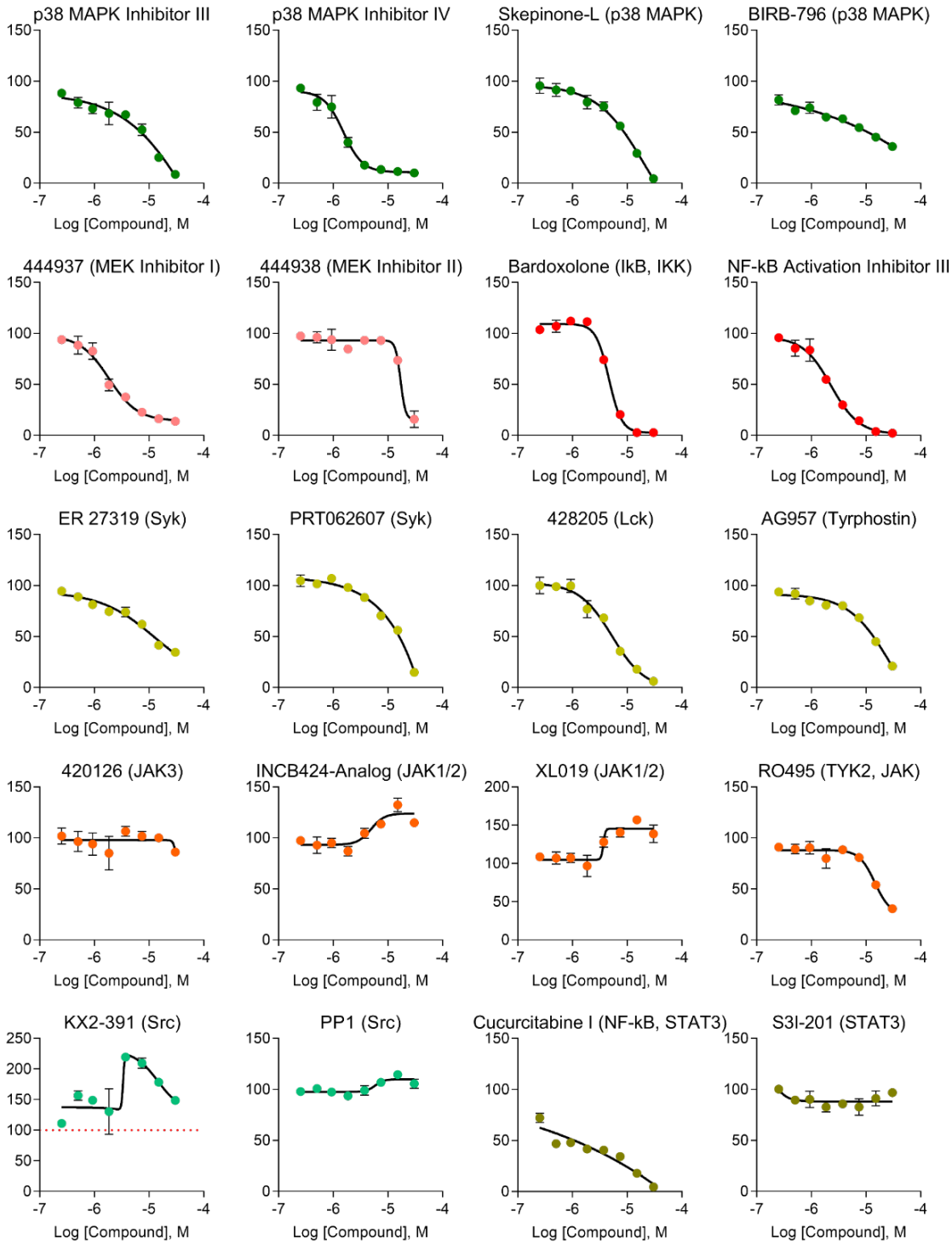

Figure 5.5. Initial concentration-dependency studies of selected hits for validation of HTS findings for other highly represented targets.

LCA results (mean normalized luminescence) against the FGF14:Nav1.6 complex from HTS hits that were selected for further studies based on target clustering. Luminescence was normalized to 0.3% DMSO controls.

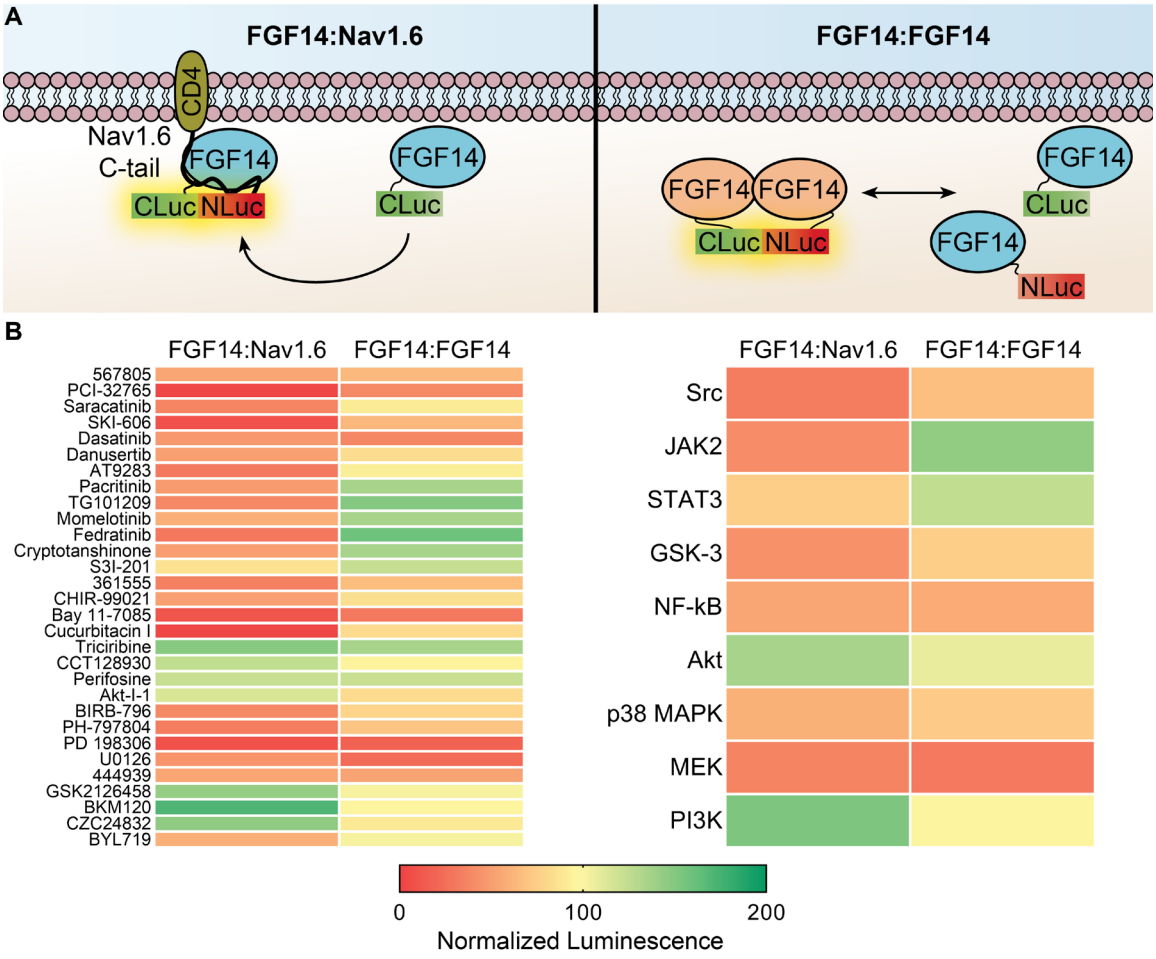

Figure 5.6. Counter-screening of inhibitors from top kinase targets against the FGF14:FGF14 dimer.

(**A**) Cartoon representation of hypothesized interactions occurring in LCA for the FGF14:Nav1.6 (left) vs. FGF14:FGF14 dimer (right). (**B**) Kinases targeted by ≥4 hits from the HTS against the FGF14:Nav1.6 complex that also revealed phosphorylation or binding motifs (or those of upstream pathways, such as Akt) in FGF14 were counter-screened against the FGF14:FGF14 dimer, using ≥2 selected compounds per target based on selectivity, potency, and availability. Left, heatmap of mean normalized luminescence for individual compounds tested against either the FGF14:Nav1.6 complex (represented in panel A, left) or FGF14:FGF14 dimer (represented in panel A, right). For counter-screening, transiently transfected HEK293 cells were seeded in 384-well plates and treated with 0.3% DMSO (n = 32) or kinase inhibitors (30 μM; n = 3 per compound). Right, the mean percent luminescence from all compounds for each kinase group is shown as a heat map for the two complexes. Note that only JAK2 inhibitors demonstrated a consistent and opposing response between the FGF14:Nav1.6 complex and FGF14:FGF14 dimer.

5.2.3. Counter-screening and differential regulation of FGF14:FGF14 homodimer by JAK2, but not Src

Select kinases targeted by ≥4 hits from the HTS against the FGF14:Nav1.6 complex were counter-screened against the FGF14:FGF14 homodimer, using ≥2 selected compounds per target based on selectivity, potency, and availability. GSK3, NF-kB, Akt, MEK, and PI3K inhibitors were tested based on our previous studies showing regulation of the FGF14:Nav1.6 complex by these pathways[46,49,57], and direct phosphorylation of FGF14 at S226 by GSK3β[80]. Conversely, Src, JAK2, and p38 MAPK inhibitors were tested based on phosphomotifs identified in the FGF14 sequence (**Table 2**). HEK293 cells transiently transfected with CLuc-FGF14 and FGF14-NLuc (**Figure 5.6A**) were treated with inhibitors (30 μM) in 384-well plates in triplicate, similarly to the primary screening against the FGF14:Nav1.6 complex. The results are shown as a heat map for both the individual compound screening results (**Figure 5.6B,** left), as well as the average effect from all inhibitors for a given kinase target (**Figure 5.6B,** right). Counter-screening revealed that JAK2 was the only target that differentially regulated the two complexes (change in complex assembly in opposing directions) (mean from all four JAK2 inhibitors: FGF14:Nav1.6, 43.65%; FGF14:FGF14, 144.6% luminescence). We also proceeded with investigations of Src due to the high confidence of FGF14:Nav1.6 complex regulation, as indicated by the high proportion of hits versus screened compounds (65%; ranked #1 out of all kinase targets). Additionally, the three predicted phosphorylation sites in FGF14 (Y158, Y162, and Y211; **Table 5.3**), as well as the moderate inhibitory effect of Src inhibitors on FGF14:FGF14 dimerization (mean from all four Src inhibitors: FGF14:Nav1.6, 32.6%; FGF14:FGF14, 66.7% luminescence) was indicative of regulation by Src on both complexes.

Based upon potency, efficacy, curve shape from the initial concentration dependency experiments, as well as inhibitor selectivity, we repurchased top JAK2 and Src inhibitors for counter-screening against the FGF14 dimer and follow-up validation studies.

While virtually all kinase inhibitors have numerous off-target effects, we proceeded with compounds that were known to be specific, and to not have identical off-target effects. Fedratinib, Pacritinib, and TG101209 preferentially inhibit JAK2 over other JAK isoforms, but Fedratinib also binds TYK2, and the latter two also target FLT3 at higher concentrations[168–170]. Momelotinib (also known as CYT387) inhibits both JAK1/2, but is not known for significant effects against either FLT3 or TYK2[169,171]. The lack of identical off-target effects among inhibitors enabled us to rule out the effect of these alternate targets.

For Src, we did not further pursue AT9283, Quercetin, or Dasatinib due to known promiscuity for many kinase targets[172]. Interestingly, the Src inhibitor KX2-391, present in all three screened libraries, was the only compound targeting Src that acted as an enhancer of the FGF14:Nav1.6 complex (**Fig 5.5**). KX2-391 is a non-ATP competitive peptide mimetic, differentiating it from the majority of available Src inhibitors, but this compound also promotes tubulin polymerization[173], and we have previously demonstrated that microtubule inhibitors act as potent enhancers of the LCA[100], which may not be biologically relevant. Therefore, we continued with Danusertib, Saracatinib, Ibrutinib, and Bosutinib for further studies targeting Src.

All eight of these compounds, including the JAK2 inhibitors Momelotinib, TG101209, Fedratinib, and Pacritinib, as well as the Src inhibitors Danusertib, Saracatinib, Ibrutinib, and Bosutinib, were additionally counter-screened against the full-length luciferase to rule out that observed LCA effects were due to modulation of luciferase alone.

Following inhibition of JAK2, but not Src, FGF14 homodimerization increased in a manner directly inverse to FGF14:Nav1.6 complex formation with a comparable degree of both efficacy (minimum vs. maximum percent luminescence for FGF14:Nav1.6 compared to FGF14:FGF14 dimerization, respectively), as well as potency (inhibitor IC_{50} against the FGF14:Nav1.6 complex vs. EC_{50} against the FGF14:FGF14 dimer) (**Figure 5.7A** and **Table 5.4**). The most potent JAK2 inhibitor was Fedratinib (FGF14:Nav1.6, IC_{50}

= 9.7 μM; FGF14:FGF14, EC_{50} = 8.2 μM), also exhibiting strong maximal but inverse effects for each complex (FGF14:Nav1.6, IC_{50} = 9.7 μM; FGF14:FGF14, EC_{50} = 8.2 μM).

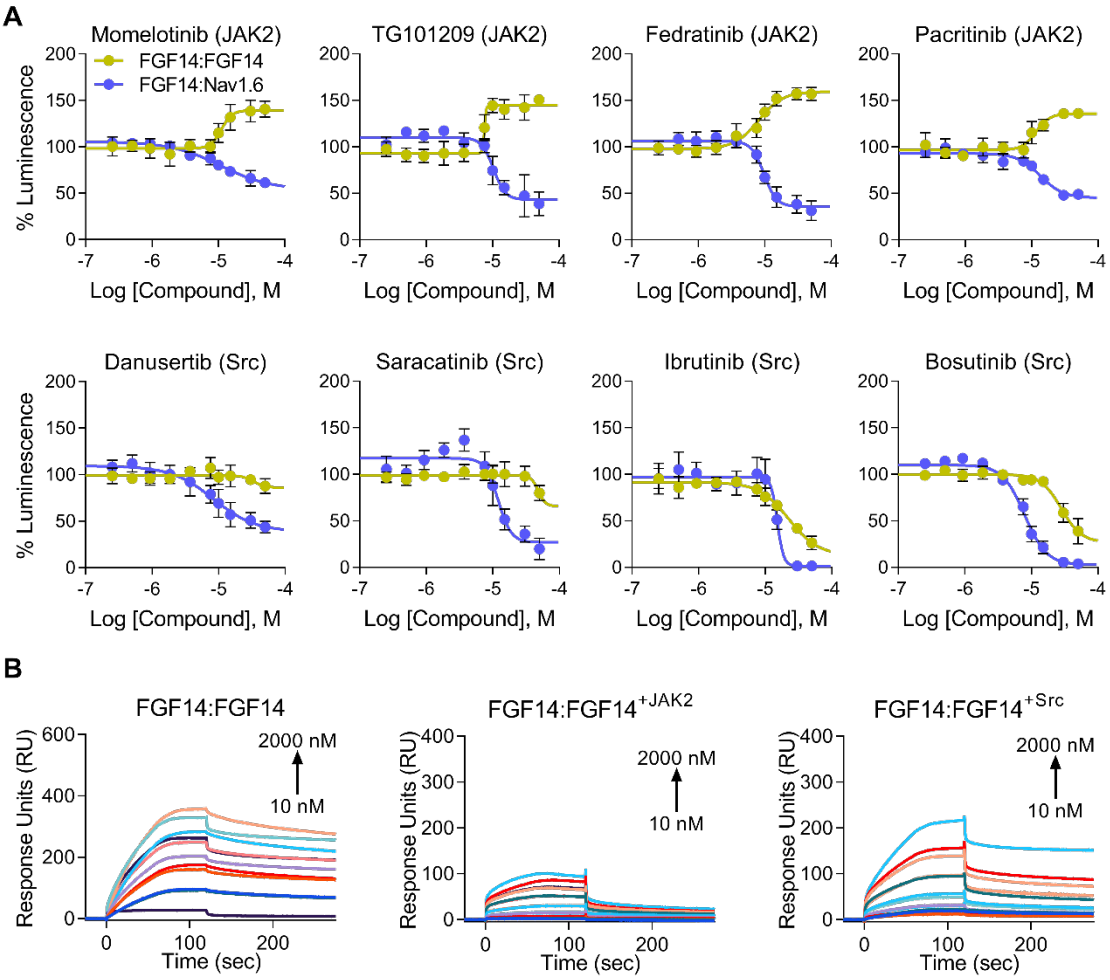

Figure 5.7. Differential regulation of the FGF14:FGF14 dimer and FGF14:Nav1.6 complex by JAK2, but not Src.

(**A)** Dose responses (10-point, *n* = 8 per concentration over two 384-well plates) were conducted against the FGF14:Nav1.6 complex (purple) for promising hits using repurchased compounds in order to validate HTS results. Positive hits were then counter-screened against the FGF14:FGF14 dimer (yellow), with the hypothesis that changes in FGF14 dimerization could be associated with inverse changes in FGF14:Nav1.6 binding. Inhibition of JAK2 but not Src, increases FGF14 dimerization in a manner directly inverse to FGF14:Nav1.6 complex formation. Estimated efficacy and potency are shown in **Table 3**. Luminescence for each well was normalized to per plate 0.3% DMSO controls (*n* = 32 per plate), and the mean normalized luminescence ± SEM is shown. **(B)** Surface plasmon resonance (SPR) sensorgrams from proteins flown across a chip with FGF14 bound (1,030 RU) using a flow rate of 50 uL/min. Purified FGF14 protein was phosphorylated *in vitro* by pre-incubation with either JAK2 or Src tyrosine kinases as indicated above each panel.

Inhibitor	Target	$FGF14^{WT}$:Nav1.6		FGF14:$FGF14^{WT}$		$FGF14^{Y158A}$:Nav1.6		FGF14:$FGF14^{Y158A}$	
		I_{Min}/E_{Max}	IC/EC_{50}	I_{Min}/E_{Max}	IC/EC_{50}	I_{Min}/E_{Max}	IC/EC_{50}	I_{Min}/E_{Max}	IC/EC_{50}
Momelotinib	JAK2	53.5	10.9	138.6	10.8	101.8	N/A	90.9	N/A
TG101209	JAK2	43.0	10.3	150.6	7.6	78.0	98.0	73.4	69.4
Fedratinib	JAK2	35.7	9.7	156.7	8.2	76.8	27.1	72.8	28.5
Pacritinib	JAK2	45.0	13.5	136.0	11.6	110.6	N/A	79.3	5.5
Danusertib	Src	38.6	8.4	86.0	34.1				
Saracatinib	Src	27.0	12.1	65.7	48.3				
Ibrutinib	Src	1.6	15.3	12.8	22.6				
Bosutinib	Src	3.2	9.7	26.8	28.1				

Table 5.4. Potency and efficacy against the FGF14:FGF14 dimer and FGF14:Nav1.6 complex by JAK2 and Src inhibitors.
Estimated potency (IC_{50} or EC_{50}, μM) and efficacy (minimal (I_{Min}) or maximal (E_{Max}) percent luminescence at the bottom plateau for inhibition and top plateau for stimulation, respectively) and for JAK2 and Src inhibitors based on the LCA data in **Figures 5.7 and 5.9**. Luminescence for each well was normalized to per plate 0.3% DMSO controls (n = 32 per plate), and the mean normalized luminescence ± SEM is shown.

For Src inhibitors, FGF14:Nav1.6 complex formation was potently inhibited (IC_{50} range: 8.4 – 15 μM) to a high degree (range: 1.6 – 38.6% luminescence). Varying degrees of inhibition were also observed for the FGF14 dimer (range: 12.8 – 86.0% luminescence), but the potency for these compounds was greatly increased compared to the FGF14:Nav1.6 complex (IC_{50} range: 28 – 48 μM).

5.2.4. High affinity FGF14:FGF14 dimerization is efficiently abolished by JAK2 phosphorylation

Next, we used surface plasmon resonance (SPR) to determine the impact of phosphorylation on the FGF14:FGF14 dimer formation using unphosphorylated recombinant FGF14 protein bound to the chip surface (1,030 RU). This revealed that the high affinity dimerization of recombinant FGF14 protein (K_D = 440 nM) was abolished upon pre-incubation with (and presumably phosphorylation by) JAK2 (K_D = 2.6 μM) or Src (K_D = 1.3 μM) kinases, with notable change in kinetics (**Figure 5.7B** and **Table 5.5**). FGF14 flowing over the chip appeared to remain tightly bound following injection stop (k_{off} = 0.000934 s^{-1}), and similar kinetics are observed for FGF14+Src, although a lesser degree of FGF14 remained bound (dissociated more quickly; k_{off} = 0.00109 s^{-1}); the association rate between the two appeared similar. Following incubation with JAK2, however, FGF14 dissociated rapidly (k_{off} = 0.00459 s^{-1}) from the FGF14 protein bound to

the chip surface. In terms of overall binding, FGF14 had the highest overall binding (~400 RU), followed by ~200 RU for FGF14+Src and ~100 RU for FGF14+JAK2. We concluded that FGF14 phosphorylated by JAK2 had overall less affinity for $FGF14^{WT}$ and bound much more transiently. For FGF14 phosphorylated by Src, we concluded that the dimerization event became overall less favorable, as well as that the dimer stability was moderately reduced. Given the much stronger phenotype with JAK2, we pursued it for further mechanistic validation studies, beginning with identifying the phosphorylation site(s).

	K_D (μM)	k_{on} (M^{-1} s^{-1})	k_{off} (s^{-1})
FGF14:FGF14	0.44	13600 ± 53	$9.34\times10^{-4} \pm 3.0\times10^{-6}$
FGF14:FGF14+JAK2	2.6	4060 ± 67	$4.59\times10^{-3} \pm 5.6\times10^{-5}$
FGF14:FGF14+Src	1.3	9120 ± 76	$1.09\times10^{-3} \pm 4.7\times10^{-6}$

Table 5.5. High affinity FGF14:FGF14 dimerization is abolished by phosphorylation by JAK2, and by Src to a lesser extent.
Kinetic constants calculated from data represented in Figure 3B. The K_D represents the average between the kinetic K_D, calculated using the simplest Langmuir 1:1 interaction model ($K_D=k_{off}/k_{on}$), and the steady-state saturation (affinity) K_D.

5.2.5. JAK2 phosphorylates $FGF14^{Y158}$

Phosphomotif scans revealed Y158 as a potential JAK2 phosphorylation site (**Table 5.3**), and homology modeling here as well as in previous studies[50,75] has demonstrated that this site is at the PPI interface of both the FGF14:FGF14 dimer and the FGF14:Nav1.6 complex (**Figure 5.2 and 5.8A**). Thus, hypothesizing that this was the site of interest, we used a 20aa peptide derived from FGF14 (aa149-168 of FGF14-1b, corresponding to the sequence KFKESVFENYYVIYSSMLYR) containing the predicted JAK2 substrate motif to confirm this as the phosphorylation site. Mass spectrometry (MALDI TOF-MS/MS) confirmed Y158 as the site of phosphorylation by JAK2 *in vitro* (**Figure 5.8B**), as identified by the presence of y_{10} (theoretical m/z of 1293.66, observed

m/z of 1293.56) and y_{11} (theoretical m/z of 1536.69, observed m/z of 1536.63) ions (1536.63-1293.56 = 243.07, corresponding to the MW of $Y(PO_3)$.

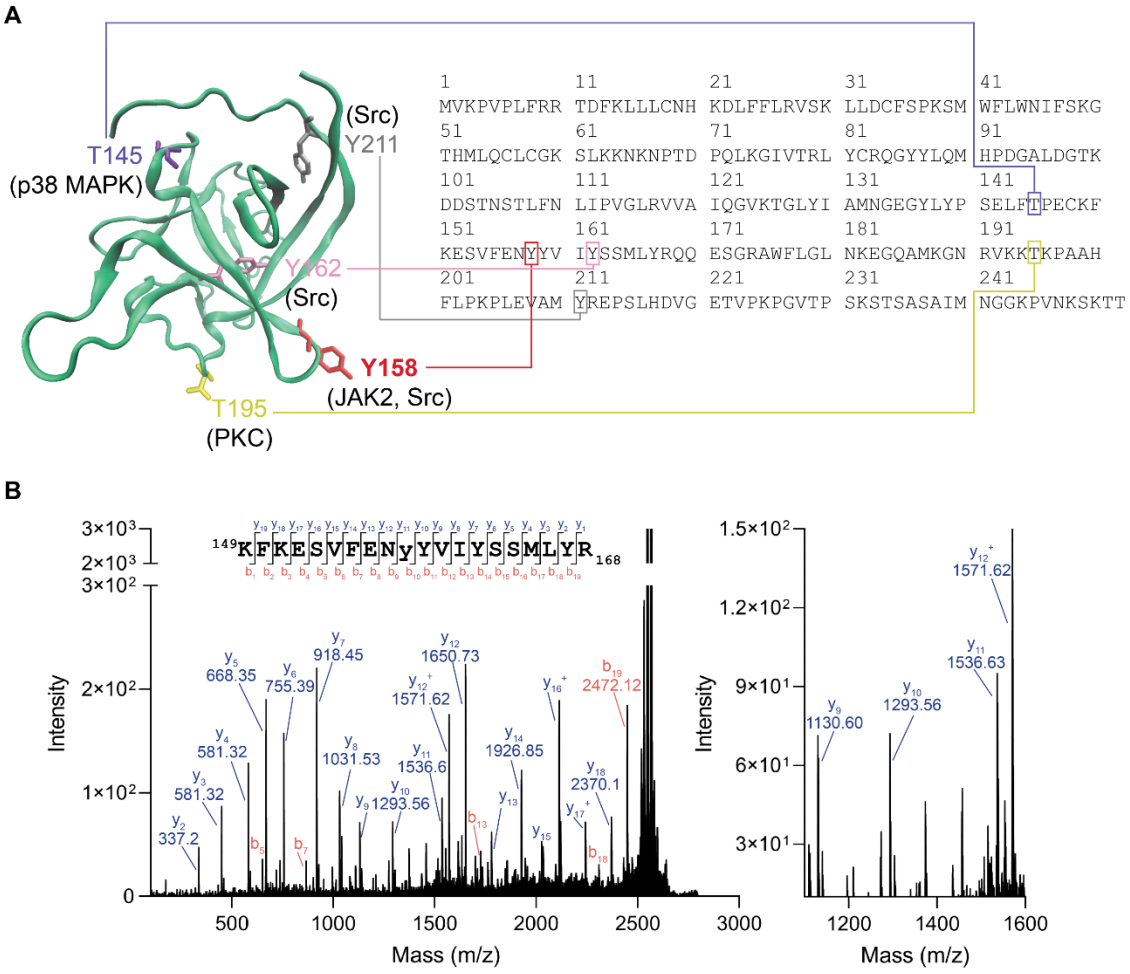

Figure 5.8. MALDI TOF-MS/MS validation of JAK2 phosphorylation of Y158 on FGF14.

(A) Homology model of an FGF14 monomer showing potential phosphorylation sites and their corresponding motif in the FGF14-1b sequence (accession number NP_787125). Y158, red, while Y162 is shown as purple. Also showing other predicted phosphorylation sites that are not at the protein:protein interaction interface, including T145, T195, and Y211. **(B)** MALDI TOF-MS/MS fragmentation spectrum of the phosphopeptide KFKESVFENyYVIYSSMLYR (y = phosphotyrosine), encompassing residues 149-168 of FGF14-1b. The presence of non-phosphorylated y10 (theoretical m/z of 1293.66, observed m/z of 1293.56) and y11 (theoretical m/z of 1536.69, observed m/z of 1536.63) ions confirms Y158 as the site of phosphorylation (1536.63-1293.56 = 243.07, corresponding to the MW of $Y(PO_3)$.

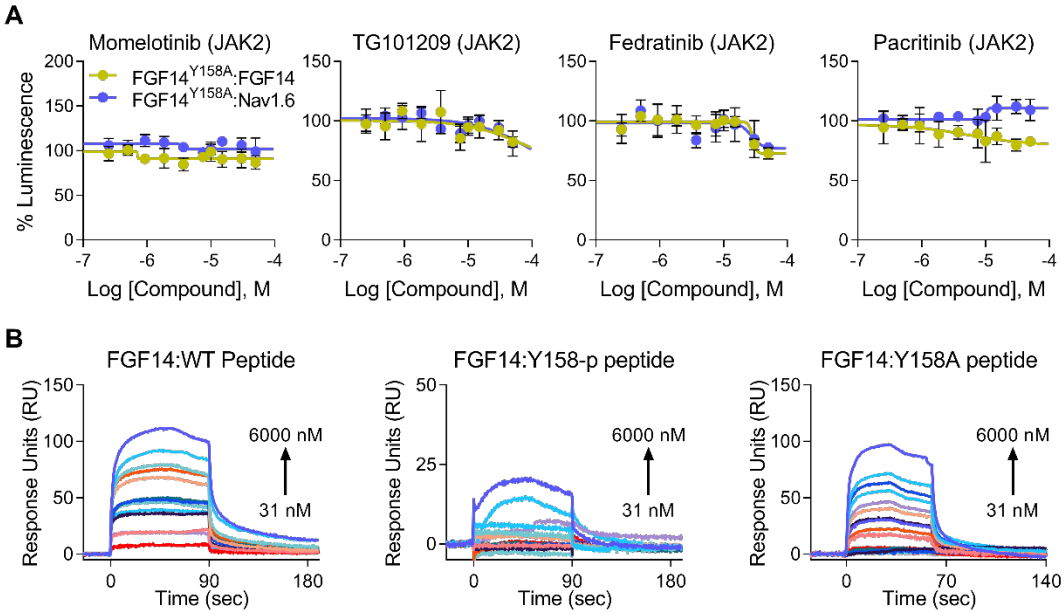

Figure 5.9. Y158 mediates both JAK2 regulation of FGF14, as well as high affinity dimerization.

A) Homology model of an FGF14 monomer showing potential phosphorylation sites and their corresponding motif in the FGF14-1b sequence (accession number NP_787125). Y158, red, while Y162 is shown as purple. Also showing other predicted phosphorylation sites that are not at the protein:protein interaction interface, including T145, T195, and Y211.(**B)** MALDI TOF-MS/MS fragmentation spectrum of the phosphopeptide KFKESVFENyYVIYSSMLYR (y = phosphotyrosine), encompassing residues 149-168 of FGF14-1b. The presence of non-phosphorylated y10 (theoretical m/z of 1293.66, observed m/z of 1293.56) and y11 (theoretical m/z of 1536.69, observed m/z of 1536.63) ions confirms Y158 as the site of phosphorylation (1536.63-1293.56 = 243.07, corresponding to the MW of Y(PO_3).

	K_D (μM)	k_{on} (M^{-1} s^{-1})	k_{off} (s^{-1})
$FGF14^{WT}$ Peptide	1.04	16500 ± 250	$4.47\times10^{-2} \pm 3.3\times10^{-4}$
$FGF14^{Y158\text{-}p}$ Peptide	146.7	297 ± 20	$8.42\times10^{-2} \pm 1.4\times10^{-3}$
$FGF14^{Y158A}$ Peptide	7.02	23820 ± 1300	$1.57\times10^{-1} \pm 1.6\times10^{-3}$

Table 5.6. Equilibrium and kinetic constants for FGF14 self-interaction by SPR.

Kinetic constants were calculated based on data represented in Figure 5B. The K_D represents the average between the kinetic K_D, calculated using the simplest Langmuir 1:1 interaction model ($K_D=k_{off}/k_{on}$), and the steady-state saturation (affinity) K_D. Note that fitting kinetic data for the phosphorylated peptide was difficult due to kinetic constants approaching limits of instrument detection, and thus the estimated values should be interpreted only qualitatively.

5.2.6. Y158 mediates both JAK2 regulation of FGF14, as well as high affinity FGF14 dimerization

To validate Y158 as the site for JAK2-dependent regulation of FGF14 and Nav1.6, an alanine point mutation (Y158A) was introduced in the CLuc-FGF14 LCA construct. This construct was used to compare the effect of JAK2 inhibition on the mutant FGF14:FGF14^{Y158A} heterodimer and FGF14^{Y158A}:Nav1.6 complexes to the corresponding FGF14 wild-type complexes (**Figure 5.7**). As expected, the effects of JAK2 inhibitors on both the FGF14:Nav1.6 complex and the FGF14:FGF14 dimer were abolished or reversed in the presence of FGF14^{Y158A} (**Figure 5.8A**), the site of JAK2 phosphorylation *in vitro*. As shown in **Table 5.4**, for the FGF14^{Y158A}:Nav1.6 complex, the effects of Momelotinib and Pacritinib were abolished, while those of TG101209 and Fedratinib were greatly reduced (78.0% and 76.8% luminescence, respectively, with these remnant inhibitory effects being observed only at much higher concentrations compared to FGF14^{WT} (i.e., Fedratinib IC_{50} shift from 9.7 μM to 27 μM). Similarly, the enhancing effect of JAK2 inhibitors on the FGF14:FGF14 dimer was reversed in the presence of FGF14^{Y158}, with high concentrations inhibiting dimerization by non-significant (Momelotinib) to moderate degrees (TG101209, Fedratinib, and Pacritinib). This may signify off-target effects due to the higher concentrations and IC_{50} values observed.

We next sought to determine how phosphorylation at Y158 changes FGF14 self-interaction (homodimerization) using SPR. Phosphorylated and non-phosphorylated peptides were flown across a chip with FGF14 bound (16,045 RU). All peptides were incubated with JAK2 kinase, but only the phospho-peptide sample received ATP. Following the phosphorylation reaction, peptides were buffer exchanged into SPR running buffer (HBS-P+). Kinetic analysis revealed completely different binding kinetics and vastly reduced binding affinity of the phosphorylated FGF14 peptide (K_D = 147 μM compared to 1.02 μM for the non-phosphorylated peptide) (**Figure 5.9B** and **Table 5.6**). Note that fitting kinetic data for the phosphorylated peptide was difficult due to kinetic

constants approaching limits of instrument detection, and thus the estimated kinetic constants should be interpreted only qualitatively. The reduced binding affinity of the Y158A peptide compared to the WT peptide demonstrates that Y158 is a key residue in mediating tight FGF14 homodimerization, as predicted by previous studies[50,75]. However, the binding kinetics are not fundamentally different compared to the WT peptide, confirming that other residues near Y158 are also important in mediating self-interaction.

5.2.7. Functional assessment of JAK2-mediated regulation of Nav1.6

To test Fedratinib modulatory effects on Nav1.6-mediated Na^+ currents, we used whole-cell patch-clamp electrophysiology of HEK293 cells stably expressing Nav1.6 (HEK-Nav1.6) that were transiently transfected with either *GFP (HEK-Nav1.6 GFP)* or *FGF14-GFP (HEK-Nav1.6 FGF14-GFP)*; each group was either treated with Fedratinib (20 μM from a stock solution dissolved in DMSO) or vehicle DMSO (**Figure 5.10**). In the HEK-Nav1.6 GFP cells pretreated with Fedratinib, the peak current density of Nav1.6-mediated transient Na^+ currents (I_{Na+}) was not statistically different (−59.43 ± 6.0 pA/pF, n=15*)* compared to DMSO treatment (−51.5 ± 3.69 pA/pF, n = 13, $p < 0.2848$; **Figure 5.10A-C**). In agreement with previous studies[50,58], expression of FGF14-GFP suppressed Nav1.6-encoded peak current density (−24.87 ± 2.99 pA/pF, n =16 vs. −59.43 ± 6.0 pA/pF, n = 15; $p < 0.0001$, student t test). In the presence of Fedratinib, the FGF14-mediated suppression of Nav1.6 current was rescued back to untreated control (−81.27 ± 11.3 pA/pF, n = 13; compared to DMSO treatment, −24.87 ± 2.99 pA/pF, n = 16, $p < 0.0001$; Student t test; **Figure 5.10C**). Further analysis revealed that in the HEK-Nav1.6 GFP category the decay time constant (τ) of I_{Na}^+ was not significantly affected by Fedratinib (1.3 ± 0.07 ms, n = 13) compared to vehicle (1.2 ± 0.05 ms, n = 10). However, τ was significantly slower in the FGF14-GFP group (1.6 ± 0.1 ms, n = 14*,* $p < 0.0052$ compared to the GFP control group, similar to as observed previously[50,58]) and Fedratinib

reversed this phenotype bringing it back to the GFP control level (1.4 ± 0.06 ms, n = 12, **Figure 5.10D** and **Table 5.7**).

As previously reported[46,50,58], in this study we also observed a depolarizing shift in the $V_{1/2}$ of activation of Nav1.6 in the FGF14-GFP group (−22.4 ± 1.1 mV, n = 12) compared to GFP control (−26.03 ± 1.1 mV, n = 14, $p < 0.0358$) and pretreatment with Fedratinib rescued this change (-26.03 ± 1.1 mV, n =14 for Nav1.6 vehicle vs. −30.56 ± 1.9 mV, n =13, $p < 0.0495$ for Fedratinib; **Figure 5.10E,G**). Likewise, expression of FGF14-GFP caused a depolarizing shift in $V_{1/2}$ of steady-state inactivation compared to the Nav1.6 GFP control group (−59.8 ± 0.5 mV, n = 12 vs Nav1.6 −62.6 ± 0.8 mV, n =11, $p < 0.0019$; **Figure 5.10F,H**) and pretreatment with Fedratinib rescued the change back to control (−30.56 ± 1.9 mV, n =13 vs. DMSO -26.03 ± 1.1 mV, n =14). The effect of Fedratinib on both activation and steady-state inactivation was specific for the FGF14-GFP group and absent in the GFP group (**Figure 5.10E-H, Table 5.7**).

Intracellular FGFs expressing the 1a N-terminal tail have been shown to induce Nav channel long-term inactivation (LTI), a slow inactivation process that controls channel availability over repetitive stimulation[174–176]. Following a 30 min incubation with either DMSO (0.01%) or Fedratinib (20 μM), LTI in all four experimental groups was evaluated using depolarizing steps (from -90 mV to -10 mV) spaced by 40 ms, a time interval that allows Nav channels to fully recover from fast inactivation. In GFP expressing cells Nav1.6 channels recovered nearly completely from LTI in control condition (DMSO, 0.01%) as well as in Fedratinib (**Figure 5.10I,J**). Interestingly, in the presence of FGF14 the fraction of Nav1.6 channels that underwent LTI was significantly lower than control resulting in potentiated I_{Na}^{+} over the course of the depolarization cycles (1.6 ± 0.1, n = 14 vs. Nav1.6 control 1.2 ± 0.05, n = 10, $p < 0.05$ to $p < 0.0001$ (pulses 2-4), Student t test; **Figure 5.10I,J**). Notably, pretreatment with Fedratinib rescued the phenotype back to the GFP control level (**Figure 5.10I,J**), suggesting that phosphorylation of FGF14 by JAK2 is required for regulation of slow inactivation of Nav1.6.

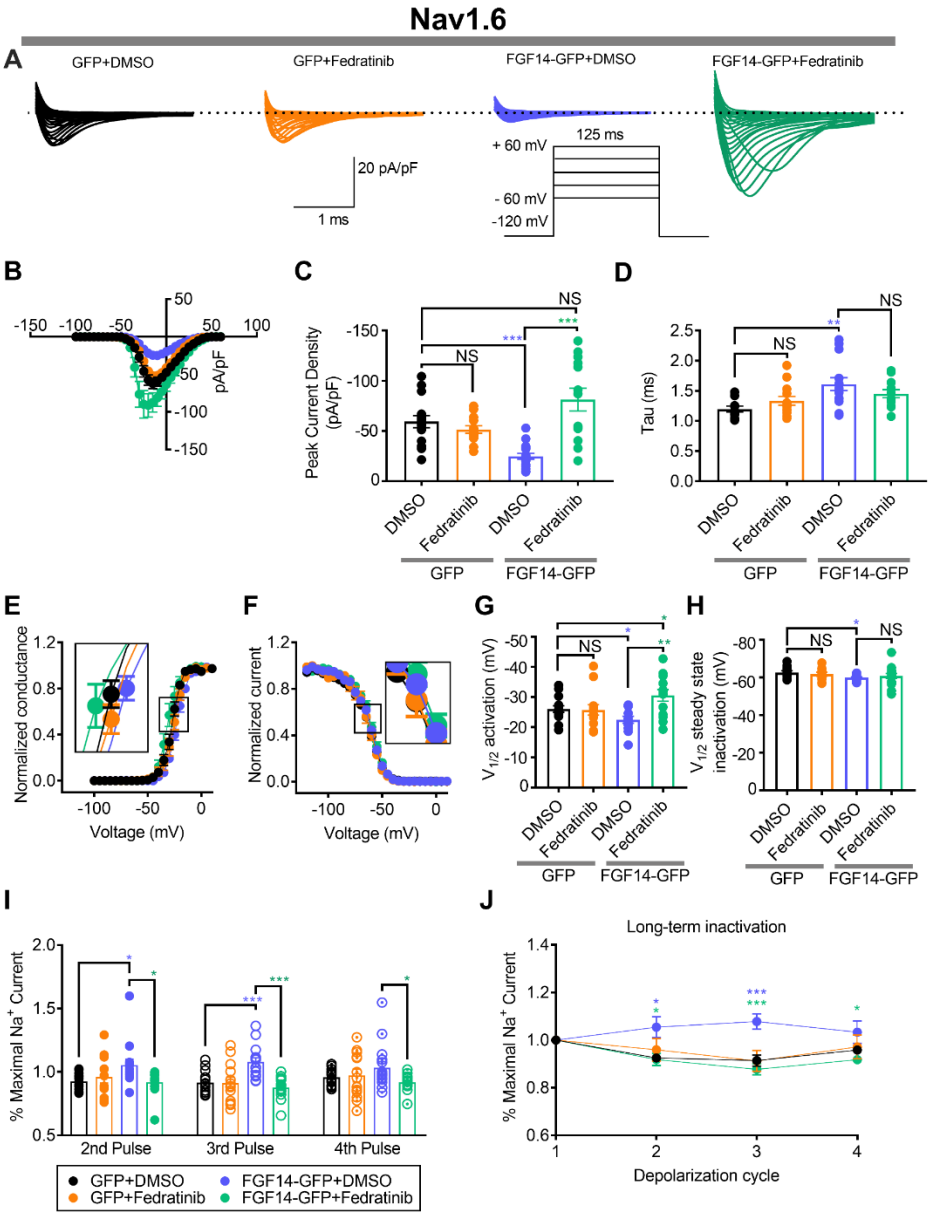

Figure 5.10. JAK2 inhibition abolishes FGF14-dependent modulation of Nav1.6 currents.
(**A**) Representative traces of Na+ transient currents (INa^+) recorded from HEK-Nav1.6 cells transiently expressing the indicated constructs in response to depolarizing voltage steps. (B) Current-voltage relationships of Ina+ from experimental groups described in (A). (C) Peak-current densities at -10 mV derived from A and B. (D) bar graph of tau of fast inactivation calculated at the peak current density (-10 mV) in the indicated experimental group in (A). (E) Nav1.6 channel conductance was plotted as a function of the membrane potential (mV) and used to extrapolate voltage-dependence of activation. (F) Steady-state inactivation was measured using a two-step protocol, and values were plotted as a function of the membrane potential (mV). Shifts in the voltage-dependence of activation and steady-state inactivation are shown in the two insets in E and F. (G) Bar graph of V1⁄2 of activation (H) Bar graph of V1⁄2 of steady-state inactivation. (I,J) Bar graph showing second, third and fourth depolarizing pulses used to study long-term inactivation (I) and corresponding summary plot (J) from the experimental groups described in (G). (*) indicates statistical differences between the GFP (black) and the FGF14-GFP (blue) groups in DMSO, while (*) indicates statistical differences in the same experimental groups in the presence of Fedratinib. Data are mean ± SEM. The statistical significance between the groups was assessed using Student's t-test; ***, p<0.0001, **, p<0.001, *, p<0.05.

Condition	Peak density	Activation	K_{act}	Steady-state Inactivation	K_{inact}	Tau (τ)
	pA/pF	mV	mV	mV	mV	ms
GFP (DMSO)	-59.4 ± 6.0 (15)	-26.03 ± 1.1 (14)	3.5 ± 0.2 (12)	-62.6 ± 9.0 (12)	7.1 ± 0.4 (12)	1.2 ± 0.05 (10)
GFP (Fedratinib)	-51.5 ± 3.7 (13)	-25.7 ± 1.7 (13)	3.9 ± 0.2 (12)	-61.7 ± 1.0 (15)	6.0 ± 0.4 (11)	1.3 ± 0.07 (13)
FGF14-GFP (DMSO)	-24.9 ± 3.0 (16)[a]	-22.4 ± 1.1 (12)[c]	4.7 ± 0.2 (10)[f]	-59.8 ± 6.0 (12)[h]	6.3 ± 0.4 (12)	1.6 ± 0.1 (14)[j]
FGF14-GFP (Fedratinib)	-81.3 ± 11.3 (13)[b]	-30.5 ± 1.9 (13)[d,e]	2.8 ± 0.3 (11)[g]	-60.8 ± 1.2 (16)	5.9 ± 0.6 (14)	1.4 ± 0.06 (12)

Table 5.7. Effect of Fedratinib on Nav1.6-mediated currents in the presence of FGF14.
[a] $P < 0.0001$, unpaired t tests compared to Nav1.6-GFP (DMSO); data are mean ± SEM.
[b] $P < 0.0001$, unpaired t tests compared to FGF14-GFP (DMSO); data are mean ± SEM.
[c] $P < 0.0358$, unpaired t tests compared to Nav1.6-GFP (DMSO); data are mean ± SEM.
[d] $P < 0.0019$, unpaired t tests compared to Nav1.6-GFP (DMSO); data are mean ± SEM.
[e] $P < 0.0495$, unpaired t tests compared to FGF14-GFP (DMSO); data are mean ± SEM.
[f] $P < 0.0017$, unpaired t tests compared to Nav1.6-GFP (DMSO); data are mean ± SEM.
[g] $P < 0.0001$, unpaired t tests compared to Nav1.6-GFP (DMSO); data are mean ± SEM.
[h] $P < 0.0144$, unpaired t tests compared to Nav1.6-GFP (DMSO); data are mean ± SEM.
[i] $P < 0.0052$, unpaired t tests compared to Nav1.6-GFP (DMSO); data are mean ± SEM.

5.3. DISCUSSION

Our results build on previous studies showing that the Nav1.6 channel complex, a fundamental determinant of neuronal firing, is regulated by phosphorylation. We have previously conducted smaller scale screening campaigns[46,49,100] that identified multiple Ser/Thr kinases, including Akt/PI3K, PKC, and GSK3β, as regulators of the FGF14:Nav1.6 complex. Follow-up studies supported these results and demonstrated extensive regulation of Nav complexes by GSK3β, controlling neuronal excitability in both diseased and healthy states[80], in part through direct phosphorylation of FGF14 at S226, as well as both the Nav1.2[93] and Nav1.6[65] channel isoforms. While these initial discoveries laid the groundwork for the present studies, prior campaigns suffered from the following limitations: *i*) small scale screening library (~385 kinase inhibitors), resulting in lack of significant target overlap between inhibitors (i.e, only 1-2 compounds/target); *ii*) kinase target representation was neither complete nor fully distributed (i.e., preference toward

Ser/Thr over Tyr kinase inhibitors; not all known kinases were represented, such as multiple tyrosine kinases); and *iii*) lack of initial rapid counter-screening studies to explore potential mechanisms, such as comparison of target effects on the FGF14:FGF14 vs FGF14:Nav1.6 complexes.

Here, we screened ~3,000 well-studied compounds and FDA-approved kinase inhibitors with diverse mechanisms and an extremely wide range of targets covering the majority of the known "kinome." The high degree of target overlap between the three screened libraries, in addition to a small degree of compound overlap (i.e., identical compound from different sources), was used as a measure of reproducibility to increase confidence in results. For instance, multiple hits targeting a common kinase, combined with similar effects being observed for the same compound across libraries, lends strong support toward that kinase being a true regulator rather than artefacts arising from inhibitor promiscuity. We selected hits through a serial selection pipeline that combined both unbiased and hypothesis-based criteria. Following exclusion of toxic compounds, "hits" were initially selected using binary Z-score and % luminescence cut-offs. Hits were then clustered by primary target, and we identified those targets with the highest proportion of hits to total number of screened compounds (**Table 5.2**), resulting in the identification of JAK2 and Src tyrosine kinases as the highest-ranking candidates. Additional high-ranking targets also corroborated findings of our previous studies that demonstrated a role of the GSK3, Akt/PI3K, NF-kB, and PKC pathways as regulators of the Nav channel[49]. Based upon these rankings, in addition to the identified phospho- and binding-motifs in the FGF14 sequence (**Table 5.3**) for corresponding kinases such as p38 MAPK, MEK, JAK2, STAT3, and Src, we selected hits for initial concentration-dependency studies (**Figures 5.4, 5.5**). This important step identified true "hits" demonstrating ideal concentration dependency behavior, separating these from compounds yielding linear dependency (often indicative of promiscuity), and we observed numerous structurally diverse JAK2 and Src inhibitors.

Following target analysis and initial concentration-dependency studies, hits were counter-screened to determine the effect of these pathways on FGF14:FGF14 dimerization. Similar to secreted FGFs, intracellular FGFs retain the ability to dimerize[44,50]. While dimerization of secreted FGFs is the essential molecular step for activation of transmembrane FGF receptors[177], the biological role of iFGF dimerization is unknown. Homodimerization of iFGFs is supported by structural evidence and homology model-guided mutations in cells, with FGF13 and FGF12 homodimers having been resolved using X-ray crystallography[44,67]. These crystallography studies also demonstrated a significant overlap between the PPI interfaces of FGFs with a variety of Nav channel isoforms mediated by the iFGF core domain, but did not investigate points of structure-function divergence between the iFGF:iFGF homodimer and iFGF:Nav complex interfaces. We have recently begun to investigate this area using a combination of in-cell assays, site directed mutagenesis and electrophysiology[50,75], and the present study builds on these findings by demonstrating the importance of a single residue in dynamically regulating the equilibrium between protein:protein complexes.

During the initial FGF14:FGF14 homodimer counter-screening, differential regulation of the homodimer vs FGF14:Nav1.6 complex species was only observed for inhibitors targeting JAK2. We hypothesize that in the cell milieu an increase in FGF14 dimerization would “sequester” monomeric FGF14, such that less monomeric FGF14 is available to bind the Nav1.6 C-terminal tail. While the two assays presented separately measure FGF14:Nav1.6 or FGF14:FGF14 binding, the FGF14 dimer is predicted to exist in both systems. For the FGF14:Nav1.6 assay, it would exist as a dimer of CLuc-FGF14:CLuc-FGF14, yielding no luminescence in the presence of luciferin; increases in this dimer would reduce the FGF14 available for binding to CD4-Nav1.6-NLuc, thereby reducing reconstituted luciferase enzyme capable of generating luminescence. Although this hypothesis cannot be directly tested using the specific LCA constructs presented here,

the high-throughput nature of said assays makes them ideal tools for hypothesis generation and guiding subsequent validation studies.

While JAK2 inhibitors resulted in increased stability of the FGF14:FGF14 dimer and inhibition of the FGF14:Nav1.6 complex, Src kinase inhibitors were largely only effective on the FGF14:Nav1.6 complex, resulting in only moderate inhibition of the FGF14 dimer, and only at high concentrations. However, phosphomotif scanning and prediction algorithms identified potential JAK2 and Src phosphorylation sites at two adjacent residues, Y158 and Y162, within an overlapping SH2 domain (**Table 5.3** and **Figure 5.8A**), and thus we hypothesized that both of these kinases could play important, albeit distinct, regulatory roles. Both Y158 and Y162 are at the β-9 sheet of FGF14 that mediates dimerization and interaction with the Nav1.6 channel. However, while Y158 is a bona fide hot-spot at the interface of both complexes[50], Y162 is buried in the β-9 sheet at a position more distal from the PPI interface, largely sequestered toward the FGF14 core by hydrophobic interactions, and is not within the 8 Å distance (> 12 Å) required for defining the residue as a hot spot (**Fig 5.3**). In addition, Y158, along with the adjacent site V160, was previously shown to mediate structure-function properties of the FGF14:FGF14 dimer and FGF14:Nav1.6 complex PPI interface[50]. Results from expanded concentration-dependency studies with repurchased JAK2 and Src inhibitors supported the findings of the counter-screening, and SPR demonstrated that phosphorylation by JAK2 altered FGF14 homodimerization kinetics to a much greater extent than phosphorylation by Src. Thus, both Src and JAK2 kinases might transduce physiologically distinct mechanisms with variable effects on FGF14 species depending on upstream signaling stimulus. Although the mechanisms of Src-mediated changes were not further studied here, the importance of Y158 in JAK2-dependent regulation of FGF14 was subsequently confirmed by observing phosphorylation of this site *in vitro* using mass-spectrometry, as well as Y158A mutagenesis studies (**Figures 5.8, 5.9**).

By providing evidence for differential effects of Y158 modification on the two FGF14 complexes, this study strengthens the hypothesis of two structurally related, but distinct PPI interfaces at the FGF14 surface, and provides new insight into how dimeric vs monomeric iFGFs might differentially function in cells. The FGF14:FGF14 homodimer and FGF14:Nav1.6 complexes were previously thought to largely share a common PPI interface. However, we show initial evidence for a single JAK2-dependent phosphorylation event that destabilizes the prior while promoting the latter. Thus, one plausible prediction is that if in close proximity to its targets, activation of JAK2 could shift the FGF14 dimer equilibrium toward free monomeric FGF14 available to bind the Nav1.6 C-terminal tail (**Fig. 5.11**), resulting in drastic changes to Nav channel function. This could be the mechanism for rapid and efficient modulation of Nav channel function in response to extracellular signals transduced through transmembrane receptors.

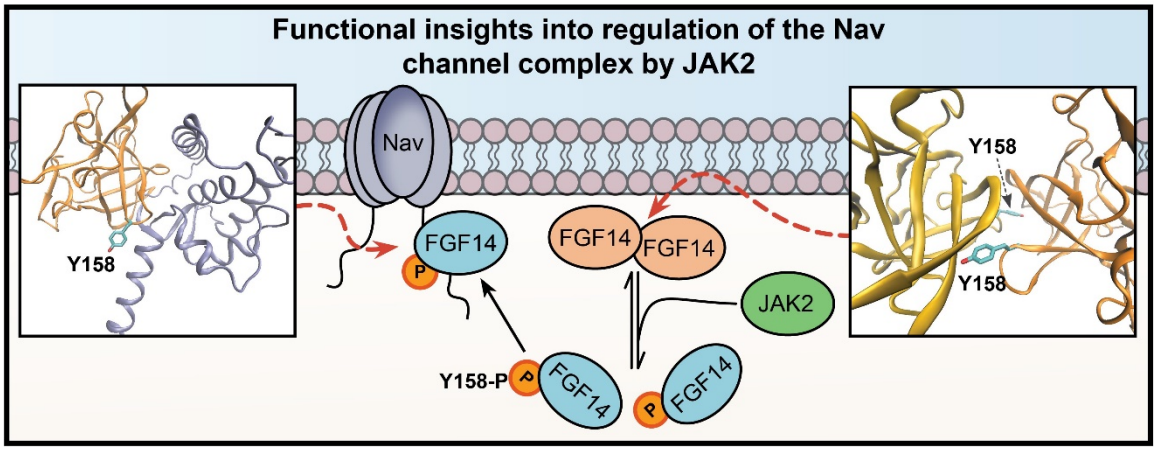

Figure 5.11. Overview of JAK2-mediated regulation of FGF14 and Nav1.6 based on results of this study.

Cartoon representation of interactions, and homology model showing the proximity of Y158 to the PPI interfaces of both the FGF14:Nav1.6 complex and FGF14:FGF14 homodimer.

The C-terminal tail of Nav channels is the primary binding site of the iFGFs[44,50,111]. However, evidence for modulation of Nav channel inactivation by iFGFs have spurred the idea that other contacts also exist outside those between the channel C-terminal tail and the iFGFs core domain. The prevailing hypothesis is that the flexible N-terminal tail of the iFGFs-1a isoforms and of FGF14-1b (which, unlike other iFGF isoforms, possesses a unique 60 aa N-terminal tail) might protrude into channel domains distal to the C-terminal tail and more proximal to the plasma membrane. The Nav channel intracellular III-IV loop, located in close proximity to the channel pore and referred to as the inactivation loop, is a postulated interacting site for the N-terminal tail of iFGFs[176]. However, whether such putative interaction with the inactivation loop is mediated by an iFGF monomer or heterodimer (i.e., FGF14:Nav1.6 complex) is unclear. In addition, studies have shown that the pore-forming Nav α subunits assemble and function as dimers[178], which could potentially accommodate two iFGF molecules per channel C-terminal tail forming a larger macromolecular complex beneath the plasma membrane.

When applied to cells expressing the Nav1.6 channel and FGF14, the JAK2 inhibitor Fedratinib normalized previously described FGF14-dependent phenotypes of Nav1.6 currents[50,58]. Those included modulation of peak-current density, voltage-dependence of activation and steady-state inactivation, as well as channel fast inactivation. In the presence of the JAK2 inhibitor, the suppression of Na^+ transient currents induced by FGF14 was rescued to the control condition (Nav1.6 channels expressed along with GFP). Likewise, FGF14 was found to slow channel entry into fast inactivation (tau), to cause a depolarizing shift in both voltage-dependence of activation and steady-state inactivation and Fedratinib rescues all these phenotypes back to control. The effect on FGF14 on Nav1.6 long-term inactivation, which leads to potentiation of Na^+ currents during repetitive stimulation, is also fully reversed by Fedratinib. As no functional effect of Fedratinib was observed on Nav1.6 channels when FGF14 was not present, we concluded that JAK2 affects Nav channel function only indirectly. By favoring FGF14 homodimerization,

Fedratinib effectively reduces the available pool of free FGF14 (monomeric) and thereby inhibits FGF14-dependent modulation of Nav channels, consistent with regulation of transport of channels to the plasma membrane[93] (supported by the changes in peak current density) as well as other complex modulatory roles likely mediated by the FGF14 N-terminal tail on Nav1.6 biophysical properties.

JAK2 is a non-receptor (protein) tyrosine kinase and is largely studied as part of the JAK/STAT pathway. Like other kinases in the same family, JAK2 serves as the catalytic signaling component for a wide range of transmembrane receptors, including those for interleukins, interferons, growth hormone, erythropoietin, and leptin[179], to contribute to physiological processes ranging from cell survival to inflammation. However, the specific role of JAK2 in neurons has been less well studied[165]. Recent evidence has shown that through activation of the STAT3 transcription factor, JAK2 plays a role in regulating apoptosis following white matter injury[180], as well as in leptin-mediated neuroprotective effects following cerebral ischemia[181]. Links have also been shown between inactivation of the JAK2-STAT5 signaling pathway and elevation of brain-derived factor (BDNF) expression in experimental models of depression-like behaviors[182].

Extending on the role of BDNF in synaptic plasticity, recent evidence has been provided for a role of JAK-STAT signaling in activity-dependent long-term depression (LTD) of CA1 synapses. Interestingly, unlike synaptic plasticity elicited by stimulation of the CA3 Schaffer collaterals, LTD induced in CA1 neurons by stimulation of extrahippocampal temporoammonic inputs requires rapid gene transcription and is dependent upon glutamate receptor internalization mediated by JAK2 activation and subsequent STAT3-driven gene transcription. In another recent study, BDNF/TrkB reduction was found associated with gene transcription upregulation, δ-secretase activity, and Aβ and Tau alterations in murine brains through activation of neuroinflammatory pathway in a JAK2/STAT3-dependent manner[183]. While the implications of JAK2 regulation of FGF14 are at present unknown, the wide spectrum of signal transduction

pathways associated with JAK2 in neurons support the idea that FGF14 phosphorylation by JAK2 could be involved in a variety of physiological processes and pathway cross-talks ranging from BDNF-dependent synaptic plasticity to neuroinflammatory signaling in the brain. BDNF-dependent synaptic plasticity and neuronal homeostasis are intimately linked to neuronal excitability[184], so it is plausible that by regulating the equilibrium between FGF14 species, JAK2 might enable neurons to dynamically adjust firing in response to transmembrane receptor signaling as part of a homeostatic regulatory loop.

Chapter 6. Rational design of FGF14:Nav1.6 inhibitors using peptidomimetics derived from FGF14

Portions of this chapter were published in *Bioorganic & Medicinal Chemistry Letters* as:

Identification of Peptidomimetics as Novel Chemical Probes Modulating Fibroblast Growth Factor 14 (FGF14) and Voltage-Gated Sodium Channel 1.6 (Nav1.6) Protein-Protein Interactions

Zhiqing Liu.[1], **Paul Wadsworth** [2], Aditya K. Singh, Haiying Chen, Pingyuan Wang, Oluwarotimi Folorunso, Pietro Scaduto, Syed R. Ali, Fernanda Laezza, and Jia Zhou

[2] **These two authors contributed equally to this work**

ABSTRACT

The voltage-gated sodium (Nav) channel is the molecular determinant of action potential in neurons. Protein-protein interactions (PPI) between the intracellular Nav1.6 C-tail and its regulatory protein fibroblast growth factor 14 (FGF14) provide an ideal and largely untapped opportunity for development of neurochemical probes. Based on a previously identified peptide FLPK, mapped to the FGF14:FGF14 PPI interface, we have designed and synthesized a series of peptidomimetics with the intent of increasing clogP values and improving cell permeability relative to the parental lead peptide. In-cell screening using the split-luciferase complementation (LCA) assay identified ZL0177 (**13**) as the most potent inhibitor of the FGF14:Nav1.6 channel complex assembly with an apparent IC_{50} of 11 μM. Whole-cell patch-clamp recordings demonstrated that ZL0177 significantly reduced Nav1.6-mediated transient current density and induced a depolarizing shift of the channel voltage-dependence of activation. Docking studies revealed strong interactions between ZL0177 and Nav1.6, mediated by hydrogen bonds, cation-π interactions and hydrophobic contacts. All together these results suggest that ZL0177 retains some key features of FGF14-dependent modulation of Nav1.6 currents. Overall, ZL0177 provides a chemical scaffold for developing Nav channel modulators as pharmacological probes with therapeutic potential of interest for a broad range of CNS and PNS disorders.

6.1. INTRODUCTION

We previously identified fibroblast growth factor 14 (FGF14) as an intracellular modulator of Nav channels, observed distinct and opposing regulatory roles of FGF14 isoforms on Nav1.2 and Nav 1.6 function, and resolved critical amino acid residues at the FGF14:Nav1.6 interface through mutation studies. FGF14 modulates amplitude and voltage dependence of Na^+ currents through direct interaction with the intracellular Nav channel C-tail[44,46,74]. Thus, probes capable of modulating this highly specific PPI interface might lead to fine-tune regulation of electrical activity in the CNS and PNS and serve as scaffolds for therapeutic development. Here, we present chemical modifications of a short peptide Ac-FLPK-$CONH_2$ (aka. FLPK) that we previously characterized[75] as an FGF14 inhibitor mapped to its PPI surface, and selected one variant, ZL0177, as a novel peptidomimetic with improved chemical profiles and demonstrated that it is functionally active against Nav1.6 mediated currents.

6.2. RESULTS

6.2.1. Peptide Synthesis and Screening

The partition coefficient of the molecule between an aqueous and lipophilic phase (logP), usually water and octanol, determines a molecule's lipophilicity that is crucial for passive membrane permeability[58,185–188]. The parent tetrapeptide FLPK has a predicted clogP value of 0.9 (calculated by ALOGPS) which is not favorable for crossing the cell membrane. The N- (R^1), C-terminal (R^3) and free NH_2 (R^2) in lysine are critical sites to improve clogP of parental peptide. Thus, we designed three series of new peptides through truncation (tripeptides) with diverse functional groups to maintain proper molecule weight, introducing hydrophobic protective groups (tetrapeptide) and incorporating non-peptide small molecules (**Table 6.1**). Compared to FLPK, all compounds have improved clogP values that indicate enhanced permeability. The synthetic route exampled by peptides **7**~**8**

and **11**~**13** is depicted in Scheme 1. (*tert*-Butoxycarbonyl)-*L*-leucyl-*L*-proline (**22**) and methyl N^6-(((9*H*-fluoren-9-yl) methoxy)carbonyl)-*L*-lysinate (**23**) were coupled in the presence of HBTU, HOBt and DIPEA to give tripeptide **7** in a quantitative yield. Boc was removed under TFA leading to **8** which is coupled with (*tert*-butoxycarbonyl)-*L*-phenylalanine to produce tetrapeptide **11**. Compound **12** was obtained through eliminating the protective group of **11**, and subsequent acetylation of **12** generated peptide **13** in a yield of 93%. All the peptides were synthesized in a similar fashion, and their structures were confirmed by ^{1}H NMR, ^{13}C NMR and HR-MS. Compounds **1** and **14** were explored previously[75], and are included herein as controls, because the parental peptide does not work in this cellular assay due to its poor cell permeability.

All newly designed and synthesized peptidomimetics were first evaluated using the LCA. Peptidomimetics were dissolved in DMSO and delivered to transfected cells via dilution in cell medium to a final concentration of 50 μM in 0.5% DMSO. Interestingly, the luminescent response was slightly enhanced by treatment with several compounds in series I (tripeptides) and series III (incorporation of non-peptide scaffolds), while compounds of series II (tetrapeptides) tended to inhibit complex formation compared to treatment with 0.5% DMSO alone (**Fig. 6.1A**). Significant enhancers identified include compounds **4**, **5**, **6**, and **12** (148.7 ± 9.2%, 142.3 ± 11.8%, 126.5 ±7.8%, and 124.1 ± 7.0%, respectively; $p < 0.05$), and significant inhibitors identified include compounds **13**, **14**, and **17** (67.9 ± 6.1%, 71.9 ± 5.6%, and 66.5 ± 5.4%, respectively; $p < 0.05$). These screening results were validated by testing peptidomimetics against the full-length luciferase (reporter) to ensure that luminescence changes did not arise from modulation of luciferase enzymatic activity alone, and no significant effects were observed (**Fig. 6.1B**).

Based on the LCA results and taking clogP values into consideration (Figure 1C), we selected compounds **13** and **17** as potential inhibitors, and **4**, **5** as potential enhancers for further validation. Compound potency and efficacy were subsequently assessed using a 5-point dose response (1, 10, 25, 50, and 100 μM), and percent luminescence (normalized

to 0.5% DMSO) is plotted in Figure 1D. Compounds **4** and **5** did not display a reasonable dose-dependent response, while compounds **13** and **17** exhibited a sigmoidal dose-response inhibition curve, with apparent IC_{50} values of 11 and 16 μM, respectively (Figure 1_SI). Additionally, these compounds were validated using the lactate dehydrogenase (LDH) cytotoxicity assay to ensure that changes in cell viability were not responsible for changes in luminescence response (**Fig. 6.1E**). Only compound **4** demonstrated significant toxicity.

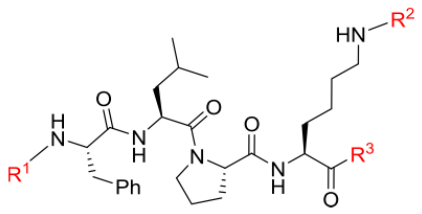

Series	Codes	Sequence	clo
Parent	–	FLPK	0.9
Tri-peptide	**1**	Cbz-FLP-NH_2	2.1
	2	Cbz-FLK(Boc)-NH_2	3.3
	3	Boc-LPK(Boc)-NH_2	2.0
	4	PLK(Boc)-NH_2	1.8
	5	LPK-NH_2	1.3
	6	Ac-PLK(Boc)-NH_2	2.1
	7	Boc-LPK(Fmoc)-OMe	4.6
	8	LPK(Fmoc)-OMe	3.2
	9	Ac-LPK(Fmoc)-OMe	3.6
	10	Cbz-FLP-OMe	3.0
Tetra-peptide	**11**	Boc-FLPK(Fmoc)-OMe	5.4
	12	FLPK(Fmoc)-OMe	4.1
	13	Ac-FLPK(Fmoc)-OMe	4.8
	14	Cbz-FLPK(Boc)-NH_2	3.5
	15	Ac-FLPK(Boc)-OH	2.2
	16	FLPK(Boc)-NH_2	1.9
	17	Bz-FLPK(Boc)-NH_2	3.3
Incorpo-ration[b]	**18**	R^1 = Ac, R^2 = Boc; R^3 = Morpholine	2.5
	19	R^1 = Ac, R^2 = Boc; R^3 = Ph	3.6
	20	R^1 = Ac, R^2 = Boc; R^3 = 2-thiazol	2.9
	21	R^1 = Ac, R^2 = H; R^3 = Ph	2.6

[a] http://www.vcclab.org/lab/alogps/start.html.
[b] Incorporation of non-peptide scaffold into FLPK.

Table 6.1 Sequences and clogP values of newly designed peptidomimetics.

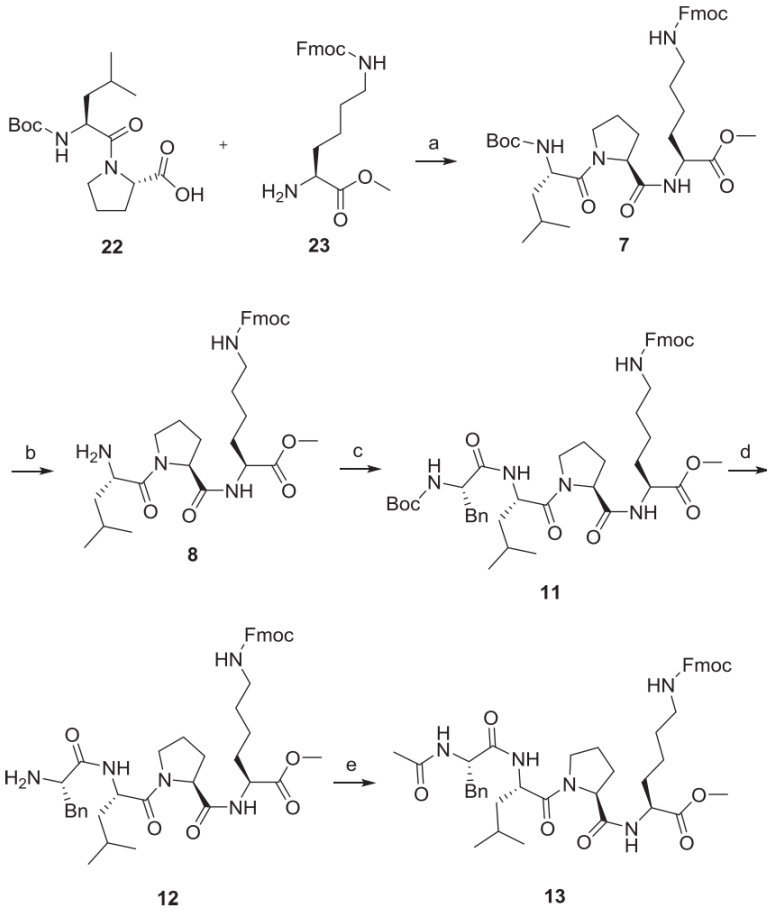

Scheme 6.1. Synthetic route of 7~8 and 11~13.
Reagents and conditions: (a) HBTU, HOBt, DIPEA, DCM, rt., quant.; (b) TFA, DCM, rt., 87%; (c) (*tert*-butoxycarbonyl)-*L*-phenylalanine, HBTU, HOBt, DIPEA, DCM, rt., 81%; (d) TFA, DCM, rt., quant.; (e) CH_3COCl, Et_3N, DCM, rt., 91%..

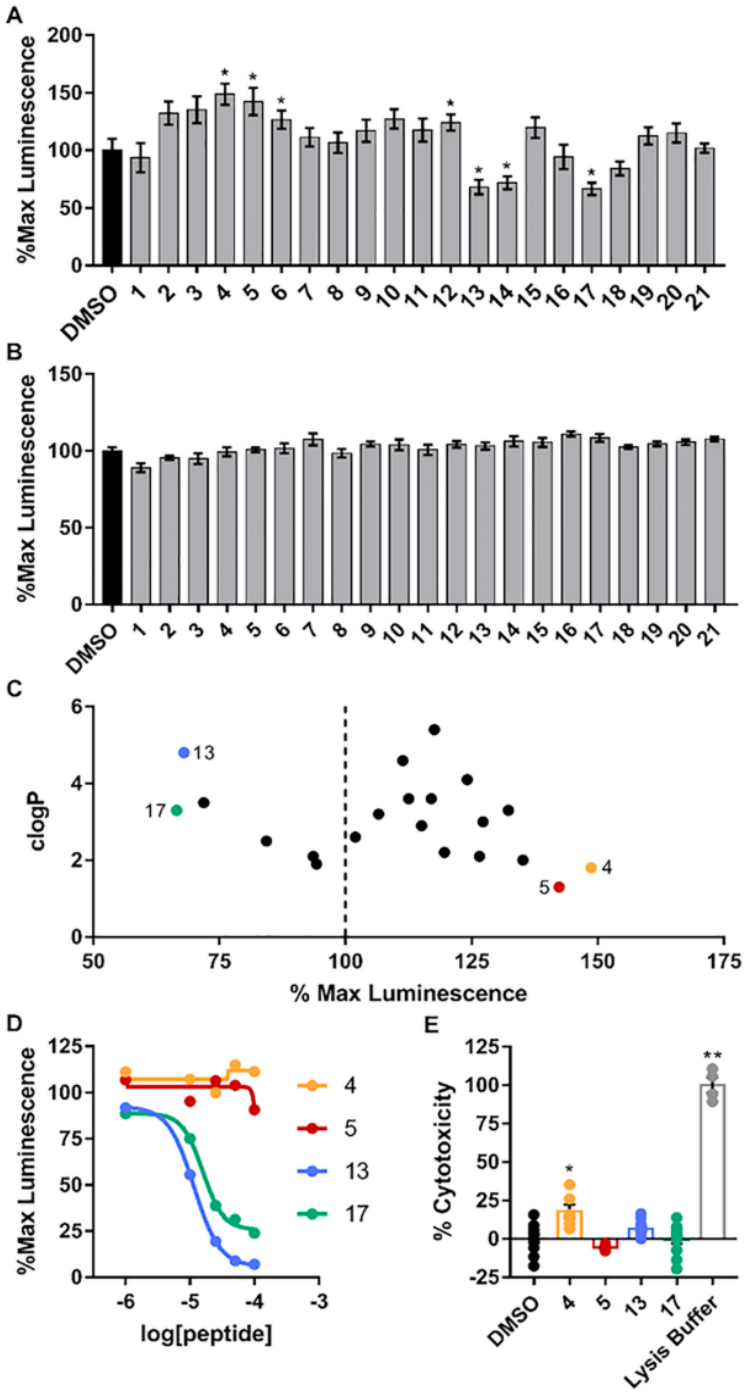

Figure 6.1. LCA screening of peptidomimetics.

A, B) Bar graphs of % maximal luminescence values derived from HEK293 cells stably expressing CLuc-FGF14 and CD4-Nav1.6-NLuc constructs using LCA (A) or transiently transfected with the full-length photinus luciferase (B) treated with either vehicle (0.5% DMSO) or compounds (final concentration = 50 μM). C) Comparison of peptidomimetic clogP values and % max luminescence responses. The top two inhibitors and enhancers (Compounds 4, 5, 13, and 17) were selected for further evaluation. D) LCA-based dose-response of compounds 4, 5, 13 and 17 in cells stably expressing CLuc-FGF14 and CD4-Nav1.6-NLuc. E) Bar graph of % cytotoxicity as measured using the LDH cytotoxicity assay of selected compounds at the concentration of 50 μM. Data are mean ± S.E.M. *, $p < 0.05$; **, $p < 0.001$.

6.2.2. Functional Validation of Peptidomimetics

To functionally validate the identified top peptidomimetic (compound **13**; ZL0177), we performed whole-cell patch-clamp electrophysiology of HEK293 cells stably expressing Nav1.6 (HEK-Nav1.6) (**Fig. 6.2**). In HEK-Nav1.6 cells pretreated for 1 h with ZL0177 (10 μM), Nav1.6-mediated peak density derived from transient Na^+ current (I_{Na}) was significantly lower (-26.65 ± 6.3 pA/pF) compared to DMSO treatment (-54.88 ± 7.4 pA/Pf,; **Fig 6.2C,D**). Further analysis revealed that ZL0177 slowed the transition of the channel from the open to the inactive state in HEK-Nav1.6 cells (2.05 ± 0.3 ms) compared to DMSO control group in (1.18 ± 0.1 ms, **Fig. 6.2B,E**). These results suggest that ZL0177 is able to mimic FGF14-induced suppression of Nav1.6 currents and effect on tau of fast inactivation[58]. This finding is different from ZL0181, which requires the presence of FGF14[58].

Effects of ZL0177 on $V_{1/2}$ of activation and steady-state inactivation were investigated. ZL0177 induced a 26.37 ± 1.5 (12) mV (DMSO) to 19.2 ± 1.3 (9) depolarizing shift ($p < 0.05$) of $V_{1/2}$ of activation (**Fig. 6.3A,B**), while it displayed no effects on $V_{1/2}$ of steady-state of inactivation (**Fig. 6.3C,D**). Furthermore, ZL0177 exhibited no effects on long-term inactivation of Nav1.6 channels (**Fig. 6.3E,F**).

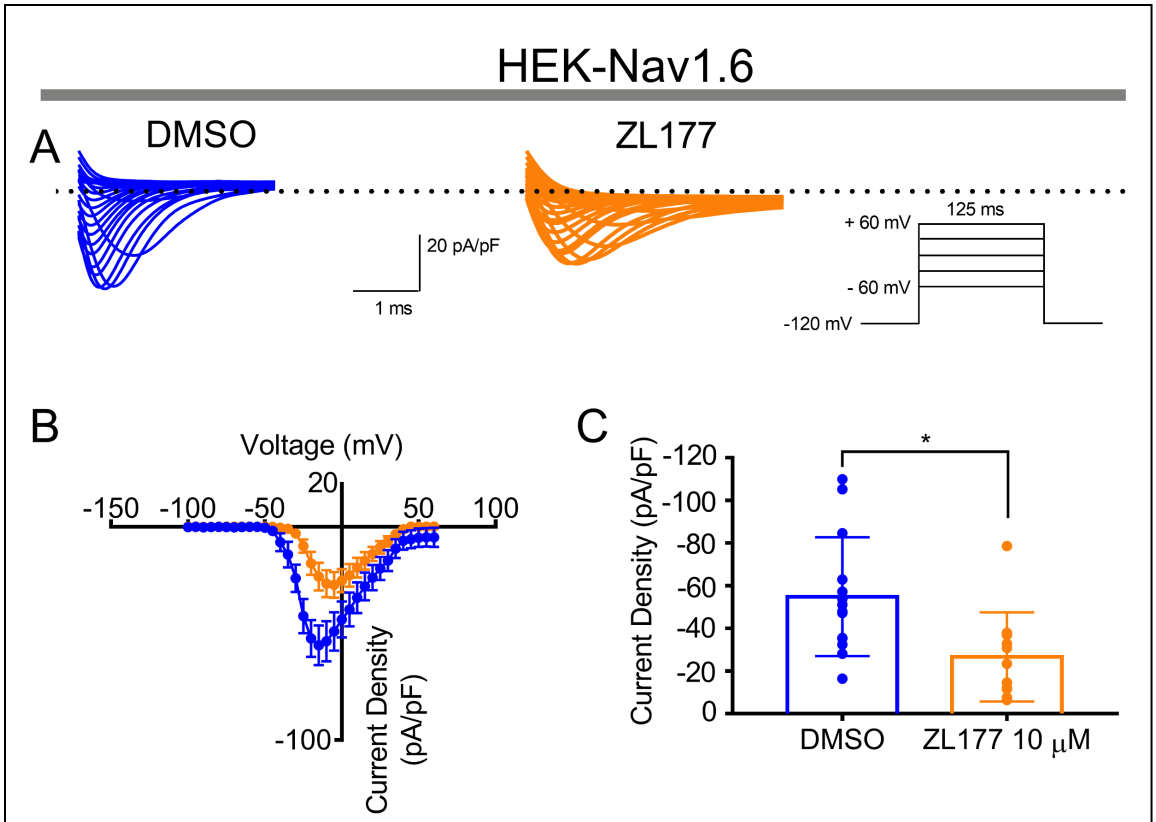

Figure 6.2. Peptidomimetic 13 (ZL0177) modulates Nav1.6 mediated Na^+ currents..

(A) Representative traces of Nav1.6-mediated transient Na^+ currents (I_{Na^+}) recorded from HEK-Nav1.6 stable cells treated with either DMSO (0.02%; blue) or ZL0177 (10 μM; orange) in response to voltage steps from -120 mV to +60 mV from a holding potential of -70 mV (inset). (B) Representative traces of experimental groups described in A in which tau (τ) of transient I_{Na^+} was estimated from a one-term exponential fitting function (red dotted line). (C) Current-voltage relationships of transient I_{Na^+} from experimental groups described in A and B. (D) Summary bar graph of peak current densities derived from C. (E) Summary bar graph of tau calculated at -10 mV in the indicated experimental groups. Data are mean ± S.E.M. *, $p < 0.05$..

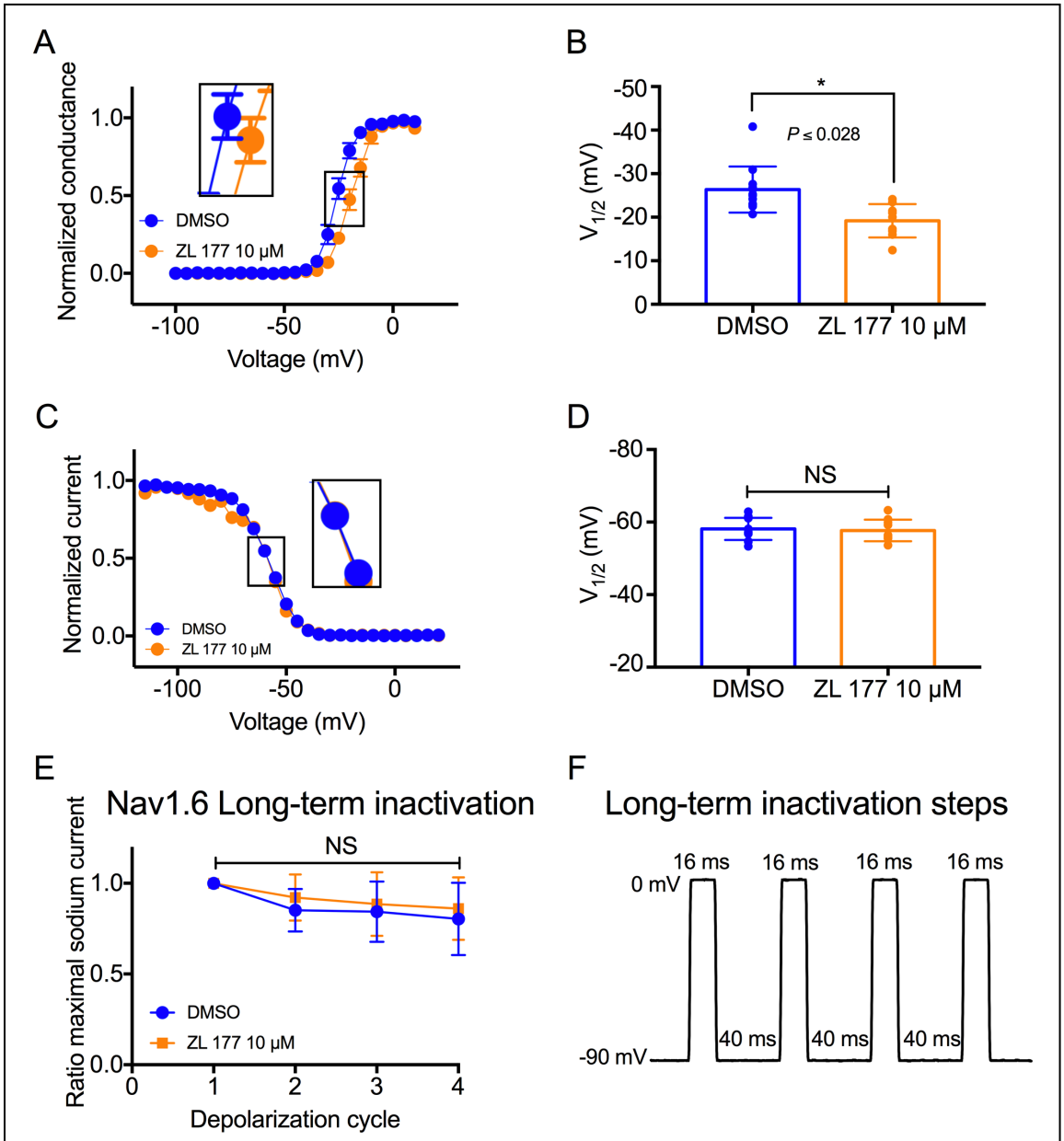

Figure 6.3. ZL0177 leads to a depolarizing shift in voltage-dependence of Nav1.6 channel activation.

(A) Representative traces of Nav1.6-mediated transient Na^+ currents (I_{Na}^+) recorded from HEK-Nav1.6 stable cells treated with either DMSO (0.02%; blue) or ZL0177 (10 μM; orange) in response to voltage steps from -120 mV to +60 mV from a holding potential of -70 mV (inset). (B) Representative traces of experimental groups described in A in which tau (τ) of transient I_{Na}^+ was estimated from a one-term exponential fitting function (red dotted line). (C) Current-voltage relationships of transient I_{Na}^+ from experimental groups described in A and B. (D) Summary bar graph of peak current densities derived from C. (E) Summary bar graph of tau calculated at -10 mV in the indicated experimental groups. Data are mean ± S.E.M. *, $p < 0.05$..

6.2.3. Docking

We next performed a docking study using the FGF14:Nav1.6 homology model (**Figure 6.4**) to characterize the specific structural features that may enable ZL0177 binding. ZL0177 docked into the interface of the Nav1.6 C-tail (**Figure 4A**), and it occupies a large and flat surface of Nav1.6 and forms critical hydrogen bonds with residues Arg1866, Asp1833 and Arg1891. Tri-peptides may be not big enough to occupy the whole surface. The hydrogen bond between O atom of acetyl group explains why compounds 12 and 16 are less active. Additionally, the phenylalanine moiety on the N-terminal of ZL0177 has a cation-π interaction, and the Fmoc group on the C-terminal is surrounded by hydrophobic and aromatic interactions with Phe1873, Tyr1883 and His1843. R3 group (For ZL0177, it is OMe) surrounded by Phe 1873 and Arg1866. The limited space appears to be not large enough to accommodate phenyl, thiazole or morpholine rings (compounds 18~21). The overlay of ZL0177 with the FGF14:Nav1.6 homology model illustrates that ZL0177 mimics the critical regions (two loops highlighted in red) at the interface of FGF14. In previous studies, we have reported that mutation of two FGF14 residues, Tyr158

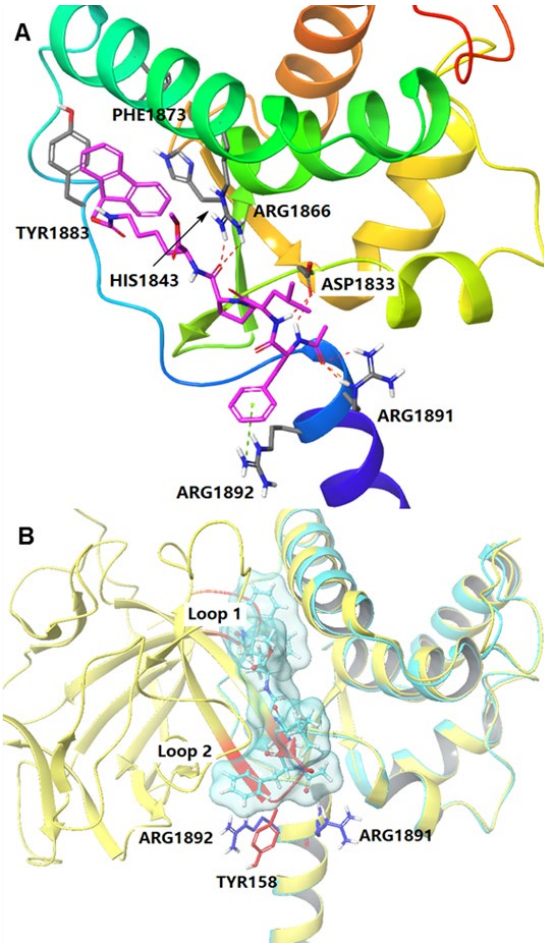

Figure 6.4. Docking of compound 13 with the Nav1.6 homology model.

A) Ribbon representation of docking studies on peptidomimetic **13** (magenta) with Nav1.6 C-tail homology model. Residues PHE1873, TYR1883, HIS1843, ARG1866, ASP1833, ARG1891 and ARG1892 were highlighted in grey. Hydrogen bonds are highlighted by red dash line and cation-π interaction is indicated in green dash line. **B**) Overlay of FGF14/Nav1.6 homology model (yellow) with compound **13** docked into Nav1.6 (light blue). Two important loops containing TYR158 of FGF14 were highlighted in red. ARG1891 and ARG1892 were colored in blue.

and Val160, impaired FGF14:Nav1.6 complex formation and prevented FGF14-dependent modulation of Nav1.6 currents[50]. Therefore, these results suggest that ZL0177 plays the role of Tyr158 and Val160 to interact with the Nav1.6 C-terminal.

6.3. CONCLUSIONS

In summary, we have designed, synthesized, and investigated a batch of cell permeable peptidomimetics based on the previously identified parental lead peptide FLPK. Among those, ZL0177 displayed potent *in vitro* activity in disrupting the PPI between FGF14:Nav1.6 with an in cell IC_{50} value of 11 μM. Importantly, ZL0177 is capable of modulating the biophysical properties of Nav1.6 currents, mimicking previously reported modulatory effects of FGF14 on Nav1.6 currents[50,58]. Docking studies revealed multiple interactions between ZL0177 and the Nav1.6 C-tail including hydrogen bonds, cation-π interactions and hydrophobic contacts. Overlay study indicated that ZL0177 mimics the critical loop of FGF14 that encompass Tyr158 and Val160, two previously identified hot-spots at the FGF14:Nav1.6 channel interface. Further investigations on ZL0177 are underway to determine target specificity and usefulness of this compound as an *in vivo* probe and therapeutic potential in the CNS and PNS.

Chapter 7. High-throughput screening of small molecule libraries to identify new probes targeting the FGF14:Nav1.6 PPI interface

ABSTRACT

Ion channel macromolecular complexes play a critical role in regulating and finely tuning neuronal firing. Minimal disturbances to these tightly controlled protein:protein interactions (**PPI**) can lead to persistent maladaptive plasticity of brain circuitry. However, these PPI interfaces are highly specific and provide ideal targets for drug development, especially in the CNS where selectivity and specificity are vital for limiting side effects. We present the initial results of a high-throughput drug screening (**HTS**) campaign targeting the PPI interface of the voltage-gated Na^+ (**Nav**) channel 1.6 and its regulatory protein, fibroblast growth factor 14 (**FGF14**). The FGF14:Nav1.6 complex is enriched in medium spiny neurons in the nucleus accumbens, and therefore compounds targeting this complex could bring about a new class of anti-depressants or mood stabilizers. Following assay optimization in 384-well plates, we conducted an in-cell HTS against the FGF14:Nav1.6 complex using the split-luciferase complementation assay (**LCA**). We screened ~45,000 small molecules and rationally-designed drug-like analogues, and compounds were ranked using Z-scores, % luminescence, and B-scores. A fluorescence-based cell viability assay was conducted in parallel, and potentially toxic compounds were excluded ($Z \leq -3$). We initially identified ~1000 hits, 640 of which failed during validation re-screening (n=3), and an additional 149 were identified as false positives based on counter-screening against luciferase ($Z \leq -3$ or $Z \geq 3$). The remaining 168 hits were then stratified by structural and chemical properties including predicted permeability (logP), and dose-dependency was assessed for compounds with the greatest potential for blood-

brain barrier permeability. We repurchased and tested 26 promising candidates, and hits were then ranked based upon their potency (EC_{50}/IC_{50}) and efficacy. Estimated in-cell IC_{50} for inhibitors ranged from 0.95 to 15 μM, while estimated EC_{50} for enhancers ranged from 0.65 to 1.21 μM. Cell-free orthogonal screenings including surface plasmon resonance (SPR) and protein thermal shift (PTC) were subsequently used to assess hit binding affinity, and *in silico* docking was used to predict potential binding sites. Lead hits were confirmed as functionally active modulators of Nav1.6 currents and neuronal firing from MSNs in the nucleus accumbens.

7.1. INTRODUCTION

Voltage-gated Na^+ (Nav) channels form macromolecular complexes that play a critical role in regulating and finely tuning neuronal firing. Minimal disturbances to these tightly controlled protein:protein interactions (**PPI**) can lead to persistent maladaptive plasticity of brain circuitry. PPI interfaces are highly specific and provide ideal targets for drug development, especially in the CNS where selectivity and specificity are vital for limiting side effects. The complex between Nav1.6 and its regulatory protein, fibroblast growth factor 14 (FGF14), is enriched in medium spiny neurons (**MSNs**) in the nucleus accumbens (**NAc**), and FGF14 dysfunction has been associated with spinocerebellar ataxia, neuropsychiatric disorders (depression, schizophrenia, bipolar disorder), and neurodegeneration, making it an excellent CNS drug target.

Using the robust in-cell assay developed in Chapter 4, here we present initial results from a high-throughput screening (HTS) campaign targeting the PPI interface of the FGF14:Nav1.6 complex. We screened ~45,000 small molecules and rationally-designed drug-like analogues in 384-well plates, and hits were initially selected using a combination of Z-scores, B-scores, and % luminescence. Initial hit validation studies, including counter-screening, cheminformatics, and dose dependency (potency, efficacy), yielded 16 inhibitors and 4 enhancers of the FGF14:Nav1.6 complex. Repurchased compounds were assessed for binding to FGF14 and Nav1.6 proteins using biophysical approaches, and top candidates are now being functionally validated as modulators of Nav1.6 currents and neuronal firing from MSNs in the NAc.

7.2. RESULTS

7.2.1. High-throughput screening and initial hit selection

We have previously developed and reported an in-cell, high-throughput assay that can be used to identify and characterize small molecule inhibitors and enhancers of the FGF14:Nav1.6 PPI[100]. This adapted form of the luciferase complementation assay (LCA) is based on the double stable HEK293 cell line expressing recombinant CLuc-FGF14 and CD4-Nav1.6 C-tail-NLuc proteins developed in Chapter 4. Similar to as in Chapters 4 and 5, these cells were seeded in 384-well plates containing compounds at a screening concentration of 30 μM (n = 1 compound per well; 320 compounds/plate), as well as negative controls (0.3% DMSO, n = 16; cells alone, *n* = 8 wells), inhibitory positive controls (MNS, concentration range: 2.5 – 30 μM, *n* = 24), and enhancer positive controls (TNF-α, *n* = 16).

Using this method, we screened 44,480 compounds from the ChemBridge DIVERSet-1 (30,080 compounds) and Maybridge HitFinder Collection (14,400 compounds) over 139 plates. Plate and batch effects were monitored through assessment of Z'-factor (Z') and a per plate concentration gradient of the inhibitory positive control (**Fig. 7.1**), as described in Chapters 2-4. A total of 23 plates were repeated due to suboptimal Z' values or significant plate effects. Overall, Z' values fell within an acceptable range for a cell-based assay (mean ± SD: inhibitor Z', 0.62 ± 0.12; enhancer Z': 0.65 ± 0.14), demonstrating the ability of our assay to distinguish both enhancers and inhibitors of the FGF14:Nav1.6 complex from background signal.

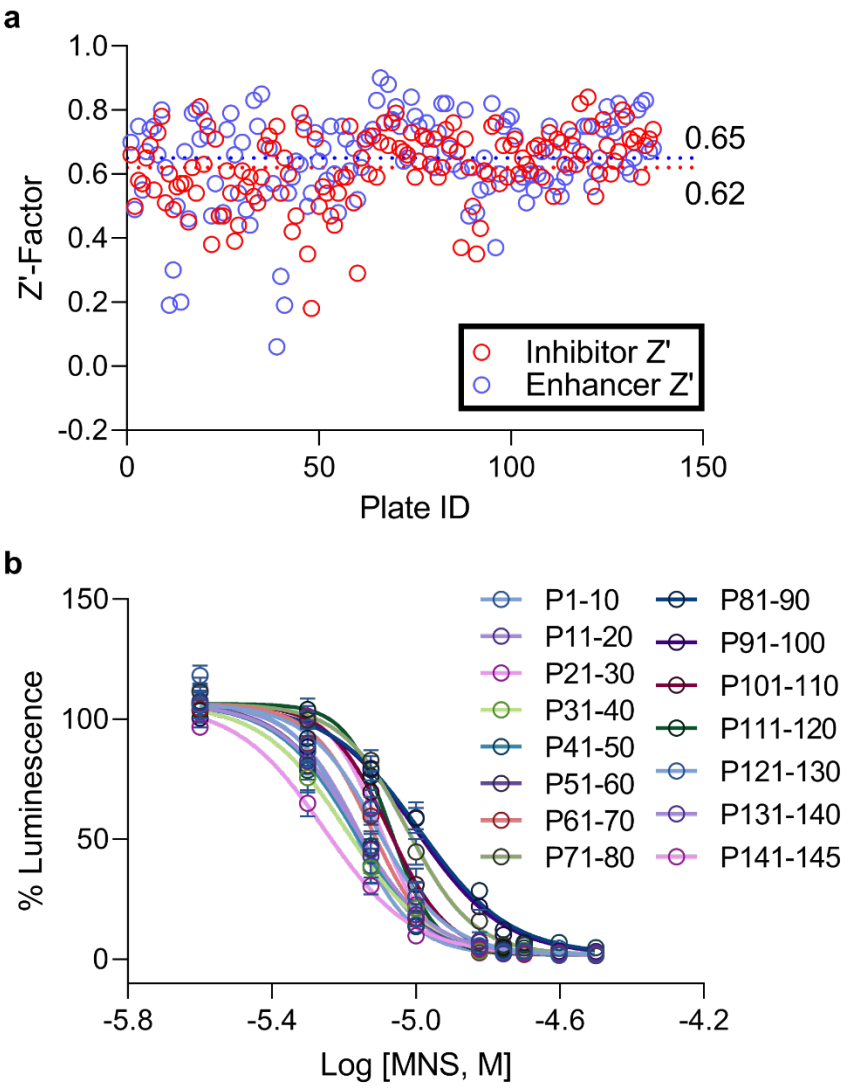

Figure 7.1. Results from the luminescence-based high-throughput screening against FGF14:Nav1.6 C-tail.

A) Z'-Factor (Z') for each screened library plate, calculated using either the inhibitor (red) or enhancer (blue) positive controls as described previously[45]. A total of 139 plates were screened, including 94 from Chembridge and 45 from Maybridge for a total of 44,480 compounds. Overall, Z' values fell within an acceptable range for a cell-based assay (mean ± SD: inhibitor Z', 0.62 ± 0.12; enhancer Z': 0.65 ± 0.14), demonstrating the ability of our assay to distinguish both enhancers and inhibitors of the FGF14:Nav1.6 complex from background signal. B) Nonlinear regression fitting for the per plate concentration gradient of the inhibitor positive control (range: 2.5 – 30 μM). for each batch of 10 plates. Luminescence for each well was normalized to on-plate 0.3% DMSO controls (n = 16 per plate), and the mean normalized luminescence ± SEM for each batch of 10 plates is shown.

Following exclusion of toxic compounds, two unbiased methods were used to select hits (**Fig. 7.2**): The first method (1) used a combination of percent maximal luminescence (Cut-offs: enhancers: % lum ≥ 170%; inhibitors: % lum ≤ 40%) and Z-scores (Cut-offs: enhancers: Z ≥ 4; inhibitors: Z ≤ -5), which were both calculated using on-plate controls (0.3% DMSO, n = 16 per plate); this method identified 1,185 hits (847 inhibitors, 338 enhancers), and the highest-ranking 960 compounds moved forward. The second method (2) used B-scores (Enhancers: B ≥ 12; Inhibitors: Z ≤ -14), which were calculated using an algorithm that accounted for plate and batch effects irrespective of per plate controls[113]. The method identified 337 hits (215 inhibitors, 122 enhancers), of which 113 met the prior method's hit selection criteria. Thus, the remaining 224 hits identified through this method were moved forward.

This combined set of 1,184 initial hits were then rescreened in triplicate (n = 3 wells over 3 independent plates) using the LCA, and the results for the Z-score hits are shown in **Figure 7.3A**. The top 544 compounds (comprised of 513 inhibitors, 31 enhancers) were then counter-screened against the full-length *p. pyralis* luciferase enzyme in transiently transfected HEK293 cells to identify false positives that act on luciferase rather than the FGF14:Nav1.6 complex. Using cut-offs of Z ≥ -3, this assay identified 152 false positives (148 from Z-score set, 4 from B-score set) that were excluded from further studies (**Fig 7.3B**). The remaining 392 compounds were then stratified by structural and chemical properties including predicted permeability (logP), and those compounds exhibiting undesirable moieties (i.e., PAINS, violation of Lipinski's Rule of 5) were excluded.

Additionally, we compared the chemical similarity of screened compounds to assess similarity between hits (**Fig. 7.4**), and analyses are still on-going to determine what chemical moieties may confer inhibitory or enhancer properties against the FGF14:Nav1.6 complex.

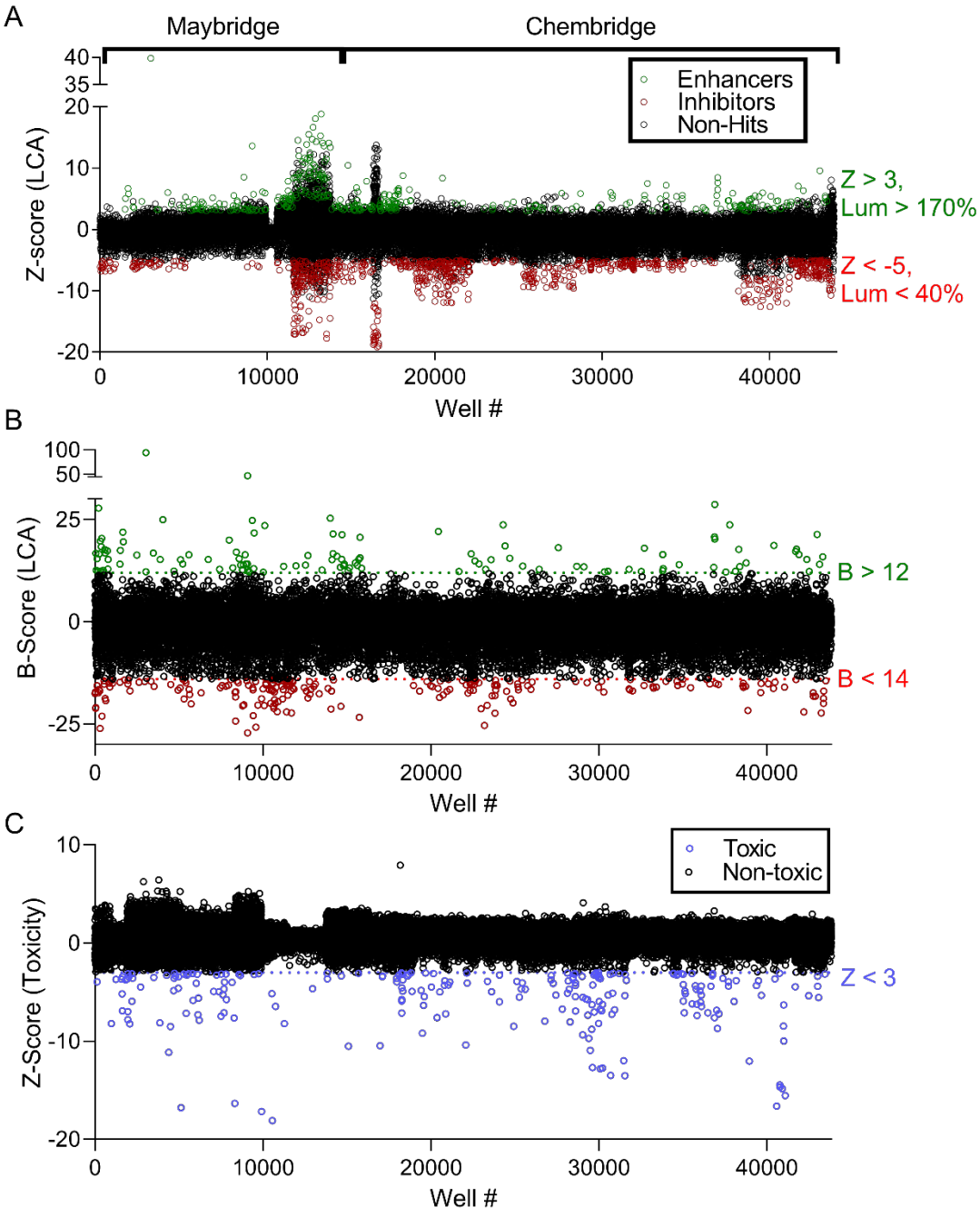

Figure 7.2. Screening LCA and toxicity assay results for the Maybridge and Chembridge libraries.
A,B) Plots of Z-scores and B-scores generated from LCA results for all screened compounds. C) Plot of Z-scores generated from CTB toxicity assay results for all screened compounds.

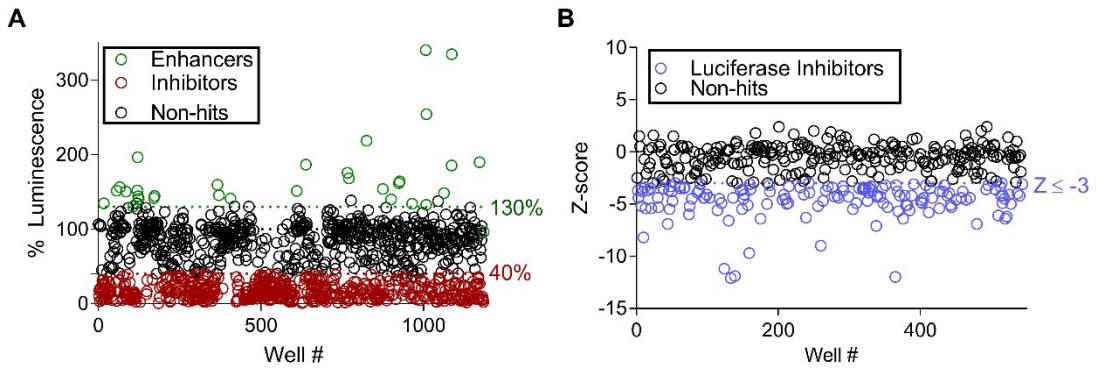

Figure 7.3. Identification and validation of hits.

A) Scatter plot of 1,184 preliminary hits that were re-screened in triplicate showing average % maximal luminescence (normalized to DMSO). Hits taken to the next stage were determined by a combination of Z-score (≥3 for enhancers, ≤-4 for inhibitors) and relative luminescence (≥ 130% for enhancers, ≤ 40% for inhibitors). (B) The remaining 544 compounds from (A) were validated by full-length luciferase assay, and Z-scores are shown for all compounds. A total of 152 compounds which significantly inhibited luminescence (Z ≤-3; shown as purple) from the full-length luciferase were eliminated at this stage.

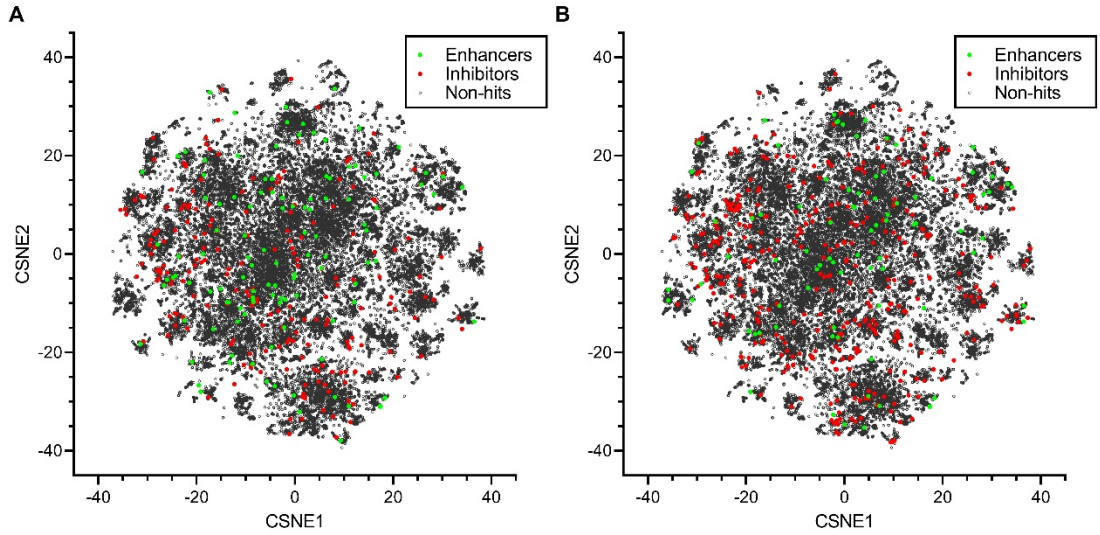

Figure 7.4. Analysis of structural similarity between hits

A) 337 hits identified by B-scores. C) 320 remaining hits following rescreening confirmation of Z-score hits.

7.2.2. Confirmation and evaluation of hit dose-dependency in cells

An 8-point dose response (n=4 per concentration) was conducted using LCA for the top 50 compounds with the greatest potential for blood-brain barrier permeability. In-cell concentration dependency was then assessed using the screening library compounds: 70 inhibitors (40 from the Z-score set, 30 from the B-score set), and 23 enhancers (15 from the Z-score set, 8 from the B-score set) (**Fig. 7.5**).

Based on potency (EC_{50}/IC_{50}) and efficacy, we repurchased 22 of the 93 compounds according to commercial availability, estimated potency and efficacy, and structural diversity. These were then tested using an expanded 10-point dose response (n=8 per concentration). For inhibitors, estimated in-cell IC_{50} ranged from 0.95 µM – 35.3 µM, while EC_{50} values ranged from 0.77 – 11 µM, as shown in **Table 7.1**

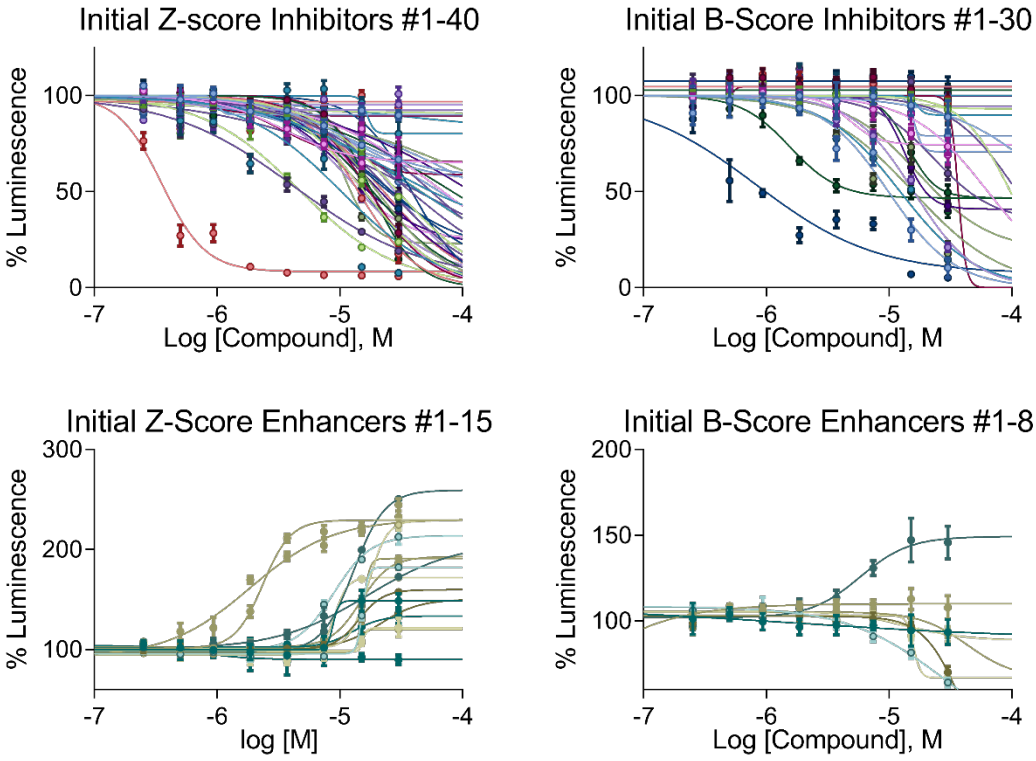

Figure 7.5. Identification and initial confirmation of hits.

As selected through chemoinformatic analysis, the top 55 compounds identified by Z-scores and the top 38 compounds identified through B-scores were validated using 8-point dose responses (n = 4 per concentration over two independent 384-well plates). Top, inhibitors. Bottom, enhancers. Luminescence for each well was normalized to on-plate 0.3% DMSO controls (n=16 per plate), and the mean normalized luminescence ± SEM is shown.

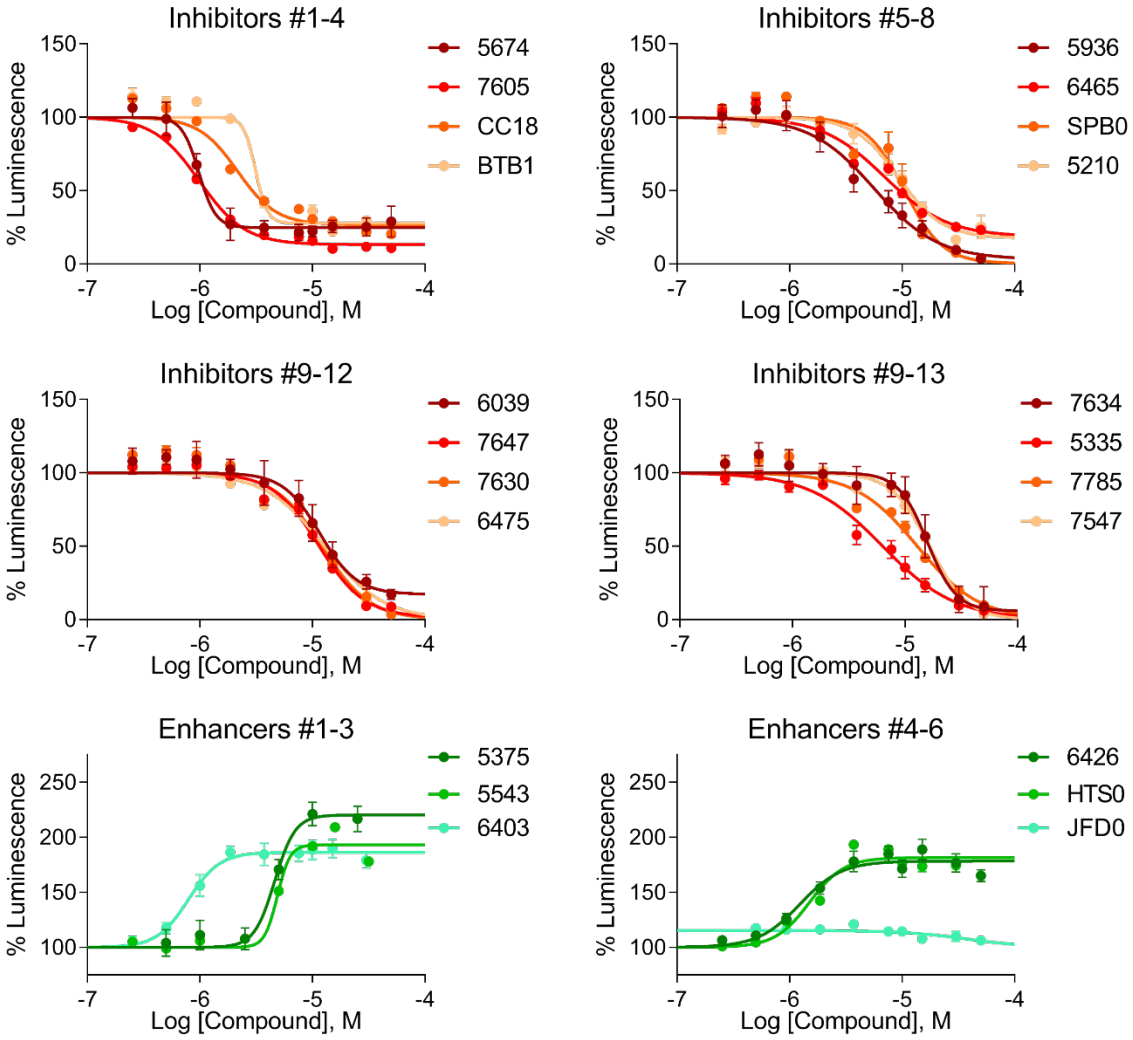

Figure 7.6. Fresh powder dose responses of top 22 repurchased hits in-cell using LCA.

The top 22 compounds (inhibitors, red; enhancers, green), selected through potency/efficacy analysis of initial dose responses were repurchased and validated using expanded 10-point dose responses (0.25 – 50 μM; n=8 per concentration over two independent 384-well plates). Luminescence for each well was normalized to per plate 0.3% DMSO controls (n=16 per plate), and the mean normalized luminescence ± SEM is shown.

7.2.3. Biophysical validation

These hits were then validated by orthogonal screening *in vitro* using the protein thermal shift (PTS) assay (**Fig 7.7**) and surface plasmon resonance (SPR) (**Fig. 7.8, 7.9**) and to determine compound binding affinity to purified FGF14 and Nav1.6 C-tail protein. Recombinant human FGF14 and Nav1.6 C-tail proteins were overexpressed in BL21 E. coli and purified using affinity chromatography (Heparin, Cobalt), ion exchange chromatography (SP-FF, Q-FF), and gel filtration (Superdex 200). Proteins were immobilized to CM5 chips (FGF14 = 17,800 RU, Nav1.6 C-tail = 6,800 RU) using amine coupling with the Biacore T100 for surface plasmon resonance (SPR) to determine binding affinity. The protein thermal shift (PTS) assay was conducted in 96-well plates (2 μg protein/well) using the QS3 rtPCR system for additional validation of hit binding.

For FGF14, all hits by PTS also displayed measurable binding affinity by SPR, and a total of 8 compounds demonstrated binding affinity of < 10 uM. For Nav1.6, four PTS hits were confirmed by SPR, and a total of 9 compounds demonstrated binding affinity of < 10 μM. One top hit was compound 5674 (cmp5674), which had an in-cell IC_{50} of 0.95 μM and bound to both FGF14 and Nav1.6 by PTS (ΔT_M= -2.05 and -3.54°C for FGF14 and Nav1.6, respectively) as well as SPR (K_D = 940 nM and 2.5 μM for FGF14 and Nav1.6, respectively).

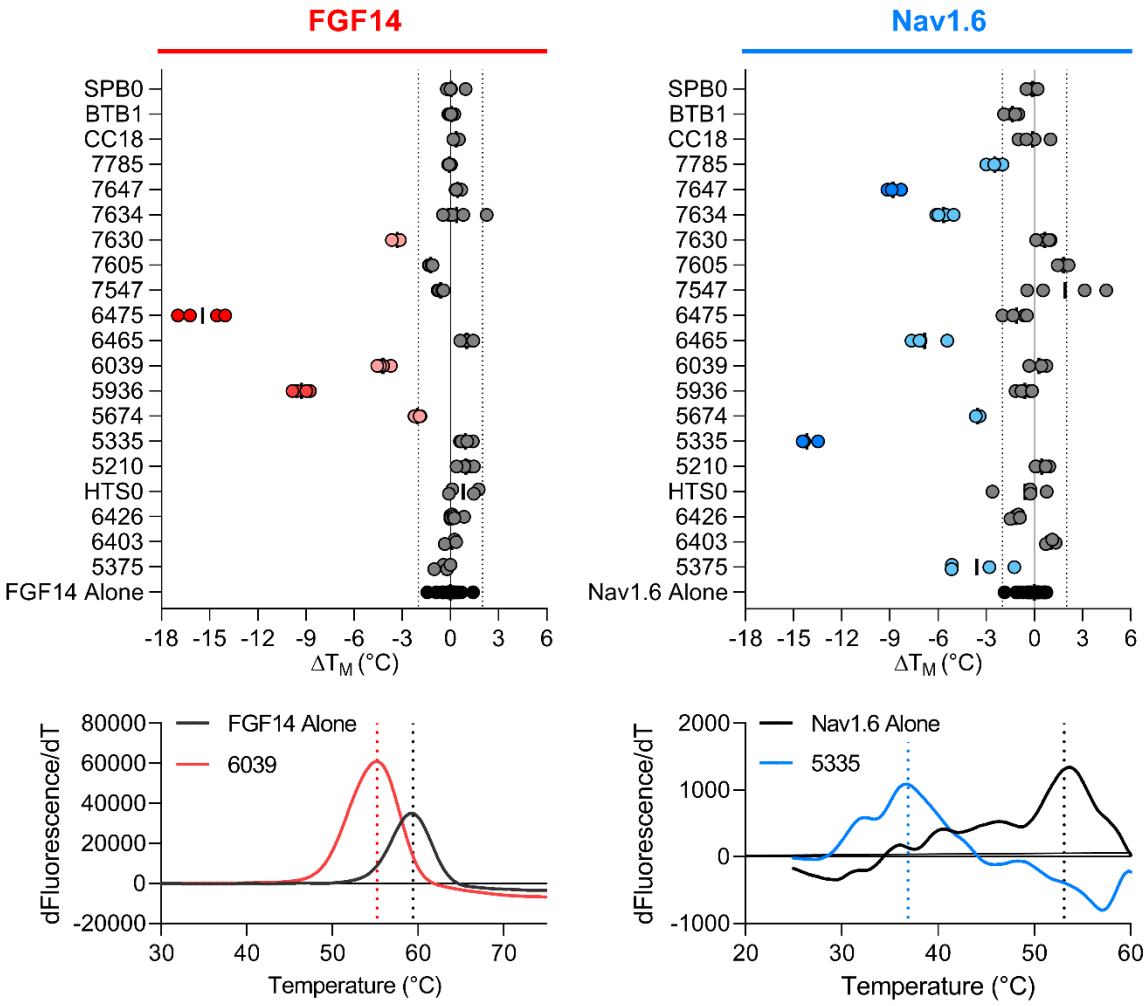

Figure 7.7. Assessment of hit binding to FGF14 and Nav1.6 C-tail binding by thermal shift.

The PTS assay using purified FGF14 or Nav1.6 C-tail protein in 96-well plates. Top, Treatments were normalized to the average T_M of per plate protein only control wells (n=8 per plate). Bottom, Representative traces of fluorescence over time with increasing temperature from wells containing either FGF14 or Nav1.6 protein alone or treated with 25 μM compound.

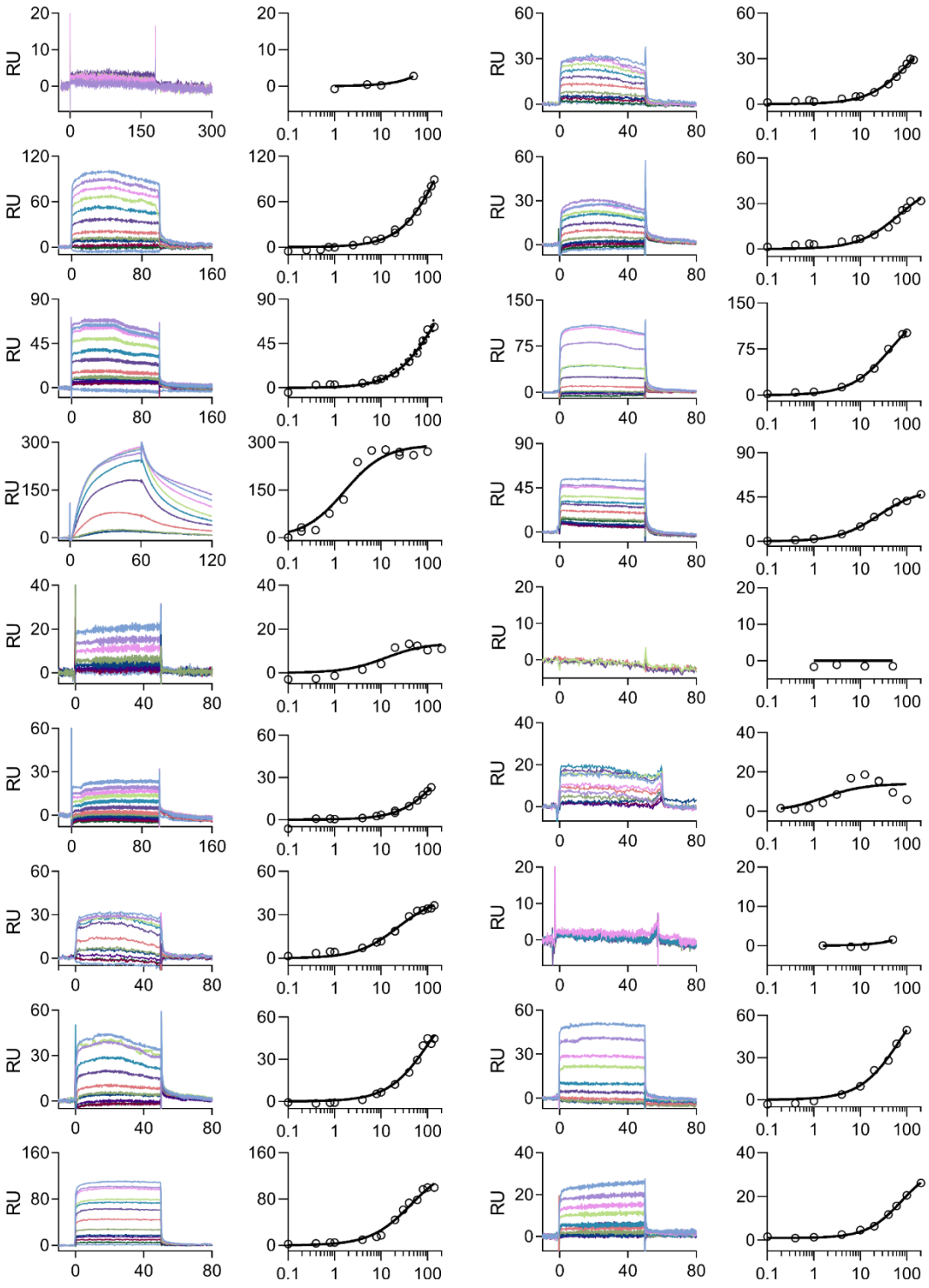

Figure 7.8. Quantification of hit binding affinity for FGF14 using SPR.

Compounds were initially screened for FGF14 binding using 4 concentrations (1.6-50 µM), and those demonstrating substantial response were subsequently tested using an expanded concentration series (0.1 – 200 µM). Compounds were dissolved in PBS-P+ containing 2% DMSO and flown over CM5 chips with FGF14 bound (17,800 RU) at 50 µL/min. The binding sensorgrams (left) and steady-state saturation plots (right) are shown. The resulting equilibrium dissociation constants (K_D), as well as kinetic association (k_{on}) and dissociation (k_{off}) rates are provided in **Table 7.1**.

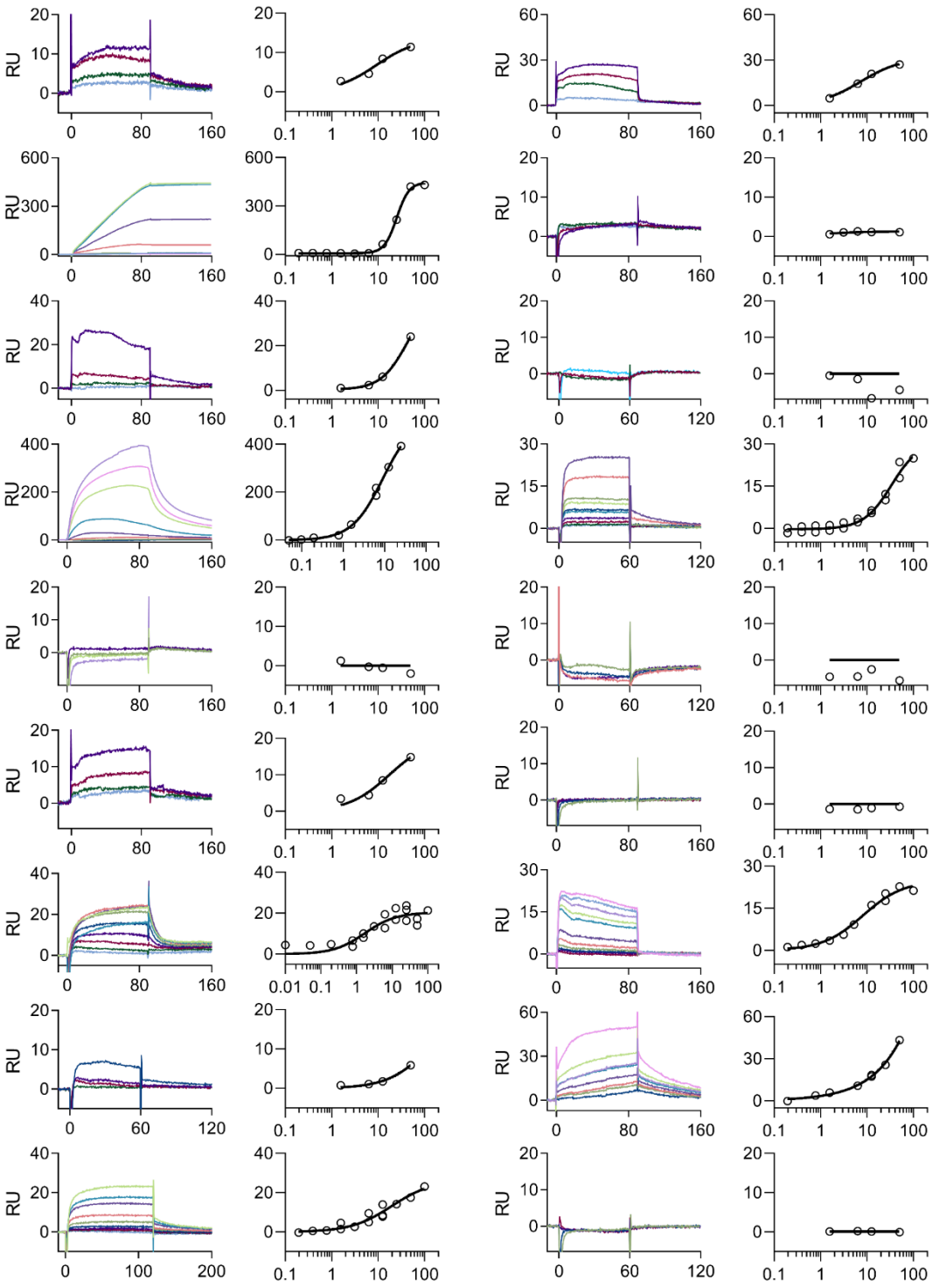

Figure 7.9. Quantification of hit binding affinity for Nav1.6 using SPR.

Compounds were initially screened for Nav1.6 binding using 4 concentrations (1.6-50 µM), and those demonstrating substantial response were subsequently tested using an expanded concentration series (0.1 – 200 µM). Compounds were dissolved in PBS-P+ containing 2% DMSO and flown over CM5 chips with Nav1.6 bound (6,800 RU) at 50 µL/min. The binding sensorgrams (left) and steady-state saturation plots (right) are shown. The resulting equilibrium dissociation constants (K_D), as well as kinetic association (k_{on}) and dissociation (k_{off}) rates are provided in **Table 7.1**.

				LCA Screening		LCA Validation			PTS, ΔT_M (°C)		SPR, K_D (μM) vs. FGF14		SPR, K_D (μM) vs. Nav1.6	
Inhibitor	MW	CLogP	tPSA	Z-score	B-score	IC_{50} (μM)	I_{Min} (%)	Efficacy	FGF14	Nav1.6	Kinetic	SS	Kinetic	SS
5210	350.4	4.24	98.4	-5.69	-3.92	9.33	17.7	4.6	1.0	0.5	> 1M	ND	3.43	9.16
5335	352.2	4.88	46.2	-5.74	-9.17	6.32	1.0	99.0	0.9	-14.2	43.78	212.2	0.07	25.13
5671	298.4	4.99	24.8	-10.95	-11.58	21.78	1.0	99.0	-1.5	-0.4	N/A	150	2.43	43.41
5674	456.9	5.21	96.5	-9.59	-8.32	0.97	25.7	2.9	-2.1	-3.5	0.94	1.56	2.5	13.16
5936	400.4	4.11	75.7	-6.62	-11.51	5.64	3.1	31.4	-9.3	-0.6	N/A	12.41	> 1 M	ND
6039	420.5	4.01	107.4	-6.99	-5.88	11.69	17.1	4.8	-4.2	-0.4	1.95	220.7	4.4	17.22
6465	467.3	5.08	66.5	-5.81	-7.31	7.01	18.7	4.4	1.0	-6.8	98	22.68	2.74	1.71
6475	490.7	5.05	66.5	-6.62	-13.74	12.79	1.0	99.0	-15.4	-1.1	0.03	55.99	> 1 M	ND
7605	294.4	2.83	52.6	-6.22	-3.85	0.99	13.2	6.6	-1.2	1.8	3.9	68.33	19	19.39
7630	347.5	4.96	55.4	-6.28	-8.51	12.19	1.0	99.0	-3.3	0.6	0.04	114.9	1.29	7.277
7634	425.7	3.93	50.8	-5.82	-10.81	15.81	5.8	16.3	1.1	-5.7	93	62.15	> 1 M	ND
7647	483.6	3.57	99.2	-10.50	-13.58	10.69	1.0	99.0	0.5	-8.8	14.63	45.62	> 1 M	ND
7785	437.5	3.95	44.8	-8.58	-1.80	12.85	1.0	99.0	-0.1	-2.4	1.52	27.02	4.09	33.48
BTB1	398.7	4.68	61.8	-6.55	-3.02	3.13	27.8	2.6	0.1	-1.4	> 1M	ND	> 1 M	ND
CC18	211.3	1.94	32.6	-12.84	-8.23	2.16	26.7	2.7	0.1	-1.7	0.08	1.634	> 1 M	ND
SPB0	344.5	4.27	49.1	-16.67	-10.64	10.52	1.0	99.0	-0.3	0.1	> 1M	ND	0.68	8.188
Enhancer	MW	CLogP	tPSA	Z-score	B-score	EC_{50} (μM)	E_{Max} (%)	Efficacy	FGF14	Nav1.6	Kinetic	SS	Kinetic	SS
5375	339.1	4.36	84.4	8.44	28.68	5.00	229.6	0.6	-0.4	-3.6	---	---	---	---
5543	4.05	17.72	252.3	3.50	52.8	4.88	193.1	0.5	---	---	ND	ND	ND	ND
6403	67.5	4.36	67.5	6.37	10.58	0.76	186.2	0.5	0.0	1.0	---	---	---	---
6426	305.8	2.76	53.5	4.52	4.87	1.00	154.0	0.4	0.7	-1.2	1.4	73.72	7.07	> 1M
HTS0	333.4	1.71	63.5	6.68	21.90	1.66	179.4	0.4	0.8	-0.6	> 1M	76.26	> 1 M	ND

Table 7.1. Summary of LCA, PTS, and SPR results for confirmed hits.
LCA screening refers to the compound scores from the primary screening (**Fig. 7.2**). LCA validation refers to values calculated from dose-dependency studies (**Fig. 7.6**). For PTS, the mean change in melting temperature (ΔT_M, °C) for each compound is shown (25 μM, n = 4 wells per treatment) based on data represented in **Figure 7.7**. For SPR, the estimated K_D (μM) was calculated by (1) fitting the response data to the simplest Langmuir 1:1 interaction model ($K_D=k_{off}/k_{on}$; "Kinetic"), and (2) the steady-state K_D ("SS") was calculated from the fitted saturation binding curve based on data represented in **Figures 7.8** and **7.9**).

7.2.4. Selectivity screening

As our goal for this campaign was to identify modulators of specifically the FGF14:Nav1.6 complex, we conducted a selectivity counter-screening. The top 20 repurchased hits were screened against the FGF13-1a:Nav1.6 C-tail, FGF13-1B:Nav1.6 C-tail, and FGF14:Nav1.2 complexes, as well as the FGF14:FGF14 dimer, using LCA in transiently transfected HEK293 cells. The purpose of assessing modulation of the FGF14:FGF14 dimer was similar in principle that discussed in Chapter 5 (i.e., compounds that reduce FGF14 dimerization could thereby increase FGF14:Nav1.6 complex assembly, and vice versa). The results are shown in **Figure 7.10**. Compounds were screened in 384-well plates at two concentrations (10 and 50 μM, n = 6 wells per concentration), and luminescence was normalized to controls (0.3% DMSO, n = 64 wells).

7.2.4. *Ex vivo* electrophysiology in medium spiny neurons from the nucleus accumbens

We pursued the top six compounds based on combined data from LCA, PTS, and SPR studies, including one enhancer (6426) and four inhibitors (5335, 5674, 7605, 7647). These compounds were tested using patch-clamp electrophysiology in medium spiny neurons (MSNs) from the nucleus accumbens (NAc) (**Fig 7.11**). We observed increased firing (number of action potentials) for compounds 5674 and, to a lesser extent, CC18. Decreased firing was observed for compounds 5335, 7605, 7647, and 5335, with the latter resulting in the most drastically reduced firing. For the purpose of the present study, we excluded compounds that exhibited opposite phenotypes between the LCA and neuronal firing (i.e., enhancer of the FGF14:Nav1.6 complex by LCA, but inhibitor of firing in MSNs). This phenomenon was observed for compounds 5674 and CC18 (inhibitor by LCA, stimulator of firing), as well as 6426 (enhancer by LCA, inhibitor of firing).

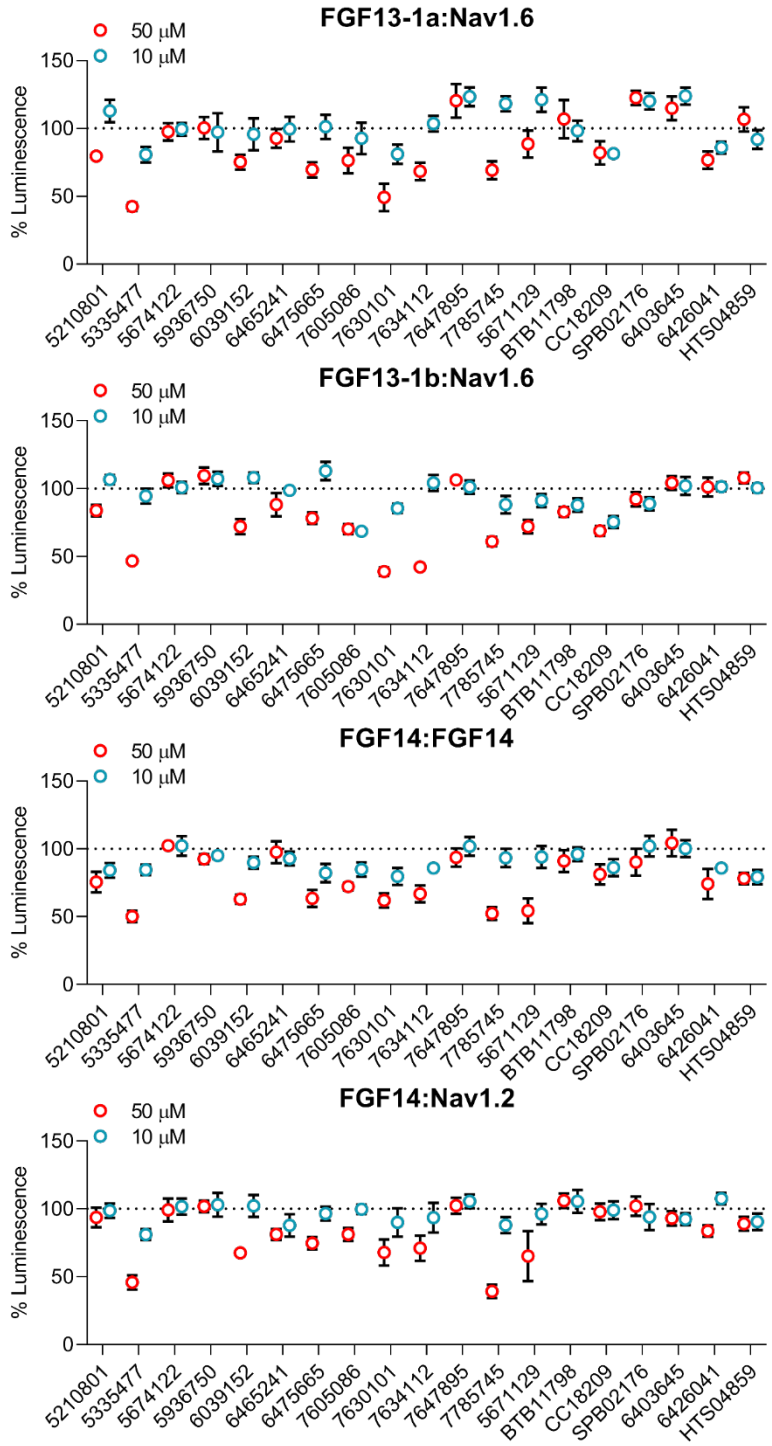

Figure 7.10. Selectivity screening.

Repurchased hits were screened against the FGF13-1a:Nav1.6 C-tail, FGF13-1B:Nav1.6 C-tail, and FGF14:Nav1.2 complexes, as well as the FGF14 Dimer, using LCA in transiently transfected HEK293 cells. n=6 replicates per concentration. Luminescence for each well was normalized to per plate 0.3% DMSO controls (n=16 per plate), and the mean normalized luminescence ± SEM is shown.

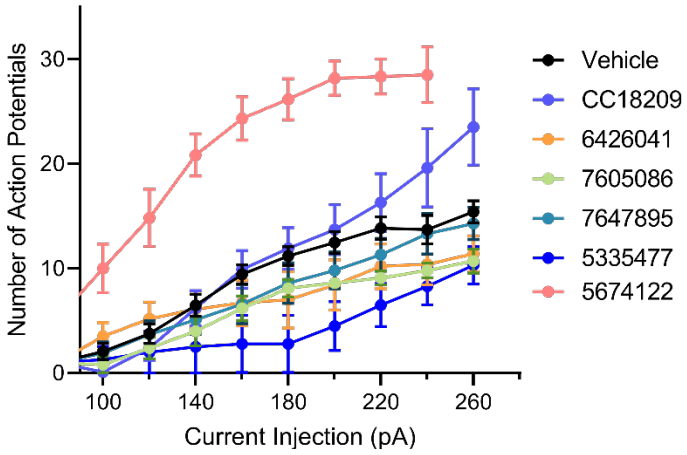

Figure 7.11. Electrophysiology of top hits in medium spiny neurons from the NAc.
Number of APs vs injected current (80-260 pA) from MSNs from NAc slices treated with vehicle (0.05% DMSO), 5335477 (130 µM), 5674122 (10 µM), 7605086 (10 µM), 7647895 (50 µM), 6426041 (2 µM), or CC18209 (20 µM). The higher concentration of 5335477 was used due to poor solubility. Data are mean ± SEM (n = 6-30). We observed increased intrinsic excitability, number of APs, and inst. firing frequency in 5674122-treated MSNs, but no significant effect on resting membrane potential, current threshold, voltage threshold, latency to first peak, maximum velocity rise, or maximum velocity decay.

7.2.4. *In silico* prediction of blood-brain barrier (BBB) permeability

Proceeding with the remaining compounds 5335, 7605, and 7647, we used a recently developed novel technique for predicting small molecule permeability to the BBB[189] in collaboration with Dr. Ulmschneider at King's College (London, UK). Compounds were simulated at 380K and 420K over 4 microseconds (20 molecules per compound). Representative trajectories for spontaneous diffusion processes of 7605, 7647, and 5335 (one molecule shown) are shown over 2000 nanoseconds (ns) at 380K in **Figure 7.12**. 7605 exhibited an excellent predicted BBB permeability, with frequent spontaneous diffusion through the apical bilayer, with ΔG = 4.71 kcal/mol (at 380K) and a free energy profile shaped similarly to that of caffeine or isoproponal[189]. 7647 demonstrated moderate predicted permeability, with ΔG = 5.32 kcal/mol (at 380K) and a free energy profile shaped similarly to that of caffeine[189]. However, 5335 exhibited poor predicted BBB permeability due to substantial hydrophobic interactions with the membrane, with ΔG = 5.83 kcal/mol (at 380K) and a free energy profile shaped similarly to that of CO_2 or diazepam[189], and resulting in the compound remaining within the lipid bilayer.

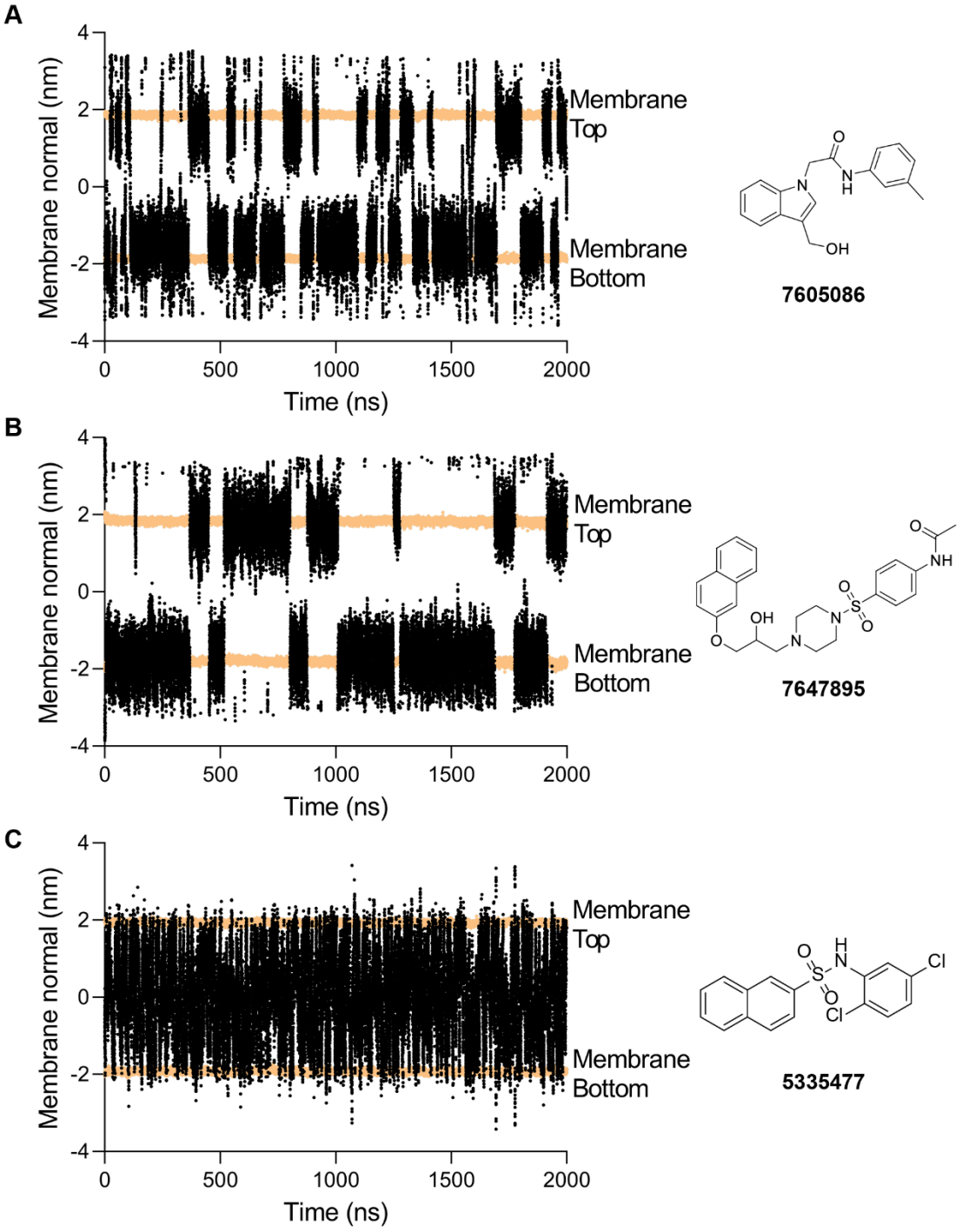

Figure 7.12. Spontaneous diffusion mechanism of compounds through the apical BBB bilayer.

Top compounds were simulated with the apical BBB membrane bilayer using a recently developed technique for predicting BBB permeability[189]. Representative trajectories for spontaneous diffusion processes of 7605 (top), 7647 (middle), and 5335 (bottom) over 2000 nanoseconds (ns) at 380K; one out of twenty molecules simulated is shown. 7605 exhibited an excellent predicted BBB permeability, with frequent spontaneous diffusion through the apical bilayer. 7647 demonstrated moderate predicted permeability. However, 5335 exhibited poor predicted BBB permeability due to substantial hydrophobic interactions with the membrane, resulting in the compound remaining within the lipid bilayer.

7.3. DISCUSSION

Following an HTS of ~45,000 small molecules and drug-like compounds from the Maybridge and Chembridge libraries, we initially had ~1,000 hits. This set was rapidly reduced during re-screening and counter-screening assays, and following chemoinformatic analysis, we had a set of ~70 promising compounds. Dose dependency studies revealed numerous compounds with poor in-cell activity, resulting in a set of ~20 hits. Subsequent biophysical testing compounds demonstrated a wide range of binding (or lack of) to both FGF14 and Nav1.6 C-tail protein. Overall, compounds bound FGF14 more frequently. Based on these results, as well as further examination of those compounds most likely to be permeable to the BBB (i.e., cLogP), we reduced the set of compounds down to the top six (five inhibitors and one enhancer) for functional analysis using electrophysiology.

Medium spiny neurons in the nucleus accumbens play a significant role in mood disorders and reward-related behaviors[65,190]. We have previously shown that both FGF14 and Nav1.6 are abundantly expressed in these neurons[58,191], and contribute to regulation of their firing patterns. Thus, we tested top candidates in MSNs with the hypothesis that compounds targeting the FGF14:Nav1.6 should modulate MSN firing (Fig. 7.11). Although all compounds affected firing to at least some extent, we observed a phenomenon of compounds exhibiting opposite phenotypes between the LCA results and firing in MSNs (i.e., enhancer of the FGF14:Nav1.6 complex by LCA, but inhibitor of firing in MSNs). For the purpose of the present study, we excluded compounds that exhibited opposite phenotypes, leaving us with the compounds 5335, 7605, and 7647 as our front-runners. However, the excellent binding kinetics exhibited by 5674 toward both FGF14 and Nav1.6 (**Fig 7.8 and 7.9**), as well as the significantly increased firing observed in MSNs, may indicate that this compound could be used for other applications. For instance, given the role of FGF14 in regulating cognitive function (Chapter 1) possible future applications of 5674 could include rescue of cognitive function in neurodegenerative diseases associated

with FGF14 (discussed in **Chapter 1**). During selectivity counter-screening (**Fig. 7.10**), we observed that compound 5335 inhibits all complexes (~40-50% luminescence), though to a lesser degree at 10 μM. In combination with the SPR and PTS results demonstrating extremely tight binding affinity to the Nav1.6 C-tail (K_D = 70 nM), this supports the idea that 5335 exerts its inhibitory activity by binding to the Nav1.6 C-tail. The observed inhibition of the FGF14:Nav1.2 complex may arise from the high sequence homology of Nav1.2 with Nav1.6. 7647 demonstrated negligible modulation of other complexes, and moderate binding to FGF14 but not Nav1.6. Conversely, compound 7605 very mildly inhibits (~80-90% luminescence) all complexes at 50 μM, but not at 10 μM. Taken together with SPR results showing moderate binding affinity of 7605 to both FGF14 (K_D = 3.9 μM) and Nav1.6 (K_D = 19 μM), this suggests that 7605 may be a true disruptor of PPI between these two proteins.

We concluded the present study with a more extensive examination of permeability to the BBB. Due to the high costs associated with animal studies, including both DMPK (distribution, metabolism, and pharmacokinetics) studies to assess bioavailability and *in vivo* BBB permeability, as well as subsequent behavioral studies, we sought to first identify those compounds with the greatest likelihood for success. As discussed above, an approach to calculate the BBB permeability of small molecules using molecular dynamic simulations has been recently developed and validated using an *in vitro* transwell assay[189]. Their study demonstrated "accurate prediction of solute permeabilities at physiological temperature using high-temperature unbiased atomic detail molecular dynamics simulations of spontaneous drug diffusion across BBB bilayers." Thus, this novel and relatively low-cost technique provided an excellent opportunity to further rank our compounds for *in vivo* studies. Our top three candidates, including 5335, 7605, and 7647, were simulated using this new technique, and revealed very high predicted permeability for 7605, followed by a moderate permeability for 7647, and low permeability for 5335 due to the compound's high hydrophobicity.

Overall, here we identify numerous potential modulators of the PPI between FGF14 and Nav1.6 that have been validated in cells and *in vitro*, functionally confirmed *ex vivo*, and finally explored *in silico* prior to labor-intensive animal studies. DMPK and behavioral of studies the top compound 7605 are currently on-going. However, given the high failure rate of compounds *in vivo*, we additionally provide a number of other top hits that can be pursued, such as 7647. In sum, these compounds, identified based on the novel approach of targeting PPI for CNS drug discovery, might represent candidates for the next generation of therapeutics for reward-related behaviors and neuropsychiatric disorders.in general.

Chapter 8. Conclusions and Future Directions

8.1. Development of a New Tool for CNS Drug Discovery

Ion channel macromolecular complexes play a critical role in regulating and finely tuning neuronal firing. The intra-molecular interactions within these complexes present an ideal pharmacologic target based on their specificity, which is essential to limit side effects in CNS drugs. However, new methods are needed for identifying compounds that could modulate these interactions. Here, we reported a robust assay for high-throughput screening (**HTS**) of small molecules based on split-luciferase complementation that could be applied to two areas: *i*) searching for mechanisms regulating ion channel complexes, and *ii*) identifying small molecules that could treat channelopathies or other CNS-related disorders associated with changes in protein:channel interactions.

In Chapter 3, we described how to construct, optimize, and miniaturize an assay capable of assessing protein:channel interactions in 96-, 384-, or 1536-well plates using a minimal functional domain (**MFD**) approach[192], and this modified form of the luciferase assay can be applied to numerous other protein:protein interactions given sufficient binding affinity. In Chapter 4, we presented the specific results from our successful development of a robust screening platform that is amenable to targeted campaigns using small molecule libraries against hot-spots at the protein:channel interface. Not only have we developed a powerful new tool for drug discovery, but the initial results from this assay identified multiple FDA-approved anti-cancer therapeutics as potential modulators of the FGF14:Nav1.6 complex. The total cost of developing a single drug that has reached Phase III clinical trials and gained marketing approval is estimated to be in the billions. As such, drugs that have failed for their originally intended target, but did not exhibit toxicity or

poor pharmacokinetics in Phase I trials, are ideal candidates for repurposing toward other medical conditions. Our results indicate that several FDA-approved drugs may modulate the FGF14:Nav1.6 complex, such as the tyrosine kinase inhibitor lestaurtinib, which is permeable to the blood-brain barrier. Follow-up studies of this compound validating its ability to modulate Nav channels *in vivo* may suggest that it could be repurposed toward CNS diseases, an area that has a long history of drug discovery failures.

Overall, this new screening platform could lead to identification of allosteric modulators of Nav channels through a traditional lead optimization phase, including a cascade of orthogonal screenings, functional assays (i.e., electrophysiology) and behavioral pharmacology[151]. Overall, we anticipate that our MFD driven platform[192] could provide the foundation for development of new classes of protein:protein interaction-based leads to treat channelopathies and other CNS disorders.

8.2. Identification of JAK2 as a Regulator of the FGF14:Nav1.6 Complex

Using this new assay to identify cellular mechanisms of Nav complex regulation, in Chapter 5 we highlight how protein tyrosine kinases (**PTKs**), and in particular JAK2, play a role in regulating the Nav1.6 channel complex. We observed a high proportion of screening hits targeting PTKs including Lck, Syk, Fyn, FLT3, Src, and JAK2, and validation studies demonstrated clear regulation of the complex by the latter two kinases. These results build on previous investigations of the relationship between PTKs and Nav channels. Direct interactions between Nav1.2 channels and Fyn[96], a tyrosine kinase closely related to Src, were found to be functionally relevant, affecting Na^+ current amplitudes and channel availability through Tyr phosphorylation induced by activation of TrkB/p75 signaling via BDNF[193]. A number of Fyn kinase phosphorylation sites have been found on

Nav channels, including Y1497 and Y1498 on Nav1.2 close to the inactivation gate[193] and others on the cardiac Nav1.5 N-terminal and C-terminal tails[62]. Additionally, both FGF14 and Nav1.6 are phosphorylated by GSK3β and thereby controlled via the IP3K/Akt/GSK3β pathway of Ser/Thr kinases downstream of receptor tyrosine kinases[46,65,194,195]. Under basal conditions, FGF14 and Nav1.6 are highly clustered at the AIS, the site of action potential initiation. Thus, it is plausible that both Ser/Thr and Tyr kinases also cluster in this compartment, forming a structurally organized signaling complex of which FGF14, the Nav1.6 channel, kinases and the transmembrane receptor are all components. In this manner, specific post-translational modifications could confer functional specificity to the Nav channel complex in distinct subcellular compartments of the neuron, contributing to specialized signaling important for firing and synaptic plasticity[95,97,183].

Based on these results, we concluded that activation of JAK2 might result in FGF14 phosphorylation, dimer dissociation, and subsequent increases in binding of monomeric FGF14 to the Nav1.6 C-terminal tail (**Fig. 8.1**). This may be the endpoint of a pathway that enables neurons to dynamically adjust firing in response to JAK2-mediated receptor signaling. In summary, our study provides evidence for novel signaling mechanisms with implications for synaptic plasticity and neuroinflammation through shifting the equilibrium of phosphorylation and PPI at the Nav channel complex.

8.3. Discovery of Novel Small Molecule Probes Targeting the FGF14:Nav1.6 Complex Interface

In Chapters 6 and 7, we used a combination of rational drug-design based on a peptide mapped to the FGF14:Nav1.6 interface, as well as HTS of large chemical libraries to identify new modulators. These new probes have been validated using an array of

methodologies: assessment of concentration-dependency in-cells revealed IC_{50} values ranging from 0.9-20 μM; SPR revealed moderate-to-high affinity binding of compounds to FGF14 and/or Nav1.6 protein, which was confirmed by the protein thermal shift assay demonstrating protein:drug binding; electrophysiology both in-cells and in slices revealed functional modulation of Na^+ currents and/or firing. With these powerful new probes, subsequent testing can now begin including distribution, metabolism, and pharmacokinetic studies. For those compounds demonstrating good bioavailability and permeability to the blood brain barrier without inducing toxicity (i.e., locomotor changes or cardiotoxicity), the next stage is for behavioral studies to assess efficacy *in vivo* using animal models of depression and other mood disorders known to arise from dysfunction in the NAc.

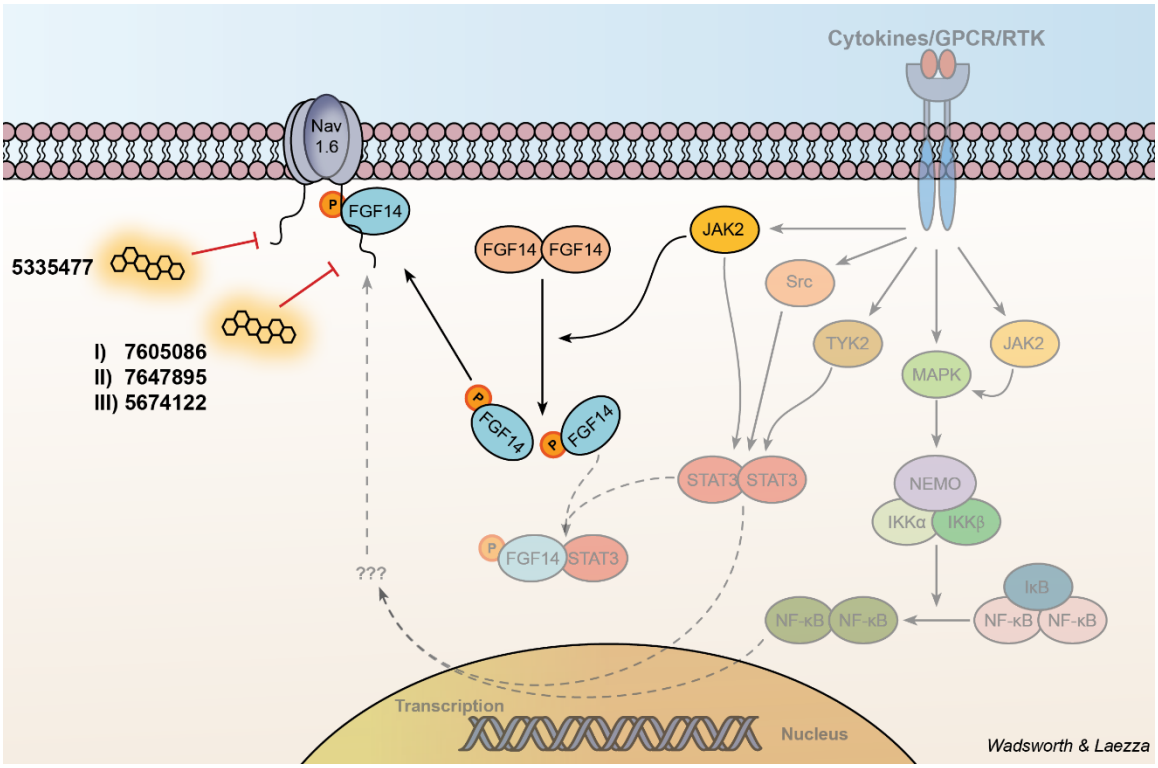

Figure 8.1. Schematic of Dissertation results.

Depicted results include initial findings that require additional confirmatory studies (dotted lines and semi-transparency for pathways and proteins predicted to regulate the Nav1.6 complex), as well as validated interactions (solid lines).

8.4. FUTURE DIRECTIONS

We have provided initial evidence for JAK2-dependent regulation of the equilibrium between FGF14:FGF14 dimerization and FGF14:Nav1.6 complex assembly. However, this was tested using two separate assay systems as described in Chapter 4. To more directly confirm that phosphorylation of FGF14 at Y158 by JAK2 leads to dimer dissociation and subsequent binding of monomeric FGF14 to the Nav1.6 C-tail, we propose to use the dual-luciferase assay. This system is similar to the LCA but can simultaneously measure two different light wavelengths that are produced from two different complexes (i.e., FGF14:FGF14 homodimer and FGF14:Nav1.6 complex) based on more specialized constructs for transfection in heterologous cells. Additionally, further investigations into the role STAT3 may play in regulating these complexes are important. Similar, albeit weaker and less consistent, results were observed for STAT3 inhibitors compared to JAK2 inhibitors from our initial HTS validation studies using LCA, and there are predicted STAT3 binding sites in the FGF14-1b sequence (Table 5.2). Inconsistency in results may arise from a STAT3 regulatory mechanism that would be more challenging to explore compared to direct phosphorylation events that alter binding in the complexes studied here. For instance, FGF14 has been observed in the nucleus, and has a nuclear translocation motif on its C-terminus. The transcription factor STAT3 could bind FGF14 and subsequently translocate into the nucleus, a pathway that would be entirely novel.

As discussed in Chapters 6 and 7, we have also provided several lead compounds targeting the FGF14:Nav1.6 complex from both our rational drug design (peptide-based), as well as our HTS campaign using the Chembridge and Maybridge compound libraries. Of these, several compounds demonstrated functional evidence for modulation of the Nav1.6 channel and/or firing in MSNs, and for others we have presented promising evidence for binding to FGF14 and/or Nav1.6. To increase confidence that they are true disruptors of the PPI between this interaction, we propose to use biophysical experiments

such as analytical ultracentrifugation (i.e., sedimentation velocity), whereby a compound that prevents protein:protein binding would be evidenced by failure to observe a peak (sedimentation coefficient) corresponding to the combined MW of the FGF14:Nav1.6 complex. However, other purified-protein-based methods are also viable options, such as: *i*) PTS assay (PPI disruptor should eliminate stabilized/higher melting temperature of the complex, yielding two peaks for either protein); *ii*) SPR (similar in theory to ternary complex experiment); or ITC (i.e., failure to observe heat release following addition of FGF14 to Nav1.6 pre-complexed with compound). While the feasibility of these biophysical experiments is limited by the quantity of purified protein available, they would provide substantial evidence for these compounds as being direct modulators of PPI.

Other methods for testing compounds in more complex systems described above, such as slice electrophysiology and ultimately preclinical behavioral assays, will provide the necessary complement to ascertain the potential clinical values of these compounds. Additional preclinical methods based on human-derived stem cells should also be considered for predicting therapeutic value of new compounds, and these will be incorporated in the drug discovery pipeline developed here.

Overall, the results in this Dissertation have demonstrated that PPI may be targetable for drug development against brain disorders. These discoveries have the potential to shift the current paradigm in CNS drug discovery, while simultaneously moving the field closer to precision medicine, a highly desirable, but not yet attainable, prospect in psychiatry.

References

1. De Lera Ruiz, M. & Kraus, R. L. Voltage-Gated Sodium Channels: Structure, Function, Pharmacology, and Clinical Indications. *J. Med. Chem.* **58**, 7093–7118 (2015).
2. Cantrell, A. R. *et al.* Molecular mechanism of convergent regulation of brain Na+ channels by protein kinase C and protein kinase A anchored to AKAP-15. *Mol Cell Neurosci* **21**, 63–80 (2002).
3. Rush, A. M. *et al.* Differential modulation of sodium channel Nav1.6 by two members of the fibroblast growth factor homologous factor 2 subfamily. *Eur. J. Neurosci.* **23**, 2551–2562 (2006).
4. Yu, F. H. & Catterall, W. A. Overview of the voltage-gated sodium channel family. *Genome Biol.* **4**, (2003).
5. Catterall, W. A. Structure and function of voltage-gated sodium channels at atomic resolution. *Exp. Physiol.* **99**, 35–51 (2014).
6. Marban, E., Yamagishi, T. & Tomaselli, G. F. Structure and function of voltage-gated sodium channels. *J. Physiol.* **508 (Pt 3**, 647–657 (1998).
7. Shen, H. *et al.* Structure of a eukaryotic voltage-gated sodium channel at near-atomic resolution. *Science (80-.).* **355**, (2017).
8. Bagnéris, C. *et al.* Role of the C-terminal domain in the structure and function of tetrameric sodium channels. *Nat. Commun.* **4**, (2013).
9. Jiang, D. *et al.* Structure of the Cardiac Sodium Channel. *Cell* **180**, 122-134.e10 (2020).
10. Catterall, W. a, Goldin, A. L. & Waxman, S. G. Nomenclature and structure-function relationships of voltage-gated sodium channels. *Pharmacol. Rev.* **57**, 397–409 (2005).
11. Catterall, W. A. From Ionic Currents to Molecular Review Mechanisms: The Structure and Function of Voltage-Gated Sodium Channels. *Neuron* **26**, 13–25 (2000).
12. Li, M. C. H., O'Brien, T. J., Todaro, M. & Powell, K. L. Acquired cardiac channelopathies in epilepsy: Evidence, mechanisms, and clinical significance. *Epilepsia* **60**, 1753–1767 (2019).
13. Mullen, S. A. & Scheffer, I. E. Translational research in epilepsy genetics: sodium channels in man to interneuronopathy in mouse. *Arch. Neurol.* **66**, 21–26 (2009).
14. Mantegazza, M. *et al.* Identification of an Nav1.1 sodium channel (SCN1A) loss-of-function mutation associated with familial simple febrile seizures. *Proc. Natl. Acad. Sci. U. S. A.* **102**, 18177–18182 (2005).
15. Bennett, D. L., Clark, A. J., Huang, J., Waxman, S. G. & Dib-Hajj, S. D. The Role

of Voltage-Gated Sodium Channels in Pain Signaling. *Physiol. Rev.* **99**, 1079–1151 (2019).

16. Wu, Y. *et al.* Selective Voltage-Gated Sodium Channel Peptide Toxins from Animal Venom: Pharmacological Probes and Analgesic Drug Development. *ACS Chem. Neurosci.* **9**, 187–197 (2018).
17. Dib-Hajj, S. D. *et al.* Voltage-gated sodium channels in pain states: role in pathophysiology and targets for treatment. *Brain Res. Rev.* **60**, 65–83 (2009).
18. Re, J. Di, Wadsworth, P. A. & Laezza, F. Intracellular fibroblast growth factor 14: Emerging risk factor for brain disorders. *Front. Cell. Neurosci.* **11**, 1–7 (2017).
19. Wang, Y. *et al.* Genetic polymorphisms in the SCN8A gene are associated with suicidal behavior in psychiatric disorders in the Chinese population. *World J. Biol. Psychiatry* **11**, 956–963 (2010).
20. Abriel, H. Cardiac sodium channel Nav1.5 and its associated proteins. *Arch. Mal. Coeur Vaiss.* **100**, 787–793 (2007).
21. Musa, H. *et al. SCN5A* variant that blocks fibroblast growth factor homologous factor regulation causes human arrhythmia. *Proc. Natl. Acad. Sci.* **112**, 12528–12533 (2015).
22. Li, Z.-M., Chen, L.-X. & Li, H. Voltage-gated Sodium Channels and Blockers: An Overview and Where Will They Go? *Curr. Med. Sci.* **39**, 863–873 (2019).
23. Patel, F. & Brackenbury, W. J. Dual roles of voltage-gated sodium channels in development and cancer. *Int. J. Dev. Biol.* **59**, 357–366 (2015).
24. Brackenbury, W. J. Voltage-gated sodium channels and metastatic disease. *Channels (Austin).* **6**, 352–361 (2012).
25. Hoeijmakers, J. G. J., Faber, C. G., Merkies, I. S. J. & Waxman, S. G. Channelopathies, painful neuropathy, and diabetes: which way does the causal arrow point? *Trends Mol. Med.* **20**, 544–550 (2014).
26. Hu, W. *et al.* Distinct contributions of Na(v)1.6 and Na(v)1.2 in action potential initiation and backpropagation. *Nat. Neurosci.* **12**, 996–1002 (2009).
27. Lorincz, A. & Nusser, Z. Molecular identity of dendritic voltage-gated sodium channels. *Science* **328**, 906–909 (2010).
28. O'Brien, J. E. & Meisler, M. H. Sodium channel SCN8A (Nav1.6): properties and de novo mutations in epileptic encephalopathy and intellectual disability. *Front. Genet.* **4**, 1–9 (2013).
29. Hargus, N. J., Nigam, A., Bertram, E. H. 3rd & Patel, M. K. Evidence for a role of Nav1.6 in facilitating increases in neuronal hyperexcitability during epileptogenesis. *J. Neurophysiol.* **110**, 1144–1157 (2013).
30. Van Wart, A. & Matthews, G. Impaired firing and cell-specific compensation in neurons lacking nav1.6 sodium channels. *J. Neurosci.* **26**, 7172–7180 (2006).
31. Focken, T. *et al.* Identification of CNS-Penetrant Aryl Sulfonamides as Isoform-Selective Na V 1 . 6 Inhibitors with Efficacy in Mouse Models of Epilepsy. (2019).

doi:10.1021/acs.jmedchem.9b01032

32. Clatot, J. *et al.* Mutant voltage-gated Na(+) channels can exert a dominant negative effect through coupled gating. *Am. J. Physiol. Heart Circ. Physiol.* **315**, H1250–H1257 (2018).

33. Huang, W., Liu, M., Yan, S. F. & Yan, N. Structure-based assessment of disease-related mutations in human voltage-gated sodium channels. *Protein Cell* **8**, 401–438 (2017).

34. Kass, R. S. The channelopathies: novel insights into molecular and genetic mechanisms of human disease. *J. Clin. Invest.* **115**, 1986–1989 (2005).

35. Hsu, W. C. J., Nilsson, C. L. & Laezza, F. Role of the axonal initial segment in psychiatric disorders: Function, dysfunction, and intervention. *Front. Psychiatry* **5**, 109 (2014).

36. Miura, S. *et al.* Spinocerebellar ataxia 27 with a novel nonsense variant (Lys177X) in FGF14. *Eur. J. Med. Genet.* **62**, 172–176 (2019).

37. Choquet, K., La Piana, R. & Brais, B. A novel frameshift mutation in FGF14 causes an autosomal dominant episodic ataxia. *Neurogenetics* **16**, 233–236 (2015).

38. Zühlke, C. *et al.* Spinocerebellar ataxia 28: a novel AFG3L2 mutation in a German family with young onset, slow progression and saccadic slowing. *Cerebellum & Ataxias* **2**, 19 (2015).

39. Camerino, D. C. & Desaphy, J. F. Grand challenge for ion channels: An underexploited resource for therapeutics. *Front. Pharmacol.* **AUG**, 1–2 (2010).

40. Thayer, D. A. & Jan, L. Y. Mechanisms of distribution and targeting of neuronal ion channels. *Curr. Opin. Drug Discov. Devel.* **13**, 559–567 (2010).

41. Blazer, L. L. & Neubig, R. R. Small molecule protein-protein interaction inhibitors as CNS therapeutic agents: current progress and future hurdles. *Neuropsychopharmacology* **34**, 126–141 (2009).

42. Laezza, F. *et al.* The FGF14F145S Mutation Disrupts the Interaction of FGF14 with Voltage-Gated Na+ Channels and Impairs Neuronal Excitability. *J. Neurosci.* **27**, 12033–12044 (2007).

43. Laezza, F. *et al.* FGF14 N-terminal splice variants differentially modulate Nav1.2 and Nav1.6-encoded sodium channels. *Mol. Cell. Neurosci.* **42**, 90–101 (2009).

44. Goetz, R. *et al.* Crystal structure of a fibroblast growth factor homologous factor (FHF) defines a conserved surface on FHFs for binding and modulation of voltage-gated sodium channels. *J. Biol. Chem.* **284**, 17883–17896 (2009).

45. Shavkunov, A. *et al.* Bioluminescence Methodology for the Detection of Protein–Protein Interactions Within the Voltage-Gated Sodium Channel Macromolecular Complex. *Assay Drug Dev. Technol.* **10**, 148–160 (2012).

46. Shavkunov, A. S. *et al.* The fibroblast growth factor 14-voltage-gated sodium channel complex is a new target of glycogen synthase kinase 3 (GSK3). *J. Biol. Chem.* **288**, 19370–19385 (2013).

47. Alshammari, T. K. *et al.* Genetic deletion of fibroblast growth factor 14 recapitulates phenotypic alterations underlying cognitive impairment associated with schizophrenia. *Transl. Psychiatry* **6**, e806 (2016).

48. Tempia, F. *et al.* Parallel fiber to purkinje cell synaptic impairment in a mouse model of spinocerebellar ataxia type 27. *Front. Cell. Neurosci.* **9**, 1–10 (2015).

49. Hsu, W. C. *et al.* Identifying a kinase network regulating FGF14:Nav1.6 complex assembly using split-luciferase complementation. *PLoS One* **10**, 1–21 (2015).

50. Ali, S. R., Singh, A. K. & Laezza, F. Identification of amino acid residues in fibroblast growth factor 14 (FGF14) required for structure-function interactions with voltage-gated sodium channel Nav1.6. *J. Biol. Chem.* **291**, 11268–11284 (2016).

51. Schesny, M., Joncourt, F. & Tarnutzer, A. A. Acetazolamide-Responsive Episodic Ataxia Linked to Novel Splice Site Variant in FGF14 Gene. *Cerebellum* (2019). doi:10.1007/s12311-018-0997-3

52. Hoxha, E., Balbo, I., Miniaci, M. C. & Tempia, F. Purkinje cell signaling deficits in animal models of ataxia. *Front. Synaptic Neurosci.* **10**, 6 (2018).

53. Bosch, M. K. *et al.* Intracellular FGF14 (iFGF14) Is Required for Spontaneous and Evoked Firing in Cerebellar Purkinje Neurons and for Motor Coordination and Balance. *J. Neurosci.* **35**, 6752–6769 (2015).

54. Sowers, M. L. *et al.* Sex-specific proteomic changes induced by genetic deletion of fibroblast growth factor 14 (FGF14), a regulator of neuronal ion channels. *Proteomes* **7**, 5 (2019).

55. Coutelier, M. *et al.* A panel study on patients with dominant cerebellar ataxia highlights the frequency of channelopathies. *Brain* **140**, 1579–1594 (2017).

56. Shimojima, K. *et al.* Spinocerebellar ataxias type 27 derived from a disruption of the fibroblast growth factor 14 gene with mimicking phenotype of paroxysmal non-kinesigenic dyskinesia. *Brain Dev.* **34**, 230–233 (2012).

57. Hsu, W. C. J. *et al.* CK2 activity is required for the interaction of FGF14 with voltage-gated sodium channels and neuronal excitability. *FASEB J.* **30**, 2171–2186 (2016).

58. Ali, S. R. *et al.* Functional Modulation of Voltage-Gated Sodium Channels by a FGF14-Based Peptidomimetic. *ACS Chem. Neurosci.* **9**, 976–987 (2018).

59. Liu, Z. *et al.* Identification of peptidomimetics as novel chemical probes modulating fibroblast growth factor 14 (FGF14) and voltage-gated sodium channel 1.6 (Nav1.6) protein-protein interactions. *Bioorganic Med. Chem. Lett.* **29**, 413–419 (2019).

60. Yan, H., Pablo, J. L. & Pitt, G. S. FGF14 Regulates Presynaptic Ca2+ Channels and Synaptic Transmission. *Cell Rep.* **4**, 66–75 (2013).

61. Xiao, M., Bosch, M. K., Nerbonne, J. M. & Ornitz, D. M. FGF14 localization and organization of the axon initial segment. *Mol. Cell. Neurosci.* **56**, 3930–403 (2013).

62. Liu, C. ju, Dib-Hajj, S. D., Renganathan, M., Cummins, T. R. & Waxman, S. G. Modulation of the cardiac sodium channel Nav1.5 by fibroblast growth factor

homologous factor 1B. *J. Biol. Chem.* **278**, 1029–1036 (2003).

63. Liu, C. J., Dib-Hajj, S. D. & Waxman, S. G. Fibroblast Growth Factor Homologous Factor 1B Binds to the C Terminus of the Tetrodotoxin-resistant Sodium Channel rNav1.9a (NaN). *J. Biol. Chem.* **276**, 18925–18933 (2001).

64. Wittmack, E. K. *et al.* Fibroblast growth factor homologous factor 2B: Association with Na v1.6 and selective colocalization at nodes of Ranvier of dorsal root axons. *J. Neurosci.* **24**, 6765–6775 (2004).

65. Scala, F. *et al.* Environmental Enrichment and Social Isolation Mediate Neuroplasticity of Medium Spiny Neurons through the GSK3 Pathway. *Cell Rep.* **23**, 555–567 (2018).

66. Itoh, N. & Ornitz, D. M. Functional evolutionary history of the mouse Fgf gene family. *Dev. Dyn.* **237**, 18–27 (2008).

67. Olsen, S. K. *et al.* Fibroblast Growth Factor (FGF) Homologous Factors Share Structural but Not Functional Homology with FGFs. *J. Biol. Chem.* **278**, 34226–34236 (2003).

68. Ornitz, D. M. & Itoh, N. The fibroblast growth factor signaling pathway. *Wiley Interdiscip. Rev. Dev. Biol.* **4**, 215–266 (2015).

69. Pablo, J. L. & Pitt, G. S. Fibroblast Growth Factor Homologous Factors: New Roles in Neuronal Health and Disease. *Neuroscientist* **22**, 19–25 (2016).

70. Smallwood, P. M. *et al.* Fibroblast growth factor (FGF) homologous factors: New members of the FGF family implicated in nervous system development. *Proc. Natl. Acad. Sci. U. S. A.* **93**, 9850–9857 (1996).

71. Liu, C. ju, Dib-Hajj, S. D., Renganathan, M., Cummins, T. R. & Waxman, S. G. Modulation of the cardiac sodium channel Nav1.5 by fibroblast growth factor homologous factor 1B. *J. Biol. Chem.* **278**, 1029–1036 (2003).

72. Rush, A. M. *et al.* Differential modulation of sodium channel Nav1.6 by two members of the fibroblast growth factor homologous factor 2 subfamily. *Eur. J. Neurosci.* **23**, 2551–2562 (2006).

73. Lou, J. Y. *et al.* Fibroblast growth factor 14 is an intracellular modulator of voltage-gated sodium channels. *J. Physiol.* **569**, 179–193 (2005).

74. Laezza, F. *et al.* The FGF14(F145S) mutation disrupts the interaction of FGF14 with voltage-gated Na+ channels and impairs neuronal excitability. *J. Neurosci.* **27**, 12033–44 (2007).

75. Ali, S., Shavkunov, A., Panova, N., Stoilova-McPhie, S. & Laezza, F. Modulation of the FGF14:FGF14 Homodimer Interaction Through Short Peptide Fragments. *CNS & Neurological Disorders - Drug Targets* **13**, 1559–1570 (2014).

76. Munoz-Sanjuan, I., Smallwood, P. M. & Nathans, J. Isoform diversity among fibroblast growth factor homologous factors is generated by alternative promoter usage and differential splicing. *J. Biol. Chem.* **275**, 2589–2597 (2000).

77. Goldfarb, M. *et al.* Fibroblast Growth Factor Homologous Factors Control Neuronal

Excitability through Modulation of Voltage-Gated Sodium Channels. *Neuron* **55**, 449–463 (2007).

78. Shakkottai, V. G. *et al.* FGF14 regulates the intrinsic excitability of cerebellar Purkinje neurons. *Neurobiol. Dis.* **33**, 81–88 (2009).

79. Bosch, M. K. *et al.* Proteomic analysis of native cerebellar iFGF14 complexes. *Channels* **10**, 297–312 (2016).

80. Hsu, W. C. J. *et al.* PPARgamma agonists rescue increased phosphorylation of FGF14 at S226 in the Tg2576 mouse model of Alzheimer's disease. *Exp. Neurol.* **295**, 1–17 (2017).

81. Xiao, M. *et al.* Impaired hippocampal synaptic transmission and plasticity in mice lacking fibroblast growth factor 14. *Mol. Cell. Neurosci.* **34**, 366–377 (2007).

82. Buffington, S. A. & Rasband, M. N. The axon initial segment in nervous system disease and injury. *Eur. J. Neurosci.* **34**, 1609–1619 (2011).

83. Emmett, M. R. *et al.* Integrative biological analysis for neuropsychopharmacology. *Neuropsychopharmacology* **39**, 5–23 (2014).

84. Kovacs, D. M., Gersbacher, M. T. & Kim, D. Y. Alzheimer's secretases regulate voltage-gated sodium channels. *Neurosci. Lett.* **486**, 68–72 (2010).

85. Gasparini, S. & Magee, J. C. Phosphorylation-dependent differences in the activation properties of distal and proximal dendritic Na+ channels in rat CA1 hippocampal neurons. *J. Physiol.* **541**, 665–672 (2002).

86. Loftis, J. L., King, D. D. & Colbert, C. M. Kinase-dependent loss of Na+ channel slow-inactivation in rat CA1 hippocampal pyramidal cell dendrites after brief exposure to convulsants. *Eur. J. Neurosci.* **18**, 1029–1032 (2003).

87. Colbert, C. M. & Johnston, D. Protein kinase C activation decreases activity-dependent attenuation of dendritic Na+ current in hippocampal CA1 pyramidal neurons. *J. Neurophysiol.* **79**, 491–495 (1998).

88. Cantrell, A. R. & Catterall, W. A. Neuromodulation of Na+ channels: an unexpected form of cellular plasticity. *Nat. Rev. Neurosci.* **2**, 397–407 (2001).

89. Scheuer, T. Regulation of sodium channel activity by phosphorylation. *Semin. Cell Dev. Biol.* **22**, 160–165 (2011).

90. Aromolaran, A. S., Chahine, M. & Boutjdir, M. Regulation of cardiac voltage-gated sodium channel by kinases: Roles of protein kinases A and C. *Handb. Exp. Pharmacol.* **246**, 161–184 (2018).

91. Berendt, F. J., Park, K.-S. & Trimmer, J. S. Multisite phosphorylation of voltage-gated sodium channel alpha subunits from rat brain. *J. Proteome Res.* **9**, 1976–1984 (2010).

92. Bréchet, A. *et al.* Protein kinase CK2 contributes to the organization of sodium channels in axonal membranes by regulating their interactions with ankyrin G. *J. Cell Biol.* **183**, 1101–1114 (2008).

93. James, T. F. *et al.* The Nav1.2 channel is regulated by GSK3. *Biochim. Biophys.*

Acta - Gen. Subj. **1850**, 832–844 (2015).

94. Wittmack, E. K., Rush, A. M., Hudmon, A., Waxman, S. G. & Dib-Hajj, S. D. Voltage-gated sodium channel Nav1.6 is modulated by p38 mitogen-activated protein kinase. *J. Neurosci.* **25**, 6621–6630 (2005).

95. Francis, K. R., Wei, L. & Yu, S. P. Src Tyrosine Kinases Regulate Neuronal Differentiation of Mouse Embryonic Stem Cells Via Modulation of Voltage-Gated Sodium Channel Activity. *Neurochem. Res.* **40**, 674–687 (2015).

96. Beacham, D., Ahn, M., Catterall, W. A. & Scheuer, T. Sites and molecular mechanisms of modulation of NaV1.2 channels by Fyn tyrosine kinase. *J. Neurosci.* **27**, 11543–11551 (2007).

97. Li, Y. *et al.* Nav1.7 is phosphorylated by Fyn tyrosine kinase which modulates channel expression and gating in a cell type-dependent manner. *Mol. Pain* **14**, (2018).

98. Humphrey, W., Dalke, A. & Schulten, K. VMD: Visual molecular dynamics. *J. Mol. Graph.* **14**, 33–38 (1996).

99. Shavkunov, A. S., Ali, S. R., Panova-elektronova, N. I. & Laezza, F. Split-Luciferase Complementation Assay to Detect Protein-Protein Interactions in Live Cells. in *Protein-Protein Interactions: Methods and Applications, Methods in Molecular Biology* **1278**, 497–514 (2015).

100. Wadsworth, P. A. *et al.* High-throughput screening against protein : protein interaction interfaces reveals anti-cancer therapeutics as potent modulators of the voltage-gated Na + channel complex. *Sci. Rep.* 1–15 (2019). doi:10.1038/s41598-019-53110-8

101. Luker, K. E. *et al.* Kinetics of regulated protein-protein interactions revealed with firefly luciferase complementation imaging in cells and living animals. *Proc. Natl. Acad. Sci.* **101**, 12288–12293 (2004).

102. Garrido, J. J. *et al.* Dynamic compartmentalization of the voltage-gated sodium channels in axons. *Biol. Cell* **95**, 437–445 (2003).

103. Garrido, J. J. *et al.* Identification of an axonal determinant in the C-terminus of the sodium channel Nav1.2. *EMBO J.* **20**, 5950–5961 (2001).

104. Garrido, J. J. *et al.* A targeting motif involved in sodium channel clustering at the axonal initial segment. *Science (80-.).* **300**, 2091–2094 (2003).

105. Sittampalam, Coussens, N. P., Brimacombe, K. & et al. Assay Guidance Manual. *Eli Lilly Co. Natl. Cent. Adv. Transl. Sci.* (2019).

106. Inglese, J. *et al.* High-throughput screening assays for the identification of chemical probes. *Nat. Chem. Biol.* **3**, 466–479 (2007).

107. Seashore-Ludlow, B. *et al.* Harnessing connectivity in a large-scale small-molecule sensitivity dataset. *Cancer Discov.* **5**, 1210–1223 (2015).

108. Amanchy, R. *et al.* A curated compendium of phosphorylation motifs. *Nature biotechnology* **25**, 285–286 (2007).

109. Blom, N., Sicheritz-Pontén, T., Gupta, R., Gammeltoft, S. & Brunak, S. Prediction of post-translational glycosylation and phosphorylation of proteins from the amino acid sequence. *Proteomics* **4**, 1633–1649 (2004).

110. Horn, H. *et al.* KinomeXplorer: An integrated platform for kinome biology studies. *Nature Methods* **11**, 603–604 (2014).

111. Wang, C., Chung, B. C., Yan, H., Lee, S. Y. & Pitt, G. S. Crystal structure of the ternary complex of a NaV C-terminal domain, a fibroblast growth factor homologous factor, and calmodulin. *Structure* **20**, 1167–1176 (2012).

112. Frostell-Karlsson, Å. *et al.* Biosensor analysis of the interaction between immobilized human serum albumin and drug compounds for prediction of human serum albumin binding levels. *J. Med. Chem.* **43**, 1986–1992 (2000).

113. Brideau, C., Gunter, B., Pikounis, B. & Liaw, A. Improved statistical methods for hit selection in high-throughput screening. *J. Biomol. Screen.* **8**, 634–647 (2003).

114. Makarenkov, V. *et al.* An efficient method for the detection and elimination of systematic error in high-throughput screening. *Bioinformatics* **23**, 1648–1657 (2007).

115. Pantoliano, M. W. *et al.* High-Density Miniaturized Thermal Shift Assays as a General Strategy for Drug Discovery. *J. Biomol. Screen.* **6**, 429–440 (2001).

116. Ahern, C. A., Payandeh, J., Bosmans, F. & Chanda, B. The hitchhiker's guide to the voltage-gated sodium channel galaxy. *J. Gen. Physiol.* **147**, 1–24 (2016).

117. Xu, L. *et al.* Voltage-gated sodium channels: structures, functions, and molecular modeling. *Drug Discov. Today* **24**, 1389–1397 (2019).

118. Stoilova-McPhie, S., Ali, S. & Laezza, F. Protein-Protein Interactions as New Targets for Ion Channel Drug Discovery. *Austin J. Pharmacol. Ther.* **1**, (2013).

119. Leterrier, C., Brachet, A., Fache, M. P. & Dargent, B. Voltage-gated sodium channel organization in neurons: Protein interactions and trafficking pathways. *Neurosci. Lett.* **486**, 92–100 (2010).

120. Molinarolo, S., Granata, D., Carnevale, V. & Ahern, C. A. Mining Protein Evolution for Insights into Mechanisms of Voltage-Dependent Sodium Channel Auxiliary Subunits. *Handb. Exp. Pharmacol.* **246**, 33–49 (2018).

121. Hoxha, E. *et al.* Emerging roles of Fgf14 in behavioral control. *Behav. Brain Res.* **356**, 257–265 (2019).

122. Wildburger, N. C. *et al.* Quantitative Proteomics Reveals Protein–Protein Interactions with Fibroblast Growth Factor 12 as a Component of the Voltage-Gated Sodium Channel 1.2 (Nav1.2) Macromolecular Complex in Mammalian Brain. *Mol. Cell. Proteomics* **14**, 1288–1300 (2015).

123. Symonds, J. D. & Zuberi, S. M. Genetics update: Monogenetics, polygene disorders and the quest for modifying genes. *Neuropharmacology* **132**, 3–19 (2018).

124. Azad, T., Tashakor, A. & Hosseinkhani, S. Split-luciferase complementary assay: applications, recent developments, and future perspectives. *Anal. Bioanal. Chem.*

406, 5541–5560 (2014).

125. Wehr, M. C. & Rossner, M. J. Split protein biosensor assays in molecular pharmacological studies. *Drug Discov. Today* **21**, 415–429 (2016).

126. Shavkunov, A. S., Ali, S. R., Panova-Elektronova, N. I. & Laezza, F. Split-luciferase complementation assay to detect channel-protein interactions in live cells. *Methods Mol. Biol.* **1278**, 497–514 (2015).

127. Fertig, N., Blick, R. H. & Behrends, J. C. Whole cell patch clamp recording performed on a planar glass chip. *Biophys. J.* **82**, 3056–3062 (2002).

128. Kanduc, D. Pentapeptides as minimal functional units in cell biology and immunology. *Curr. Protein Pept. Sci.* **14**, 111–120 (2013).

129. Deriu, D. *et al.* Determination of the minimal functional ligand-binding domain of the GABAB(1b) receptor. *Biochem. J.* **386**, 423–431 (2005).

130. Wang, W. *et al.* Kif2C minimal functional domain has unusual nucleotide binding properties that are adapted to microtubule depolymerization. *J. Biol. Chem.* **287**, 15143–15153 (2012).

131. Zhou, Y. *et al.* Cross-linking of Orai1 channels by STIM proteins. *Proc. Natl. Acad. Sci.* **115**, E3398–E3407 (2018).

132. Zhou, Y. *et al.* The STIM-Orai coupling interface and gating of the Orai1 channel. *Cell Calcium* **63**, 8–13 (2017).

133. Ma, G. *et al.* Molecular Determinants for STIM1 Activation During Store- Operated Ca2+ Entry. *Curr. Mol. Med.* **17**, 60–69 (2017).

134. Inglese, J. *et al.* High-throughput screening assays for the identification of chemical probes. *Nat. Chem. Biol.* **3**, 466–479 (2007).

135. Chai, S. C., Goktug, A. N. & Chen, T. Liquid handling devices in drug discovery: When, what, why? *Eur. Pharm. Rev.* **18**, 11–14 (2013).

136. Szabat, M. *et al.* High-content screening identifies a role for Na+ channels in insulin production. *R. Soc. Open Sci.* **2**, (2015).

137. Rajwa, B. Effect-size measures as descriptors of assay quality in high-content screening: A brief review of some available methodologies. *Assay Drug Dev. Technol.* **15**, 15–29 (2017).

138. Wang, Y. L., Wang, Y., Tong, L. & Wei, Q. Overexpression of calcineurin B subunit (CnB) enhances the oncogenic potential of HEK293 cells. *Cancer Sci.* **99**, 1100–1108 (2008).

139. Trask, O. J. Guidelines for microplate selection in high content imaging. *Methods Mol. Biol.* **1683**, 75–88 (2018).

140. Obergrussberger, A. *et al. Automated patch clamp analysis of nAChα7 and Nav1.7 channels*. *Current Protocols in Pharmacology* (2014). doi:10.1002/0471141755.ph1113s65

141. Oliva, M. K. *et al.* Physiological and genetic analysis of multiple sodium channel

variants in a model of genetic absence epilepsy. *Neurobiol. Dis.* **67**, 180–190 (2014).

142. Bradley, J. R. TNF-mediated inflammatory disease. *J. Pathol.* **214**, 149–160 (2008).

143. McFarlane, S. M. *et al.* Differential activation of nuclear factor-kappaB by tumour necrosis factor receptor subtypes. TNFR1 predominates whereas TNFR2 activates transcription poorly. *FEBS Lett* **515**, 119–126 (2002).

144. Roskoski, R. J. RAF protein-serine/threonine kinases: structure and regulation. *Biochem. Biophys. Res. Commun.* **399**, 313–317 (2010).

145. Rath, N. & Olson, M. F. Rho-associated kinases in tumorigenesis: re-considering ROCK inhibition for cancer therapy. *EMBO Rep.* **13**, 900–908 (2012).

146. Eriksen, J., Jorgensen, T. N. & Gether, U. Regulation of dopamine transporter function by protein-protein interactions: new discoveries and methodological challenges. *J. Neurochem.* **113**, 27–41 (2010).

147. Tesmer, J. J. G. Pharmacology. Hitting the hot spots of cell signaling cascades. *Science* **312**, 377–378 (2006).

148. Wenthur, C. J., Gentry, P. R., Mathews, T. P. & Lindsley, C. W. Drugs for allosteric sites on receptors. *Annu. Rev. Pharmacol. Toxicol.* **54**, 165–184 (2014).

149. Nickols, H. H. & Conn, P. J. Development of allosteric modulators of GPCRs for treatment of CNS disorders. *Neurobiol. Dis.* **61**, 55–71 (2014).

150. Tarnawa, I., Bolcskei, H. & Kocsis, P. Blockers of voltage-gated sodium channels for the treatment of central nervous system diseases. *Recent Pat. CNS Drug Discov.* **2**, 57–78 (2007).

151. Stoilova-McPhie, S., Ali, S. & Laezza, F. Protein-Protein Interactions as New Targets for Ion Channel Drug Discovery. *Austin J. Pharmacol. Ther.* **1**, 1–12 (2013).

152. Luttrell, L. M., Maudsley, S. & Bohn, L. M. Fulfilling the Promise of 'Biased' G Protein-Coupled Receptor Agonism. *Mol. Pharmacol.* **88**, 579–588 (2015).

153. Avanzini, G. *et al.* The impact of genetic and experimental studies on classification and therapy of the epilepsies. *Neurosci. Lett.* **667**, 17–26 (2018).

154. Tarnok, A., Pierzchalski, A. & Valet, G. Potential of a cytomics top-down strategy for drug discovery. *Curr. Med. Chem.* **17**, 1719–1729 (2010).

155. Aoto, J., Nam, C. I., Poon, M. M., Ting, P. & Chen, L. Synaptic Signaling by All-Trans Retinoic Acid in Homeostatic Synaptic Plasticity. *Neuron* **60**, 308–320 (2008).

156. Cordon-Barris, L. *et al.* Mutation of the 3-Phosphoinositide-Dependent Protein Kinase 1 (PDK1) Substrate-Docking Site in the Developing Brain Causes Microcephaly with Abnormal Brain Morphogenesis Independently of Akt, Leading to Impaired Cognition and Disruptive Behaviors. *Mol. Cell. Biol.* **36**, 2967–2982 (2016).

157. Weiss, J. B. *et al.* Anaplastic Lymphoma Kinase and Leukocyte Tyrosine Kinase: Functions and genetic interactions in learning, memory and adult neurogenesis. *Pharmacol. Biochem. Behav.* **100**, 566–574 (2012).

158. Mangieri, R. A., Maier, E. Y., Buske, T. R., Lasek, A. W. & Morrisett, R. A. Anaplastic Lymphoma Kinase Is a Regulator of Alcohol Consumption and Excitatory Synaptic Plasticity in the Nucleus Accumbens Shell. *Front. Pharmacol.* **8**, 533 (2017).

159. Mascarenhas, J. *et al.* Phase II trial of Lestaurtinib, a JAK2 inhibitor, in patients with myelofibrosis. *Leuk. Lymphoma* **60**, 1343–1345 (2019).

160. Brodeur, G. M. & Bagatell, R. Mechanisms of neuroblastoma regression. *Nat. Rev. Clin. Oncol.* **11**, 704–713 (2014).

161. Mellesmoen, A., Sheeler, C., Ferro, A., Rainwater, O. & Cvetanovic, M. Brain Derived Neurotrophic Factor (BDNF) Delays Onset of Pathogenesis in Transgenic Mouse Model of Spinocerebellar Ataxia Type 1 (SCA1). *Front. Cell. Neurosci.* **12**, 509 (2018).

162. Obeid, M., Rosenberg, E. C., Klein, P. M. & Jensen, F. E. Lestaurtinib (CEP-701) attenuates 'second hit' kainic acid-induced seizures following early life hypoxic seizures. *Epilepsy Res.* **108**, 806–810 (2014).

163. Medlej, Y. *et al.* Lestaurtinib (CEP-701) modulates the effects of early life hypoxic seizures on cognitive and emotional behaviors in immature rats. *Epilepsy Behav.* **92**, 332–340 (2019).

164. Catterall, W. A. Signaling complexes of voltage-gated sodium and calcium channels. *Neurosci. Lett.* **486**, 107–116 (2010).

165. Nicolas, C. S. *et al.* The role of JAK-STAT signaling within the CNS. *Jak-Stat* **2**, e22925 (2013).

166. Remy, I. & Michnick, S. W. A highly sensitive protein-protein interaction assay based on Gaussia luciferase. *Nat. Methods* **3**, 977–979 (2006).

167. Park, S. Y., Kim, Y. H. & Park, G. Cucurbitacins attenuate microglial activation and protect from neuroinflammatory injury through Nrf2/ARE activation and STAT/NF-κB inhibition. *Neurosci. Lett.* **609**, 129–136 (2015).

168. Singer, J. W., Al-Fayoumi, S., Taylor, J., Velichko, S. & O'Mahony, A. Comparative phenotypic profiling of the JAK2 inhibitors ruxolitinib, fedratinib, momelotinib, and pacritinib reveals distinct mechanistic signatures. *PLoS One* **14**, 1–14 (2019).

169. Singer, J. W. *et al.* Comprehensive kinase profile of pacritinib, a nonmyelosuppressive janus kinase 2 inhibitor. *J. Exp. Pharmacol.* **8**, 11–19 (2016).

170. Aittomäki, S. & Pesu, M. Therapeutic targeting of the JAK/STAT pathway. *Basic Clin. Pharmacol. Toxicol.* **114**, 18–23 (2014).

171. Pardanani, A. *et al.* CYT387, a selective JAK1/JAK2 inhibitor: In vitro assessment of kinase selectivity and preclinical studies using cell lines and primary cells from polycythemia vera patients. *Leukemia* **23**, 1441–1445 (2009).

172. Uitdehaag, J. C. M. *et al.* A guide to picking the most selective kinase inhibitor tool compounds for pharmacological validation of drug targets. *Br. J. Pharmacol.* **166**,

858–876 (2012).

173. Smolinski, M. P. *et al.* Discovery of Novel Dual Mechanism of Action Src Signaling and Tubulin Polymerization Inhibitors (KX2-391 and KX2-361). *J. Med. Chem.* **61**, 4704–4719 (2018).

174. Venkatesan, K., Liu, Y. & Goldfarb, M. Fast-onset long-term open-state block of sodium channels by A-type FHFs mediates classical spike accommodation in hippocampal pyramidal neurons. *J. Neurosci.* **34**, 16126–16139 (2014).

175. White, H. V., Brown, S. T., Bozza, T. C. & Raman, I. M. Effects of FGF14 and NaVβ4 deletion on transient and resurgent Na current in cerebellar Purkinje neurons. *J. Gen. Physiol.* **151**, 1300–1318 (2019).

176. Dover, K., Solinas, S., D'Angelo, E. & Goldfarb, M. Long-term inactivation particle for voltage-gated sodium channels. *J. Physiol.* **588**, 3695–3711 (2010).

177. Sarabipour, S. & Hristova, K. Mechanism of FGF receptor dimerization and activation. *Nat. Commun.* **7**, 10262 (2016).

178. Clatot, J. *et al.* Voltage-gated sodium channels assemble and gate as dimers. *Nat. Commun.* **8**, 2077 (2017).

179. Hubbard, S. R. Mechanistic insights into regulation of JAK2 tyrosine kinase. *Front. Endocrinol. (Lausanne).* **8**, 1–7 (2018).

180. Chen, X. M., Yu, Y. H., Wang, L., Zhao, X. Y. & Li, J. R. Effect of the JAK2/STAT3 signaling pathway on nerve cell apoptosis in rats with white matter injury. *Eur. Rev. Med. Pharmacol. Sci.* **23**, 321–327 (2019).

181. Zhang, W., Jin, Y., Wang, D. & Cui, J. Neuroprotective effects of leptin on cerebral ischemia through JAK2/STAT3/PGC-1-mediated mitochondrial function modulation. *Brain Res. Bull.* **156**, 118–130 (2020).

182. Tian, R. H., Bai, Y., Li, J. Y. & Guo, K. M. Reducing PRLR expression and JAK2 activity results in an increase in BDNF expression and inhibits the apoptosis of CA3 hippocampal neurons in a chronic mild stress model of depression. *Brain Res.* **1725**, 146472 (2019).

183. Wang, Z.-H. *et al.* Deficiency in BDNF/TrkB Neurotrophic Activity Stimulates delta-Secretase by Upregulating C/EBPbeta in Alzheimer's Disease. *Cell Rep.* **28**, 655-669.e5 (2019).

184. Turrigiano, G. Homeostatic signaling: the positive side of negative feedback. *Curr. Opin. Neurobiol.* **17**, 318–324 (2007).

185. Liu, X., Testa, B. & Fahr, A. Lipophilicity and Its Relationship with Passive Drug Permeation. *Pharm. Res.* **28**, 962–977 (2011).

186. Refsgaard, H. H. F. *et al.* In Silico Prediction of Membrane Permeability from Calculated Molecular Parameters. *J. Med. Chem.* **48**, 805–811 (2005).

187. Leung, S. S. F., Mijalkovic, J., Borrelli, K. & Jacobson, M. P. Testing Physical Models of Passive Membrane Permeation. *J. Chem. Inf. Model.* **52**, 1621–1636 (2012).

188. Bennion, B. J. *et al.* Predicting a Drug's Membrane Permeability: A Computational Model Validated With in Vitro Permeability Assay Data. *J. Phys. Chem. B* **121**, 5228–5237 (2017).

189. Wang, Y. *et al.* An experimentally validated approach to calculate the blood-brain barrier permeability of small molecules. *Sci. Rep.* **9**, 1–11 (2019).

190. Francis, T. C. & Lobo, M. K. Emerging Role for Nucleus Accumbens Medium Spiny Neuron Subtypes in Depression. *Biol. Psychiatry* **81**, 645–653 (2017).

191. Alshammari, M. A., Alshammari, T. K. & Laezza, F. Improved Methods for Fluorescence Microscopy Detection of Macromolecules at the Axon Initial Segment. *Front. Cell. Neurosci.* **10**, 5 (2016).

192. Sadaghiani, A. M. *et al.* Identification of Orai1 channel inhibitors by using minimal functional domains to screen small molecule microarrays. *Chem. Biol.* **21**, 1278–1292 (2014).

193. Ahn, M., Beacham, D., Westenbroek, R. E., Scheuer, T. & Catterall, W. A. Regulation of NaV1.2 channels by brain-derived neurotrophic factor, TrkB, and associated Fyn kinase. *J. Neurosci.* **27**, 11533–11542 (2007).

194. Minichiello, L. TrkB signalling pathways in LTP and learning. *Nat. Rev. Neurosci.* **10**, 850–60 (2009).

195. Noorolyai, S., Shajari, N., Baghbani, E., Sadreddini, S. & Baradaran, B. The relation between PI3K/AKT signalling pathway and cancer. *Gene* **698**, 120–128 (2019).

Vita

Paul Alexander Wadsworth was born on November 27th, 1991 in Irving, Texas to Marion and Roy Wadsworth. He is the fourth of six children, including Ellen, Charles, John, Michael, and Ann Wadsworth. Paul obtained his high school diploma from Grapevine High School. In 2010, Paul moved to Chicago, Illinois and attended Loyola University Chicago where he earned his Bachelor of Science in Bioinformatics with a minor in neuroscience. While at Loyola, he also continued his music education (piano) with Anthony Molinaro, as well as conducted *in silico* protein research under the guidance of Drs. Dali Liu and Kenneth Olsen. In 2011, Paul attended a summer research internship studying nanophotonics at the University of New Mexico in Albuquerque. He entered the combined M.D./Ph.D. program at UTMB (Galveston, TX) in the Summer of 2014, and began the program with his first research rotation with Dr. B.M. Pettitt that resulted in co-authorship on a manuscript published in the Journal of Proteome Research. In the late Summer of 2016, Paul then entered the PhD phase of the program under the mentorship of Dr. Fernanda Laezza. During this time, Paul has had the pleasure of mentoring five high-school and undergraduate students. Additionally, Paul was awarded the highly prestigious PhRMA Fellowship in Pharmacology in 2019 for his research project. At the time of defending this Dissertation, Paul has co-authored a total of five publications, two of which he is first-author. Additionally, two first-author manuscripts are submitted and currently under review, while two others are in preparation.

Permanent address: 149 San Fernando Dr., Galveston, Texas 77550.

This dissertation was typed by Paul Alexander Wadsworth.